UNIVERSIDAD DE JAÉN
ESCUELA POLITÉCNICA
SUPERIOR DE JAÉN
DEPARTAMENTO DE INGENIERÍA
MECÁNICA Y MINERA

TESIS DOCTORAL

STUDY OF THE STABILITY OF JETS AND WAKED. APPLICATION TO WAKE PAST SLENDER BODIES WITH BLUNT TRAILING ADGE

PRESENTADA POR:
JOSÉ IGNACIO JIMÉNEZ GONZÁLEZ

DIRIGIDA POR:
DR. D. CARLOS MARTÍNEZ BAZÁN
DR. D. ENRIQUE SANMIGUEL ROJAS

JAÉN, 12 DE JULIO DE 2013

ISBN 978-84-8439-413-6

PhD Thesis

Study of the stability of jets and wakes

Application to the wake past slender bodies with blunt trailing edge

José Ignacio Jiménez González

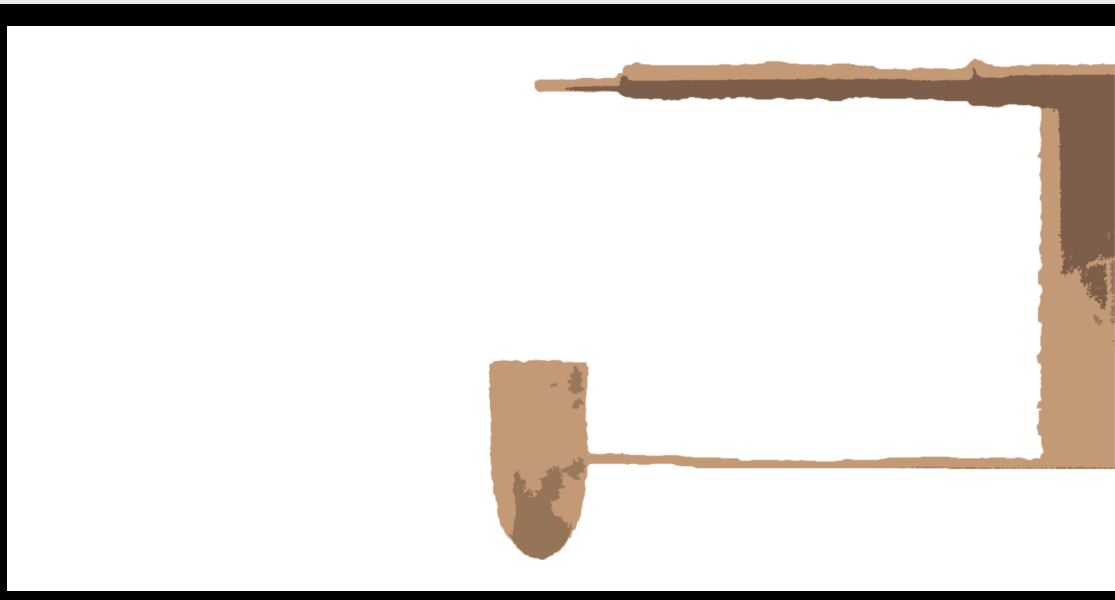

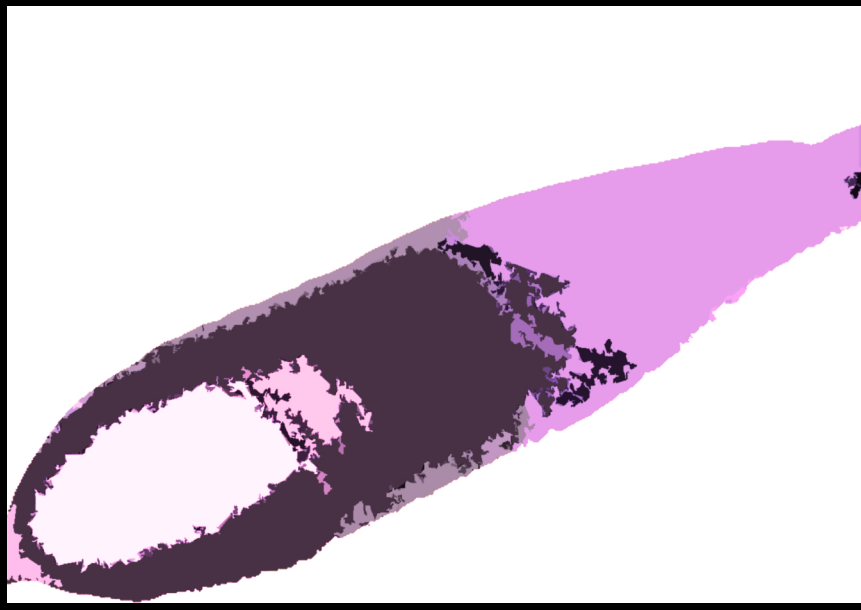

Universidad de Jaén

UNIVERSIDAD DE JAÉN

Study of the stability of jets and wakes. Application to the wake past slender bodies with blunt trailing edge

Tesis Doctoral

Autor
José Ignacio Jiménez González

Directores
Prof. Carlos Martínez Bazán Dr. Enrique Sanmiguel Rojas

Jaén, Julio 2013

DEPARTAMENTO DE INGENIERÍA MECÁNICA Y MINERA
Escuela Politécnica Superior

Study of the stability of jets and wakes. Application to the wake past slender bodies with blunt trailing edge

Autor
José Ignacio Jiménez González

Directores de Tesis
Prof. Carlos Martínez Bazán Dr. Enrique Sanmiguel Rojas

Jaén, Julio 2013

A mis padres, hermanos, abuelas y Fee.

Tesis doctoral

Study of the stability of jets and wakes. Application to the wake past slender bodies with blunt trailing edge

Autor: José Ignacio Jiménez González

Directores de Tesis:
Prof. Carlos Martínez Bazán Dr. Enrique Sanmiguel Rojas

Firma del Tribunal Calificador:

Firma

Presidente: Prof. Jacques Magnaudet
Vocal: Prof. Vassilis Theofilis
Secretario: Dr. Alejandro Sevilla Santiago
Suplente: Dr. José Manuel Gordillo Arias de Saavedra
Suplente: Prof. Julio Soria

Calificación:

Jaén, de Julio de 2013

Agradecimientos

Muchas personas han contribuido de diversa forma a que esta Tesis haya sido posible, y sin su apoyo y ayuda hoy no estaría escribiendo estas líneas. Principalmente quiero agradecer a mis directores de Tesis, Carlos y Enrique, todo lo que han hecho por mí y por este trabajo. Gracias por haber intentado siempre transmitirme aquello que os apasiona, por vuestra habilidad para explicar y simplificar los problemas, por haber confiado siempre en mí y ser pacientes cuando las cosas no han salido, y por no escatimar en ánimos cuando había algún resultado. A Enrique, mi más sincero agradecimiento por tu aprecio, por poner a mi disposición todos tus recursos y tu tiempo, por guiarme por la senda del numérico y la estabilidad, haciéndolo todo más fácil, y por acudir al rescate cuando lo he necesitado, sobre todo en esta última fase de la tesis, en la que, a pesar de la distancia, no has parado de motivar e insuflar ánimos. Y Carlos, difícilmente puedo resumir el sentimiento de agradecimiento en unas pocas palabras, pero en síntesis, gracias por haberme dado esta oportunidad maravillosa de poder trabajar contigo y aprender de tí, por enseñarme a disfrutar de la Mecánica de Fluidos y hacerme creer que todo se puede conseguir con trabajo, por estar siempre disponible, y en general por tu amistad.

También quisiera agradecer muy especialmente a las personas que me han guiado durante las estancias de investigación realizadas en otros centros. Éstas son Alejandro Sevilla, de la Universidad Carlos III de Madrid, y Pierre Brancher y Christophe Airiau, del Institut de Mécanique des Fluides de Toulouse. Gracias Alejandro, no sólo por tu dedicación y tiempo durante mi estancia en Madrid, si no porque una parte de esta tesis es también tuya, porque has sido una pieza importante, incluso desde antes de que empezase, y porque con tu pasión y motivación has sido un ejemplo a seguir. Y a Pierre Brancher, por su ayuda inestimable y tiempo, su cercanía y predisposición a explicar y ayudar durante mis periodos en Toulouse.

Muy sinceramente, quiero dar la gracias a mis compañeros y amigos de la Universidad de Jaén: José Carlos, Rocío y Cándido. Porque hemos compartido mucho y sufrido juntos, porque habéis contribuido a que estos años hayan merecido la pena, y por haber sido una motivación extra para continuar trabajando con alegría y disfrutando de todo lo hecho. Por formar esa pequeña familia, muchas gracias. En ella incluyo lógicamente a Cosme, tú también has contribuido enormemente a sacar este trabajo adelante. No me quiero olvidar tampoco de compañeros durante las estancias: de toda la gente del Departamento de Ingeniería Térmica y de Fluidos de la Universidad Carlos III de Madrid, especialmente de Mariano y César; y de Luigi, Omar y Marc, del Institut de Mécanique des Fluides de Toulouse. Incluyo también en este grupo de gente que ha hecho más llevadero el trabajo durante este tiempo a Juan, Rosa, María Jesús y Bea.

Por último, quiero dar las gracias a mi soporte más necesario: mi familia. A mis padres, por su apoyo incondicional en todo este largo proceso de formación, porque han sido fundamentales para superar los momentos de debilidad que han surgido, por confiar siempre en mí, y por su cariño, les estaré siempre agradecido. A mis hermanos, Jesús y Carlos, por su amistad, por estar siempre ahí, porque han hecho que todo haya sido más fácil, y en definitiva, por la felicidad que me han aportado. También les debo parte del ánimo y la felicidad en todo este tiempo a mis abuelas. Finalmente, quiero dar las gracias a Fee, por ser tan especial y enseñarme a ver la vida de otra manera, por apoyarme y ser paciente durante todo este largo periodo en la distancia, lleno de

incertidumbre y dudas (Danke für deine Geduld und deine Liebe). A todos ellos, gracias.

Resumen

El flujo tras cuerpos romos es una configuración típica en multitud de aplicaciones de ingeniería, como por ejemplo, la industria aeronaútica, la industria automovilística o la ingeniería civil. La geometría de los cuerpos romos provoca la separación masiva de la capa límite y la creación de una estela que se extiende espacialmente detrás del cuerpo. Esto se traduce en una gran fuerza de arrastre actuando sobre el cuerpo y, bajo determinadas circunstancias, en una estela no estacionaria caracterizada por el desprendimiento alternativo de vórtices, que conlleva riesgo de vibraciones y resonancias para el cuerpo y generación de ruido. La importancia de estos problemas ha dado lugar a una rica literatura y gran número de trabajos que tratan sobre la descripción de los regímenes inestables y el desarrollo de estrategias de control para estelas tras configuraciones axilsimétricas. No obstante, a pesar de su relevancia, la secuencia de regímenes inestables que desemboca en la turbulencia en estelas tras cuerpos esbeltos de base roma no se comprende completamente a fecha de hoy. Por tanto, esta Tesis tiene por objeto la caracterización de estelas laminares tras este tipo de cuerpos, y aprovechar el conocimiento obtenido para investigar el efecto de tres métodos de control de tipo pasivo. Diversas técnicas han sido empleadas con este objetivo: experimentos de anemometría de hilo caliente, análisis de estabilidad lineal global y simulaciones numéricas tridimensionales.

La primera parte de la tesis está dedicada a la descripción de las bifurcaciones y los regímenes inestables que aparecen para números de Reynolds crecientes, en la estela de cuerpos esbeltos de base roma con cabeza elipsoidal, a bajos números de Reynolds. Las diferentes técnicas empleadas demuestran que una primera bifurcación regular supercrítica rompe la axilsimetría, evolucionando el flujo hacia un régimen estacionario que muestra una simetría planar, de manera similar a lo que sucede en la estela de la esfera. Una segunda bifurcación supercrítica de tipo Hopf desencadena el inicio del desprendimiento periódico de vórtices, mientras que la simetría planar se mantiene. Se muestra igualmente que una tercera bifurcación de tipo Hopf tiene lugar a números de Reynolds ligeramente superiores, asociada con el comienzo de una modulación de baja frecuencia en el desprendimiento de vórtices, reteniendo igualmente la simetría planar, de manera contraria al caso de la esfera. Además, se analiza el efecto de la relación de esbeltez del cuerpo en las propiedades de estabilidad, encontrando que incrementar el valor de la relación de aspecto mencionada conlleva el aumento del valor de los Reynolds críticos para los que se producen las transiciones.

El análisis de las propiedades de estabilidad de estelas tras cuerpos esbeltos de base roma continúa con la implementación de métodos de control de tipo pasivo para un cuerpo de relación de esbeltez igual a 2. Primeramente se investiga el soplado de base homogéneo, demostrando que tanto el régimen de desprendimiento periódico de vórtices como el estado estacionario son estabilizados cuando los valores de soplado en la base superan sendos valores críticos. Estos valores de soplado necesarios para la estabilización de la estela crecen con el número de Reynolds. La influencia de la densidad es también evaluada de manera experimental por medio de soplado ligero, no observado diferencias importantes respecto al soplado homogéneo. Por otro lado, la adición de una cavidad en la base del cuerpo se adopta como segunda estrategia de control. Se demuestra que valores crecientes de la longitud de la cavidad tienen un efecto estabilizador igualmente creciente respecto a las bifurcaciones primera y segunda, aunque este efecto tiene un límite asintótico alrededor de

un valor de 0.7 para la relación entre la longitud de la cavidad y el diámetro del cuerpo. En este sentido, la estabilización depende de manera similar del diámetro de la cavidad, ya que no se ha observado ningún efecto para valores por debajo de 0.6 de la relación entre el diámetro de la cavidad y el diámetro del cuerpo.

Finalmemte, inspirado en el giro aplicado a este tipo de cuerpos en turbomaquinaria o vuelo de proyectiles, se estudia la estela tras cuerpos esbeltos de base roma con rotación, centrándose el análisis en las modificaciones de las propiedades de estabilidad y fuerzas hidrodinámicas que la rotación ocasiona. En este sentido, se muestra que bajos niveles de giro estabilizan la estela, recuperando la axilsimetría y, además, los regímenes inestables existentes en la estela natural sin giro se vuelven complejos, comportándose como ondas rotatorias cerca de los límites de la axilsimetría. Además, se observa un nuevo régimen para valores elevados de rotación y bajos números de Reynolds. Se demuestra que la desestabilización de tres modos globales distintos está detrás del panorama descrito de regímenes inestables.

Los resultados presentados en esta memoria están recogidos parcialmente o en su totalidad en las siguientes publicaciones:

- **Publicación 1.** P. Bohorquez, E. Sanmiguel-Rojas, A. Sevilla, J.I. Jiménez-González, C. Martínez-Bazán, C., 2011.
  Stability and dynamics of the laminar wake past a slender blunt-based axisymmetric body. *J. Fluid. Mech.* **676**, 110-144.
- **Publicación 2.** E. Sanmiguel-Rojas, J.I. Jiménez-González, P. Bohorquez, G. Pawlak, C. Martínez-Bazán, 2011.
  Effect of base cavities on the stability of the wake behind slender blunt-based axisymmetric bodies. *Phys. Fluids* **23**, 114103-11.
- **Publicación 3.** J.I. Jiménez-González, E. Sanmiguel-Rojas, A. Sevilla, C. Martínez-Bazán, 2013.
  Laminar flow past a spinning bullet-shaped body at moderate angular velocities. *Aceptado para su publicación en J. Fluids Struct.*
- **Publicación 4.** J.I. Jiménez-González, A. Sevilla, E. Sanmiguel-Rojas, C. Martínez-Bazán, 2013.
  Global stability analysis of the axisymmetric wake past a spinning bullet-shaped body. *Enviado a Phys. Fluids.*
- **Publicación 5.** J.I. Jiménez-González, P. Brancher, C. Martínez-Bazán, 2013.
  Long-time and short-time evolution of perturbations for parallel round jets. *En preparación para ser enviado a Phys. Fluids.*

Palabras clave: Estabilidad y control de estelas, cuerpo axilsimétrico, cuerpo esbelto de base roma, transiciones, control pasivo, soplado de base, cavidades traseras, cuerpo rotatorio, estabilidad lineal BiGlobal, crecimiento transitorio, chorros paralelos.

Abstract

Flow past bluff bodies is a typical configuration in many engineering applications, as for instance, aeronautic industry, cars industry or civil engineering, etc. Bluff-bodies geometry provokes the massive separation of the boundary layer and creation of a spatially developing wake behind the body. This translates into large drag force opposed to the body motion, and under certain circumstances, into an unstable wake that features alternate vortex shedding, entailing risks of vibrations and resonances on the body, and noise generation. The importance of such problems has given rise to rich literature and many works about the description of unstable regimes and development of control strategies for wakes behind axisymmetric configurations. However, despite of their relevance, the sequence of unstable regimes leading to turbulence in wakes behind slender bodies with blunt-trailing edge is nowadays not completely understood. Therefore, this Thesis aims at shedding some light on laminar wakes behind these kind of bodies, and takes advantage of the insight gained to investigate the effect of three passive control methods. Diverse techniques have been used with this purpose, namely, hot-wire anemometry experiments, global linear stability analyses and three-dimensional numerical simulations.

The first part of the dissertation is devoted to describe the bifurcations and unstable regimes taking place with increasing Reynolds numbers, at the wake of bullet-shaped bodies with rounded ellipsoidal nose, at low Reynolds numbers. The different techniques employed demonstrate that a supercritical regular axisymmetry-breaking bifurcation, leads the flow towards a steady regime that shows planar symmetry, in line with the sphere. A second supercritical Hopf bifurcation triggers the onset of vortex shedding, while keeping the planar symmetry. It is also shown that a third Hopf bifurcation occurs at Reynolds numbers slightly higher, associated to the beginning of a low frequency modulation in the shedding, retaining also the planar symmetry. Moreover, the effect of the body length-to-diameter ratio on the stability properties is analyzed, finding that increasing this ratio value entails increasing values of the critical Reynolds numbers for which the bifurcations described take place.

The analysis of the stability properties of wakes behind bullet-shaped bodies continues with the implementation of passive control methods for a body of length-to-diameter ratio equals 2. Firstly, homogeneous base bleed is investigated, proving that both the vortex shedding regime and the steady state are stabilized when two progressive critical values of bleed are injected through the base. The values of bleed required for the stabilization of the wake increases with the Reynolds number. The influence of density is also experimentally evaluated by means of light bleed, observing no important differences with regards to homogeneous bleed. On the other hand, the addition of a rear cavity at the base of the body is adopted as the second control strategy. We prove that increasing the cavity length has a growing stabilizing effect regarding the first steady and second oscillatory bifurcations, this effect reaching an asymptotic limit around a cavity-length-to-body-diameter ratio equal 0.7. In this sense, the stabilization depends also on the cavity diameter, since for cavity-diameter-to-body-diameter ratios below 0.6 no effect is observed.

Finally, inspired on the spinning motion of this kind of bodies in turbomachinery or projectile flight, we study the wake behind a rotating bullet-shaped body, focusing on the modifications of the stability properties and hydrodynamic forces that rotation brings. It is shown that low level of

spin stabilizes the wake, retrieving the axisymmetry, and in addition, the unstable regimes existing at the natural wake become more complex, behaving as rotating waves close to axisymmetry borders. Furthermore, a new unstable regime is observed at high values of rotation and low Reynolds numbers. We prove that the destabilizations of three distinct global linear modes are behind the picture of unstable regimes described.

The results presented in this dissertation are comprised in part or totally in the following publications:

- **Paper 1.** P. Bohorquez, E. Sanmiguel-Rojas, A. Sevilla, J.I. Jiménez-González, C. Martínez-Bazán, C., 2011.
  Stability and dynamics of the laminar wake past a slender blunt-based axisymmetric body. *J. Fluid. Mech.* **676**, 110-144.
- **Paper 2.** E. Sanmiguel-Rojas, J.I. Jiménez-González, P. Bohorquez, G. Pawlak, C. Martínez-Bazán, 2011.
  Effect of base cavities on the stability of the wake behind slender blunt-based axisymmetric bodies. *Phys. Fluids* **23**, 114103-11.
- **Paper 3.** J.I. Jiménez-González, E. Sanmiguel-Rojas, A. Sevilla, C. Martínez-Bazán, 2013. Laminar flow past a spinning bullet-shaped body at moderate angular velocities. *Accepted for publication in J. Fluids Struct.*
- **Paper 4.** J.I. Jiménez-González, A. Sevilla, E. Sanmiguel-Rojas, C. Martínez-Bazán, 2013. Global stability analysis of the axisymmetric wake past a spinning bullet-shaped body. *Submitted to Phys. Fluids.*
- **Paper 5.** J.I. Jiménez-González, P. Brancher, C. Martínez-Bazán, 2013.
  Long-time and short-time evolution of perturbations for parallel round jets. *Under preparation to be submitted to Phys. Fluids.*

Keywords: Wakes stability and control, axisymmetric body, bullet-shaped body, transitions, passive control, base bleed, rear cavities, body rotation, BiGlobal linear stability, transient growth, parallel jets.

Contents

Agradecimientos **i**

Resumen **iii**

Abstract **v**

Contents **vii**

1 Introduction and Formulation **1**
1.1 Introduction . . . 1
1.2 Problem formulation . . . 3
1.2.1 Linearized problem (BiGlobal Linear Stability) . . . 4
1.2.2 The Stuart-Landau model . . . 6
1.3 Outline of the dissertation . . . 8

2 Natural laminar wake behind bullet-shaped bodies **9**
2.1 Introduction . . . 9
2.2 Experimental and numerical techniques . . . 12
2.2.1 Experimental details . . . 12
2.2.2 BiGlobal Linear Stability analysis . . . 14
2.2.3 Numerical techniques . . . 16
2.3 Description of unstable modes at the wake . . . 18
2.3.1 Wake of a $\ell = 2$ body . . . 18
2.3.2 Effect of ℓ on the stability properties . . . 29
2.4 Transients at the wake . . . 32
2.4.1 Experimental results . . . 33
2.4.2 Numerical simulations . . . 36
2.5 A note on the comparison between sphere and bullet-shaped bodies wakes . . . 38
2.6 Conclusion . . . 39

3 Wake control through passive methods (I): base bleed and rear cavities **43**
3.1 Introduction . . . 43
3.2 Problem definition and techniques . . . 45
3.2.1 Problem definition . . . 45
3.2.2 Experimental details . . . 45
3.2.3 BiGlobal Linear Stability analysis . . . 45
3.2.4 Numerical techniques . . . 47
3.3 Base bleed control . . . 49

3.3.1 Homogeneous base bleed (S=1) . . . 49
3.3.2 A note on the stabilizing effect of light base bleed (S=0.14) . . . 55
3.4 Rear cavities . . . 55
3.4.1 Cavity effects on the first-stationary bifurcation . . . 56
3.4.2 Cavity effects on the second-oscillatory bifurcation . . . 61
3.5 Conclusion . . . 64

4 Wake control through passive methods (II): body rotation 67
4.1 Introduction . . . 68
4.2 Problem definition and techniques . . . 69
4.2.1 Problem definition . . . 69
4.2.2 BiGlobal Linear Stability analysis . . . 70
4.2.3 Numerical techniques . . . 71
4.3 Flow regimes and dynamics of the wake behind a spinning $\ell = 2$ body. . . . 72
4.3.1 Flow characteristics at $\Omega = 0.1$ and increasing values of Re . . . 73
4.3.2 Analysis of the bifurcations for $\Omega = 0.1$ . . . 80
4.3.3 Flow characteristics for $\Omega \leq 0.4$ . . . 83
4.3.4 Flow characteristics for $0.4 < \Omega \leq 0.6$ . . . 90
4.4 Unstable global modes at the wake of a spinning $\ell = 2$ body . . . 92
4.4.1 Stability characteristics for $\Omega \leq 0.4$ . . . 92
4.4.2 Stability characteristics for $0.4 < \Omega \leq 1$ . . . 98
4.4.3 Physical interpretation of results . . . 102
4.5 Conclusion . . . 104

5 Conclusions and future work 107
5.1 General conclusions . . . 107
5.2 Future work . . . 109

A Description of the BiGlobal Linear Stability code 113
A.1 Base flow computation and grid interpolation . . . 113
A.2 EVP assembly . . . 116
A.2.1 Differentiation matrices . . . 118
A.3 Standard EVP solver . . . 121
A.4 Postprocessing . . . 123

B Long-time and short-time evolution of perturbations for parallel round jets 125
B.1 Introduction . . . 125
B.2 Problem formulation and numerical method . . . 127
B.2.1 Steady flow . . . 127
B.2.2 Modal stability analysis . . . 128
B.2.3 Transient Growth analysis . . . 130
Large time transient: Adjoint problem . . . 131
Short and Finite-time transient: Optimal Perturbation analysis . . . 132
B.2.4 Coordinate transform and treatment of singularities . . . 133
B.2.5 Numerical convergence and validation . . . 134

B.3 Results and discussion 137
B.3.1 Temporal stability: modal analysis 137
Parametric study 138
Eigenfunctions 144
B.3.2 Transient Growth 145
Large time analysis 145
Short and finite-time analysis 150

References **155**

List of Tables

2.1 Experimental and numerical values of vortex shedding Strouhal number for several $Re > Re_{co}^{exp}$, for a body of $\ell = 2$. Numerical Reynolds numbers corresponds to $Re = 415, 420, 430, 440, 450, 460$ and 470 respectively. 25

2.2 Values of the experimental Landau constant at saturation at several $Re > Re_{co}$, for a body of $\ell = 2$. 34

3.1 Grid convergence study for the leading eigenvalue growth rate, σ_{r1}, at $Re = 350$ and $|m| = 1$, for a $\ell = 2$ body, using finite differences of $\mathcal{O}(6)$ and different grids. Note that Sp represents the results obtained by using a spectral collocation method, and $\epsilon_{j,sp}$ is the relative error between $\sigma_{r1}(j)$ and $\sigma_{r1}(Sp)$. 47

3.2 Drag coefficient, C_d, and Grid Convergence Index, $GCI_{j+1,j}$, obtained for a body of ℓ= 2 with a cavity of length $h/D = 0.7$ and diameter $D_c/D = 29/30$ at $Re =$ 400, using three different meshes: fine (1), medium (2) and coarse (3). The grid convergence index has been obtained from Eq.(3.3) with $R = 0.67$, $\alpha = 2^{1/3}$ and n= 1.73 given by Eq.(3.2). 48

3.3 Drag coefficients of a solid base body, C_{d0}, C_{d0}^{p} and C_{d0}^{v}, at Reynolds numbers $Re = 300$ and $Re = 400$. 58

4.1 Grid convergence study based on the two leading eigenvalues, σ_1 and σ_2 respectively, found for $\Omega = 0.5$ and $Re = 350$, for several meshes of size ratio $n_{g(j+1)} \simeq n_{g(j)} \times$ 1.3. Also shown are the maximum relative error, $\epsilon_{j,j+1}(\%) = \{\Re[\sigma_2(j)] - \Re[\sigma_2(j+1)]\}/\Re[\sigma_2(j)] \times 100$, and the computational time needed to solve the EVP, $t_{\mathrm{EVP}}(s)$. 71

4.2 Order of the method, n, and grid convergence index, $\mathrm{GCI}_{j+1,j}$, defined in Eq.(3.3), obtained using the azimuthal velocity, v, and the axial velocity, w, at two different points. The simulations were performed at $Re = 350$ and $\Omega = 0.5$. 71

4.3 Drag coefficient, C_d, of a sphere rotating in the streamwise direction at $Re = 250$ and $\Omega = 0.1$, obtained by other authors and in this Thesis, by using a Van Leer limiter (VL), as well as a linear interpolation scheme (CD) for the convective term. The error, $\epsilon_{C_{d_i}} = |C_{d_i} - C_{d_{ref}}|/C_{d_{ref}} \times 100$, was calculated using the results reported by Poon *et al.* [116] as reference. 73

4.4 Values of characteristic Strouhal numbers for $\Omega = 0.1$ at different Re, for the frequency associated to the wake rotation, $St_{\omega l}$, and the spiral vortex shedding frequency, St_{vs}. Also included are the values of the vortex shedding Strouhal numbers obtained numerically, St_0^{DNS}, and experimentally, St_0^{EXP}, reported in Chapter 2 for a non-rotating body. 76

4.5 Values of St_{vs} and $St_{\omega l}$ for low Ω at $Re = 430$. 78

4.6 Frequencies associated to main and secondary (in brackets, when exists) peaks of lift components spectra, obtained for $\Omega = 0.1$, 0.2, 0.25, 0.3 and 0.4 at several values of Re close to Re_{c2} and Re_{c3}. For monochromatic spectra, values correspond to $St_{\omega l}$ ($\Omega \leq 0.2$ and $Re \leq 410$) and $St_{\omega h}$ ($\Omega \geq 0.2$ and $Re \geq 390$). 87
4.7 Strouhal numbers associated to the lift components spectra, and lift coefficient, C_l, for $\Omega = 0.5, 0.55$ and 0.6, at $Re = 340, 380, 400$ and 420. 91
4.8 The values of Re_{c1} and St predicted by the global stability analysis (GLS) for different values of Ω (St obtained at $Re = 330, 340, 350$ and 380 for $\Omega = 0.05, 0.1, 0.15$ and 0.2, respectively), compared with those obtained from the numerical simulations (DNS). The relative errors, $\epsilon_f(\%) = |f_{GLS} - f_{DNS}|/f_{DNS} \times 100$, being f either Re_{c1} or St, are also shown. 95
4.9 Critical Reynolds numbers for the destabilization of the HF mode, Re_{c3}, and Strouhal numbers obtained at $Re = 400$, for several values of Ω. Also shown are the values obtained in Section 4.3.3 with direct numerical simulations (DNS). The relative errors, $\epsilon_f(\%) = |f_{GLS} - f_{DNS}|/f_{DNS} \times 100$, being f either Re_{c3} or St, are also listed. . . 96
4.10 Strouhal numbers obtained through global stability analysis, St_{GLS}, and three-dimensional numerical simulations, St_{DNS}, determined numerically, for $\Omega = 0.55$ and $\Omega = 0.6$, at $Re = 340$ and 400. The relative error, $\epsilon_{St}(\%) = |St_{GLS} - St_{DNS}|/St_{DNS} \times 100$, is also shown. 99

A.1 Grid convergence index for the basic flow, $GCI_{j+1,j}$, applied to the particular case of $\Omega = 0.1$ and $Re = 330$, obtained for the azimuthal, V^0, and the axial, W^0, components of the velocity, at two different downstream locations near the body base, being $\alpha = 2^{1/2}$, $n_V \simeq 2.07$ and $n_W \simeq 2.00$. 116
A.2 Coefficients matrix for the Taylor expansions linear combination. 119
A.3 Effect of β on the leading eigenvalue σ_1 obtained with the Arnoldi method ($m_A = 100$) for the EVP of a spinning $\ell = 2$ body at $Re = 330$ and $\Omega = 0.2$. 122

B.1 Comparison of Re_{cr} for fully developed jet. 135
B.2 Summary of k_{max} and k_{tr} values for several $1/\theta$ and $Re = 1000$. 141

List of Figures

1.1 Scheme of the problem and axisymmetric computational domains (dashed line represents inlet for final global stability mesh, see Appendix A). Inset illustrates side (left) and rear (right) views of the coordinate system. 4

2.1 Sketch of the hot-wire anemometer experimental set-up. 13

2.2 Sketch of the studied axisymmetric body with a rounded ellipsoidal nose. (a) Solid body, (b) hollow body used in the experiments with base bleed and, (c) image of the different solid bodies with length-to-diameter ratios $\ell = 1, 2, 3, 4$ and 6, respectively. Included in [15]. 14

2.3 (a) Computational domain for the simulations of the flow around a body of $\ell = 2$, and (b) details of the meshed body. 16

2.4 (a) Domain decomposition into 222 subdomains. The thin solid lines correspond to the subdomain boundaries. (b) Grid detail close to the body for 12×12 nodes distributed according to the Gauss-Lobato-Chebyshev points in each subdomain for a body of $\ell = 2$. Included in [15]. 17

2.5 (a) Side (top) and top (bottom) views of iso-surfaces of streamwise vorticity $\varpi = \pm 0.05$ for $Re = 320$; and (b) side (top), top (bottom) and rear perspective (right) views of a streamline for $Re = 320$. Note that in (a) the dark-coloured and the light-coloured threads correspond to negative and positive ϖ respectively. 18

2.6 (a) Side (top) and top (bottom) views of iso-surfaces of streamwise vorticity $\varpi = \pm 0.05$ for $Re = 350$; and (b) same views of vortical structures visualized using Q-criterion, $Q > 0$. Note that in (a) the dark-coloured and the light-coloured threads correspond to negative and positive ϖ respectively. 19

2.7 (a) Eigenvalue spectrum for $Re = 350$, $|m| = 1$ and $\ell = 2$. (b) Isolines of the real part of the normalized eigenfunctions $\hat{u}$, $\hat{v}$, $\hat{w}$ and $\hat{p}$ for the eigenvalue marked with a square in (a). The eigenfunctions have been normalized with $\|\hat{\mathbf{q}}\|_\infty$. Included in [15]. 20

2.8 (a) Squared velocity distribution centroid radius r_{ec}^2 versus Re and (b) velocity magnitude contours for $Re = 320$ and $z = 5$. Lines in (a) represent linear fits, while the thick red line in (b) indicates the base of the body. 21

2.9 (a) Drag coefficient, (b) lift coefficient and (c) squared lift coefficient versus Re (solid line represents linear fit). In (a) dotted line stands for extrapolation of the axisymmetric flow drag. 22

2.10 (a) Side views and (top) views of positive (light color) and negative (dark color) streamwise vorticity iso-surfaces ($\varpi = \pm 0.04$), representing a shedding period for $Re = 415$. 23

2.11 Vortical structures ($Q > 0$) for $Re = 415$ and $\ell = 2$ (colored by streamwise vorticity ϖ). 23
2.12 (a) Temporal transient evolution $C_l(t)$ at $Re = 415$, after perturbing the flow from $Re = 410$, and oscillations modulus $|A| = |C_l(t)|$ (dashed line); (b) logarithmic representation of normalized modulus $|A|/|A|_{sat}$, being $|A|_{sat}$ the modulus at saturation ($t > 1300$), and exponential fit (dotted line); and (c) power spectral density at saturation for $C_l(t)$ shown in (a). 24
2.13 (a) Eigenvalue spectrum for $Re = 518$, $|m| = 1$ and $\ell = 2$. (b) Isolines of the real part of the normalized eigenfunctions $\hat{u}$, $\hat{v}$, $\hat{w}$ and $\hat{p}$ for the eigenvalue marked with a circle in (a). The eigenfunctions have been normalized with $\|\hat{\mathbf{q}}\|_\infty$. Included in [15]. 25
2.14 (a) Temporal evolution of streamwise velocity fluctuations $w'(t)$ behind the $\ell = 2$ body, measured at $z = 3$, for $Re = 394$ (top) and 429 (bottom); and (b) corresponding power spectral densities. 26
2.15 Square of the amplitude of the streamwise velocity fluctuations versus Reynolds for a $\ell = 2$ body, and $(r, z) = (0, 3)$. 26
2.16 Power spectral density of the streamwise velocity fluctuations $w'(t)$ as a function of St and downstream position z, for a $\ell = 2$ body and (a) $Re = 446$, (b) $Re = 500$, (c) $Re = 590$ and (d) $Re = 802$. Inset in (a) includes the spectrum for $z = 7$ in logarithmic scale. 27
2.17 Analysis of the RSP mode: (a) Iso-surfaces of streamwise vorticity, $\varpi = \pm 0.04$; (b) power spectral density corresponding drag (dotted line) and lift (solid line) temporal evolutions at $Re = 500$; and (c) phase diagram (C_l, C_d) for several Re. Note that inset in (b) represents the evolution with Re of the squared streamwise velocity oscillations amplitude at St_l, $|A_l|^2$, together with the linear fit providing with Re_{co2}. 29
2.18 Power spectral density of the streamwise velocity fluctuations $w'(t)$, taken at $z = 7$, as a function of St for a $\ell = 2$ body and (a) $Re = 500$, (b) $Re = 590$. 30
2.19 Energy of the streamwise velocity fluctuations $|A|^2_{sat}$ obtained experimentally at $(r = 0, z = 3)$, as function of the Reynolds number for the different bodies of $\ell = 1, 2, 3, 4$ and 6. Included in [15]. 30
2.20 Dependence of the critical Reynolds numbers on the aspect ratio of the body, ℓ. Comparison among the results given by linear BiGlobal stability analysis, numerical simulations for $\ell = 1$ (from [15]) and 2, and experiments for $\ell = 1, 2, 3, 4$ and 6. Included in [15]. 31
2.21 (a) Transient of raw velocity signal, $A_{raw}(t) = w'(t)$ and (b) filtered velocity signal, $A_f(t) = w'_f(t)$, obtained at $z = 3$ and (c) hot-wire anemometer output voltage, $OE_p(t)$, close to the body base (z=0.5). Note that dashed vertical lines in (c) determine the duration of the switch-off transient time. Experimental measurements taken for a body of $\ell = 2$ at $Re \simeq 455$. 32
2.22 Experimental (a) instantaneous growth rate $d(\log|A|)/dt$ and (b) instantaneous frequency $d\phi/dt$, versus $|A|^2/|A|^2_{sat}$ obtained for a body of $\ell = 2$ at $Re \simeq 455$. 34
2.23 Experimental dependence on Re of (a) growth rate, σ_{r2}, (b) initial frequency, σ_{i2}, and (c) Landau constant, c, obtained for a body of $\ell = 2$. Note that vertical bars define 95% confidence intervals of fitting processes. 35

2.24 Numerical (a) instantaneous growth rate $d(\log|A|)/dt$ and (b) instantaneous frequency $d\phi/dt$, versus $|A|^2/|A|^2_{sat}$ at $Re = 415$, for $C_l(t)$. 36

2.25 Numerical instantaneous growth rate $d(\log|A|)/dt$ versus $|A|^2$ at $Re = 320$, for $C_l(t)$. 37

2.26 (a) Global amplitude estimation $|A|^2$ versus z for the sphere (circles) and $\ell = 2$ body (asterisks); and amplitude per unit volume, $|\mathbf{u}_m|^2$, at $z = 10$ for (b) $\ell = 2$ body and (c) sphere. Note that the symmetry plane at the three-dimensional wake is depicted by a grey dashed line at the insets. 39

3.1 Detail of the axisymmetric GLS computational domain, for a $\ell = 2$ body with $h/D = 0.7$ and $D_c/D = 0.8$. Included in [126]. 46

3.2 Details of the computational mesh at the $\ell = 2$ body with $h/D = 0.7$ and $D_c/D = 0.86$. (a) Frontal-side and (b) rear-side views. Included in [126]. 47

3.3 (a) Evolution of streamwise velocity fluctuations, $w'(t)$, with homogeneous base bleed, for $C_b = 0, 0.018, 0.023$ and 0.026, at $z = 3$ and $Re = 500$; and (b) corresponding power spectral densities. 50

3.4 Power spectral densities, PSD with homogeneous base bleed, for $C_b = 0, 0.03$ and 0.2, at $z = 7$ and $Re = 590$. 50

3.5 Experimental squared normalized saturation amplitude versus bleed coefficient for several Re. Note that solid horizontal lines represents values of marginal amplitude $\epsilon = 0.03$ (3%) and 0.02 (2%) respectively. Included in [15]. 51

3.6 Evolution of the streamwise velocity saturation amplitude, $|A|^2_{sat}$, versus Reynolds numbers for $C_b = 0.014$. 52

3.7 Eigenvalue spectra for a body with aspect ratio $\ell = 2$, $Re = 500$, $|m| = 1$ and base bleed coefficients (a) $C_b = 0$, (b) $C_b = 0.040$, (c) $C_b = 0.060$ and (d) $C_b = 0.080$, respectively. The unstable eigenvalue corresponding to the steady bifurcation has been marked with a square. Included in [15]. 53

3.8 Evolution of the critical base bleed coefficients with the Reynolds number for an ellipsoidal rounded nose body of aspect ratio $\ell = 2$, obtained with the GLS analysis and HWA experiments. Results from numerical simulations (DNS) and local linear stability analysis (LLS) by Bohorquez *et al.* [15] are included for comparison and validation. Taken and modified from [15]. 54

3.9 Evolution of the experimental critical base bleed coefficients with the Reynolds number for a $\ell = 2$ body, obtained by light base bleed (circles) and homogeneous base bleed (asterisks). 55

3.10 (a) Dependence of the critical Reynolds numbers corresponding to the first, stationary bifurcation, Re_{cs}, with the cavity length, h/D, for a cavity diameter of $D_c/D = 29/30$. Comparison between the results given by global linear stability analyses (solid line) and the three-dimensional numerical simulations (squares), for the stationary bifurcation. (b) Effect of the cavity diameter, D_c/D, on the critical Reynolds numbers for the stationary bifurcation. Cavity lengths $h/D = 0.2$ (dashed line) and $h/D = 0.7$ (solid line). Included in [126]. 57

3.11 Effect of the cavity length on the (a) pressure drag coefficient C_d^p, (b) viscous drag coefficient C_d^v and (c) drag coefficient C_d, for a body of cavity diameter $D_c/D = 29/30$ and Reynolds numbers $Re = 300$ (dashed line) and $Re = 400$ (solid line). The drag coefficients C_{d0}^p, C_{d0}^v and C_{d0} correspond to a body without base cavity, i.e. $D_c/D = 0$. Included in [126]. 57

3.12 Effect of the cavity diameter on the (a) pressure drag coefficient C_d^p, (b) viscous drag coefficient C_d^v and (c) drag coefficient C_d, for a body with a cavity length of $h/D = 0.7$ at Reynolds numbers $Re = 300$ (dashed line) and $Re = 400$ (solid line) respectively. 58

3.13 Pressure contours of the steady axisymmetric field obtained for four bodies with a cavity of diameter $D_c/D = 29/30$ and lengths (a) $h/D = 0$, (b) $h/D = 0.2$, (c) $h/D = 0.7$ and (d) $h/D = 1$ at $Re = 400$. Included in [126]. 59

3.14 Effect of the cavity diameter, D_c/D, on downstream evolution of the axisymmetric (a) radial velocity at $r = 0.5$, $U(r = 0.5, z)$, and (b) axial velocity at $r = 0$, $W(r = 0, z)$, at $Re = 400$. The different curves correspond to cavities of length $h/D = 0.7$ and diameters $D_c/D = 0$, 0.6, 0.8 and 0.9. Included in [126]. 59

3.15 Eigenvalue spectra for $|m| = 1$, for four bodies with a cavity of diameter $D_c/D = 29/30$ and lengths (a) $h/D = 0$, (b) $h/D = 0.2$, (c) $h/D = 0.7$ and (d) $h/D = 1$, respectively, at $Re = 400$. Squares indicate the eigenvalues corresponding to the first-stationary bifurcation ($\sigma_i = 0$). 60

3.16 Isolines of the real part of the normalized eigenfunctions $\widehat{u}$, $\widehat{v}$, $\widehat{w}$ and $\widehat{p}$ of the eigenvalues marked with the squares in Fig. 3.15, for cavity lengths (a) $h/D = 0$, (b) $h/D = 0.2$, (c) $h/D = 0.7$ and (d) $h/D = 1$. Here, the eigenfunctions are normalized with $\|\hat{\mathbf{q}}\|_\infty$. 61

3.17 Contours of constant streamwise vorticity, $\omega_z = \pm 0.05$, for $Re = 500$. (a) Solid base body and (b) a body with a cavity of length $h/D = 0.7$ and diameter $D_c/D = 0.86$. (c) Detail of the vorticity contours inside the cavity. Included in [126]. 62

3.18 Hot-wire measurements of the fluctuations of the streamwise component of the velocity, $w'(t)$, and the corresponding power spectral density at $r = 0$, $z = 3$ for $Re = 465$ and two cavities of diameter $D_c/D = 0.86$ and lengths (a) $h/D = 0$ and (b) $h/D = 0.2$. Included in [126]. 62

3.19 Energy of the streamwise velocity fluctuations, w'^2_{fc}, versus the Reynolds number, obtained experimentally, at (r = 0, z = 3) for cavities of diameter $D_c/D = 0.86$ and different lengths, $h/D = 0$, 0.2, 0.4, 0.7 and 1.0. Included in [126]. 63

3.20 Effect of the length of a cavity with $D_c/D = 0.86$ on the critical Reynolds number corresponding to the oscillatory bifurcation, Re_{co}, obtained experimentally and from three-dimensional numerical simulations. Here $\triangledown$ and $\triangle$ correspond to the upper and lower limits obtained numerically for a cavity of $h/D = 0.7$ considering a body misaligned 1° with the free-stream. Included in [126]. 64

4.1 Detail of the axisymmetric GLS computational domain, for a spinning $\ell = 2$ body. 70

4.2 Temporal evolution of the drag and lift coefficients for a sphere at $Re = 250$ and $\Omega = 0.1$. Included in [58]. 72

4.3 Wake structures visualized by contours of constant streamwise vorticity, $\varpi_z = 0.2$ (dark-coloured contour) and $\varpi_z = -0.2$ (light-coloured contour), for a spinning body of aspect ratio $\ell = 2$ and $\Omega = 0.1$ at (a) $Re = 330$, (b) $Re = 370$ and (c) $Re = 430$. Included in [58]. 73

4.4 Temporal evolution of streamwise vorticity contours at $z = 1$ during a period of revolution $T = 2\pi/\Omega_{sl}$ (dark contours are positive values while light contours represent negative values). Notice that, as the solid body, the fluid structures rotate in the positive z direction, although with a rotation velocity, Ω_{sl}, different from that of the body, Ω. In this figure the base of the body is shown with a thick line, and a dashed line has been included to identify the body rotation. Included in [58]. . . . 74

4.5 Left column: Time series of C_l (solid line), C_{l_x} (dashed line) and C_{l_y} (dotted line), for a rotating body of aspect ratio $\ell = 2$ and $\Omega = 0.1$ at (a) $Re = 370$ and (b) $Re = 430$. Right column: Power Spectral Density associated to C_{l_x}. The inset displays a zoom of the spectrum at $Re = 430$, in semi-logarithm scale, showing the presence of three characteristic frequencies, namely $St_{\omega l}$ and $St_{\rm vs} \pm St_{\omega l}$. Included in [58]. 75

4.6 Time series of the lift components $C'_{l_{x'}}$ (solid line) and $C'_{l_{y'}}$ (dotted line) in the frame of reference S', that rotates with an angular velocity Ω_{sl}, for (a) $Re = 370$ and (b) $Re = 430$. The inset in Fig. 4.6(b) displays the Power Spectral Density of $C'_{l_{x'}}$ and $C'_{l_{y'}}$, showing the characteristic vortex shedding frequency, $St_{\rm vs}$. Included in [58]. . 76

4.7 Phase diagrams of the lift components for different Reynolds numbers at $\Omega = 0.1$. Included in [58]. 77

4.8 (a) Squared centroid eccentricity of the contours of velocity magnitude at $z = 1$ versus the Reynolds number, together with a linear fit (solid line), and a cubic polynomial fit (dotted line); and (b) lift coefficient C_l as a function of Re (time averaged values for $Re = 420, 430$ and 440), for $\Omega = 0.1$. Included in [58]. 78

4.9 (a) Total drag coefficient C_d (solid line), viscous drag C_d^v (dashed line) and pressure drag C_d^p (dash-dotted line), and (b) dimensionless recirculation length ℓ_r as a function of Re (time averaged value for $Re = 420, 430$ and 440), for $\Omega = 0.1$. The dashed line in Fig. 4.9(b) represents the extrapolation of ℓ_r considering a non-bifurcated flow. Included in [58]. 79

4.10 Instantaneous projected streamlines and contours of the pressure coefficient, C_p, in the (y_m, z)-plane, where y_m is aligned with the direction of maximum lift, for $\Omega = 0.1$ and (a) $Re = 330$, (b) $Re = 370$ and (c) $Re = 430$. Included in [58]. 80

4.11 (a) Determination of $Re_{c1}(\Omega = 0.1)$ by linear fit of the energy of the saturated amplitude of C_{l_x}, $|A|^2_{sat}$, versus Re. (b) Determination of the temporal decay rate of lift component $C_{l_x}(t)$ at $Re = 330$, beginning the simulation from the saturated solution at $Re = 340$. Included in [58]. 81

4.12 Stuart-Landau model for the first bifurcation: (a) Instantaneous growth rate $d \log |A|/dt$ and (b) instantaneous frequency $d\phi/dt$, versus $|A|^2$, at $Re = 340$ and $\Omega = 0.1$. Included in [58]. 82

4.13 (a) Power Spectral Density (in arbitrary units) of $C_l(t)$ (solid line), $C_d(t)$ (dotted line) and $C'_{l_{x'}}(t)$ (dashed line) for an arbitrary initial phase, at $Re = 425$ for $\Omega = 0.1$, and (b) squared saturation amplitude of the lift magnitude, $|A|^2_{sat}$, as a function of Re. Included in [58]. 83
4.14 Stuart-Landau model for the second bifurcation: (a) Instantaneous growth rate $d\log|A|/dt$ and (b) instantaneous frequency $d\phi/dt$, versus $|A|^2$, at $Re = 420$ and $\Omega = 0.1$. Included in [58]. 84
4.15 Vortical structures visualized by streamwise vorticity contours, $\varpi_z = \pm 0.2$, for $\Omega = 0.2$ at (a) $Re = 380$, (b) $Re = 390$ and (c) $Re = 430$. Included in [58]. 84
4.16 Time series of the lift component $C_{l_x}(t)$ (left side) and Power Spectral Density (right side) for $\Omega = 0.2$ and: (a) $Re = 390$, (b) $Re = 400$, (c) $Re = 410$ and (d) $Re = 420$. Included in [58]. 85
4.17 Phase diagrams, C_{l_x} vs C_{l_y}, for $\Omega = 0.2$ and different values of Re indicated in the plots. Included in [58]. 86
4.18 Phase diagrams, C_{l_x} vs C_{l_y}, for $\Omega = 0.25$ and different values of Re indicated in the plots. Included in [58]. 87
4.19 Bifurcation diagram for the spinning bullet-shaped body in the (Ω, Re) parameter plane, where the transitions are identified by means of different symbols: ◁ - Re_{c1}, ◀ - Re_{c2} and ◀ -Re_{c3}. The different wake states correspond to the following Regions: I-axisymmetric, II-frozen, IIIa-spiral unsteady and IIIb-spiral frozen. Additionally, the regimes found by Pier [113] for the sphere have been included for comparison (see grey dashed lines and grey tags), together with the transition $Re_{c1}(\Omega)$ (grey continuous line). Included in [58]. 88
4.20 Evolution with Ω of the Strouhal numbers $St_{\omega l}$ (○-frozen, ●-spiral unsteady), $St_{\rm vs} + St_{\omega l}$ (■-spiral unsteady) and $St_{\omega h}$ (□-spiral frozen) at: (a) $Re = 380$, (b) $Re = 390$ and (c) $Re = 430$. Vertical dashed lines stand for the different transitions found for increasing Ω. Included in [58]. 88
4.21 Evolution of the ratios Ω_{sl}/Ω and Ω_{sh}/Ω with Re for different values of Ω, corresponding respectively to the frozen Regions II and IIIb shown in Fig. 4.19. Included in [58]. 89
4.22 (a) Mean drag coefficient $\overline{C}_d$ and (b) mean lift coefficient $\overline{C}_l$ as functions of Ω, for $Re = 380$, $Re = 390$ and $Re = 430$, and different modes (I-empty symbols, II-black filling symbols, IIIa-dark grey filling symbols and IIIb-light grey filling symbols). Dashed lines in (a) represent quadratic fits. Included in [58]. 90
4.23 Phase diagrams, C_{l_x} vs C_{l_y}, for (a) $\Omega = 0.5$, (b) $\Omega = 0.55$ and (c) $\Omega = 0.6$, and different values of Re indicated in the plots. 91
4.24 Isosurfaces of streamwise vorticity, $\varpi_z = 0.2$ (dark-coloured contour), and $\varpi_z = -0.2$ (light-coloured contour) for a spinning bullet-shaped body with $\Omega = 0.55$ and $Re = 340$. 92
4.25 Eigenvalue spectra for $Re = 330$, $m = -1$ and: (a) $\Omega = 0$, (b) $\Omega = 0.05$, (c) $\Omega = 0.1$, (d) $\Omega = 0.15$ and (e) $\Omega = 0.2$. The circled mode stands for the LF mode (SS mode at $\Omega = 0$), while the squared one represents the HF mode. 93
4.26 Eigenvalue spectra for $\Omega = 0.15$, $m = -1$ and: (a) $Re = 330$, (b) $Re = 340$ and (c) $Re = 350$. 94

4.27 (a) Growth rate, σ_r, as a function of Re for the two leading eigenvalues, namely the LF mode (•) and the HF mode (□), for $0.21 \leq \Omega \leq 0.25$ and $m = -1$ (binding lines represent linear fits); and (b) eigenvalue spectrum for $\Omega = 0.232$, $Re = 395$ and $m = -1$. 95
4.28 Eigenvalue spectra for $Re = 390$ (left column), $Re = 400$ (right column) and $m = -1$ when (a) $\Omega = 0.25$, (b) $\Omega = 0.3$ and (c) $\Omega = 0.4$. 97
4.29 Isocontours of the real part of the normalized axial velocity eigenfunction, $\Re(\hat{w})/\|\hat{q}\|_\infty$, associated to the leading eigenvalue at (a) $\Omega = 0$ and $Re = 330$, (b) $\Omega = 0.15$ and $Re = 350$, and (c) $\Omega = 0.25$ and $Re = 400$. 98
4.30 Snapshots of the temporal evolution of the contours of normalized axial velocity disturbance, $\Re(w')$, defined in Eq.(4.4), associated to the leading eigenmode, evaluated at $z = 1$, for (a) $\Omega = 0.15$ and $Re = 350$, (b) $\Omega = 0.25$ and $Re = 400$. The time interval between snapshots is $T/4$, being $T = 2\pi/\sigma_i$. 99
4.31 Eigenvalue spectra and contours of the real part of the normalized axial velocity leading eigenfunction, $\Re(\hat{w})/\|\hat{\mathbf{q}}\|_\infty$, for (a) $Re = 340$ and (b) $Re = 400$. Each subfigure, (a) and (b), displays spectra for $\Omega = 0.5$ (left top) and $\Omega = 0.55$ (right top), and contours of $\Re(\hat{w})/\|\hat{\mathbf{q}}\|_\infty$ for $\Omega = 0.55$ (bottom). 100
4.32 Eigenvalue spectra obtained for a body rotating with a velocity $\Omega = 0.55$ at $Re = 400, 380, 360, 340, 300, 270, 240, 220$ and 210. Arrows indicate the direction of decreasing Re. 101
4.33 Bifurcation diagram in the (Ω,Re) parameter plane, according to the results of numerical simulations (DNS) and global stability analysis (GLS). The different wake states correspond to the following regions: I axisymmetric, II frozen, IIIa spiral unsteady, IIIb high-frequency spiral frozen and IV medium-frequency spiral frozen. 101
4.34 Effect of the rotation parameter Ω on the base flow (a) axial velocity and (c) pressure at the axis $r = 0$, $W(r = 0, z)$ and $P(r = 0, z)$ respectively, and (c) radial velocity U at $r = 0.5$, $U(r = 0.5, z)$, for $\Omega = 0, 0.15, 0.25, 0.4, 0.5, 0.6$ and 0.65, when $Re = 400$.103

A.1 Diagram of the BiGlobal linear stability code and different steps followed. 114
A.2 Low resolution example of a grid used to interpolate the basic flow (U^0, V^0, W^0), calculated by ANSYS Fluent®, and to obtain the EVP basic flow, (U, W, W), for the BiGLS code of finite differences of $\mathcal{O}(6)$, where $S1, S2, S3$ denote the subdomains into which the grid is divided. 116
A.3 Structure of the discrete linear operator $\mathbf{A}$ and sparsity degree, from dark grey (dense matrix) to not-colored (empty matrix). 118
A.4 Schemes of computational points involved in the $\mathcal{O}(6)$ differentiation and discretization of some components of linear operator $\mathcal{A}$ (Eq.1.11), affecting the field variable f. Coefficients of differentiation matrices and other terms in Figs.A.4(a),(b) and (c) are omitted. 120
A.5 Detail of the differentiation matrix D2 structure, obtained by means of (a) finite differences of $\mathcal{O}(6)$ and (b) spectral methods using Langrangian polynomials interpolation of $n = 10$. Discontinuity of pattern in (b) is due to the change of spectral box. 121

B.1 (a) Base flow velocity profiles and (b) vorticity of profiles for different $K = 1/4\theta$. . 128

B.2 Effect of mapping parameters N and r_{max} on amplification factors for: $1/\theta = 30$ ($Re = 75$), a) $k = 0.5$ and b) $k = 4.65$; and $1/\theta = 4$ ($Re = 10000$), c) $k = 0.1$ and d) $k = 2$. Each graphic depicts, from top to bottom, tests corresponding: $r_{max} = 100$, 200, 300, 400, 500 and 800. The ticks around centered values of ω_i denote an interval $\Delta\omega_i = \pm 1.5 \cdot 10^{-5}$. 135
B.3 Perturbation growth rate for a fully developed jet as a function of Re and k. . . . 136
B.4 Pressure eigenfunctions and azimuthal vorticity for: (a,b) SL mode and (c,d) JC mode for an axisymmetric perturbation with $k = 2.297$ and a jet profile of $1/\theta = 10$ when $Re = 1000$. 137
B.5 Growth rate for azimuthal modes $m = 0$ and $m = 1$ when (a) $1/\theta$ =7 and (b) $1/\theta = 14$ and Re =1000. (c) Growth rate for $m = 1$ scaled with the aspect ratio. . 138
B.6 Unstable azimuthal modes when $Re = 1000$ and: (a) $1/\theta = 2$, (b) $1/\theta = 4$, (c) $1/\theta = 10$ and (d) $1/\theta = 20$. Arrow indicates the sense of growing m. 139
B.7 Evolution of the main stability properties with $1/\theta$ when Re =1000. 140
B.8 Unstable azimuthal modes when $1/\theta = 20$ and: (a) $Re = 100$ and (b) $Re = 1000$. Arrow indicates the sense of growing m. 141
B.9 Evolution of the main stability properties with $1/\theta$ when Re =100. 142
B.10 Dependence of $1/\theta_{cr}$ on Re (and most unstable modes according to regions). Thin lines show constant values of Re_θ: 25 (solid), 175 (dashed), 400 (dotted) and 1000 (dashed-dotted). 143
B.11 Eigenfunctions of u_z and u_r for $m = 0$, obtained at $Re = 1000$ and: (a-b) $1/\theta = 4$ and $k = 0.3$, (c-d) $1/\theta = 4$ and $k = 1.7$, (e-f) $1/\theta = 16$ and $k = 0.3$, (g-h) $1/\theta = 16$ and $k = 7.2$. Values are normalized with $\sqrt{E}$. Note that absolute values (thick solid lines), real parts (thin solid lines) and imaginary part (dashed lines) of $\hat{u}_r$ and $\hat{u}_z$ are represented. 143
B.12 Eigenfunctions of u_z and u_r for $m = 1$, obtained at $Re = 1000$ and: (a-b) $1/\theta = 4$ and $k = 0.3$, (c-d) $1/\theta = 4$ and $k = 1.7$, (e-f) $1/\theta = 16$ and $k = 0.3$, (g-h) $1/\theta = 16$ and $k = 7.2$. Values are normalized with $\sqrt{E}$. Note that absolute values (thick solid lines), real parts (thin solid lines) and imaginary part (dashed lines) of $\hat{u}_r$ and $\hat{u}_z$ are represented. 144
B.13 Isocontours of azimuthal vorticity obtained at $Re = 1000$ and $m = 0$ (left column) and $m = 1$ (right column), for: (a-b) $1/\theta = 4$ and $k = 0.3$, (c-d) $1/\theta = 4$ and $k = 1.7$, (e-f) $1/\theta = 16$ and $k = 0.3$, and (g-h) $1/\theta = 16$ and $k = 7.2$. 145
B.14 Isocontours of axial vorticity obtained at $Re = 1000$ and $m = 1$ for: (a) $1/\theta = 4$ and $k = 0.3$, (b) $1/\theta = 4$ and $k = 1.7$, (c) $1/\theta = 16$ and $k = 0.3$, (d) $1/\theta = 16$ and $k = 7.2$. 146
B.15 Structure of eigenfunctions for the dominant mode, obtained at $Re = 1000$, $1/\theta_{cr}$ and $k = k_{tr} = 2.2146$. (a-d) Profiles of modulus of u_z and u_r (thick solid), and its real (thin solid) and imaginary parts (thin dashed). (e-f) Isocontours of azimuthal vorticity, Ω_θ. 146
B.16 Isocontours of azimuthal vorticity for the direct (a,c,e) and adjoint (b,d,f) dominant modes, obtained for $1/\theta = 10$, $Re = 1000$ and $m = 1$ when (a,b) $k = 0.3$, (c,d) $k = k_{max} = 2.131$ and (c,d) $k = 4.3$. 147

B.17 Isocontours of azimuthal vorticity for the direct (a,c,e) and adjoint (b,d,f) dominant modes, obtained for $1/\theta = 10$, $Re = 1000$ and $m = 0$ when (a,b) $k = 0.3$, (c,d) $k = k_{max} = 2.297$ and (e,f) $k = 4.3$. 147
B.18 Energy gain for $1/\theta = 10$ and $Re = 1000$ of the most unstable perturbations for (a) $m = 0$ ($k = k_{max} = 2.297$) and (b) $m = 1$ ($k = k_{max} = 2.131$). The thin dashed-dotted line represents the asymptotic gain predicted by Eq.(B.29) for large time when the direct mode is excited by its counterpart adjoint mode, and the thick solid line is the gain evolution obtained by optimal perturbation analysis when the adjoint mode is the initial condition and τ is large. The dashed line stands for the energy growth given by the direct mode. Circles are the energy gain at each optimal time. 148
B.19 Gain ratio η for the unstable range of k when $1/\theta = 10$ and: (a) $Re = 100$, (b) $Re = 1000$ and (c) $Re = 10000$. 149
B.20 Gain ratio η for the unstable range of k when $Re = 1000$ and: (a) $1/\theta = 4$, (b) $1/\theta = 10$ and (c) $1/\theta = 16$. 149
B.21 (a,b) Gain evolution, $G(\tau)$, obtained through optimal perturbation analysis, for $1/\theta = 10$ when $Re = 1000$ and: (a) $k = 0.3$, (b) $k = 4.3$. (c) Evolution of the transition optimal time, τ_{tr}, with k and $1/\theta$ when $Re = 1000$. 150
B.22 (a) Evolution with the optimal time of the inner product between the optimal perturbation and the adjoint mode, $(\hat{\mathbf{v}}_\mathbf{0}, \mathbf{a})$, for $1/\theta = 10$ when $Re = 1000$ and $k = 4.3$. (b) Evolution of τ_+ with k for $1/\theta = 4$, 10 and 16, when $Re = 1000$. $1/\theta$ grows in the sense of the arrow. 150
B.23 Isocontours of azimuthal vorticity: Evolution of the optimal initial condition for a time horizon $\tau = 0.5$ and perturbation (a) $m = 0$ and (b) $m = 1$, with $k = k_{max}(m)$ when $1/\theta = 10$ and $Re = 1000$. 151
B.24 Isocontours of azimuthal vorticity: Evolution of the optimal initial condition for a time horizon $\tau = 2$ and perturbation (a) $m = 0$ and (b) $m = 1$, with $k = k_{max}(m)$ when $1/\theta = 10$ and $Re = 1000$. 152
B.25 Isocontours of azimuthal vorticity: Evolution of the optimal initial condition for a time horizon $\tau = 5$ and perturbation (a) $m = 0$ and (b) $m = 1$, with $k = k_{max}(m)$ when $1/\theta = 10$ and $Re = 1000$. 152

CHAPTER
ONE

Introduction and Formulation

1.1 Introduction

Flow past bluff bodies is a widespread configuration in many engineering applications, taking place wherever there is fluid stream flowing around a body or a body in motion. Examples of such systems are found for instance, in aeronautic industry, cars industry, turbomachinery, physics of sports, civil engineering, architecture, etc. Bluff-bodies geometry provokes a massive separation of the boundary layer at a detachment point, that depends on the shape and the Reynolds number, giving rise to a wake that develops spatially behind the body. In the case of blunt-based bodies, like afterbodies (bullet-shaped bodies), the existence of a rear edge determines the location of separation, and a consequent drastic change in the flow topology downstream. This flow separation creates a low pressure region at the near wake, that translates into a drag force, opposed to the body motion. On the other hand, it is well known that wakes behind bluff bodies undergo progressively, from the axisymmetric stable state, several bifurcations with increasing Reynolds numbers, leading to different regimes that are associated with the existence of unstable modes at the wake, and the subsequent interactions among them. The onset of unsteadiness at the wakes occurs generally at low Reynolds numbers, and takes place in form of alternate vortex shedding. This vortex generation and shedding, that enhances the drag, creates a regular pressure change that leads to transversal forces distribution acting on the body, entailing consequently vibrations, noise generation and resonances. The implications of these unstable regimes along with the relevance of the flow configuration, justify the intense work devoted to the characterization of wakes behind bluff bodies, like cylinders [157], or other three-dimensional bodies (see [66] and references therein), and the development of control strategies [133, 23]. However, despite of the importance of the geometry, and unlike in the case of the sphere and disks, the pattern of transitions and unstable regimes leading to turbulence in the wake of slender axisymmetric blunt-based bodies is not perfectly understood nowadays. Within this frame, the present Thesis aimed at shedding some light on this issue, focusing on the study of the laminar wake behind bullet-shaped bodies at low Reynolds numbers, and the control of the unstable regimes, which can be applied only after a deep characterization of modes and flow features.

As said, the occurrence of different regimes present at wakes behind bluff bodies are related to changes in the stability properties of the flow. In this sense, under certain conditions determined by some critical parameter (Reynolds number), wakes behind bluff bodies are known to exhibit strong intrinsic dynamics acting as *oscillators* (absolute instability), insensitive to external noise of low amplitude (see for instance [53] and references therein), that differs from a second type of behavior, namely, a *noise amplifier*, for which external perturbation are amplified and convected downstream

(convective instability)[1]. The oscillator nature is related to a limit-cycle dynamics, that acts as an attractor for the flow when it is perturbed, and often leads to self-sustained oscillations. A classical example of such intrinsic behavior is the aforementioned alternate von-Karman vortex shedding in the wake of cylinders [157] or other bluff bodies, as for instance, the sphere [3], occurring for a wide range of Reynolds number, from laminar to fully turbulent flows. This kind of behavior is associated to the existence of an absolutely unstable spatial region where self-sustained resonances occur, and perturbations are amplified [106], being the concept of absolute instability coined within the frame of weakly non-parallel assumption for the base flow (slow streamwise development) [53]. On the other hand, a broader approach allows to explain the intrinsic dynamics of wakes in terms of the existence of unstable *global* modes sustained by the flow. This *global* stability concept was proposed by Theofilis [145], based on the solution of the eigenvalue problem (EVP) arising from linearization of Navier-Stokes equations, and does not establish a streamwise base flow evolution limitation. A connection between absolute instability of weakly non-parallel flows [53] and global instability [145], was done by Pier [112] for the wake of a sphere, finding the existence of a region of absolute instability in the near wake of the sphere, what accounts for the onset of global instability (although quantitative discrepancies exists due to the weakly non-parallel base flow assumption).

The latter work, together with other previous papers on stability of wakes [102, 89, 16], have demonstrated the capability of global linear stability analysis to predict transitions and describe linear states of the wake (more precisely, BiGlobal, since the base flow is inhomogeneous in two directions). The importance of global modes computation lies in the capability of the stability analysis to provide with valuable information about flow behavior and the underlying physics, with a considerably less computational cost than three-dimensional numerical simulations. This, a priori, advantageous approach has been adopted in many recent works, dealing with multiple flow configurations, as the comprehensive reviews by Theofilis [145, 146] showed. Moreover, the knowledge of global modes provides with an useful insight on the possible transient growth and the control of growing disturbances [50] (although additional techniques would be required to tackle these problems). Accordingly, it proves useful to study the flow configuration proposed in this Thesis using the approach of global modes, aimed at finding out the instability mechanisms that lie behind the unstable regimes existing at the laminar wake of bullet-shaped bodies.

Albeit, the onset of unsteadiness has been proven to result from the non-linear interaction of dominant modes in the wakes of sphere and disks [34], so that linear BiGlobal analysis alone might not be able to offer a complete picture of the problem. Consequently, the characterization of the wake regimes, including wake structures and hydrodynamics forces, should be accomplished by means of three-dimensional numerical simulations and experiments. The combination of these techniques have allowed to identify properly the topologies of different states and their dynamics in wakes of axisymmetric bodies, for a wide range of Reynolds, from laminar to turbulent wakes, being a classical example the wake of the sphere (see e.g. [149, 66, 17]). Additionally, shedding frequencies have been traditionally characterized, as they provide with a direct indication of the modes present and the possible nonlinear interaction among them. Experimentally, this task can be easily accomplished through hot-wire anemometry (see e.g.[132]), that offers high temporal resolution, and allows to study transients dynamics at the wake with a relative low cost.

[1]From a global point of view, amplification of external perturbations and their convection away from unstable regions is as a consequence of the non-normality of the evolution operator of linearized Navier-Stokes equations [24] (see Chapter 5).

As far as the control of unstable regimes is concerned, the insight about the instability mechanism and the unstable modes at low and transitional Reynolds numbers, provides with valuable information for the flow control strategies, that could be applied only to more realistic applications after a complete understanding of their basic operation. The little work existing on the transition to turbulence of wakes behind slender axisymmetric blunt-base bodies, encouraged us to focus on low Reynolds regimes, but it is reasonable to think that the unstable modes and control strategies discussed herein would have applicability at larger Reynolds numbers. This hypothesis is suggested by the fact that similar unstable helical structures are observed behind the sphere both at laminar and turbulent Reynolds numbers [142, 11]. Moreover, for slender axisymmetric blunt-based bodies both the flow topology and base bleed performance as control mechanism are similar [135, 127] at low and large Reynolds numbers. That said, among the different approaches existing for flow control [23], passive methods have been chosen for the present work. On one hand, passive methods are generally easier to implement, although its performance depends on the flow features, which must be first thoroughly characterized. And, on the other hand, axisymmetric bodies wakes exhibit large sensitivity to modifications of base flow in the recirculation bubble [88], what suggests that they could be somewhat controllable through passive methods. In this sense, base bleed and rear cavities emerge as interesting methods, due to the large modification of the steady base flow that they entail. Both methods have been largely investigated in the past (e.g. [158, 10, 49, 135, 153]), with evident success on the wake stabilization, and with the additional ability to reduce the drag. Besides, body rotation is the third mechanism investigated in this dissertation. The study was inspired by the implementation of spin in projectile flights, where it induces stabilization of the trajectory (Magnus effect), although the nature of this effect could be different from that expected here. Furthermore, rotating slender axisymmetric bodies are widely found in many applications, as e.g. turbomachinery or archery, so that the results obtained could be of relevance.

Concluding, due to the importance in engineering applications of this flow configuration and the lack of literature regarding low Reynolds numbers wakes, the motivation of this dissertation is mainly to shed some light on the pattern of bifurcations and unstable regimes that the laminar flow past bullet-shaped bodies undergoes with increasing Reynolds number. The insight gained will be used to apply three passive control methods, namely, base bleed, rear cavities and body rotation.

1.2 Problem formulation

The flow configuration (see Fig.1.1) consists of a bullet-like body of length-to-diameter ratio $\ell = L/D$, with an ellipsoidal nose of 2:1 major-to-minor axis ratio and a sharp trailing edge, aligned with a flow of uniform velocity w_∞, density ρ_∞ and viscosity μ_∞. The equations governing the flow are the three-dimensional, incompressible Navier-Stokes equations,

$$\nabla \cdot \mathbf{u} = 0, \tag{1.1}$$

$$\frac{\partial \mathbf{u}}{\partial t} + \mathbf{u} \cdot \nabla \mathbf{u} + \nabla p - \frac{1}{Re} \nabla^2 \mathbf{u} = 0, \tag{1.2}$$

being $\mathbf{u} = (u, v, w)$ and p the velocity and pressure fields respectively expressed in cylindrical coordinates, (r, θ, z), that are made dimensionless using D, w_∞, D/w_∞ and $\rho_\infty w_\infty^2$, as scales of length, velocity, time and pressure. Thus, two non-dimensional parameters characterize the

problem, namely, the Reynolds number, $Re = \rho_\infty w_\infty D/\mu$, and the aspect ratio ℓ. Two additional dimensionless parameters govern the problem when a rear cavity is added to the base, namely the non-dimensional cavity length h/D and cavity diameter dimensionless D_c/D. On the other hand, when base bleed is applied, fluid is injected through the base with uniform velocity w_b, density ρ_b and viscosity μ_b. Therefore, three new dimensionless parameters can be defined, namely, the bleed coefficient, referred to as the bleed-to-freestream velocity ratio, $C_b = w_b/w_\infty$, the bleed-to-freestream density ratio, $S = \rho_b/\rho_\infty$, and the bleed-to-freestream viscosity ratio, $\eta = \mu_b/\mu_\infty$. Finally, when the body rotates with angular velocity ω, a dimensionless rotation parameter can be defined, $\Omega = \omega D/2w_\infty$, being it the ratio between the azimuthal velocity at the surface of the body and the freestream velocity. Thus, in the remaining of the dissertation all the magnitudes appearing will be non-dimensional, unless otherwise stated or units included.

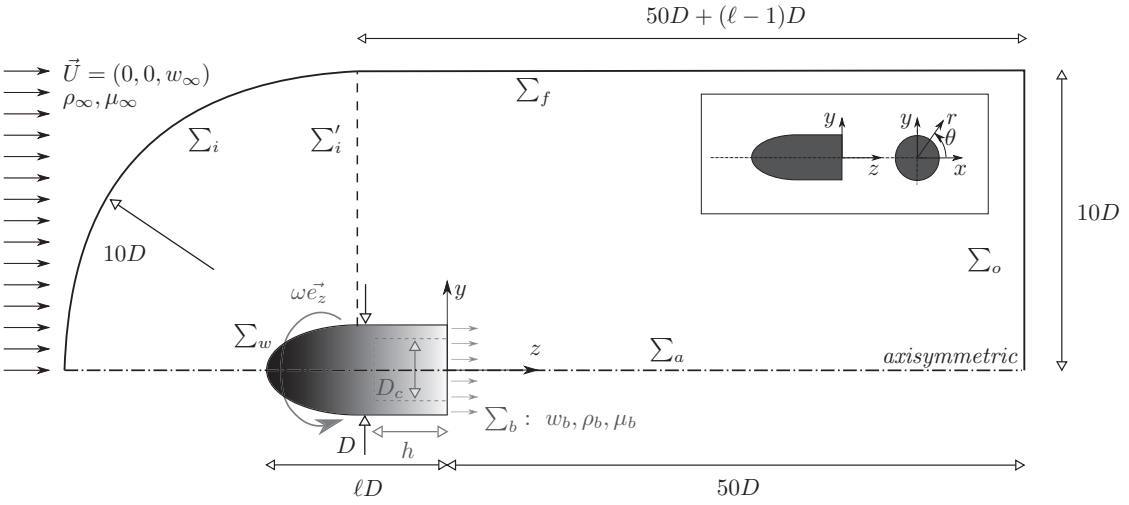

Figure 1.1: Scheme of the problem and axisymmetric computational domains (dashed line represents inlet for final global stability mesh, see Appendix A). Inset illustrates side (left) and rear (right) views of the coordinate system.

1.2.1 Linearized problem (BiGlobal Linear Stability)

The complete three-dimensional incompressible equations will be discretized to solve numerically the wake behind the bullet-shaped body (see Fig.1.1). However, the BiGlobal linear stability problem is formulated differently, namely, by considering a perturbed flow as the superposition of a steady axisymmetric basic flow $[\mathbf{U}(\mathbf{x}), P(\mathbf{x})]$ and small amplitude disturbances, $[\mathbf{u}'(\mathbf{x}, t), p'(\mathbf{x}, t)]$,

$$[\mathbf{u}(\mathbf{x}, t), p(\mathbf{x}, t)] = [\mathbf{U}(\mathbf{x}) + \mathbf{u}'(\mathbf{x}, t), P(\mathbf{x}) + p'(\mathbf{x}, t)]. \tag{1.3}$$

Here, the basic velocity, $\mathbf{U}(\mathbf{x}) = [U(r,z), V(r,z), W(r,z)]$, and pressure, $P(r,z)$, fields, are the solution of the steady, axisymmetric version of Eqs.(1.1) and (1.2),

$$\nabla \cdot \mathbf{U} = 0, \tag{1.4}$$

$$\mathbf{U} \cdot \nabla \mathbf{U} + \nabla P - \frac{1}{Re}\nabla^2 \mathbf{U} = 0, \tag{1.5}$$

along with appropriate boundary conditions, while $[\mathbf{u}'(\mathbf{x},t), p'(\mathbf{x},t)]$ satisfy the unsteady Navier-Stokes equations linearized around the base state, namely,

$$\nabla \cdot \mathbf{u}' = 0, \tag{1.6}$$

$$\frac{\partial \mathbf{u}'}{\partial t} + \mathbf{U} \cdot \nabla \mathbf{u}' + \mathbf{u}' \cdot \nabla \mathbf{U} + \nabla p' - \frac{1}{Re}\nabla^2 \mathbf{u}' = 0, \tag{1.7}$$

that in compact form, read

$$-\frac{\partial}{\partial t}\mathbf{q}' = \mathcal{L}(\mathbf{U})\mathbf{q}'. \tag{1.8}$$

Equation (1.8), subjected to an appropriate set of boundary conditions, constitutes an initial value problem, where $\mathbf{q}' = (\mathbf{u}', p')$, and $\mathcal{L}(\mathbf{U})$ denotes the linear stability operator (the Jacobian). In the stability analysis we are only concerned with the modal problem, i.e. with the eigenmodes associated to Eq.(1.8). Furthermore, since the base flow is steady and axisymmetric, the resulting eigenvalue problem is BiGlobal [145], and is formulated by means of the Ansatz,

$$[\mathbf{u}', p'] = [\hat{\mathbf{u}}(r,z), \hat{p}(r,z)]e^{\sigma t + im\theta}, \tag{1.9}$$

being $\sigma_r = \Re(\sigma)$ the growth rate of each mode, $\sigma_i = \Im(\sigma)$ its angular frequency, $m \in \mathbb{Z}$, the azimuthal wavenumber, and $(\hat{\mathbf{u}}, \hat{p})$ the global eigenfuncions. Introducing Eq.(1.9) into Eq.(1.8) yields the following generalized eigenvalue problem (EVP),

$$\mathcal{A}\hat{\mathbf{q}} = \sigma\mathcal{B}\hat{\mathbf{q}}, \tag{1.10}$$

where $\hat{\mathbf{q}} = (\hat{\mathbf{u}}, \hat{p})^T = (\hat{u}, \hat{v}, \hat{w}, \hat{p})^T$ is the eigenfunction vector, and $\mathcal{A}$ and $\mathcal{B}$ are the following linear operators,

$$\mathcal{A} = \tag{1.11}$$

$$\begin{pmatrix} \frac{\partial}{\partial r} + \frac{1}{r} & \frac{im}{r} & \frac{\partial}{\partial z} & 0 \\ \mathbf{U}\cdot\nabla + \frac{\partial U}{\partial r} - \frac{1}{Re}\left(\nabla^2 - \frac{1}{r^2}\right) & -\frac{2V}{r} + \frac{2}{Re}\frac{im}{r^2} & \frac{\partial U}{\partial z} & \frac{\partial}{\partial r} \\ \frac{\partial V}{\partial r} + \frac{V}{r} - \frac{2}{Re}\frac{im}{r^2} & \mathbf{U}\cdot\nabla + \frac{U}{r} - \frac{1}{Re}\left(\nabla^2 - \frac{1}{r^2}\right) & \frac{\partial V}{\partial z} & \frac{im}{r} \\ \frac{\partial W}{\partial r} & 0 & \mathbf{U}\cdot\nabla + \frac{\partial W}{\partial z} - \frac{1}{Re}\nabla^2 & \frac{\partial}{\partial z} \end{pmatrix},$$

$$\mathcal{B} = -\begin{pmatrix} O & O & O & O \\ O & I & O & O \\ O & O & I & O \\ O & O & O & I \end{pmatrix}, \tag{1.12}$$

where O and I are the null and identity operators, respectively. By numerically solving Eq.(1.10) the leading global modes $\hat{\mathbf{q}}$ of the axisymmetric flow around the bullet-shaped body can be identified, together with the stability limits of the axisymmetric steady state and subsequent stability regions.

1.2.2 The Stuart-Landau model

The Stuart-Landau equation, introduced by Landau [73] and derived by Stuart [140] for the stability of parallel flows, is a single degree freedom model and represents a normal form of a Hopf bifurcation, i.e. the flow bifurcates towards an oscillatory limit-cycle solution from a steady flow. It describes the weakly nonlinear dynamics of the fundamental mode of a perturbation after the transition, and has been applied satisfactorily for wakes behind bluff bodies, such cylinders [119, 32, 147] or spheres [42, 148, 132] among others, modeling the wake behavior as an oscillator. Although comprehensive studies and developments can be found in the literature (see for instance [32] for a complete derivation), we shall briefly summarize in this section its basics, to apply it later to our problem.

In this sense, as highlighted before, the initial value problem defined by Eq.(1.8), with time independent coefficients, accepts as general solution the superposition of normal modes $\mathbf{q}'(\mathbf{x},t) = \hat{\mathbf{q}}(\mathbf{x})e^{\sigma t}$, where $\sigma = \sigma_r + i\sigma_i$, being σ_r the growth rate and σ_i the frequency. It is well-known that space-confined eigenvalue problems give rise to a discrete spectrum, so σ represents a set of eigenvalues associated to corresponding eigenfunctions $\hat{\mathbf{q}}$. On the other hand, when the flow bifurcates at a given critical $Re = Re_c$, there is just a marginal stable, fundamental, global mode $\sigma^f = \sigma_r^f + i\sigma_i^f$ (along with its conjugate), with $\sigma_r^f = 0$, that will be destabilized immediately as Re increases over Re_c, denoting the superscript f the fundamental mode under study. This eigenvalue is associated to an eigenfunction $\hat{\mathbf{q}}_\mathbf{f}$, and its projection will be the only amplifying as the time evolves. Hence, a complex amplitude $A(t)$ can be defined in order to study the instability temporal evolution from small magnitude to saturation of this fundamental mode, in such a way that we can approximate the modulus as $|A(t)| \sim e^{\sigma_r^f t}$, but only for short times, since the evidence shows that this amplitude does not grow constantly but it eventually saturates. Furthermore, the characteristic growth time scale, which is of the order $\mathcal{O}[\left(\sigma_r^f\right)^{-1}]$, must be sufficiently larger than the natural oscillating period of the mode, $T = 2\pi/\sigma_i^f$, but short enough to keep the perturbation small, to avoid that harmonics and nonlinearities arise and deform the fundamental mode. This sets a limit of validity for these assumptions given by $\sigma_r^f \ll \sigma_i^f$, what applies close to the onset of instability, i.e. small values of $(Re - Re_c)$. Thus, with these limitations, it is possible to describe the dynamics of the fundamental mode as a truncation of the following expansion of $A(t)$, that is, the Landau equation,

$$\frac{dA}{dt} = (\sigma_r^f + i\sigma_i^f)A - (l_r + il_i)|A|^2 A + h.o.t., \tag{1.13}$$

where l_r and l_i are real and correspond to Landau cubic coefficients, and the growth rate σ_r^f acts as the bifurcation parameter with $\sigma_r^f = 0$ at the bifurcation. This equation can be likewise obtained from a weakly nonlinear expansion of the perturbed Navier-Stokes equations [32, 42], by assuming that the fundamental mode does not vary during the transient time, and is just valid in the vicinity of a bifurcation.

The second term in the right hand side of Eq.(1.13) determines the nature of the bifurcation. Thus, if $l_r > 0$, the bifurcation is supercritical, what means that higher order terms in Eq.(1.13) are not required for the amplitude to saturate, what conversely happens for subcritical bifurcations, i.e. $l_r < 0$. In the case of the bullet-shaped body of interest in this Thesis, the Hopf bifurcation is by definition supercritical and we expect the first regular bifurcation to be as well supercritical (as for the sphere [148]), so we will deal initially with the third order truncation of the Landau

model. This expansion can be now separated into two equations, if we use the polar representation, $A(t) = |A(t)|e^{i\phi(t)}$, with $|A(t)|$ being the modulus of the complex amplitude $A(t)$, and $\phi(t)$ its real phase. Thus, Eq.(1.13) is equivalent to the pair of real differential equations,

$$\frac{d\log|A|}{dt} = \sigma_r^f - l_r|A|^2, \tag{1.14}$$

$$\frac{d\phi}{dt} = \sigma_i^f - l_i|A|^2, \tag{1.15}$$

where the derivatives $d\log|A|/dt$ and $d\phi/dt$, that correspond to the instantaneous growth rate and the instantaneous frequency respectively, are shown to be linear functions of $|A|^2$, being l_r and l_i local gradients. From Eq.(1.15), it is seen that σ_i^f is the onset frequency, existing for null amplitude, and it should be distinguished from the saturation (or characteristic shedding) frequency, that will be introduced below.

The coefficients included in Eqs.(1.14) and (1.15) have been shown to be all functions of Re, with mostly weak dependencies except for σ_r^f, what can be deduced easily from the eigenvalue parameters. Thus, for a supercritical bifurcation, the first two right-hand side terms in Eq.(1.13) must be of similar magnitude in the vicinity of the transition and consequently σ_r^f has to be of order $\mathcal{O}(|A|^2)$, along with the distance from the transition, $(Re - Re_c)$, where Re_c is given by $\sigma_r^f(Re_c) = 0$. Thus, by assuming Taylor expansions in the neighborhood of Re_c for σ_r^f and σ_i^f, we can obtain the following approximations,

$$\sigma_r^f = \frac{d\sigma_r^f}{dRe}(Re_c)(Re - Re_c) + \mathcal{O}\left[(Re - Re_c)^2\right], \tag{1.16}$$

$$\sigma_i^f = \sigma_i^f(Re_c) + \frac{d\sigma_i^f}{dRe}(Re_c)(Re - Re_c) + \mathcal{O}\left[(Re - Re_c)^2\right], \tag{1.17}$$

so that, if the higher order terms are neglected, linear dependencies with Re remain. Moreover, at saturation, since $d|A|/dt = 0$, the amplitude can be expressed from Eq.(1.14) as $|A|_{sat} = (\sigma_r^f/l_r)^{1/2}$, and consequently, according to Eq.(1.16), it is proportional to the squared root of the distance from criticality $(Re - Re_c)^{1/2}$,

$$|A|_{sat} = \left(\frac{1}{l_r}\frac{d\sigma_r^f}{dRe}[Re_c]\right)^{1/2}(Re - Re_c)^{1/2}. \tag{1.18}$$

Furthermore, Eq.(1.15) becomes $d\phi_{sat}/dt = \sigma_{i\ sat}^f = \sigma_i^f - c\sigma_r^f$ at saturation, where $c = l_i/l_r$ is usually referred to as the *Landau constant*, and measures the shift in frequency during the transient regime towards the saturated state $c = (\sigma_i^f - \sigma_{i\ sat}^f)/\sigma_r^f$, where $\sigma_{i\ sat}^f = 2\pi f_{sat}$ denotes the characteristic shedding angular frequency, being f_{sat} the linear frequency at saturation, and represents a global parameter of the wake, as it will be shown below. This Landau constant could be as well defined locally as $(d\log A/dt - \sigma_r^f)/(d\phi/dt - \sigma_i^f)$, being then a function of $|A|^2$ [147].

The Stuart-Landau model does not consider spatial variables, so a comment must be made about its limitations in this sense. The parameters σ_r^f and σ_i^f are independent of position since they belong to the global mode that exist at the wake. On the contrary, l_r and l_i are local parameters and depend on location (e.g.[32]), something that can be easily seen for l_r, from $|A|_{sat} = (\sigma_r^f/l_r)^{1/2}$, since it is an experimental and numerical fact that $|A|_{sat}$ changes with location (see for instance results in Section 2.3). As far as the Landau constant is concerned, it does not depend on position when saturation is established, owing to its functional relation $c = f(\sigma_r^f, \sigma_i^f, \sigma_{i\ sat}^f)$, but it is a function of the amplitude and location before reaching such a state [147]. Thus, it seems that

the temporal "constant" nature of c at saturation is just a consequence of the slow deformation of the fundamental mode as the amplitude grows when compared to the amplification time scale [32]. Therefore, the applicability of the Landau model is restricted to Re close to Re_c, where σ_r^f is still small. Thus, the transient dynamics can be unequivocally described by means of three global parameters, namely, σ_r^f, σ_i^f and c at saturation.

Finally, in line with the formulation exposed for a Hopf bifurcation, the real Landau model version given by Eq.(1.14) has been successfully used to describe the behavior of the perturbation amplitude for the axisymmetry-breaking regular bifurcation in the wake of the sphere [42, 148], and it constitutes a normal form representation of a pitchfork bifurcation [31]. In this case, there is just a steady mode being destabilized at $Re = Re_c$, with $\sigma = \sigma_r^f$, and the amplitude describing the perturbation evolution, A, will be real. Thus, for a supercritical bifurcation, Eq.(1.14) gives a saturation amplitude $|A|_{sat} = (\sigma^f/l)^{1/2}$, where $l = l_r$.

1.3 Outline of the dissertation

The present dissertation is organized as follows. Chapter 2 is devoted to characterize the pattern of transitions and unstable modes leading the natural wake behind bullet-shaped bodies to unsteadiness. The study includes a description of the effect of the body aspect ratio on the transitions and the characteristic Reynolds numbers at which they take place. Transients dynamics are analyzed using the Stuart-Landau model. Chapter 3 includes a study on the stabilizing effect of two passive control strategies, namely, base bleed and rear cavities, focusing on the effect they have on transitions, and showing that axisymmetry is retrieved when the base bleed coefficient reaches some critical value and the cavity has a critical size respectively, both depending on the Reynolds number. Chapter 4 describes in detail the unstable regimes existing at the wake of a rotating bullet-shaped body for a wide range of rotation parameters, illustrating how it is possible to stabilize completely the wake under certain conditions. Besides, some unstable modes behave like rotating waves, what is a consequence of the problem symmetry. Chapter 5 collects the main conclusions of the Thesis and future work. Finally, Appendix A includes a description of the code used to perform global stability analysis in this dissertation, whereas Appendix B is devoted to a study on the modal (direct and adjoint) and non-modal stability properties of a round parallel jet, as example of the potential application of this methodology to other flow configurations.

CHAPTER
TWO

Natural laminar wake behind bullet-shaped bodies

This chapter is intended to present a thorough study on the stability properties of wakes behind slender axisymetric bodies with blunt trailing edge, made by means of BiGlobal linear stability analysis, hot-wire anemometry experimental measurements and three-dimensional numerical simulations. It is found that the wake behind these axisymmetric slender bodies exhibits a pattern of transition leading to vortex shedding similar to that of the sphere wake, i.e.: an axisymmetry-breaking regular transition (at $Re = Re_{cs}$) and an oscillatory Hopf bifurcation (at $Re = Re_{co}$) take place, leading respectively to a *steady state* planar-symmetry mode, SS, and *reflectional symmetry preserving* mode, RSP. The BiGlobal stability analysis shows that the first bifurcation corresponds to a three-dimensional $|m| = 1$, steady perturbation, and the stability characteristics do not change during the presence of the SS mode at the wake ($Re_{cs} \leq Re < Re_{co}$). However, at $Re = Re_{co}$ a second eigenmode becomes unstable, which corresponds to a three-dimensional $|m| = 1$ and oscillating perturbation. A comparison between methods shows how BiGlobal stability analysis overestimates Re_{co}, due to the use of an axisymmetric basic flow for $Re > Re_{cs}$. Besides, the wake behind bullet-shaped bodies exhibits particularities regarding a third oscillatory Hopf bifurcation, found at $Re = Re_{co2}$, consisting in a low modulation of the shedding frequency, and preserving the planar symmetry. On the other hand, a parametric study on the aspect ratio ℓ has shown that increasing the boundary layer thickness (increasing ℓ) has a stabilizing effect, providing with larger critical values of Re. Finally, the Stuart-Landau model has been used to describe the dynamics of the transient at the wake of a $\ell = 2$ body, finding similarities with other axisymmetric bodies.

This chapter is comprised, in part, in the paper "Stability and dynamics of the laminar wake past a slender blunt-based axisymmetric body", by P. Bohorquez, E. Sanmiguel-Rojas, A. Sevilla, J. I. Jiménez-González and C. Martínez-Bazán, published in the Journal of Fluid Mechanics [15].

2.1 Introduction

The study of laminar flows past bluff bodies has been addressed by many authors in the past, due to their relevance in engineering and physical applications. The insight about instabilities arising at low Reynolds numbers and flow topology is relevant for an optimal control of the flow, even for turbulent applications, for which similar instabilities could occur, as for instance vortex shedding phenomena [135]. Within this frame, several numerical, experimental and stability analyses have dealt with wakes behind bluff bodies at different regimes [106, 157], although still many features of the transitions leading to turbulence are not totally understood. In this sense, two-dimensional bluff bodies have received much more attention than axisymmetric bluff bodies, in spite of their

practical relevance and applications, apart from spheres and disks [66].

The sequence of unstable modes at the wake of spheres and disks leading to turbulence are rich, and some common characteristics and peculiarities exist between them. For instance, a large experimental background exists about the sphere regimes for laminar and transitional Reynolds numbers, and it is known that the wake of the sphere remains axisymmetric up to $Re \simeq 210$, where a symmetry breaking bifurcation takes place. This regular bifurcation is a consequence of the destabilization of a $|m| = 1$ azimuthal linear mode [102, 112], that gives rise to a pair of steady counterrotating streamwise vortices arranged symmetrically in a plane, as observed experimentally [125, 108]. A second linear unstable mode arises through a Hopf bifurcation at $Re \simeq 277$, again after the destabilization of an azimuthal $|m| = 1$ perturbation [102, 112]. From the transition, an unsteady vortex shedding regime emerges, where hairpin-vortices are shed, with constant orientation (see for instance [132]), whilst retaining the planar symmetry of the prior mode. On the other hand, a change in the orientation of the hairpin vortices have been observed for $Re > 350 - 400$ [125, 19], that seems to be connected to a new low-frequency modulation observed with spectral analysis of temporal signals. Regarding the disk, the BiGlobal stability analysis of Natarajan & Acrivos [102] reported a similar pattern of transitions to unsteadiness, but at different Reynolds numbers.

The experiments of Brücker [19] also showed that wakes behind bullet-shaped bodies with a blunt trailing edge undergo the same basic bifurcations as the sphere, but take place at higher Reynolds numbers, what means that the aspect ratio plays a major role on the stability properties of the wakes, as Schouveiler & Provansal [131] demonstrated in the case of a three-dimensional cylinder. The same authors showed that the Hopf bifurcations taking place at these cylinder and sphere wakes can be described successfully by means of the Stuart-Landau model [108, 132]. However, important differences exist for the value of the Landau parameters with respect to two-dimensional bodies.

As mentioned, hydrodynamic stability techniques have been widely used in the past, since they represent a simplification of the Navier-Stokes equations, which have been just suitable for direct numerical resolution in the recent years. In this sense, the BiGlobal approach [102] seems to describe quite accurately the instabilities taking place, although it considers an axisymmetric base flow to compute the second bifurcation, once the base flow is clearly three-dimensional. Even assuming this limitation, it is evident that its predictions are better that those attempts made with local stability concepts, whose application is not successful in the case of strongly non-parallel flows. Indeed, for instance, the results of Pier [112] for the wake of a sphere clearly show that the theory of non-linear global modes, developed for weakly non-parallel flows [114], fails at predicting the onset of global oscillations. In such cases, either direct numerical simulations or global stability analyses (BiGlobal or TriGlobal [145]) are required in order to obtain quantitatively reliable results. In particular, a detailed non-linear description of the sequence of bifurcations which take place for increasing Reynolds numbers in the flow around axisymmetric bodies has been possible only recently. Thus, Schwarz *et al.* [134] performed direct numerical simulations of the laminar flow around a bullet-shaped body at Reynolds numbers 500 and 1000, showing that the dynamics of the wake is controlled by a global instability of large-scale helical instability modes, resulting from the simultaneous destabilization and subsequent non-linear interaction of a pair of counter-rotating $m = \pm 1$ azimuthal modes. Afterwards, Johnson & Pattel [60] and Tomboulides & Orszag [149] carried out direct numerical simulations of the flow past a sphere showing very good agreement

with the BiGlobal stability analysis of Nataraja & Acrivos [102] within the linear regime. Ghidersa & Dŭsek [42] provided with a non-linear theory for both the axisymmetry breaking and oscillatory bifurcations in the wake of the sphere, and performed direct numerical simulations of the linearized and fully non-linear Navier-Stokes equations, showing good agreement with the previous works [112]. The direct numerical simulations due to Kim & Choi [65] for the flow past a hemisphere revealed that, after the first steady symmetry-breaking bifurcation, the subsequent Hopf bifurcation does not preserve the symmetry plane. A third bifurcation takes place at a higher critical Reynolds number, in which a plane of symmetry reappears and, finally, a fourth one leads to an aperiodic state. This phenomenology was later found to apply also to the wake of a thin disk by Fabre *et al.* [34], and Shenoy & Kleinstreuer [138]. In addition, numerical simulations of the flow around a thick disk with length-to-diameter ratio 1/3 have been performed by Auguste *et al.* [8], providing a detailed description of the subsequent non-linear states leading to the appearance of chaos in the wake. Auguste *et al.* [8] identified a sequence of states considerably more complex than the corresponding scenario for the infinitely thin disk, including regimes previously unobserved in other geometries.

A theoretical explanation of the different non-linear states observed in experiments and numerical simulations has been given recently for the wakes of a sphere and an infinitely thin disk by Fabre *et al.* [34], and by Auguste *et al.* [8] for the thick disk case. In particular, Fabre *et al.* [34] and Auguste *et al.* [8] took advantage of the fact that the Reynolds numbers associated to the first two bifurcations are close to each other to develop a weakly non-linear description based on multiple codimension bifurcation theory [45, 71], showing close agreement with direct numerical simulations. In addition, a first-principles calculation of the coefficients associated to the weakly nonlinear modal expansion has been recently given by Meliga *et al.* [87] for the thin disk case, by means of the adjoint operator technique. Unfortunately, the theory of multiple codimension bifurcations applied to the wake of axisymmetric bodies [34, 87] requires that the corresponding branches bifurcating from the original steady axisymmetric state are close enough, so that the amplitude of the nonlinear saturated state appearing after the first bifurcation is small. A possible measure of this distance is provided by the relative difference between the critical values of the Reynolds number associated to both instability modes, $\Delta = (Re_{co} - Re_{cs})/Re_{cs}$, where Re_{cs} and Re_{co} denote the critical Reynolds numbers corresponding to the steady and oscillatory bifurcations, respectively. In the case of the thin disk wake the parameter $\Delta \ll 1$, and thus the normal form theory can be applied. However, it has been recently found by Sanmiguel-Rojas *et al.* [127] that, for the wake of a blunt-based cylindrical body, the parameter $\Delta \sim \mathcal{O}(1)$, and the theory of multiple codimension bifurcations is thus questionable for this kind of body. Moreover, taking into account the substantial differences found between the thin and thick disk cases, discussed above, it is expected that the wake of the slender blunt-based body will also present specific features, which are worth considering in detail given the practical importance of this geometry.

The main goal of this chapter is to provide with a complete picture of the unstable modes and bifurcations existing for low Reynolds at the wake of bullet-shaped bodies, by means of experiments, direct numerical simulations and BiGlobal stability analysis. The dynamics of the unstable modes in the vicinity of the bifurcations will be also analyzed with the Stuart-Landau model, in order to determine the nature of the bifurcations. Finally, the effect of the boundary layer thickness, estimated through the body aspect ratio, on the stability properties will be likewise evaluated. Thus, this chapter is organized as follows: experimental and numerical techniques are described in

Section 2.2, description of unstable modes and values of critical Reynolds are presented in Section 2.3. Analysis of transient dynamics with the Stuart-Landau model are included in Section 2.4, and a comparison between the sphere and the $\ell = 2$ body wakes below the onset of unsteadiness is done in Section 2.5. Finally, conclusions about results are drawn in Section 2.6.

2.2 Experimental and numerical techniques

2.2.1 Experimental details

Hot Wire Anemometry (HWA) experiments have been performed in order to characterize the second oscillatory bifurcation at the wake, and the unstable mode emerging through it. The procedure consisted in recording temporal signals of streamwise velocity, $w(t)$, with a single probe, from which the oscillations amplitude were computed, in order to determine the critical Reynolds number at which the Hopf bifurcation takes place, $Re = Re_{co}^{exp}$. The HWA experiments were carried out in a vertical wind tunnel of 20×20 cm^2 cross section (see Fig.2.1), with a turbulence intensity lower than 0.8% for the whole range of velocities measured. Different bodies of diameter D=1 cm, and length-to-diameter ratios $\ell = 1, 2, 3, 4$ and 6, respectively, were used to determine the effect of the boundary layer thickness at the separation point on the stability properties of the flow (see figures 2.2a and 2.2c). The body, which was aligned with the free stream, was held with a hollow needle of external diameter 1 mm, that was welded internally to the body. The junction was located upstream of the base at $z = -\ell/2$ for all bodies, and it was polished externally to obtain a fully smooth outer surface. To verify that the holding device did not introduce any perturbation in the flow, we measured the velocity fluctuations at the base edge ($r = 0.5$) for several downstream locations, and no oscillations were observed for any Re and any body, in the region around $St = fD_{nd}/w_\infty \simeq 0.2$, where D_{nd} is the needle diameter. Furthermore, the HWA single probe was located at several downstream positions downstream of the body base, in order to quantify the variation of the amplitude with the axial coordinate z, and to obtain Re_{co}^{exp} where the oscillations energy was the largest.

On the other hand, base bleed was used as well to inhibit the emission of vortices from the base of the body, in order to carry out the transient experiments described in Section 2.4 (to get more detailed information about how this control mechanism works and the complete set-up, see Chapter 3). Thus, the supporting needle was connected to the compressed airline and a hollow slender body as shown in Fig.2.2(b). The level of gas flow rate injected through the body base for wake control, was established so that oscillations were not noticeable at the HWA signal anymore, for the unstable Re at hand. Afterwards, a valve at the entrance of the holding needle was used to switch off the flow and initiate the transient.

To register the velocity signals, we used a TSI®-IFA 300 Constant Temperature Hot Wire Anemometer equipment (CTA), whose operation principle is briefly described next. In this sense, plenty of previous works are devoted to CTA devices and HWA systems in general, and more comprehensive information can be found for instance in Tropea *et al.* [152]. That said, the CTA includes a bridge and an amplifier controlling a 5 microns heated sensor of resistance R_w, that is located in series with a large bridge resistance ($R_p = 10$ Ohms) to increase the bridge voltage and its fluctuations, and therefore the resolution. Besides, the bridge has a passive arm made up by a large resistance R_2 and an adjusting resistance R_c, that set the wire overheat, according to a

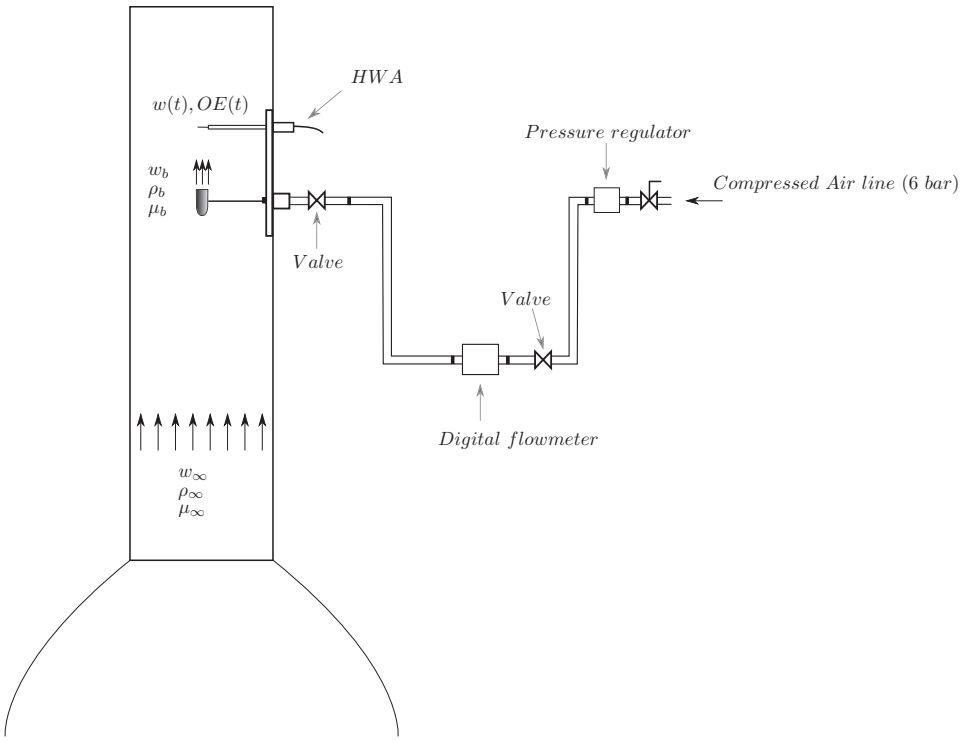

Figure 2.1: Sketch of the hot-wire anemometer experimental set-up.

bridge ratio $R_2/R_p = 25$. Then, when the heated wire ($T_\mathrm{w} \simeq 250C$) is cooled by exposure to the flow, the resistance changed (T_w and R_w are proportionally related) and a voltage is measured in the middle of the bridge by the operational amplifier. Thus, an electrical current, I_w, is fed to the sensor by the operational amplifier, in such a way that the former wire resistance is restored, and therefore the temperature. Hence, if $w(t)$ changes, the upper bridge $E_p(t)$ voltage will change to supply the current needed in order to comply with the resistance requirement and, therefore, it can be used as the anemometer output.

Considering the heat transfer balance from the wire, King's law for an incompressible flow around an infinite cylinder can be adapted to estimate the bridge voltage as $E_p^2 = C_1 + C_2 w^{\frac{1}{2}}$, where C_1 and C_2 are constants that include convection and conduction effects. This fitting law is used by the TSI®1129 Air Velocity Calibrator to create a calibration velocity curve for the single probe that will be used to measure. In this sense, when the equipment acquires velocity signals, a thermocouple is connected to the IFA 300 CTA to precisely correct the bridge voltage values obtained at calibration, and, consequently, it gives the actual velocity values. Finally, the system allows to obtain the bridge voltage as an optimized output voltage signal, OE, to achieve maximum resolution from the A/D Board provided. Thus, OE is obtained after subtracting an offset to E_p and multiplying it by a gain, that are calculated for each sensor. Finally, it must be pointed out that velocity signals were recorded with an acquisition frequency of 1000 Hz, and a long duration (256 seconds), so that transient effects of the flow caused by incoming perturbations are properly identified later during postprocess stage.

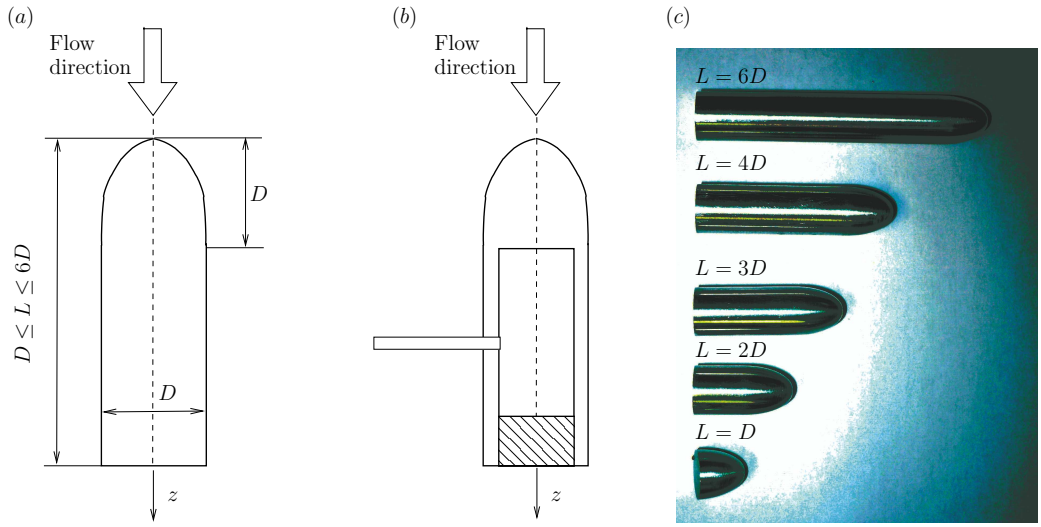

Figure 2.2: Sketch of the studied axisymmetric body with a rounded ellipsoidal nose. (a) Solid body, (b) hollow body used in the experiments with base bleed and, (c) image of the different solid bodies with length-to-diameter ratios $\ell = 1, 2, 3, 4$ and 6, respectively. Included in [15].

2.2.2 BiGlobal Linear Stability analysis

The EVP (1.10) was solved by means of an in-house code developed within the Fluid Mechanics Group at the University of Jaén. The first version of this code, introduced by Sanmiguel *et al.* [127], discretizes the linear operators $\mathcal{A}$ and $\mathcal{B}$ by using a Chebyshev collocation decomposition method, and was used during this Thesis to study the unstable linear global modes of the natural wakes. This code is suited for axisymmetric base flows without swirl and its foundations will be summarized in the present chapter. On the other hand, a second version of this code was developed later on, in order to overcome some geometrical limitations of the spectral collocation approach. This new version employs sixth-order finite differences schemes for non-uniform meshes, and it was used to study the wake behind bodies with rear cavities (see Chapter 3) and spinning bodies (see Chapter 4). Appendix A is devoted to describe the basics of the general code, but focusing on the differentiation by means of finite differences.

The first step in the resolution of Eq.(1.10) is solving the steady axisymmetric flow around the body, whose velocity and pressure fields, $\mathbf{U}(\mathbf{x}) = [U(r,z), 0, W(r,z)]$ and $P(r,z)$ respectively, and derivatives appear as part of the linear operator $\mathcal{A}$. The equations of the base flow (1.4) and (1.5) were solved by means of the Finite Volume code ANSYS Fluent®, within an adequate axisymmetric domain selected after the one used for the three-dimensional simulations (see Fig.1.1). Convenient boundary conditions were set for the axisymmetric steady problem, namely: $\mathbf{U}(\mathbf{x}) = (0, 0, w_\infty)$ at Σ_i, $\mathbf{U}(\mathbf{x}) = 0$ at Σ_w, $\mathbf{n}\cdot\mathbf{u} = 0$ at Σ_f, $P(\mathbf{x}) = \mathbf{n}\cdot\nabla\mathbf{U}(\mathbf{x}) = 0$ at Σ_o, and the axis condition for Σ_a. Equations were discretized with second order accuracy schemes (linear interpolation) for $\mathbf{U}$ and P. For the axisymmetric steady basic flow the pressure-velocity coupling was achieved in a segregated manner through the Semi Implicit Method for Pressure Linked Equation (SIMPLE) algorithm with under-relaxation, adjusted to increase the stability of the calculation by enhancing the coefficient matrix diagonal dominance [55]. An estimation of the discretization error was done

through a grid convergence study, in order to select the grid size that provided with converged results. Thus, a grid size of approximately 52.000 cells was adequate for the current problem, since doubling the number of nodes sheds relative errors below 1% for any quantity measured, and as it shown in Appendix A (see Table A.1), the simulations performed with this grid size provided accurate results even when flow has a strong swirl component.

Once the base flow was computed, the solution was mapped onto a non-uniform grid (see Fig.2.4) of size n_g, whose rectangular domain extended from $z = -\ell + 1$ to $z = 50$, as Fig.1.1 shows. Thus, the generalized EVP was solved within this domain, establishing standard boundary conditions for stability problems [146],

$$\mathbf{x} \in \Sigma_i', \Sigma_w, \Sigma_f : \quad \hat{\mathbf{u}} = 0, \tag{2.1}$$

$$\mathbf{x} \in \Sigma_o : \quad \hat{p}\mathbf{n} - \nabla\hat{\mathbf{u}} \cdot \mathbf{n}/Re = 0, \tag{2.2}$$

$$\mathbf{x} \in \Sigma_a : \quad \begin{cases} |m| = 0, & \hat{u}, \hat{v}, \partial\hat{w}/\partial r = 0, \\ |m| = 1, & \hat{u} \pm i\hat{v} = 2\partial\hat{u}/\partial r \pm i\partial\hat{v}/\partial r = \hat{w} = 0, \\ |m| > 1, & \hat{\mathbf{u}} = 0. \end{cases} \tag{2.3}$$

As seen in Eq.(2.3), at $r = 0$ (2.3), the axisymmetric conditions obtained by Khorrami *et al.* [63] were imposed in order to ensure the boundedness and smoothness of the solution. On the other hand, Eq.(2.2) stands for zero normal stress and was satisfactorily used for linear stability analisis [102].

As discretization technique we used the Chebyshev collocation-decomposition method that, basically, consists in dividing the computational domain into a block-structured grid with fictitious overlapping interfaces, with block sizes smaller in the surroundings of the body due to the larger gradients existing there. The functions were approximated by $n \times n$ tensor-product Lagrangian polynomials in the local computational space $[-1, 1] \times [-1, 1]$, and fitted using $(n + 1) \times (n + 1)$ nodes distributed according to Gauss-Lobatto-Chebyshev points, where n is the polynomial degree.

This code was first introduced in Sanmiguel *et al.* [127], where grid convergence studies were performed in order to determine the optimal domain size, the number or subdomains and the order n of the polynomials. In this sense, it is shown that the domain selected here is adequate, since no substantial variations were found in [127] when the downstream and radial extension were doubled. The outcome of a second grid convergence study provided with a grid of 222 subdomains and 12×12 nodes distributed according to the Gauss-Lobatto-Chebyshev points in each subdomain, that represents a total number of spectral nodes of $n_g = 27259$, what was enough to obtain a good convergence of the eigenvalues for the domain selected.

Once the operators stated in Eq.(1.10) are discretized and the boundary conditions are added, the generalized EVP (1.10), presents $4n_g \times 4n_g$ matrices, and must be solved in a large size grid of order $n_g \sim O(10^4 - 10^5)$, what makes the QZ algorithm, aimed at recovering the full spectrum, impractical. Hence, the well-known iterative Arnoldi method [7], based on the Krylov subspace, was used to solve an standard EVP obtained by means of a *shift and invert* strategy [146], $(\mathbf{A} - \beta\mathbf{B})^{-1}\mathbf{B}\hat{\mathbf{q}} = 1/(\sigma - \beta)\hat{\mathbf{q}}$, where we looked for the least stable part of the spectrum, i.e. the largest magnitude eigenvalues in the vicinity of the shift parameter β[1].

[1]In order to perform the calculations for the eigenvalues recovery, we used routines of MATLAB®, based on the ARPACK library [76] (see Appendix A for more details).

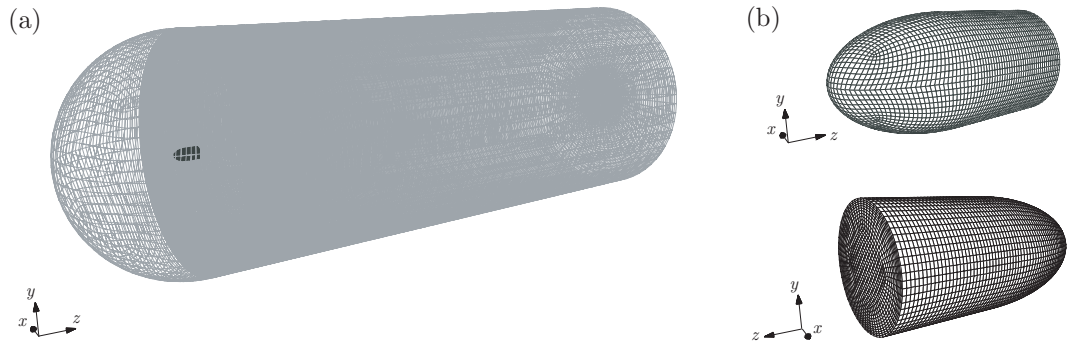

Figure 2.3: (a) Computational domain for the simulations of the flow around a body of $\ell = 2$, and (b) details of the meshed body.

2.2.3 Numerical techniques

In order to describe the topology of the unstable modes at the wake of bullet-shaped bodies, three-dimensional numerical simulations of the flow past a bullet-shaped body of $\ell = 2$ were performed, by using OpenFOAM® (Open Source Field Operation and Manipulation), an open source CFD Toolbox that implements the Finite Volume method. Comprehensive information about the schemes implemented in this code, and finite volume method can be found under the official website (www.openfoam.org) or [55].

Navier-Stokes equations, (1.1) and (1.2), were solved for the $\ell = 2$ body within a domain (see Fig.1.1) enclosed by a hemisphere of radius $10D$ and a cylindrical surface that extends 50 diameters downstream from the body base. This domain was chosen in line with previous works on the sphere, where the outflow location ranged in general between $25D$ [42, 149, 137] and $30D$ [17]; and other three-dimensional bluff bodies (like disks, spheroid or rings), where it varies generally from 10 [8] to 25 [137, 85]. Besides, transversal and upstream extensions lie usually in the range $8D - 25D$, accounting for the disparity of values the domain geometric differences, and corresponding the lower bound to tubular-like domains [42, 149, 17] (what yields negligible blockage factors of 0.1% approximately). Additionally, further validation of this domain size is given by the test made for the BiGlobal stability analysis for a truncated cylinder with blunt base (see precedent subsection), where the eigenvalue problem solution barely changes when the radial and downstream extensions are doubled [127].

The formulation of the problem is closed by choosing appropriate boundary conditions. Hence, a uniform streamwise velocity, $(0, 0, 1)$, was imposed at the inlet Σ_i, whereas the no-slip boundary condition is imposed at the body surface Σ_w. At the outer radial boundary Σ_f, we imposed a slip boundary condition $\mathbf{n}\cdot\mathbf{u} = 0$, where $\mathbf{n}$ is the outward normal, whereas at the downstream outlet Σ_o we implemented an outflow condition, that consists of imposing a Neumann boundary condition for the velocity, $\mathbf{n}\cdot\nabla\mathbf{u} = 0$, and a Dirichlet condition for the pressure, $p = 0$, that is equivalent to setting the normal component of the stress tensor to zero: $-p + 2\mu_\infty \partial w/\partial n \simeq -p = 0$, when μ_∞ is small [149].

The computational mesh, which included approximately 2.9×10^6 nodes distributed as $106(r)\times 60(\theta)\times460(z)$, was selected by performing a thorough grid refinement study, including an estimation of the discretization order, as described in more detail in Chapter 3 for a body with rear cavities, what provided with an estimation of the discretization order of $n \simeq 1.73$, that is slightly lower

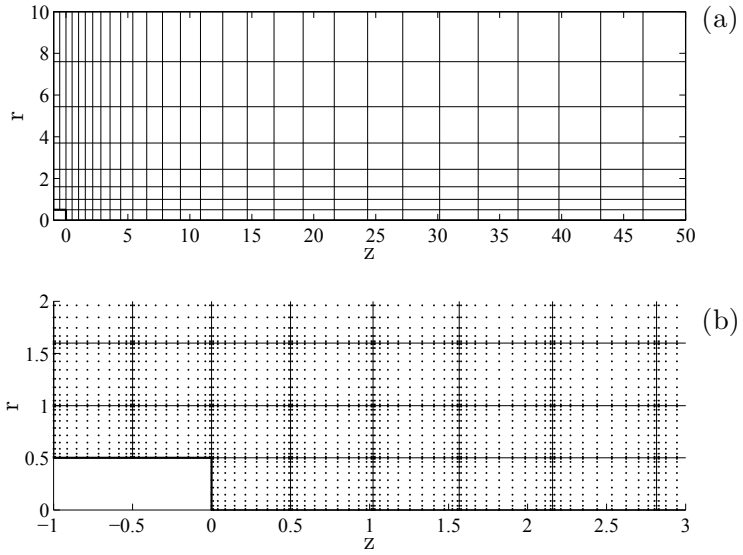

Figure 2.4: (a) Domain decomposition into 222 subdomains. The thin solid lines correspond to the subdomain boundaries. (b) Grid detail close to the body for 12×12 nodes distributed according to the Gauss-Lobato-Chebyshev points in each subdomain for a body of $\ell = 2$. Included in [15].

than the theoretical truncation error (second order) due to the fact that we have used limiters in our method, (see Ferziger and Perić [39]). In this sense, among the different choices available in OpenFOAM® for the spatial discretization, we decided to use second-order-accurate linear interpolation for the diffusion term, while, for the convection term, we selected a total variation diminishing scheme, by using a van Leer limiter [141]. This hybrid scheme is appropriate to avoid numerical oscillations stemming from grid regions where the local mesh Reynolds number is high enough [103]. On the other hand, the temporal discretization was performed by blending a Crank Nicholson scheme with implicit Euler integration, to ensure boundedness of the solution, and the pressure-velocity coupling was treated through the pressure-implicit split-operator (PISO) algorithm [54], always ensuring a time step small enough for the Courant number to be below 0.5. Besides, since the average non-orthogonality of the mesh is smaller than 3°, we avoid the use of non-orthogonality correctors, that are known to increase the computational cost [55, 15]. Finally, validation of the numerical schemes were obtained by means of performing additional simulations for the sphere (see Section 2.5), that provided with a critical Re for the steady bifurcation of 210 approximately, in good agreement with those reported by other authors (e.g. [102, 149]). All the computations were parallelized in 8-12 blocks, taking approximately between one and four weeks, depending whether the cases simulated were highly or marginally supercritical respectively. Furthermore, long saturated converged signals were obtained for the sake of accuracy in the spectral analysis.

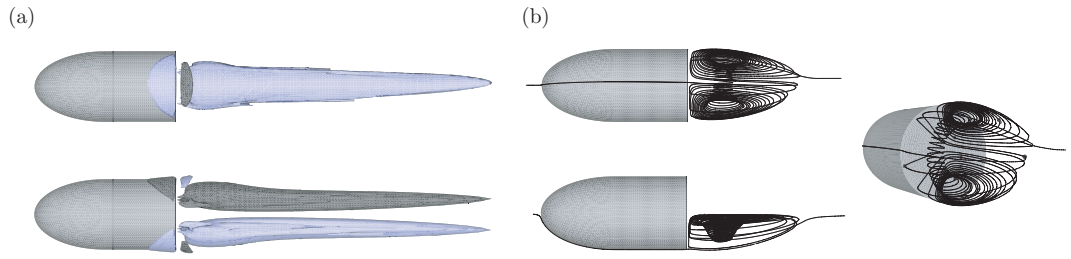

Figure 2.5: (a) Side (top) and top (bottom) views of iso-surfaces of streamwise vorticity $\varpi = \pm 0.05$ for $Re = 320$; and (b) side (top), top (bottom) and rear perspective (right) views of a streamline for $Re = 320$. Note that in (a) the dark-coloured and the light-coloured threads correspond to negative and positive ϖ respectively.

2.3 Description of unstable modes at the wake

In this section we present the results of the study on the laminar wake behind bullet-shaped bodies (Fig.1.1) and its unstable modes, performed with the techniques previously described. First, we describe the flow past a $\ell = 2$ body, the unstable modes and the critical Reynolds numbers for which the bifurcations take place. Secondly, we study the effect of the aspect ratio ℓ on the critical Reynolds numbers; and finally, we study the nature of the bifurcations at the wake of the $\ell = 2$ body using the Stuart-Landau model.

2.3.1 Wake of a $\ell = 2$ body

As appointed by Brücker [19], the aspect ratio has a strong stabilizing influence on the wake, and thus, the wake behind a $\ell = 2$ body remains axisymmetric for higher values of Re than for the sphere. In fact, our three-dimensional numerical simulations showed that the wake undergoes a transition slightly below $Re = 320$ that breaks the axisymmetry and leads the wake toward a state with bifid planar symmetric wake (Fig.2.5), similar to that of the sphere, where two elongated counterrotating threads of streamwise vorticity extend downstream from the base of the body. Like the case of the sphere, these structures are not perfectly aligned with the flow, since their axis are not exactly parallel to z-axis, because of the velocity induced at the centreline by both vortices that shifts them out of horizontal ($y = 0$)-plane. However, as already mentioned, they are symmetric with respect to a plane, that in our case, is selected by the lack of rotational symmetry at the mesh, being it established at an angle of 45° with respect to the x-axis (see Fig.2.3b), so that the side and top views presented in this chapter were obtained after applying a 45° rotation. The near wake structure features shoulders upstream of the body that suggest that the unstable nature of the destabilized mode is global. Furthermore, secondary lobes (see Fig.2.5a) are induced by the interaction between primary threads and the incident stream. Besides, in Fig.2.5(b) we present a streamline, located at the positive axial vorticity half of the near wake, which reveals partially the structure of the recirculation region. It can be seen how the toroid is not closed (as it would be for an axisymmetric wake), but the fluid entrains the toroid through the upper eddy, where

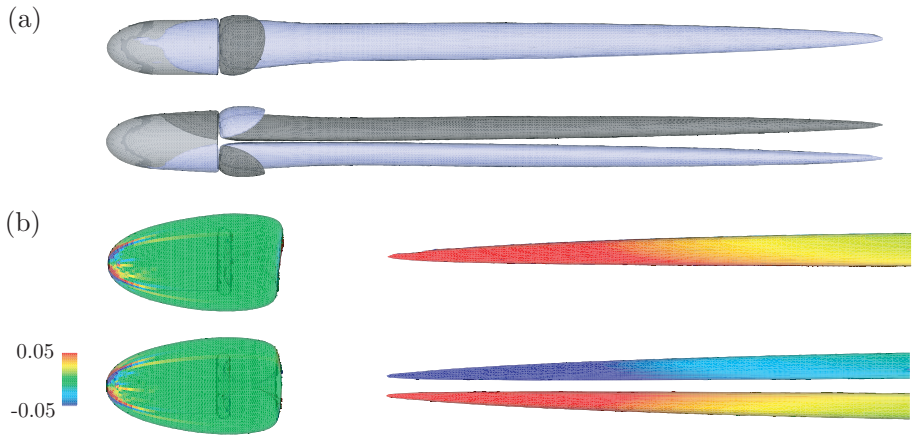

Figure 2.6: (a) Side (top) and top (bottom) views of iso-surfaces of streamwise vorticity $\varpi = \pm 0.05$ for $Re = 350$; and (b) same views of vortical structures visualized using Q-criterion, $Q > 0$. Note that in (a) the dark-coloured and the light-coloured threads correspond to negative and positive ϖ respectively.

it spirals clockwise (side view), decreasing the radius of the movement, until it reaches the upper core, from which it is ejected towards the lower eddy. The rotation here is counterclockwise and projects the flow outwards, until eventually it is ejected towards the upper half and then released in the flow on the same side of the recirculation. This behavior can be explained in terms of the destabilization mechanism proposed by Johnson & Pattel [60], who suggested that the flow from the spirally inward core towards the spirally outward one occurs due to an azimuthal pressure disturbance of the ring of minimum pressure at the recirculation vortex cores below Re_{cs}.

As Re increases, the elongated threads extend further downstream and its eccentricity becomes more pronounced, what, as it will be shown, accounts for the increment in the lift force. This fact is observed in Fig.2.6, that depicts the wake for $Re = 350$. Additionally, the topology can be as well studied by identifying the core of vortical structures, what will permit comparing our results with flow visualizations and vortices at the wake of other bodies. In this sense, we have used iso-surfaces of Q-criterion to identify vortical structures alongside the streamwise vorticity, being Q the second invariant of the velocity gradient $\nabla\mathbf{u}$, defined as $Q := ||\varsigma||^2 - \frac{1}{2}||\mathbf{S}||^2$, where ς is the rotation tensor and $\mathbf{S}$ the strain tensor, $\varsigma := \frac{1}{2}(\nabla\mathbf{u} - \nabla\mathbf{u}^T)$, $\mathbf{S} = \frac{1}{2}(\nabla\mathbf{u} + \nabla\mathbf{u}^T)$. Although this magnitude could fail to detect vortex cores when the external strain is strong [57], it is related to the λ_2 criterion used in many previous works for the sphere [60] or hemisphere [65], since $Q = -\frac{1}{2}(\lambda_1 + \lambda_2 + \lambda_3)$, where $\lambda_1 \geq \lambda_2 \geq \lambda_3$ are eigenvalues of $\mathbf{S}^2 + \varsigma^2$. Besides, it has a direct physical interpretation, even for $Q < 0$ [124]. In this sense, Fig. 2.6(b) shows the vortical structures for $Q > 0$, and lets us identify the two threads, that extends downstream towards the outflow, but progressively loosing intensity of swirl motion in the z-axis. The slow diffusion timescale $D^2\rho/\mu$ promotes the strength and shape conservation of such threads [148]. Furthermore, there is a shroud surrounding the body that is connected to the azimuthal vorticity that the boundary layer induces, and the recirculation region. The empty zone between the shroud and the tails could be due to the strong strain ($Q < 0$) to what the flow is subjected as a consequence of the external shear and the suction from the low pressure recirculation region.

The steady planar-symmetric state is present also at the sphere and disk wakes, for which the

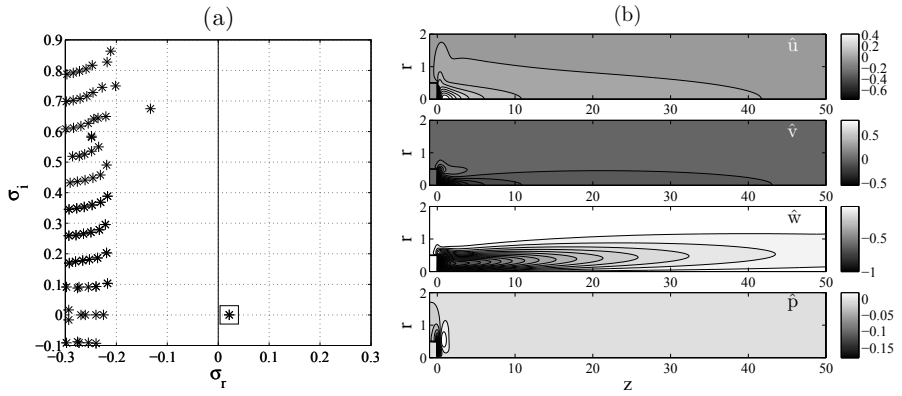

Figure 2.7: (a) Eigenvalue spectrum for $Re = 350$, $|m| = 1$ and $\ell = 2$. (b) Isolines of the real part of the normalized eigenfunctions $\hat{u}$, $\hat{v}$, $\hat{w}$ and $\hat{p}$ for the eigenvalue marked with a square in (a). The eigenfunctions have been normalized with $\|\hat{\mathbf{q}}\|_\infty$. Included in [15].

bifurcation is shown to take place due to the destabilization of a *Steady State* mode (SS) [34]. In this sense, our BiGlobal linear stability analysis (GLS) predicts likewise the destabilization of a steady eigenvalue ($\sigma_{i1} = 0$), corresponding to a three-dimensional helical $|m| = 1$ perturbation, for a $Re = Re_{cs}^{GLS}$ between 320 and 330. Prior the bifurcation, the dominant eigenvalue is damped, having a negative growth rate $\sigma_{r1} < 0$, but as Re increases, it approaches the marginal stability, $\sigma_{r1} = 0$, until it eventually is destabilized, $\sigma_{r1} > 0$, at $Re = Re_{cs}^{GLS}$. To compute Re_{cs}^{GLS}, we proceeded as in Bouchet *et al.* [17], by taking advantage of the fact that close to the transition, the growth rate σ_{r1} of the leading eigenvalue grows linearly with Re; then, from linear interpolation we obtained $Re_{cs}^{GLS} \simeq 327$. Figure 2.7(a) shows the spectrum of the bifurcated wake at $Re = 350$, where just the $|m| = 1$ linear steady eigenmode is unstable, what agrees with the results from the numerical simulations. Besides, the eigenfunctions $\hat{\mathbf{q}}$ corresponding the leading eigenmode are plotted in Fig. 2.7(b), showing as well the slender topology of the vortices aligned with the stream.

The SS mode is present at the wake at least until $Re = 410$, and consequently it remains steady and planar symmetric, but as said, the eccentricity will change as Re increases, and therefore the hydrodynamics forces will be also modified. Moreover, the evolution of the asymmetry degree with Re in a (x, y)-plane can be used to determine the critical Re for which the bifurcation takes place [101]. In this sense, Fig.2.8 shows the evolution of the squared centroid radius of the velocity magnitude distribution r_{ec}^2 for several Re and locations downstream of the base. As seen, in the range of Re studied, r_{ec}^2 grows almost linearly with Re, what can be utilized to obtain Re_{cs}^{DNS} as the extrapolation of the linear fit to $r_{ec}^2 = 0$. In addition, several downstream locations are included in Fig.2.8(a), from what it can be inferred that the asymmetry of the wake is large in the near wake and grows slightly with z initially, but this trend has an inflection location from where it decays. This can be due to the weakening of the streamwise vorticity with z shown in Fig.2.6, that would induce a feebler crossflow velocity and therefore smaller eccentricity. Anyway, the linear fits for all series provide with a similar value of critical Re, namely $Re_{cs}^{DNS} \simeq 318$.

On the other hand, the increment of Re within the SS mode regime affects likewise the hydro-

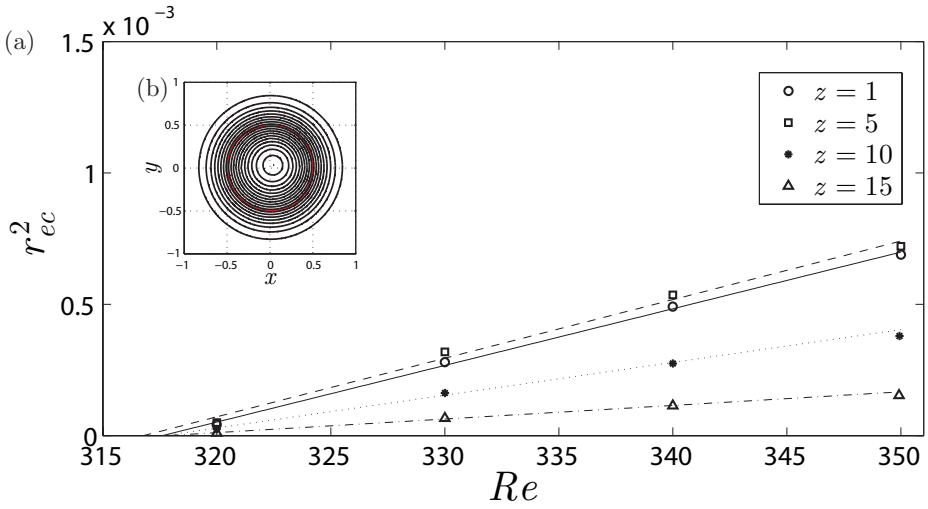

Figure 2.8: (a) Squared velocity distribution centroid radius r_{ec}^2 versus Re and (b) velocity magnitude contours for $Re = 320$ and $z = 5$. Lines in (a) represent linear fits, while the thick red line in (b) indicates the base of the body.

dynamic forces, which are characterized by the lift, C_l, and drag, C_d, coefficients, defined as,

$$C_l = \frac{F_l}{\frac{1}{2}\rho w_\infty^2 A_l} = C_l^p + C_l^v, \tag{2.4}$$

$$C_d = \frac{F_d}{\frac{1}{2}\rho w_\infty^2 A_d} = C_d^p + C_d^v, \tag{2.5}$$

where F_l and F_d are the dimensional lift and drag forces, superscripts stand for their pressure and viscous contributions respectively, and $A_l = \pi D^2/4 + D^2$, $A_d = \pi D^2/4$ are the corresponding projected areas (note that the lift coefficient based on the frontal area, $C_l(A_d)$, can be easily obtained as $C_l(A_d) = C_l\,(1 + 4/\pi)$). Figure 2.9(a) displays the evolution of C_d with Re, alongside with the drag obtained for a forced axisymmetric flow (dashed line) and, as expected, the SS mode fosters the drag [17] (due to higher centrifugal acceleration at the eddies cores and therefore lower pressure). On the other hand, as the growth on eccentricity suggested, the lift coefficient grows as well with Re (Fig.2.9b), and more interestingly, its squared value follows a linear increasing trend with Re, as Fig.2.9(c) shows (solid line). In this sense, the linear trends featured by $r_{ec}^2(z)$ and C_l^2 with Re indicate the global nature of such properties, characterizing the unstable mode since they are proportional to its amplitude, and therefore complying with real Landau model (1.14) (see Section 2.4). Again, the linear extrapolation to zero of C_l^2 in Fig.2.9(c) provides with $Re \simeq 318$.

At $Re = 415$, the flow computed by the numerical simulations shows an unsteady vortex shedding regime (see Fig.2.10), where vortices of opposite sign are shed alternatively, while the planar symmetry is preserved. This new time-depending state is the counterpart of the first unsteady regime of the sphere, that emerges as a consequence of the destabilization of a *reflectional symmetry preserving* mode (RSP) [34]. The new unstable global mode seems to arise at the wake of the sphere as a consequence of a convectively unstable mode at the far wake, that become globally unstable at $Re = Re_{co}$. Thus, the two vortex exhibit a growing kinking with Re, as it approaches Re_{co}, due to the self-interaction of the vortex threads, resulting in a Crow-type instability [47, 132].

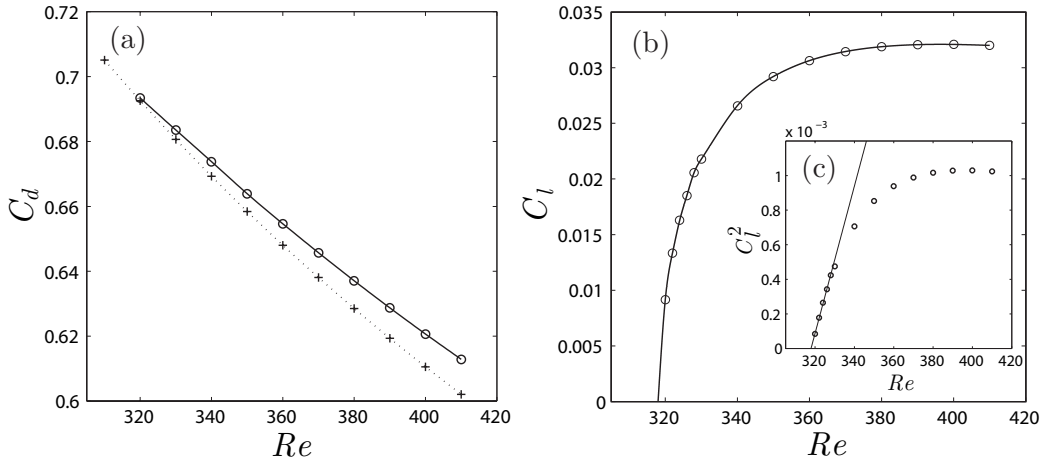

Figure 2.9: (a) Drag coefficient, (b) lift coefficient and (c) squared lift coefficient versus Re (solid line represents linear fit). In (a) dotted line stands for extrapolation of the axisymmetric flow drag.

More recently, Bohorquez & Parras [14] demonstrated numerically the existence of this peristaltic oscillation for a bullet-shaped body of $\ell = 9.8$.

The iso-surfaces of streamwise vorticity illustrate this new unsteady wake for $Re = 415$ at Fig.2.10 during a shedding period. As observed, the shedding process consists in the release from the base of vortices oriented always in the same direction, and the generation of counter-rotating induced vortices that are broken and carried downstream with the main inner vortices. These vortices grow and alternate in the far wake with the inner vortices. Furthermore, Fig.2.11 shows the vortical structures by means of Q-criterion, what gives further insight on the flow topology. It is clear that hairpin vortices can be identified on the top side of the structure, being its legs the streamwise vortices of Fig.2.10, while the induced vortices are attached at the bottom part of the legs. Note that, there are barely differences between these structures and those of the sphere, (see for instance [148]), so that these hairpin-vortices are expected to be observed in experimental visualization. Obviously, such affirmation about vortices must be interpreted with care when extrapolated to flow visualizations, but some conclusion can be drawn from the former. For instance at the sphere wake, dye-injection has generally provided with visualization of constantly oriented hairpin-vortices (see e.g. [132]), while as said, induced vortices appear as well at the vortical structures coming out from simulations. However, Johnson & Pattel [60] showed that the experimentally observed kinking existing at the vortices legs [125] for the RSP mode ($Re = 300$) seems to be connected to the numerically well captured induced vortices.

The unsteady vortex shedding translates into oscillating velocity and forces temporal evolutions that let us obtain from spectral analysis the shedding characteristic Strouhal number, $St_{sat} = f_{sat}D/w_\infty$, being f_{sat} the saturation frequency. In this sense, Fig.2.12 displays the transient of $C_l(t)$ when the flow is perturbed by varying the Reynolds from $Re = 410$ to 415. As seen, at $Re = 415$ the flow is already unstable and the lift oscillates, undergoing a transient in which the oscillations amplitude modulus, $|A(t)| = |C_l(t)|$ (dotted top line in Fig.2.12a), grows initially exponentially, according to the normal modes form, until eventually it saturates and reaches a constant value $|A|_{sat}$. Through a linear fit in a logarithmic scale (dotted line in Fig.2.12b), the

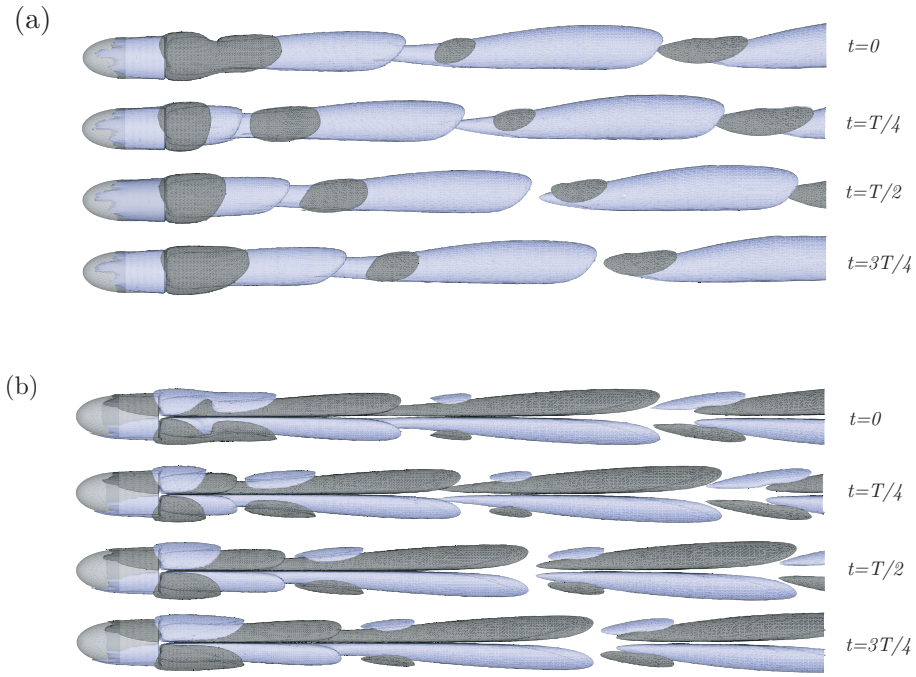

Figure 2.10: (a) Side views and (top) views of positive (light color) and negative (dark color) streamwise vorticity iso-surfaces ($\varpi = \pm 0.04$), representing a shedding period for $Re = 415$.

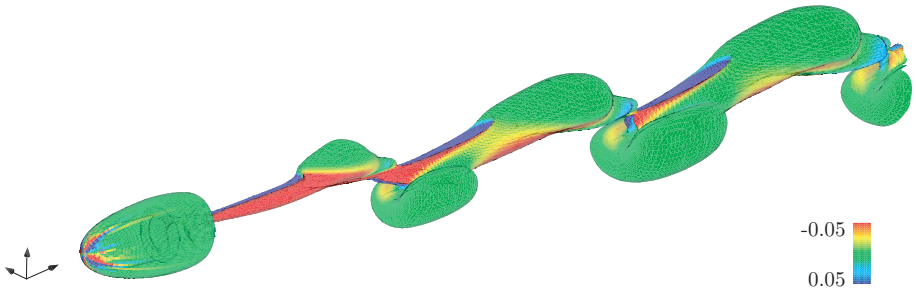

Figure 2.11: Vortical structures ($Q > 0$) for $Re = 415$ and $\ell = 2$ (colored by streamwise vorticity ϖ).

growth rate σ_{r2} can be estimated. By means of the mentioned fit, we obtained $\sigma_{r2} \simeq 0.0028$, that as it will shown, is almost identical to the value provided by the real part of Stuart-Landau model (1.14) ($\sigma_{r2} \simeq 0.0029$), and no big underprediction is found numerically, as appointed by Schumm *et al.* [133] when both methods were compared in experiments for a different bluff body. By decreasing Re until $Re = 410$ from 415, the RSP is stabilized, and lift oscillations decay in a transient, dying out eventually. A new exponential fit provides with a negative σ_{r2}, and, since according to Stuart-Landau (Eq.1.16), in the vicinity of the bifurcation the growth rate behaves linearly (see for instance [133, 17]); a linear interpolation between $\sigma_{r2}(Re = 410)$ and $\sigma_{r2}(Re = 415)$ can be performed to figure out the bifurcation threshold [42], obtaining $Re_{co}^{DNS} \simeq 413$. On the

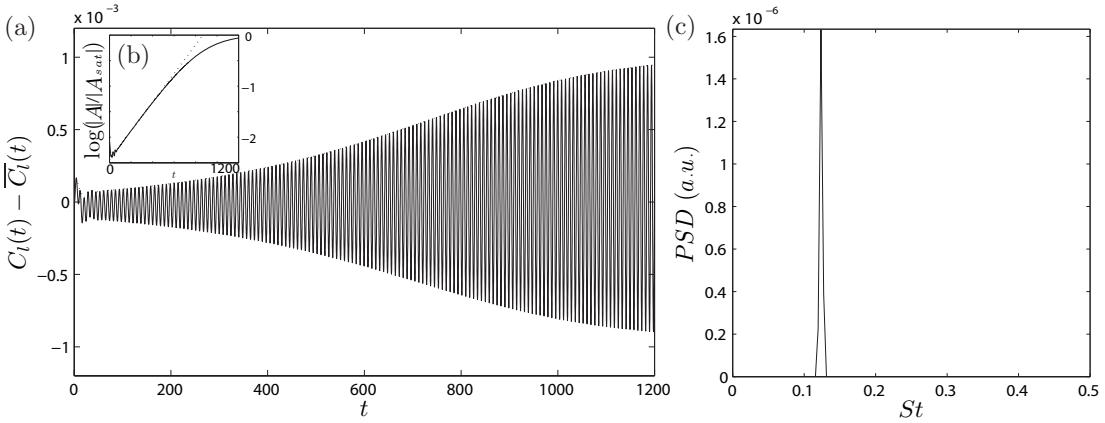

Figure 2.12: (a) Temporal transient evolution $C_l(t)$ at $Re = 415$, after perturbing the flow from $Re = 410$, and oscillations modulus $|A| = |C_l(t)|$ (dashed line); (b) logarithmic representation of normalized modulus $|A|/|A|_{sat}$, being $|A|_{sat}$ the modulus at saturation ($t > 1300$), and exponential fit (dotted line); and (c) power spectral density at saturation for $C_l(t)$ shown in (a).

other hand, once the transient settled down, we carried out the spectral analysis of $C_l(t)$ in order to obtain St_{sat}, whose value is 0.1234, as Figure 2.12(c) illustrates.

Our BiGlobal stability analyses predicts the destabilization of a pair of complex conjugate eigenvalues ($\sigma_i \neq 0$), defining a Hopf bifurcation, at $Re_{co}^{GLS} \simeq 518$, what represents a considerable difference with respect to the transition threshold predicted by the numerical simulations, $Re_{co}^{DNS} \simeq 413$, or the experiments $Re_{co}^{DNS} \simeq 412.4$ (see below). The overprediction in the critical Reynolds number of the second bifurcation is clearly due to the use of an axisymmetric base flow for Reynolds numbers higher than the one corresponding to the first, steady bifurcation. Notice that, at supercritical Reynolds numbers, $Re > Re_{cs}$, the original basic flow is already perturbed and, in particular, is no longer axisymmetric due to the three-dimensional nature of the first bifurcation mode, $|m| = 1$. Figure 2.13(a) shows the spectrum for $Re_{co}^{GLS} \simeq 518$, where the eigenvalue corresponding to the unstable oscillatory mode has been marked with a circle. This second transition corresponds to a three-dimensional, $|m| = 1$, and oscillating perturbation with a Strouhal number $St = \sigma_{i2}/2\pi \approx 0.102$, whose associated normalized eigenfunctions have been plotted in Fig.2.13(b), showing a spatially periodic structure similar to those obtained in the numerical simulations. The discrepancy between the vortex shedding Strouhal numbers obtained from the global stability analysis and the numerical simulations indicates that the exact structure of the global modes and its temporal frequency must be determined by means of a global stability analysis with a three-dimensional base flow (TriGlobal instability analysis [145]), in line with Tezuka & Suzuki [144], though such task is kept as part of future work and was not accomplished during this Thesis. However, it must be noted that a similar BiGlobal linear analysis performed for the sphere by Natarajan & Acrivos [102] gave values of Re_{co} very close to those obtained by means of three-dimensional numerical simulation and experiments. Although, not surprisingly, the error in their St prediction at the transition in comparison with experiments and simulations is approximately 15% (if our GLS results are compared with the numerical simulations for $Re < 500$, the errors for the St are approximately of 17%).

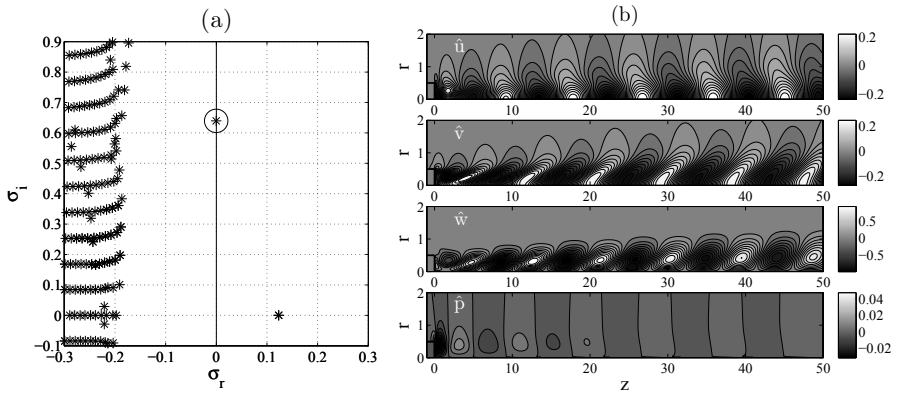

Figure 2.13: (a) Eigenvalue spectrum for $Re = 518$, $|m| = 1$ and $\ell = 2$. (b) Isolines of the real part of the normalized eigenfunctions $\hat{u}$, $\hat{v}$, $\hat{w}$ and $\hat{p}$ for the eigenvalue marked with a circle in (a). The eigenfunctions have been normalized with $\|\hat{\mathbf{q}}\|_\infty$. Included in [15].

Re	415	423	432	439	449	462	470
St_{sat}^{Exp}	0.1231	0.1232	0.1232	0.1251	0.1260	0.1287	0.1303
St_{sat}^{DNS}	0.1234	0.1247	0.1268	0.1284	0.1307	0.1318	0.1328

Table 2.1: Experimental and numerical values of vortex shedding Strouhal number for several $Re > Re_{co}^{exp}$, for a body of $\ell = 2$. Numerical Reynolds numbers corresponds to $Re = 415, 420, 430, 440, 450, 460$ and 470 respectively.

In addition to performing three-dimensional numerical simulations, we also carried out hot wire anemometer measurements to obtain experimentally the critical Reynolds number for the second, oscillatory bifurcation, Re_{co}^{exp}, and to characterize the RSP mode for increasing supercritical Re. Thus, we recorded long streamwise velocity signals $w(t)$ behind the body, which were oscillating for $Re > Re_{co}$, as Fig.2.14 depicts for $Re \simeq 429$. The computation of spectra from zero-mean signals (Fig.2.14b), obtained after subtracting to $w(t)$ their averaged value, $w'(t) = w(t) - \bar{w}(t)$, allowed us to determine experimentally the dependence of Strouhal number with Re, reported in Table 2.1, where it can be seen an increasing trend of St with Re. Notice that the values of experimental and numerical St are quite similar in the range of Re investigated.

To experimentally determine the critical value of the Reynolds number, Re_{co}^{exp}, we calculated the evolution with the Reynolds number of the squared amplitude of the streamwise velocity fluctuations $w'(t)$, $|A|_{sat}^2$, defined here as

$$|A|_{sat}^2 = \int_{f_{sat}-\Delta f_d}^{f_{sat}+\Delta f_u} PSD(f)\, df, \tag{2.6}$$

where $PSD(f)$ is the Power Spectral Density obtained from the velocity measurements, f_{sat} is the characteristic, shedding frequency and, Δf_d and Δf_u correspond to the interval of frequency around f_{sat} for which the power spectral density drops down to 1% the peak value. A linear increase of $|A|_{sat}^2$ with the Reynolds number near the critical value indicates that the transition to the oscillatory regime corresponds to a Landau-Hopf bifurcation (Eq.1.18). The critical value of the Reynolds number was then determined by linear regression of the experimental measurements

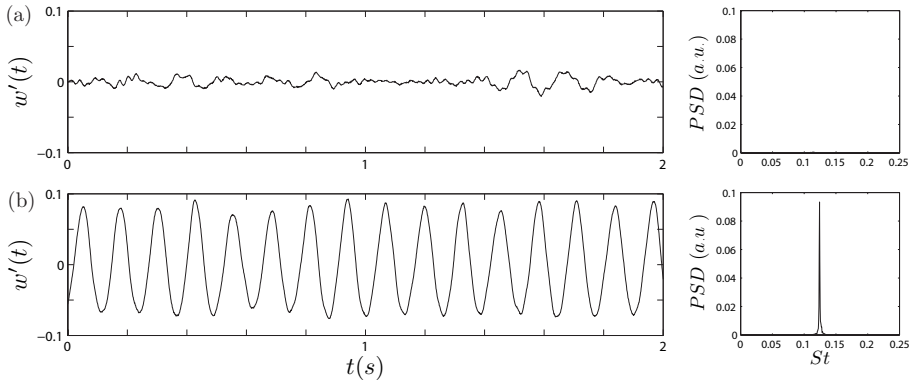

Figure 2.14: (a) Temporal evolution of streamwise velocity fluctuations $w'(t)$ behind the $\ell = 2$ body, measured at $z = 3$, for $Re = 394$ (top) and 429 (bottom); and (b) corresponding power spectral densities.

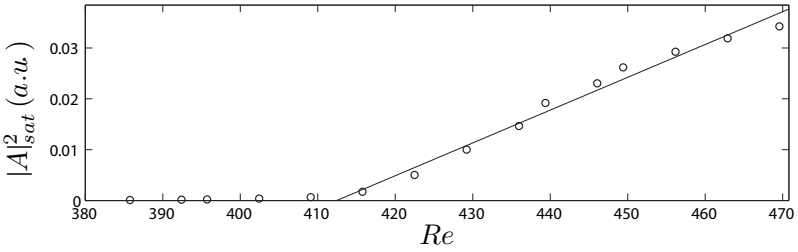

Figure 2.15: Square of the amplitude of the streamwise velocity fluctuations versus Reynolds for a $\ell = 2$ body, and $(r, z) = (0, 3)$.

of $|A|^2_{sat}$ near criticality. In this sense, Fig.2.15 shows the dependence of the energy of the velocity fluctuations, $|A|^2_{sat}$, at $(r = 0, z = 3)$ with the Reynolds number near the critical point for a $\ell = 2$ body, together with the linear fit, according to Eq.(1.18), that gives $Re^{exp}_{co} \simeq 412.4$. Notice that the prediction of the oscillatory bifurcation given by the three-dimensional numerical simulations for a bullet-like body of aspect ratio equal to 2, $Re_{co} \simeq 413$, is nearly identical to the experimental one, $Re^{exp}_{co} \simeq 412.4$. In fact, the agreement between the experimental and the numerical results confirms that the size of the computational domain and the grid resolution have been adequately chosen to obtain accurate results. Additionally, the streamwise velocity series were likewise acquired at $(r = 0, z = 2)$ and $(r = 0, z = 7)$, to study the influence of the location on Re^{exp}_{co}, and unlike $|A|^2_{sat}$, that changes considerably with z (see Fig.2.16 for high supercritical Re), it was found the critical Reynolds to be independent of the location (discrepancies in values below 1%), as it was expected since the RSP oscillatory mode is globally unstable and therefore it emerges everywhere at the wake. Moreover, no hysteretic behavior was observed on the evolution of $|A|^2_{sat}$ with Re, what suggests that the bifurcation is supercritical (as it will shown with more detail in Section 2.4). Interestingly, in line we the case of the sphere [108], the downstream location of maximum energy decreases with Re, as Fig.2.16 illustrates. It is worth mentioning that in the range of low supercritical Reynolds, $Re < 440$, spectra are mainly monochromatic, dominating clearly the main shedding frequency against low energy harmonics. Above this value, non-linearities are important and harmonics have

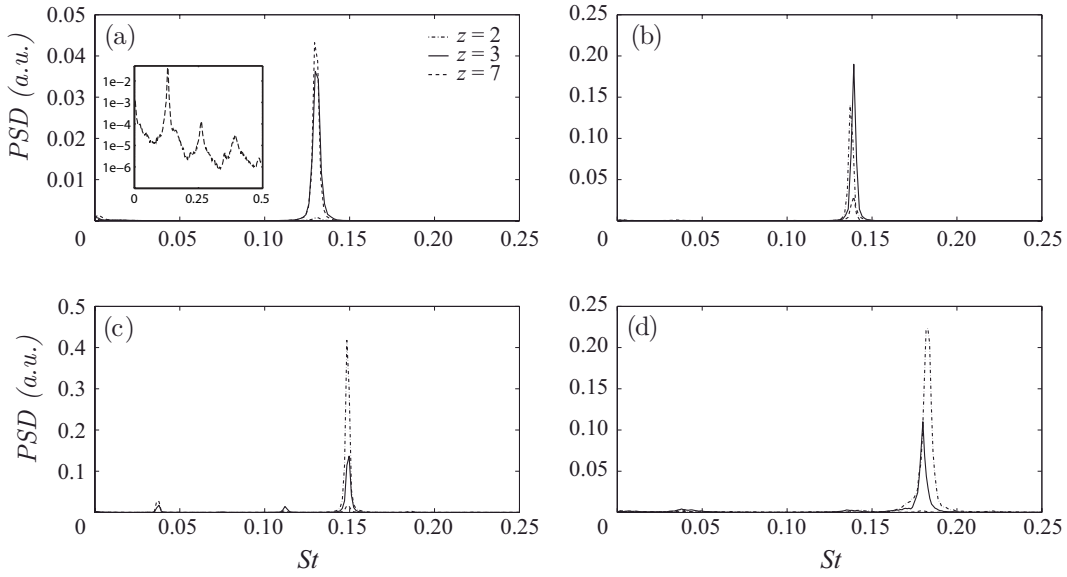

Figure 2.16: Power spectral density of the streamwise velocity fluctuations $w'(t)$ as a function of St and downstream position z, for a $\ell = 2$ body and (a) $Re = 446$, (b) $Re = 500$, (c) $Re = 590$ and (d) $Re = 802$. Inset in (a) includes the spectrum for $z = 7$ in logarithmic scale.

orders of magnitude similar to that of the characteristic peak, being more noticeable in the far wake (see inset in Fig.2.16a) than close to the body. Consequently, we calculated Re_{co}^{exp} by means of the measurements of the streamwise velocity spectra at $z = 3$, where most of the energy was contained at the characteristic peak, even for large Re. Notice in Fig.2.15 that, for $Re > 460$ the energy contained at the main frequency shedding seems to change its growing trend, due to the development of harmonics, and the transfer of energy between the main peak and the secondary ones.

When the Reflectional Symmetry Preserving mode emerges, hydrodynamics forces are time-dependent and their amplitude varies with Re. Figure 2.17(c) shows phase diagrams (C_l, C_d) as a function of Re. Thus, within the RSP region with monochromatic spectra or dominated by the fundamental peak, the phase diagrams are closed and periodic, featuring a regular orbit, until approximately $Re = 490$ (note that at $Re = 490$ the orbit is not purely periodic due to the energetic harmonics). However, a strong change in the wake dynamics occurs between $Re = 490$ and 495, as Figure 2.17(c) illustrates. This fact is associated to the onset of a new low frequency modulation taking place at the wake, that produces quasi-periodic orbits in the phase diagrams. This quasi-periodicity becomes more pronounced as Re increases, and at $Re = 500$ the orbit is irregular. The low modulation of the shedding process can be related to the destabilization of a new mode at the wake, that preserves the planar symmetry, as Fig.2.17(a) depicts for $Re = 500$ by means of streamwise vortices. As it can be observed, there is a low frequency cycle of strong shedding activity identified by means of broaden vortical structure (tag B in Fig.2.17a), followed by periods of low activity or natural shedding (tag A in Fig.2.17a). The shedding of packed intense vortices, that have an approximate period four times longer than the natural shedding one, is accompanied by an oscillation of the shoulders extending upstream of the base. A spectral analysis of forces

actuating on the body reveals the change at the wake, as Fig.2.17(b) displays for $Re = 500$. The low modulation frequency, identified as St_l, is approximately one-fourth of the natural shedding frequency, St_{sat} (whose peak contains now a similar value of energy to that of St_l), as it could have been figure out by inspection of Fig.2.17(a). A closer look at the spectrum shows that the flow at $Re = 500$ seems to be locked, being $St_{sat} = 4St_l$ and the remaining peaks, harmonics of St_l. This locking process is a consequence of the non-linear interaction between St_l and St_{sat}, that has been observed with less intensity from $Re \simeq 495$. In fact, although it is not shown here for the sake of conciseness, when $Re = 495$, the spectrum is clearly dominated by St_{sat}, but has weak peaks at $St_l \simeq St_{sat}/4$ along with the second and third harmonics of St_{sat}. The growth of the peaks at St_l and non-linear interactions $St_{sat} - St_l$ and $St_{sat} + St_l$ occurs by means of energy transfer from the leading peak occurring at St_{sat}. These facts explain the orbit quasi-periodicity of phase diagrams (C_l, C_d) in Fig.2.17.

A similar low frequency modulation has been widely reported for the sphere for Re sufficiently large, although there are discrepancies about its bound value. Thus, for instance Schouveiler & Provansal [132] observed experimentally a modulation for $Re > 360$, with a ratio St_{sat}/St_l ranging between 3 and 4. This observation coincides with other experimental [125] and numerical works [95, 149], that highlighted the connection between this new bifurcation and the symmetry breaking, based on the azimuthal orientation change of vortex shedding. In this sense, Brücker [19] was able to describe these differences between the low frequency modulation for sphere and a bullet-shaped body of $\ell = 5$ and rounded nose slightly different to ours, finding that for the latter, there was no variation of the vortices orientation at the Re studied $(500, 700, 1000)$, and being $St_{sat}/St_l > 10$, what suggests that this ratio would grow with ℓ.

The numerical low frequency modulation was also captured experimentally for a $\ell = 2$ body at $Re > 500$ approximately, as Figure 2.18 shows. Thus, the spectra of the experimental streamwise velocity fluctuations obtained experimentally, show already at $Re = 500$ the existence of a energetic peak at St_l, whose value is approximately $St_{sat}/4.05$, together with non-linear interactions of both frequencies, like for instance $St_{sat} - St_l$. These peaks grow with Re, and eventually, at far downstream locations, their energy is similar to that corresponding the dominant peak, as Fig.2.18(b) illustrates. Interestingly, as described by Schouveiler & Provansal [132] for the sphere ($Re > 414$), and already discussed for the numerical results, at $Re = 590$ it seems that a locking of the frequencies has been produced and St_{sat} is now a harmonic of St_l, more precisely $St_{sat} = 4St_l$. However, it must be emphasized that this locking has not been observed so clearly for signals recorded at the near wake.

A deeper numerical analysis of the spectra around this new transition allowed us to obtain the third critical Reynolds, Re_{co2}, and to study the nature of this symmetry preserving bifurcation. Thus, in line with the one reported succinctly by Bouchet *et al.* [17] for the sphere when $Re \geq 325$, we found that the new transition corresponds to a Hopf bifurcation. In this sense, the inset in Fig.2.17(b) displays the evolution with Re of the squared streamwise velocity oscillations amplitude at St_l, $|A_l|^2$, and it can be observed that the growth trend of $|A_l|^2$ is linear. Hence, we performed a fit following Eq.(1.18) (dashed line in inset of Fig.2.17b) to obtain $Re_{co2} \simeq 493.2$. More bifurcations leading to symmetry preserving regimes from unsteady states have been also reported previously, for instance at the wake of a thick circular disk, also characterized by the persistence of planar symmetry and the appearance of a secondary frequency close to one-third of the leading one for Reynolds numbers above 217 [8]. However, unlike in the present case, in the case of a thick disk

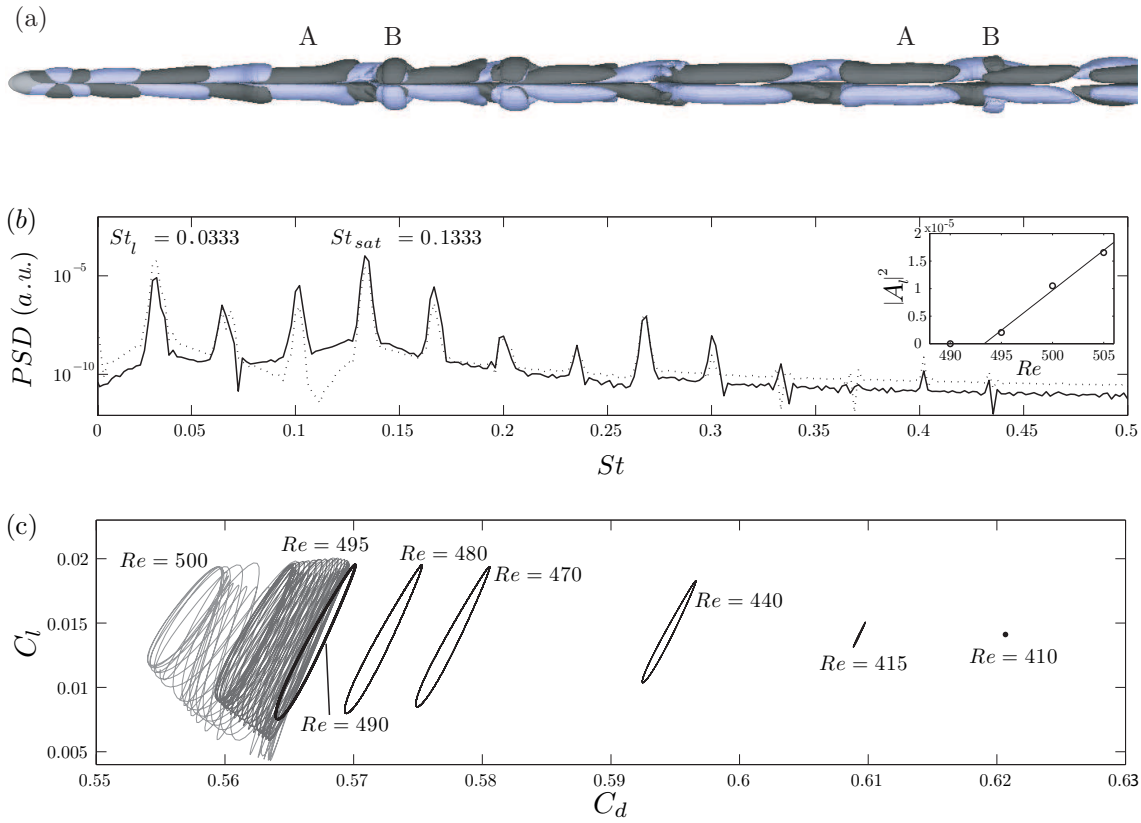

Figure 2.17: Analysis of the RSP mode: (a) Iso-surfaces of streamwise vorticity, $\varpi = \pm 0.04$; (b) power spectral density corresponding drag (dotted line) and lift (solid line) temporal evolutions at $Re = 500$; and (c) phase diagram (C_l, C_d) for several Re. Note that inset in (b) represents the evolution with Re of the squared streamwise velocity oscillations amplitude at St_l, $|A_l|^2$, together with the linear fit providing with Re_{co2}.

this flow regime results after a sequence of bifurcations occurring at lower Reynolds numbers. For a bullet-shaped body, Brücker [19] suggested that the third instability at the wake could appear again as a pair of counter-rotating helical modes of same amplitude and phase velocity, leading their simultaneous existence to planar oscillations at the wake. Nevertheless, in order to understand the complicated flow dynamics, techniques more complex than those used in the present work, like the global dynamic modes [129], would be needed.

2.3.2 Effect of ℓ on the stability properties

As a second part of the study on natural wakes behind bullet-shaped bodies, we analyzed the influence of the aspect ratio on the critical values of Re for the first and second bifurcations, by means of GLS analysis and experiments respectively. Thus, we determined experimentally Re_{co}^{exp} for bodies whose lenght-to-diameter ratio ℓ varied from 1 to 6. As mentioned before, we obtained critical values of the Reynolds number at z= 2, 3, 5 and 7, finding discrepancies always smaller than 1%. Special care was taken in our experiments to align the bodies under study with the

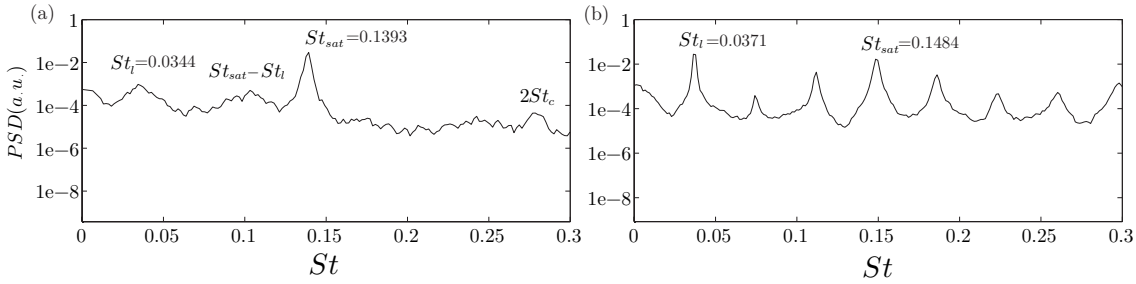

Figure 2.18: Power spectral density of the streamwise velocity fluctuations $w'(t)$, taken at $z = 7$, as a function of St for a $\ell = 2$ body and (a) $Re = 500$, (b) $Re = 590$.

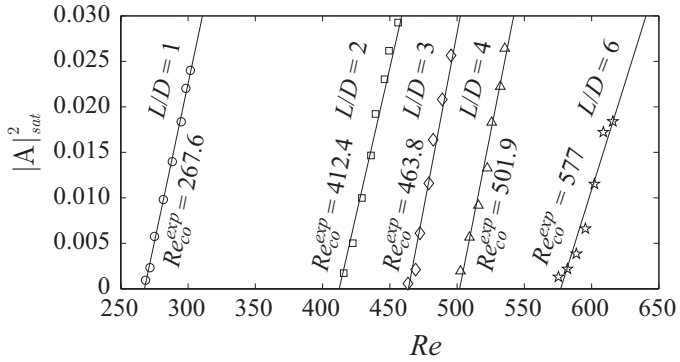

Figure 2.19: Energy of the streamwise velocity fluctuations $|A|^2_{sat}$ obtained experimentally at $(r = 0, z = 3)$, as function of the Reynolds number for the different bodies of $\ell = 1, 2, 3, 4$ and 6. Included in [15].

freestream, however, a small misaligment could result in errors of the order of 5%. Figure 2.19 shows the dependence of the energy of the velocity fluctuations, $|A|^2_{sat}$, at $(r = 0, z = 3)$ with the Reynolds number near the critical point for bodies of aspect ratio $\ell = 1$, 2, 3, 4 and 6 respectively, indicating that Re_{co}^{exp} increases with ℓ. Notice that the prediction of the oscillatory bifurcation given by the numerical simulations reported in Section 2.3.1 for a bullet-like body of aspect ratio equal to 2, $Re_{co}^{DNS} \simeq 413$, is nearly identical to the experimental one, $Re_{co}^{exp} \simeq 412.4$. Similarly, the modes observed with the GLS analysis for the body aspect ratio $\ell = 1$ are the same as those found for $\ell = 2$, and the critical Reynolds number obtained from the numerical simulations performed in Bohorquez *et al.* [15] for a body of $\ell = 1$, $Re_{co}^{DNS} \simeq 254$, agrees fairly well with the experimental value obtained, $Re_{co}^{exp} \simeq 267.6$. Since this second transition is also due to a reflectional symmetry preserving mode, there are important differences in the phenomenology of the hemielliptic geometry considered in this work with respect to the hemisphere, which exhibits a second reflectional symmetry breaking mode [65]. The numerical simulations performed in Bohorquez *et al.* [15] showed that the relative difference between the critical values of the Reynolds number associated to the SS and RSP modes, $\Delta^{DNS} = (Re_{co}^{DNS} - Re_{cs}^{DNS})/Re_{cs}^{DNS}$, is 0.18 for $\ell = 1$, and our simulations gives $\Delta^{DNS} \simeq 0.299$ for $\ell = 2$. Consequently, the assumption of simultaneously nearly neutral modes, e.g. [34], is questionable for afterbodies, as we will discuss below.

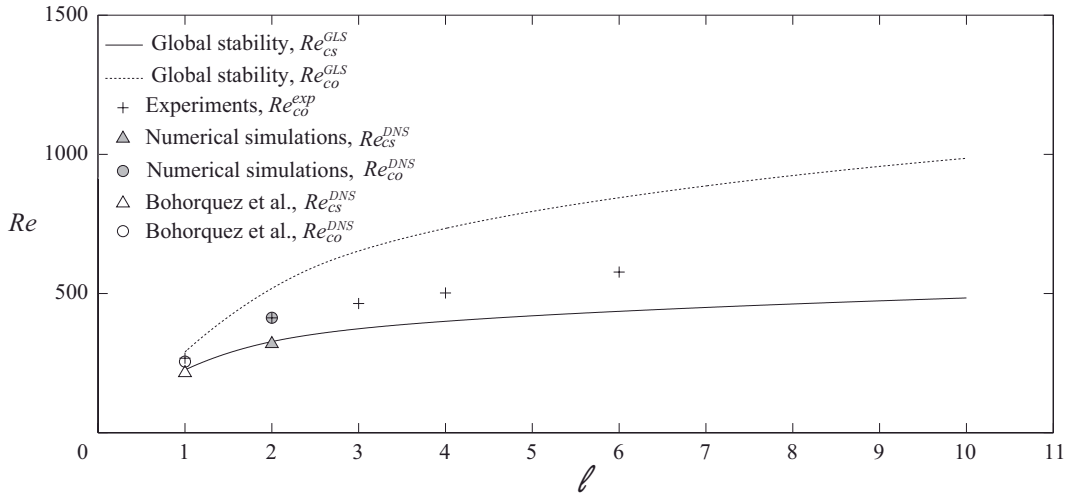

Figure 2.20: Dependence of the critical Reynolds numbers on the aspect ratio of the body, ℓ. Comparison among the results given by linear BiGlobal stability analysis, numerical simulations for $\ell = 1$ (from [15]) and 2, and experiments for $\ell = 1, 2, 3, 4$ and 6. Included in [15].

The same qualitative behaviour has been observed as the body aspect ratio, ℓ, is modified. Figure 2.20 shows the effect of ℓ on the critical Reynolds numbers, obtained from our experimental measurements, numerical simulations and BiGlobal linear stability for $|m| = 1$, together with the numerical simulations results of Bohorquez *et al.* [15] for $\ell = 1$. It can be observed that, in the particular case of $\ell = 1$ and 2, the critical Reynolds number for the first, steady bifurcation given by BiGlobal linear stability analysis agrees very well with that obtained from the numerical simulations, $Re_{cs}^{GLS} \simeq Re_{cs}^{DNS}$ (numerical simulations for larger bodies, $\ell > 2$, were not performed). Furthermore, as mentioned above, the predictions of the critical Reynolds number for the second, oscillatory bifurcation obtained numerically also agree with the experimental results, $Re_{co}^{DNS} \simeq Re_{co}^{exp}$, however the BiGlobal stability analysis considerably overestimates the critical Reynolds number associated to the oscillatory bifurcation. Thus, the value of $\Delta^{GLS} = (Re_{co}^{GLS} - Re_{cs}^{GLS})/Re_{cs}^{GLS}$, based on the BiGlobal linear stability analysis, varies from 0.29 for $\ell = 1$ to 1.04 for $\ell = 10$, indicating that the effect of considering an unperturbed base flow on the stability analysis induces larger errors in the prediction of Re_{co} and St as ℓ increases. Indeed, the relative gap between the critical Reynolds numbers for the sphere is nearly equal to that of our hemi-ellipse, but the BiGlobal linear stability analysis works much better for the sphere [102, 112]. Consequently, it is expected that the saturated amplitude of the mode yielding the transition to the SS-state is much larger for the geometries analyzed herein than for the sphere, although as it will be shown, this statement is not exactly true. It is worth mentioning that Δ also increases with the Mach number for an afterbody (see [89, 90]), and thus the theoretical quantification of the reflectional symmetry preserving mode in the compressible regime may also deserve the use of either three-dimensional global stability analysis [144] or three-dimensional numerical simulations. Figure 2.20 also shows that, as ℓ increases, the critical Reynolds numbers increases for both modes, indicating that the wake is more stable for longer bodies.

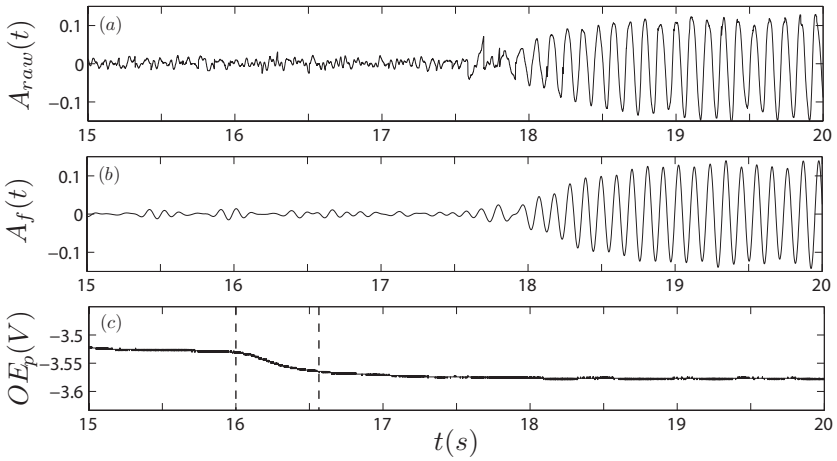

Figure 2.21: (a) Transient of raw velocity signal, $A_{raw}(t) = w'(t)$ and (b) filtered velocity signal, $A_f(t) = w'_f(t)$, obtained at $z = 3$ and (c) hot-wire anemometer output voltage, $OE_p(t)$, close to the body base (z=0.5). Note that dashed vertical lines in (c) determine the duration of the switch-off transient time. Experimental measurements taken for a body of $\ell = 2$ at $Re \simeq 455$.

2.4 Transients at the wake

As said, the onset of unsteadiness at the wake occurs through a Hopf bifurcation, that destabilizes a linear global mode, which leads to limit-cycle oscillations. The nature of the initial outlined transitions occurring at low values of Re and its nonlinear dynamics can be studied by means of the well-known Stuart-Landau model (Eq.1.13), as it has been extensively proven for other three-dimensional bodies (e.g.[132, 137]). On the other hand, a real version of such model, can be also describe satisfactorily the weakly non-linear dynamics of the first regular bifurcation [42, 148]. Furthermore, the possible hysteretic behavior of the transitions is also determined by the coefficients of the Landau equation (Eq.1.13), i.e. by the *supercritical* or *subcritical* nature of the bifurcation. In this sense, although no hysteresis has been found neither experimentally nor numerically, and the resemblance among the unstable modes encountered and those of the sphere is large (whose wake features supercritical bifurcations), it is worth examining this fact through the Landau model, to learn more about the transitions nature. Therefore, we will apply the model to a $\ell = 2$ body.

The coefficients in Eqs.(1.14) and (1.15) have been determined experimentally at several supercritical Re, close to the second unsteady bifurcation, $Re = Re_{co}$, namely $Re = 423, 432, 444, 455$ and 465, to study the dependence of $\sigma_r^f = \sigma_{r2}$, $\sigma_i^f = \sigma_{i2}$ and c with Re. On the other hand, numerical simulations in the vicinity of the first steady bifurcation at $Re = Re_{cs}$ and the second oscillatory one at $Re = Re_{co}$, have been used to determine accurately the global parameters and compare them with the experiments, that in general contain a higher level of noise and will lead to higher errors, although at lower time cost. Therefore, the computation of the first bifurcation parameters, σ_1 and l, will be performed by means of numerical simulations.

2.4.1 Experimental results

Firstly, the experiments were carried out by means of a single hot wire anemometer (HWA) in a wind tunnel (see Fig.2.1), that was used to monitor the streamwise velocity behind the body of length-to-diameter $\ell = 2$, $w(t)$, and its equivalent HWA output voltage, $OE(t)$, at a single point located at $z = 3$ (location that provided with the most energetic oscillations). This local approach has been proven to describe satisfactorily the transient behavior of the global mode for other geometries [32]. To produce transient growth at supercritical Re, we proceeded as indicated in [132], namely, by suppressing initially the vortex-shedding through base bleed (see Chapter 3 for more details about this kind of passive control) and interrupting suddenly the base flow, so that fundamental mode velocity fluctuations begin to evolve into limit-cycle oscillations and saturate eventually. The experimental set-up, sketched in Fig.2.1, consisted basically of a compressed air line feeding the rear part of the body through the holding needle, together with a valve that controlled the base flow and its switching-off. In line with [133], the HWA raw signal, $A_{raw}(t)$ (Fig.2.21a), that corresponds to $w'(t)$, must be processed in order to reduce the noise level and to select the characteristic shedding frequency, f_{sat}, associated to the dominant global mode. Thus, we used a Chebyshev band-pass filter around f_{sat}, $BPF(f_{sat})$, with a frequency pass window $\Delta f = \pm 0.15\% f_{sat}$, to obtain a smooth signal (Fig.2.21b), $A_f(t) = FFT^{-1}[\widetilde{A}_{raw}(t)] = FFT^{-1}\{BPF(f_c) \times FFT[A_{raw}(t)]\}$, where FFT and FFT^{-1} stand for the discrete Fast Fourier Transform and its inverse, respectively. The filtered signals obtained constituted a more suitable data to study the transient process, although, close to the transition ($Re \simeq 413$), this procedure was not enough to improve the quality of the signal, since the signal-to-noise ratio is low, and large errors could be induced. Hence, we will study the dominant global mode saturation process for $Re \geq 423$, performing the analysis close to the threshold through numerical simulations, where the raw signals are barely affected by noise problems and the calculated coefficients will be more reliable. Another limitation of these experiments is the fact that the switch-off time of the bleed must be small compared to the perturbation growth time. As observed in Fig.2.21(c), the base bleed switch-off time is considerable shorter ($t \simeq 0.5\ s$) that the time taken by the velocity signal to reach the saturation state at $Re \simeq 455$ ($2\ s$), that corresponds to one of the largest Re investigated.

Once the signal has been processed, time and velocity fluctuations were made dimensionless by using the scales w_∞/D and w_∞, respectively, so hereafter we refer to t and $A_f(t)$ as dimensionless magnitudes. Now, the filtered signal, $A_f(t)$, constitutes the real part of the complex amplitude, $\Re[A(t)]$, while its Hilbert transform is the imaginary part, i.e.: $\Im[A(t)] = FFT^{-1}[-i\widetilde{A}_f(t)]$. Therefore, the modulus $|A(t)|$ and phase ϕ can be built as $|A(t)| = \sqrt{\Re[A(t)]^2 + \Im[A(t)]^2}$ and $\phi = tan^{-1}\{\Re[A(t)]/\Im[A(t)]\}$, and its temporal derivatives included in Eqs.(1.14) and (1.15) can be evaluated by means of centered second-order finite differences. These derivatives are then used to obtain the Landau equation parameters. For instance, at $Re \simeq 455$, the signal plotted in Fig.2.21(a) provides with two functional variations of derivatives (see Fig.2.22) that approximately feature linear behavior, as the cubic Landau model suggests. The amplitude equation (Fig.2.22a) allows us to obtain the growth rate from the extrapolation of the linear fit to zero amplitude as $\sigma_{r2} = d\log|A|/dt[|A|^2 = 0]$, while the slope gives the real cubic coefficient $l_r = d(d\log|A|/dt)/d(|A|^2)$. Likewise, the phase equation linear fit (Fig.2.22b) provides with the angular frequency at zero amplitude, $\sigma_{i2} = d\phi/dt[|A|^2 = 0]$, and its gradient defines the complex cubic coefficient $l_i = d(d\phi/dt)/d(|A|^2)$. Combination of both equations yields the Landau constant, $c = li/lr$, that can be likewise obtained as the total shift in frequency during the linear phase, as

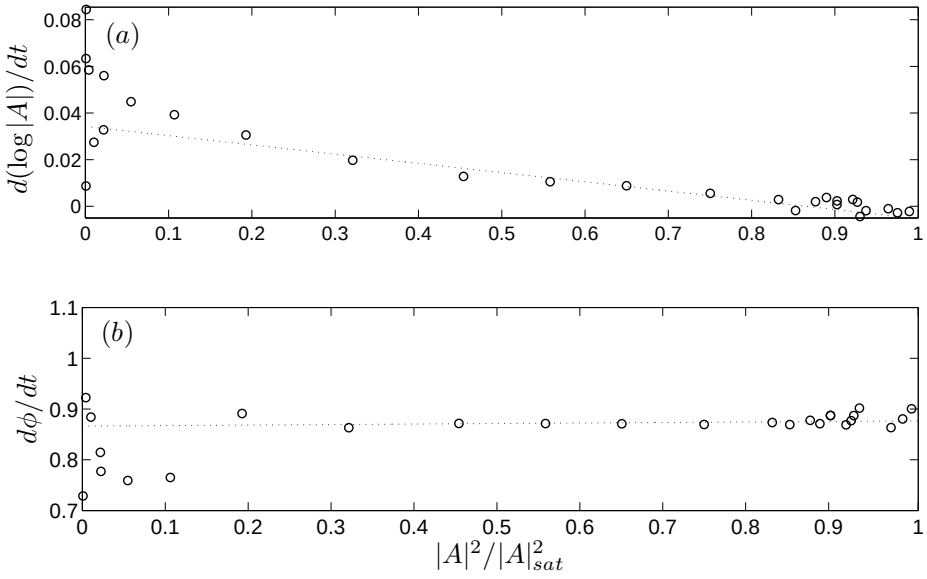

Figure 2.22: Experimental (a) instantaneous growth rate $d(\log|A|)/dt$ and (b) instantaneous frequency $d\phi/dt$, versus $|A|^2/|A|^2_{sat}$ obtained for a body of $\ell = 2$ at $Re \simeq 455$.

Re	423	432	444	455	465
c	-0.3547	-0.57	-0.54	-0.52	-0.38

Table 2.2: Values of the experimental Landau constant at saturation at several $Re > Re_{co}$, for a body of $\ell = 2$.

$c = (\sigma_{i2} - \sigma_{i2sat})/\sigma_{r2}$ (in the case at hand of $Re \simeq 455$, $\sigma_{r2} \simeq 0.035$, $\sigma_{i2} \simeq 0.861$ and $c \simeq -0.52$). This procedure was repeated for the five values of Re investigated, computing σ_{r2}, σ_{i2} and c for each one, whose values are displayed in Fig.2.23, together with the 95% confidence intervals given by the fitting process. Thus, for each Re investigated, we have performed linear fits aimed at maximizing the coefficient of determination R^2 between variables, so that the initial period, associated to the base bleed transient, was neglected in general. In this sense, the amplitude equation shed always values for this coefficient close to the unity, what translated into robust values of σ_{r2} (uncertainty bars are small for this parameter) and l_r; however, the phase equation accepts worse fitting, what affects mostly l_i and accounts for the high level of error that c features, especially at low Re, since the amplitude is still small and the noise hinders the quality of the signal.

As Fig.2.23 shows, the evolution of σ_{r2} and σ_{i2} is approximately linear with Re in the range studied, as Eqs.(1.16) and (1.17) suggests, being stronger the dependence for σ_{r2}. The linear fit for the growth rate, allows to determine the threshold of the bifurcation, Re_{co},

$$\sigma_{r2} = [0.0004164 \pm 0.00007](Re - [411.86 \pm 6.5]), \tag{2.7}$$

that is almost identical to the value obtained in Section 2.3 by fitting the square of the amplitude modulus according to Eq.(1.18). Besides, the onset frequency σ_{i2} grows also with Re, although

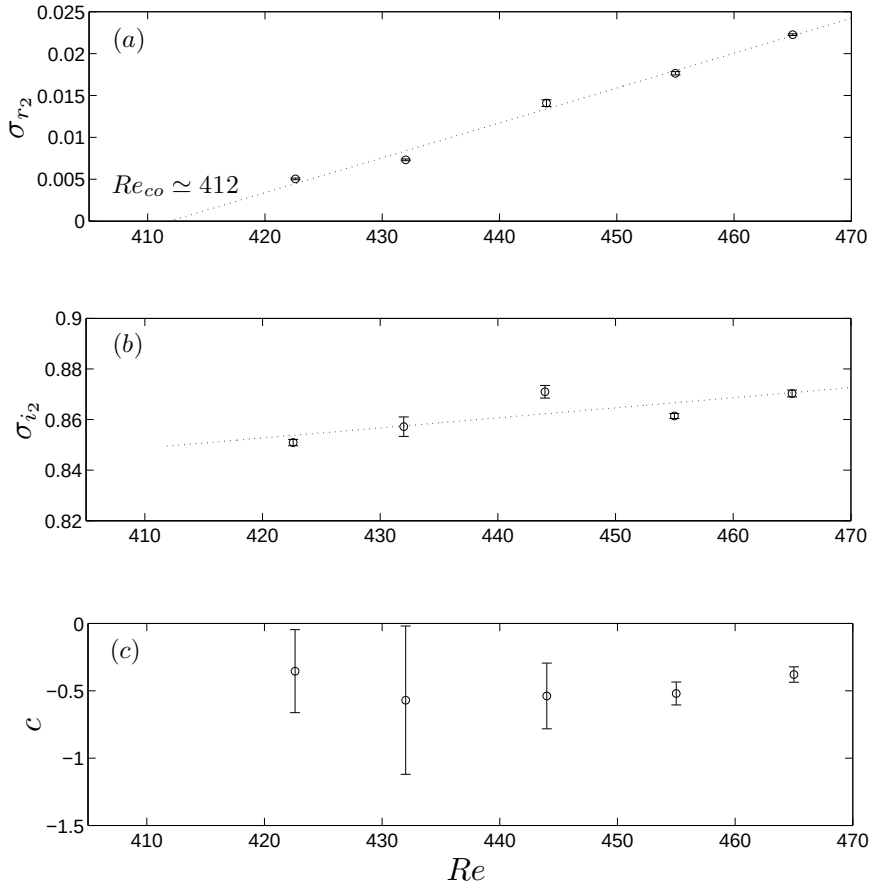

Figure 2.23: Experimental dependence on Re of (a) growth rate, σ_{r2}, (b) initial frequency, σ_{i2}, and (c) Landau constant, c, obtained for a body of $\ell = 2$. Note that vertical bars define 95% confidence intervals of fitting processes.

its linear fit contains a higher error. On the other hand, the Landau constant at saturation has been determined with lower accuracy (Fig.2.23c), due to small growth in frequency during the transients and indetermination in the fitting of Eq.(1.15). Nevertheless, its values, included in Table 2.2, are comprised between -0.35 and -0.6 approximately, being similar to those found for other three-dimensional bluff bodies, like the sphere (values around $c \simeq -0.5$ [148, 132]) or toroid [137]. Furthermore, except for the first value in this series, $|c|$ seems to decay with Re, mirroring the trend found experimentally for the sphere [132], for which there is a pronounced fall in its absolute value $|c|$ when Re is approximately a 10% of Re_c, that it is interpreted as a limit of the model. In our case, $|c|$ decays somewhere between $Re = 455$ and 465, what constitutes approximately an increase in Re of 10% from Re_{co} as well, setting a bound for the application of the Landau model in line with that of the sphere.

Finally, to conclude with the experimental study of the Stuart-Landau model, a comment should be made on the effect of ℓ. In this sense, it was proven in Section 2.3 that the Landau equation held for the evolution with Re of the squared fluctuations amplitude, $|A|^2_{sat}$, for any ℓ. More interestingly, the slope of the linear fits shown in Fig. 2.19 are similar for most of the bodies

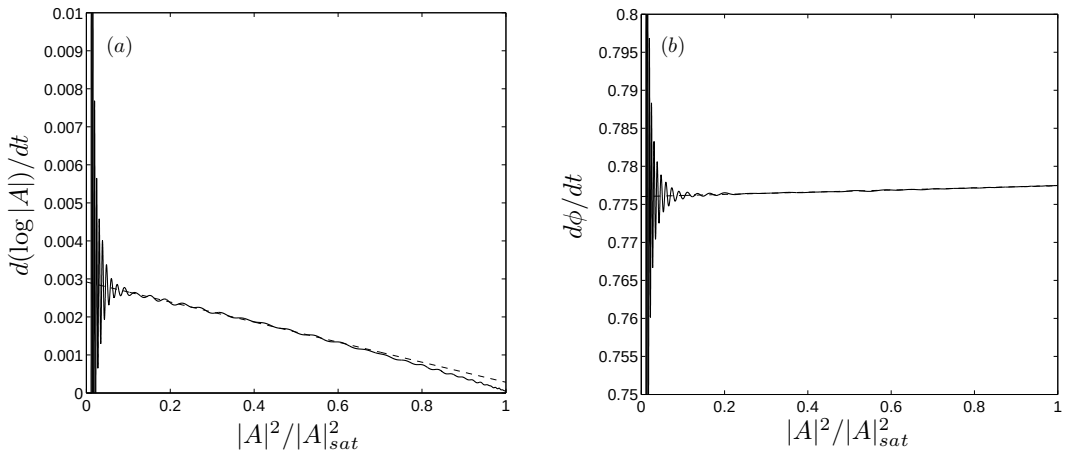

Figure 2.24: Numerical (a) instantaneous growth rate $d(\log|A|)/dt$ and (b) instantaneous frequency $d\phi/dt$, versus $|A|^2/|A|^2_{sat}$ at $Re = 415$, for $C_l(t)$.

under study, except for $\ell = 6$. This means that, once the second unstable mode has been triggered, the value of $|A|^2_{sat}$ for a fixed $\Delta Re = Re - Re_{co}(\ell)$, is approximately similar for $\ell \leq 5$, so that the mode evolves in a similar way regardless of the geometry. Hence, since l_r is a function of $|A|^2_{sat}$ and, the factor $1/l_r\,(d\sigma_r^f/dRe)[Re_c]$ remains approximately constant for increasing ℓ, thus, considering a constant fitting ΔRe for $\ell \leq 5$, $d\sigma_r^f/dRe[Re_c]$ should be independent as well of the aspect ratio for $\ell \leq 5$. These similarities between different geometries lead us to think that it is quite likely that the results obtained here for the Landau constant, would not differ much if they were reproduced for $\ell \leq 5$. Consequently, it indicates that the parameters would basically only depend on the nature of the mode, and that they would be similar as long as the same mode takes place at the wake behind different configuration bodies (see for instance results for Mode I in Sheard *et al.* [137]). Nevertheless additional experiments would be needed to confirm this hypothesis.

2.4.2 Numerical simulations

To accurately characterize the transient for both, the stationary and the oscillating bifurcations, we computed the global parameters of the Landau model by using our numerical results obtained through three-dimensional simulations, described in Section 2.3.1. Now, we will focus on a single value of Re for each transition that lie close enough to the respective thresholds, namely $Re = 320 > Re_{cs} \simeq 318$ and $Re = 415 > Re_{co} \simeq 413$. For both bifurcations we will apply the model to a global variable, i.e. the lift coefficient $C_l(t)$, that could be a better characteristic variable of the instability magnitude than a local variable. In this sense, this global approach has been already tested for the cylinder [147], with results that mimic the transient behavior at the near wake. In the case of the regular bifurcation, $C_l(t) = 0$ prior to bifurcation, giving rise to a non-zero constant value when the flow bifurcates at a given Re, so that $A(t)$ is real, whereas the Hopf bifurcation renders this magnitude periodic and hence, $A(t)$ is complex.

Let us start with the unsteady bifurcation, in order to set first a comparison with experiments. Unlike the experimental raw data, the temporal signal of $C_l(t)$ was smooth and no filtering of the

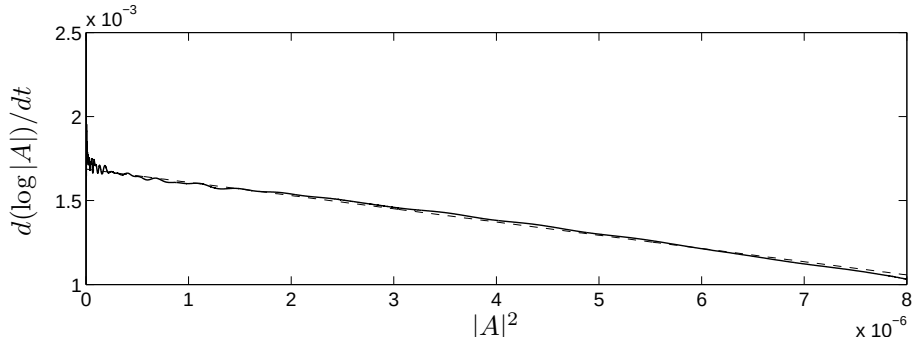

Figure 2.25: Numerical instantaneous growth rate $d(\log|A|)/dt$ versus $|A|^2$ at $Re = 320$, for $C_l(t)$.

signal was required, but simply subtracting its mean value. Again, the real part of $A(t)$ is $C_l(t)$, while its Hilbert transform is the imaginary part, so we proceed from here as explained for the experiments to obtain Eqs.(1.14) and (1.15), whose results are shown in Fig.2.24 for $Re = 415$. This value of Re is very close to the transition, so its results can be taken as a good characterization of the bifurcation. Thus, after a short initial transient, the linear fit in the amplitude equation (Fig.2.24a) provides with a growth rate $\sigma_{r2} \simeq 0.0029$ and a positive $l_r \simeq 0.00143$ (negative gradient), representing a supercritical bifurcation. As observed, the fit fails to describe the final step of the saturation process, indicating that higher order terms are required in Eq.(1.13) to completely describe the whole process; however, except for this final period, the linear model is quite accurate. This slight nonlinear trend has also been observed in the case of the sphere (e.g. [42]) and is even more pronounced in toroids [137]. Regarding the phase evolution, Fig.2.24(b) illustrates the growth in frequency during the transient, providing $\sigma_{i2} \simeq 0.776$ and $l_i \simeq -0.00264$, what yields $c = -0.542$. This value of the Landau constant is quite similar to the average value provided experimentally (Table 2.2), and is almost identical to the sphere Landau constant near the threshold ($c = -0.554$ in [148], for $Re - Re_{co} = 1$). The good agreement between different geometries is not surprising, since, as commented earlier, the Hopf bifurcation in both cases gives rise to the same kind of RSP mode, sharing their wakes many common features (e.g. topology and shedding frequencies). In this sense, Sheard *et al.* [137] investigated the effect of the aspect ratio on c, by comparing the sphere and different toroids, finding that, regardless of the aspect ratio, the Landau constant barely changes, as long as the bifurcation evolves towards the same kind of mode, as occurs in the case at hand of bullet-shaped bodies. Therefore, as discussed earlier, no big differences would be expected if the length-to-diameter ratio ℓ were varied.

Finally, to conclude with this section, we analyze briefly the nature of the regular axisymmetry-breaking bifurcation. The beginning of the transient analyzed at $Re = 320$ ($Re - Re_{cs} \simeq 2$) is illustrated in Fig. 2.25, where the negative slope of the linear fit proves that the bifurcation is supercritical as well. The linear fit of the transient (dashed line in Fig.2.25), provides with values of $\sigma_r \simeq 0.0017$ and $l_r \simeq 78.7$.

2.5 A note on the comparison between sphere and bullet-shaped bodies wakes

As mentioned, numerical simulations were performed as well for the wake of the sphere, in order to set a direct comparison with the bullet-shaped body and to validate the computational domain and the numerical schemes used in this work (see Section 2.2). In this sense, applying our numerical procedures for the case of the sphere, we observed that the first bifurcation takes place at $Re_{cs}^{sp} \simeq 210$, what is in close agreement with the values previously published, see e.g.[60]. As for the bullet-shaped body (Fig.2.8), we computed the eccentricity of velocity magnitude contours at several downstream locations, and fitted the evolution of their squared values with Re, in order to obtain Re_{cs}^{sp}. Besides, we computed the axisymmetric solutions for supercritical $Re > Re_{cs}^{sp}$, to evaluate how much they deviate from the three-dimensional flow at a given Re. Thus, it could be determined, whether the SS unstable mode at the wake of the bullet-shaped body reaches a saturated amplitude higher than that corresponding to the same mode for the sphere, just below the transition towards the RSP corresponding modes.

The global non-linear mode amplitude was computed for both bodies defining an energy estimation parameter, in line with what Thompson & Provansal [148] applied. Thus, for a given Re and a fixed location z downstream from the base, we computed the difference between the three-dimensional velocity field, $\mathbf{u}_{3D}$, and the axisymmetric field, $\mathbf{u}_{2D}$, denoting it as mode velocity field, $\mathbf{u}_m = \mathbf{u}_{3D} - \mathbf{u}_{2D}$, and subsequently obtained the global amplitude per unit length as,

$$|A|^2 = \frac{1}{D^2 w_\infty^2} \int_\Sigma |\mathbf{u}_m|^2 dS, \tag{2.8}$$

integrating over Σ that corresponds to the whole (r, θ)-plane enclosed by the domain at the given z. The global amplitude estimation was calculated for both bodies at values of Re that provide with the same value of Δ_s approximately, where $\Delta_s = (Re - Re_{cs})/Re_{cs}$. Thus, we chose $Re = 270$ and $Re = 410$ for the sphere and bullet-shaped body respectively, which are Reynolds numbers lower than the corresponding Re_{co}, but close to the respective bifurcation values, providing $\Delta_s \simeq 0.29$ for both cases, and compute $|A|^2$ at several positions downstream. Figure 2.26(a) shows the distribution of the global amplitude in z for both bodies, calculated after integrating the global amplitude per unit volume $|\mathbf{u}_m|^2$ in each downstream location. As it clearly seen there, the sphere mode amplitude is higher than the $\ell = 2$ body counterpart, what means that just below the second transition, the sphere wake deviates more from the axisymmetric flow. Moreover, insets 2.26(b) and 2.26(c) illustrates $|\mathbf{u}_m|^2$ at $z = 10$, for the sphere and the $\ell = 2$ body[2], showing that the sphere mode affects a larger region of the domain.

More results that reinforce this idea of a more perturbed mode in the case of the sphere, is given by the differences in drag coefficient between three-dimensional and axisymmetric solutions in terms of relative error, $(C_d^{3D} - C_d^{2D})/C_d^{2D} \times 100$. Thus, for the sphere, at $Re = 270$ ($\Delta_s \simeq 0.29$) we obtained an approximate decrease of 2%, in line with the results of Bouchet *et al.* (see Fig. 10 in [17]), whereas for the bullet-shaped body, at $Re = 410$ ($\Delta_s \simeq 0.29$), this relative error is 1.79% approximately. Therefore, it is clear that the saturated amplitude of the unstable SS mode just below the second bifurcation, for a gap $\Delta_s \simeq 0.29$, is higher in the case of the sphere than for the $\ell = 2$ body.

[2]They resemble surprisingly the local symmetric $m = +1$ eigenfuctions reported by Pier [112] for the linear stability of the sphere planar symmetric wake

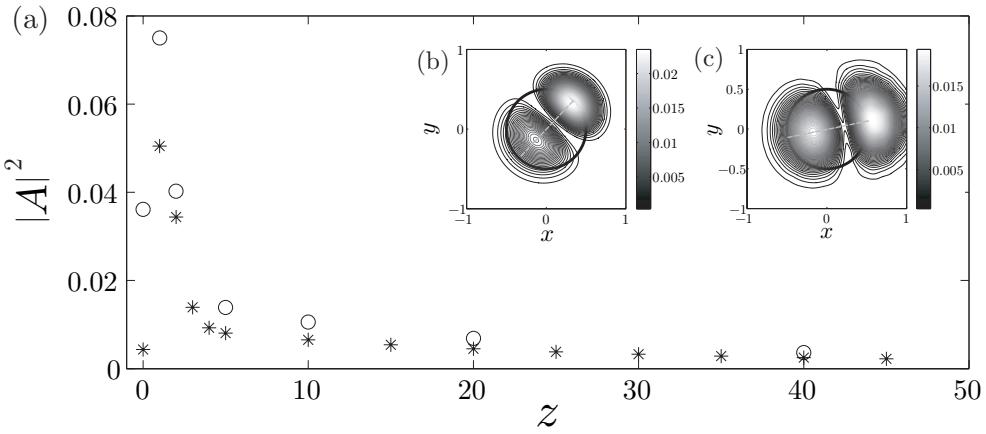

Figure 2.26: (a) Global amplitude estimation $|A|^2$ versus z for the sphere (circles) and $\ell = 2$ body (asterisks); and amplitude per unit volume, $|\mathbf{u}_m|^2$, at $z = 10$ for (b) $\ell = 2$ body and (c) sphere. Note that the symmetry plane at the three-dimensional wake is depicted by a grey dashed line at the insets.

2.6 Conclusion

Experiments, numerical simulations and BiGlobal linear stability analysis were used to perform a detailed study of the laminar wake behind a slender axisymmetric body with a 2:1 ellipsoidal nose and a blunt trailing edge at zero angle of attack. The work focused on the instabilities taking place in the flow for increasing values of the Reynolds number up to $Re = 2000$, contemplating also the effect of the body length-to-diameter ratio in the range $1 \leq \ell \leq 10$.

For increasing Reynolds numbers both the three-dimensional numerical simulations and the BiGlobal stability analysis predicted the existence of a first steady axisymmetry-breaking bifurcation, as it is known to happen in the case of other axisymmetric bodies like spheres or disks. We showed that this steady bifurcation takes place at a critical value of the Reynolds number, $Re_{cs}(\ell)$, which slightly increases with the aspect ratio of the body. The values computed from the numerical simulations and the stability analysis, Re_{cs}^{DNS} and Re_{cs}^{GLS}, respectively, were in very good quantitative agreement for the case studied $\ell = 2$. In such a case, the corresponding values were given by $Re_{cs}^{DNS} \simeq 318$ and $Re_{cs}^{GLS} \simeq 327$. Similarly to the cases of the sphere and the disk, the structure of the steady wake prevailing for $Re > Re_{cs}(\ell)$ is planar-symmetric and features a double-threaded structure consisting of a pair of counter-rotating streamwise vortices oriented at an angle with respect to the symmetry axis of the body. A second oscillatory bifurcation was shown to exist at a higher value of the Reynolds number, Re_{co}, whose values are given by Re_{co}^{exp}, Re_{co}^{DNS} and Re_{co}^{GLS} according to experiments, numerical simulations, and BiGlobal stability analysis, respectively, all of which increase with ℓ. The numerical simulations revealed that, as happens in the case of a sphere, the symmetry plane which appears in the wake at $Re = Re_{cs}$, is preserved for $Re > Re_{co}$, and is thus a *symmetry preserving mode* according to Fabre *et al.* [34]. Experiments and numerical simulations were in good quantitative agreement, $Re_{co}^{exp} \simeq Re_{co}^{DNS}$, providing further validation for the numerical code. The critical Reynolds numbers were found to be $Re_{co}^{exp} \simeq 412.4$ and $Re_{co}^{DNS} \simeq 413$. However, the BiGlobal linear stability analysis predicts an oscillatory bifurcation for a Reynolds number which is significantly higher than the predicted

by the experiments and the numerical simulations, giving for instance $Re_{co}^{GLS} \simeq 518$ for $\ell = 2$. The errors in the predictions made by the BiGlobal stability analysis for the critical Reynolds number associated to the oscillatory bifurcation are due to the use of an axisymmetric basic flow for Reynolds numbers higher than the one corresponding to the first bifurcation. This error is substantially larger for the bullet-like geometry considered in the present work than in the cases of a sphere and a thin disk studied by Pier [112] and Fabre *et al.* [34]. In the particular case of the wake of a thin disk, a natural explanation for the relatively small error in the value of Re_{co} predicted by the BiGlobal linear stability analysis applied to the axisymmetric base flow is the fact that the relative gap in the critical Reynolds numbers, $\Delta^{GLS} = (Re_{co}^{GLS} - Re_{cs}^{GLS})/Re_{cs}^{GLS} \ll 1$ [34]. However, since the values of Δ^{GLS} are similar in the cases of the sphere [112] and the hemiellipse considered in this thesis, this argument alone cannot explain the smaller relative error obtained for the sphere. Furthermore, it was proven that the saturated amplitude of the the steady state mode evaluated at Reynolds number close to the critical Reynolds number corresponding to the onset of the oscillating mode, Re_{co}, is larger for the case of the sphere that for a $\ell = 2$ body, although they have similar values. This finding, that seems to go against the above argument, deserves further study and is left for a future work. The difference $(Re_{co}^{GLS} - Re_{co}^{exp})$ was found to increase with the aspect ratio of the body, ℓ. These results imply, in particular, that care must be taken when studying the oscillatory regimes of afterbody wakes, specially for large aspect ratio geometries. Even though the relative quantitative errors involved in using axisymmetric base states in global stability analyses have been shown to be high in these cases, this approach has been routinely used in recent works [89, 90]. In addition, the results reported in the present Thesis may also serve as benchmark for more involved three-dimensional linear stability analyses [144, 112].

On the other hand, we observed differences between the wakes of slender blunt-based bodies and other previously studied geometries like the sphere, hemisphere or disk. First, it is noteworthy that the symmetry plane which appears in the wake after the first steady bifurcation is preserved for Reynolds numbers up to $Re = 500$, even in the presence of strong non-linear interactions of the shed vortical structures, and subsequent harmonic generation. In contrast, although wakes of other objects like spheres and disks present also a RSP regime, the corresponding range of Reynolds numbers is narrower. In addition, we found the existence of a new regime in which the wake interacts with the boundary layer on the solid body, inducing a periodic oscillation with a frequency of about 1/4 of the leading one. This new symmetry preserving mode takes place through a Hopf bifurcation at $Re_{co2} \simeq 493.2$, in line with the bifurcation reported by Bouchet *et al.* [17] accompanied by the onset of a second oscillation frequency on the wake of a sphere at $Re \sim 325$. The new mode reported herein resemble the "Honky-Tonky"mode, that has recently been observed in the wake of a thick disk by Auguste *et al.* [8] for $Re \gtrsim 217$, where the lowest frequency is given by approximately 1/3 of the leading one. However, in the case of a thick disk, this flow regime, characterized by the presence of a secondary low frequency while preserving the reflectional symmetry, manifests after a sequence of flow bifurcations not found in the configuration under study in this work. Additionally, experimental measurements and numerical simulations showed the strong non-linear interaction between the low frequency modulation and the natural shedding frequency, registering a locking of both frequencies for $Re \leq 500$ and $\ell = 2$, in such a way that $St_{sat} = 4St_l$.

Furthermore, the Stuart-Landau model was used to study, numerical and experimentally, the transients at the wake, occurring after the wake bifurcates at $Re = Re_{cs}$ and $Re = Re_{co}$, concluding

that both transitions are supercritical (non hysteretic). Regarding the oscillatory bifurcation, the numerical simulations performed at $Re = 415$, near the threshold, allowed us to determine accurately the value of the Landau constant, $c \simeq -0.542$, which in turn is almost identical to that numerically obtained for the sphere in the vicinity of the shedding onset ($c \simeq -0.554$ [148]). Besides, the experimental behavior of the evolution with Re of $|A|^2_{sat}$ for different ℓ, suggests that the dependence of c on the aspect ratio and geometry is very weak, and it is basically determined by the kind of unstable mode present at the wake. Additionally, the experimental results showed also that the third-order truncation is approximately valid for a range of $Re > Re_{co}$ with $Re \sim 1.1 Re_{co}$, in line with the sphere findings [132].

CHAPTER
THREE

Wake control through passive methods (I): base bleed and rear cavities

This chapter is devoted to explore the suitability of two passive mechanisms, namely, base bleed and rear cavities, to stabilize the flow behind a bullet-shaped body of $\ell = 2$. Both the axisymmetry-breaking regular transition (at $Re = Re_{cs}$) and the oscillatory Hopf bifurcation (at $Re = Re_{co}$) can be stabilized by injecting a certain amount of fluid through the base of the body, quantified here as the bleed-to-freestream velocity ratio, $C_b = w_b/w_\infty$. The results obtained by means of experiments and BiGlobal linear stability analysis (GLS) are presented in a parameter plane spanned by Re and C_b, that can be divided into three regions: in region I, defined by $C_b > C_{b1}^*$, the wake is steady and axisymmetric; in region II, for which $C_{b2}^* < C_b < C_{b1}^*$, the wake is steady but planar-symmetric, and in region III, where $C_b < C_{b2}^*$, vortex structures are periodically shed. The comparison shows that GLS underestimates C_{b2}^*, due to the use of an axisymmetric basic flow for $Re > Re_{cs}$ (see Chapter 2). The aforementioned techniques alongside three-dimensional numerical simulations have been used to analyze the influence of base cavities of length h and diameter D_c. Thus, for a given value of D_c/D, it is observed that Re_{cs} increases monotonically as h/D increases, reaching an asymptotic value which depends on D_c/D, at $h/D \approx 0.7$. Likewise, for a fixed value of h/D, we study the effect of the cavity diameter D_c/D on the critical Reynolds number. No effect on Re_{cs} is observed over the range $0 \leqslant D_c/D \lesssim 0.6$, but, Re_{cs} shows a monotonic growth for $0.6 \lesssim D_c/D < 1$. On the other hand, for steady flows, the drag coefficient decreases with the length of the cavity reaching an asymptotic minimum for $h/D \gtrsim 0.5$ and $D_c/D \to 1$.

This chapter is comprised, in part, in the papers: (1) "Stability and dynamics of the laminar wake past a slender blunt-based axisymmetric body", by P. Bohorquez, E. Sanmiguel-Rojas, A. Sevilla, J. I. Jiménez-González and C. Martínez-Bazán, published in the Journal of Fluid Mechanics [15]; and (2) "Effect of base cavities on the stability of the wake behind slender blunt-based axisymmetric bodies", by E. Sanmiguel-Rojas, J. I. Jiménez-González, P. Bohorquez, G. Pawlak and C. Martínez-Bazán, published in Physics of Fluids [126].

3.1 Introduction

As detailed throughout Chapter 2, at moderate Reynolds numbers below a critical value, $Re < Re_{cs}$, the flow around axisymmetric bodies is axisymmetric, and it develops a pair of steady streamwise vortices (see Fig.2.5a) breaking the axial symmetry when the first instability threshold is reached at $Re = Re_{cs}$ and the SS mode sets in. The loss of axisymmetry implies the onset of a lift force, which could induce a deviation of the body from the trajectory it would follow if the

flow were axisymmetric. The wake steadiness ends when the RSP mode emerges, as the Reynolds number increases beyond a critical value, $Re > Re_{co}$, and vortex shedding begins. Consequently, stabilization of the second mode is also of practical importance in order to avoid the potential generation of fluctuating dynamic loads. There are several mechanisms traditionally used to improve the aerodynamics of afterbodies, i.e. geometrical modifications of the base of the body [155, 153], base bleed [106], base suction [48], among others (see Choi *et al.* [23] for a comprehensive review). Among the large variety existing, we will first apply to our problem configuration base bleed and rear cavities.

Several works have demonstrated that the presence of base bleed has a strong stabilizing effect, suppressing effectively vortex shedding and lowering the drag coefficient, on two-dimensional bluff-body wakes [158, 159, 10, 133, 48, 86, 6], and three-dimensional axisymmetric bodies, like the sphere [132] or slender blunt-based bodies, either for laminar [127] or turbulent wakes [135], where likewise, the large-scale helical structures can be inhibited when a critical level of base flow is injected. More precisely, Sanmiguel *et al.* [127] demonstrated for a truncated $\ell = 5$ cylinder, by means of GLS analysis, that the unstable linear modes present at the wake, unsteady and steady, could be fully stabilized with increasing base bleed if the bleed coefficient reached two critical values considered, C^*_{b2} and C^*_{b1}, stabilizing the unsteady and steady mode respectively, with $C^*_{b2} < C^*_{b1}$. Moreover, base bleed control of unsteadiness in a compressible afterbody wake has been recently investigated by Meliga *et al.* [90] through a BiGlobal linear stability analysis of the basic axisymmetric state. Besides, it has been shown by local linear stability analysis, that a lower bleed density improves the efficiency of stabilization, inhibiting the absolute instability at the wake at lower C_b as the ratio between bleed and free-stream densities decreases [136].

On the other hand, rear cavities have been widely investigated in two-dimensional bodies [68, 21], and it is well established that they promote drag reduction by weakening vortex shedding and increasing base pressure [97]. Three-dimensional bluff bodies shared some of the aforementioned characteristic effect due to cavities, as drag reduction [153]. However, most of previous work has been devoted towards analysis of the effects of base bleed or of the shape of the body base on the total drag and base pressure in the transonic/supersonic regime at Reynolds numbers with a lower limit of $Re \sim \mathcal{O}(10^4)$, e.g. Morel [99]. However, very little is known about the effect of such a method on the sequence of transitions leading to turbulence in wakes behind bluff bodies at $Re \sim \mathcal{O}(10^2)$–$\mathcal{O}(10^3)$, although this knowledge is essential in order to predict the dependence of fluid dynamics variables, such as the base pressure and the total drag, as a function of Reynolds number and the geometry of the body.

Hence, this chapter describes the effect of base bleed and rear cavities on the physics of the wakes generated downstream of a bullet-like body with $\ell = 2$ (flow topology, field variables and stability properties) at low Reynolds numbers, to evaluate the efficiency of both control methods, by combining experiments, direct numerical simulations and BiGlobal linear stability analyses. We start with the description of the numerical methods and experimental techniques in Section 3.2. Next, the base-bleed and cavities effects on the first-stationary and second-oscillatory bifurcations are presented in Sections 3.3 and 3.4, respectively. Finally, we present conclusions in Section 3.5.

3.2 Problem definition and techniques

3.2.1 Problem definition

As illustrated in Fig.1.1, the flow configuration consists of a bullet-like body of length-to-diameter ratio $\ell = 2$, aligned with the free stream. The application of base bleed implies that a stream is injected at the base of the body, with uniform velocity w_b, density, ρ_b, and viscosity, μ_b. Hence, besides the Reynolds number, Re, three new dimensionless parameters characterize the problem, namely, the bleed coefficient, defined as the bleed-to-freestream velocity, $C_b = w_b/w_\infty$, the bleed-to-freestream density ratio, $S = \rho_b/\rho_\infty$, and the bleed-to-freestream viscosity ratio, $\eta = \mu_b/\mu_\infty$. On the other hand, the study of laminar wakes behind a $\ell = 2$ body with rear cavities, constitutes a slightly modified version of the problem introduced in Chapter 2, with two additional geometrical parameters, i.e. the dimensionless cavity depth, h/D, and cavity diameter, D_c/D. In the present work we investigated the effect of cavities of diameter $0 \leq D_c/D < 1$ and depth $0 < h/D \leq 1$.

3.2.2 Experimental details

Following the experimental procedure described to characterize the second oscillatory bifurcation at the wake of different aspect ratios ℓ, we performed HWA measurements for both the base bleed and rear cavities problems. For the former problem, the goal was to determine experimentally the critical bleed coefficient that inhibits the fluctuations of velocity behind the body, $C_b = C_{b2}^*$, for a given Re at the wake of a body of $\ell = 2$, using homogeneous (air, $S = 1$) and light (helium, $S \simeq 0.138$ (20^oC)) bleed fluids. Similarly, streamwise velocity signals were recorded for the calculation of the second bifurcation critical Reynolds number, Re, for the same body with rear cavities of depth $h/D = 0.2, 0.4, 0.7$ and 1 and $D_c/D = 0.86$.

The base bleed set-up is shown in Fig.2.1, and details of the adapted body for blowing is given in Fig.2.2(b). The holding needle, used to inject the control fluid, was actually a syringe needle attached through a Luer connector to the facility that feeds the air or helium, depending on the kind of bleed fluid used. This facility links the body to a general 6 bar compressed air line (homogeneous bleed) or a pressurized Helium bottle (light bleed), and was made up of several valves, a *Aalborg*® digital mass flowmeters to control the air or Helium flow, sealing connectors and plastic tubes for the junctions between devices. Besides, we carried out several downstream measurements at different radial positions to check the uniformity of base bleed, getting almost identical values of streamwise velocity at these locations. In addition, in order to make sure that the base bleed was uniform, we performed Helium shadowgraph to visualize the flow, confirming that the injection was even.

3.2.3 BiGlobal Linear Stability analysis

Base bleed problem was also tackled with the GLS analysis code described in Chapter 2, with the sole difference existing due to a modified boundary condition for the Finite Volume code used to solve the base flow, namely, at the body base, Σ_b (see Fig.1.1), we imposed a uniform flow with constant velocity, $\mathbf{U_b} = (0, 0, w_b)$. The EVP (1.10) was solved for $Re \leq 2000$ and $C_b < 0.13$, in order to determine critical bleed coefficients, C_{b2}^* and C_{b1}^*, inhibiting the RSP and SS mode respectively.

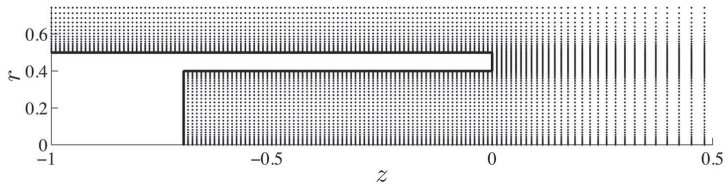

Figure 3.1: Detail of the axisymmetric GLS computational domain, for a $\ell = 2$ body with $h/D = 0.7$ and $D_c/D = 0.8$. Included in [126].

The spectral collocation code, described in Chapter 2 and introduced in Sanmiguel *et al.* [127], has the advantage of the "spectral accuracy", i.e. achieved exponential convergence when spatial resolution increases. However, the differentiation matrices constructed by using Chebyshev or Legendre polynomials are dense and ill-conditioned matrices [151], posing some instability problems when they are too large. On the other hand, the code was designed for rectangular domains without conformal mapping, dealing with geometrical irregularities by means of spectral rectangular boxes. Thus, the introduction of a rear cavity at the body, with $D_c/D \lesssim 1$, would imply the creation of an additional very thin box, corresponding to the wall cavity thickness (see Fig.3.1), where to fit the $(n+1)$ Gauss-Lobatto points, being $n = 11$ the chosen Lagrange polynomial order. Consequently, the small spatial interval characterizing this region near the cavity edge would lead to highly ill-conditioned differentiation matrices. Hence, a new approach was selected for the collocation and differentiation in the present EVP problem. Once the base flow was solved (see Section 2.2), a new grid was used to discretize the operators $\mathcal{A}$ and $\mathcal{B}$ in Eq.(1.10). Figure 3.1 displays a detail of the new computational grid for a $\ell = 2$ body with a rear cavity ($h/D = 0.7, D_c/D = 0.8$). As observed, the nodes are clustered around the wall, and the resolution is increased close to the edges to deal with the large field gradients existing there, and the singularities of the corners.

After mapping the base flow onto the new computational domain, the axial and radial spatial derivatives in matrix $\mathcal{A}$ (see Eq.1.11) were computed using finite differences of sixth order truncation error for non-uniform grids [96]. The lower order of finite differences schemes, $\mathcal{O}(6)$, compared with spectral method, was somehow compensated by increasing the resolution of the interpolant nodes (although the real convergence order is affected by the base flow, $\mathcal{O}(2)$). Thus, a grid convergence study was performed for a $\ell = 2$ body without cavity, $h/D = 0$, in order to determine the resolution required to obtain a converged discrete spectrum, and as Table 3.1 shows, the leading eigenvalue at $Re = 350$ was already converged when $n_g \simeq 49200$ nodes. On the other hand, although the number of nodes were doubled with respect to spectral methods, memory requirement were not so demanding, since finite differences give rise to sparser differentiation matrices than spectral methods (see Appendix A for more details about the matrices structure). This is a consequence of the markedly local nature of finite differences, since, in this case, the stencil used for one coordinate derivative involves the functional values at the point where the derivative is evaluated and the three next to him in both directions (conversely, spectral methods involve the whole the domain and are then "global"). As seen, the increase in the grid resolution is effective at overcoming this lack of global behavior.

On the other hand, since variables are mapped on a collocated grid arrangement, filters derived from compact schemes of fourth order [77] were used to obtain smooth and clean eigenfunction solutions, without spurious oscillations of short wave length (see Appendix A). Finally, it must be

Mesh	n_r	n_z	n_g	σ_{r1}	$\epsilon_{j,Sp}(\%)$
1	142	456	~ 63900	0.021681	0.2729
2	124	400	~ 49200	0.021680	0.2682
3	109	351	~ 38000	0.022783	5.3695
Sp	-	-	~ 27300	0.021622	-

Table 3.1: Grid convergence study for the leading eigenvalue growth rate, σ_{r1}, at $Re = 350$ and $|m| = 1$, for a $\ell = 2$ body, using finite differences of $\mathcal{O}(6)$ and different grids. Note that Sp represents the results obtained by using a spectral collocation method, and $\epsilon_{j,sp}$ is the relative error between $\sigma_{r1}(j)$ and $\sigma_{r1}(Sp)$.

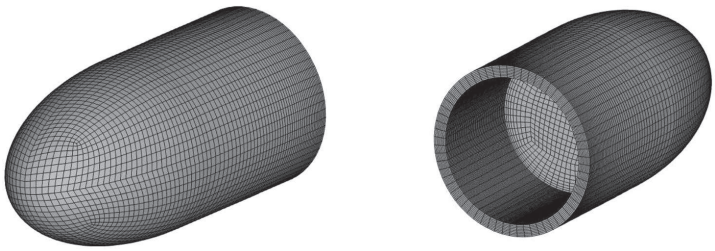

(a) (b)

Figure 3.2: Details of the computational mesh at the $\ell = 2$ body with $h/D = 0.7$ and $D_c/D = 0.86$. (a) Frontal-side and (b) rear-side views. Included in [126].

said that the values of derivatives at the boundaries were obtained by using one-sided formulae, and that the boundary conditions were identical to those described in Chapter 2.

3.2.4 Numerical techniques

Along with HWA experiments and GLS analysis, three-dimensional numerical simulations, using OpenFOAM®, were performed in order to describe the flow topology past a bullet-like body of $\ell = 2$ with rear cavities of depth $h/D = 0.2, 0.4, 0.7$ and 1, respectively, and $0 < D_c/D < 1$. Moreover, the effect of the cavities on the drag coefficient, C_d, was likewise analyzed. The computational domain and numerical schemes used have been described already in Chapter 2, and the computational mesh (see details of the body mesh in Fig.3.2) was selected after performing a grid convergence study, that is detailed below.

The simplest way to estimate the discretization errors is that based on the Richardson [120] extrapolation method which assumes that the calculations can be done on a grid sufficiently fine to achieve a monotonic convergence. In fact, in a grid refinement study, the value of a given variable estimated from the Richardson extrapolation is the value that would be obtained if the cell grid size tended to zero. Roache [121] generalized the Richardson extrapolation by introducing n^{th}-order methods to provide an estimation of the grid-independent solution as,

$$f_{exact} \simeq f_j + \frac{f_j - f_{j+1}}{\alpha^n - 1}, \tag{3.1}$$

where f is any field value or integral quantity discretized on fine (j) and coarse (j+1) meshes,

Mesh	n_r	n_θ	n_z	mesh nodes	C_d	$GCI_{j+1,j}(\%)$
1	133	75	579	$\sim 5.7 \times 10^6$	0.61512	0.62442
2	106	60	460	$\sim 2.9 \times 10^6$	0.61575	0.93072
3	84	48	365	$\sim 1.5 \times 10^6$	0.61669	————

Table 3.2: Drag coefficient, C_d, and Grid Convergence Index, $GCI_{j+1,j}$, obtained for a body of $\ell = 2$ with a cavity of length $h/D = 0.7$ and diameter $D_c/D = 29/30$ at $Re = 400$, using three different meshes: fine (1), medium (2) and coarse (3). The grid convergence index has been obtained from Eq.(3.3) with $R = 0.67$, $\alpha = 2^{1/3}$ and $n = 1.73$ given by Eq.(3.2).

α is the fine-to-coarse grid size refinement ratio in a coordinate direction, and n is the order or convergence rate of the method, which may be computed from three consecutive grids as (see Ferziger and Perić [39]),

$$n = \frac{log\left(\frac{f_{j+2}-f_{j+1}}{f_{j+1}-f_j}\right)}{log(\alpha)}. \tag{3.2}$$

To ensure that monotonic convergence is reached, the convergence ratio, $R = (f_{j+1} - f_j)/(f_{j+2} - f_{j+1})$, must fall within the interval $0 < R < 1$ before applying the Richardson extrapolation. Thus, the Grid Convergence Index can be defined from Eq.(3.1) as,

$$GCI_{j+1,j}(\%) = 3\left|\frac{f_{j+1} - f_j}{f_j(\alpha^n - 1)}\right| \times 100, \tag{3.3}$$

as a measure of how well the numerical solution approaches the grid-independent, asymptotic value. In addition, the Grid Convergence Index provides a conservative convergence measure for grid refinement studies, based on estimated fractional error derived from the generalization of Richardson extrapolation (see Roache [121]).

Table 3.2 summarizes the results of a convergence study performed using three different grids with a refinement ratio of $\alpha \simeq 2^{1/3}$: fine (1), medium (2) and coarse (3). In this case the study was based on the drag coefficient, C_d, obtained for a body with a cavity length $h/D = 0.7$ and diameter $D_c/D = 29/30$ at $Re = 400$. Notice that the convergence condition for C_d is monotonic since $R = 0.67 < 1$. The estimated order of the method, $n \simeq 1.73$, is slightly lower than the theoretical truncation error (second order in this case) due to the fact that we used limiters in our method (see Ferziger and Perić [39]). Table 3.2 shows that there is a decrease in the grid convergence index as the grid is refined, $GCI_{2,1} < GCI_{3,2}$. However the grid convergence index obtained with the finest grid, $GCI_{2,1}$, is only slightly lower than that obtained with the medium one, $GCI_{3,2}$, indicating that both meshes are close to the grid-independence solution and that a further refinement of the grid will not provide substantial improvement in the numerical results. Thus, since the computational time increases by a factor of four in the time-dependent simulations, the medium mesh, consisting of $106(r) \times 60(\theta) \times 460(z)$ nodes, was judged to have the best precision to computational cost ratio, and was selected to perform all the calculations included in this work. Finally, parallel computations were carried out in 8-12 mesh blocks.

3.3 Base bleed control

As mentioned above, it was demonstrated through a BiGlobal linear stability analysis by Sanmiguel *et al.* [127] that increasing base bleed coefficients stabilize both the unsteady and steady modes present at the wake of a slender axisymmetric body with blunt base. In this sense, we extend here this investigation, applying it to a $\ell = 2$ body with a rounded nose. However, the base flow used by Sanmiguel *et al.* [127] consisted in an axisymmetric steady solution of Navier-Stokes, and, as already discussed in Chapter 2, this assumption leads to wrong predictions of Re_{co}, since the wake is not axisymmetric at the onset of unsteadiness due to the symmetry-breaking mode which bifurcates at smaller values of the Reynolds number. Therefore, we expect likewise C^*_{b2} to be affected by this approach. Therefore, we will determine by means of GLS analysis the value of C^*_{b1} as a function of Re, whilst we will study experimentally the stabilization of the unsteady RSP mode and obtain the critical bleed coefficients, $C^*_{b2}(Re)$, that inhibit vortex shedding.

Additionally, the influence of density on the base bleed was experimentally investigated, by performing experiments of light base bleed ($S \simeq 0.14$) with Helium flowing through the base.

3.3.1 Homogeneous base bleed (S=1)

Two kind of experiments were performed to analyze the effect of base bleed on the stability of the wake regarding the RSP mode, namely, first, keeping Re fixed and increasing the bleed coefficient C_b, or second, keeping C_b constant while increasing Re. Let us start our discussion with the HWA measurements of the first kind. The procedure followed to obtain C^*_{b2} can be summarised as follows: for a fixed value of Re, the hot-wire probe was located at the downstream position of maximum oscillation amplitude in the absence of base bleed, discussed in Chapter 2 (see Fig.2.16), and the streamwise velocity signal was then recorded for several values of C_b. As an example, Fig. 3.3(a) shows the streamwise velocity fluctuations obtained at $Re = 500$ and $C_b = (0, 0.018, 0.023, 0.026)$. In this case the measurements were performed at $z = 3$ following the maximum-energy criterion mentioned. As observed, the fluctuations amplitude decreases progressively when base bleed increases, until eventually it reaches a value for which the oscillations are barely indiscernible, or whose amplitudes are of noise order. The spectra represented in Fig.3.3(b) reveal the strong stabilizing effect of base bleed already observed at the signals: a relatively small value of $C_b = 0.018$ provides with a nearly 4-fold decrease in the amplitude of the spectral peak with respect to the case without base bleed, $C_b = 0$, without introducing significant changes in its width. This stabilizing effect persists for increasing values of C_b, for the particular cases of $C_b = 0.023$ and 0.026. In view of the energy contained at the shedding peak of $C_b = 0.026$ and the corresponding temporal signal $w'(t)$, it could be considered that the oscillations are suppressed, and that this value of bleed is close to the critical bleed coefficient C^*_{b2}. However, it has been observed that there is always some energy associated to fundamental shedding frequency, even when C_b is considerably large and visually no oscillations are seen. Therefore, we will define a quantitative criterion for the determination of C^*_{b2} below. On the other hand, although it is known for two-dimensional bodies wakes that the Strouhal number decreases experimentally with C_b [49, 86], we have not observed any strong dependence of St with C_b, unlike what it is observed with respect to Re.

When Re is increased, the oscillations amplitude also increases as a consequence of a larger global linear mode amplitude, and therefore larger base bleeds are required to inhibit oscillations. This is shown in Fig.3.4, that depicts spectra for $Re = 590$ from signals taken at $z = 7$, and as

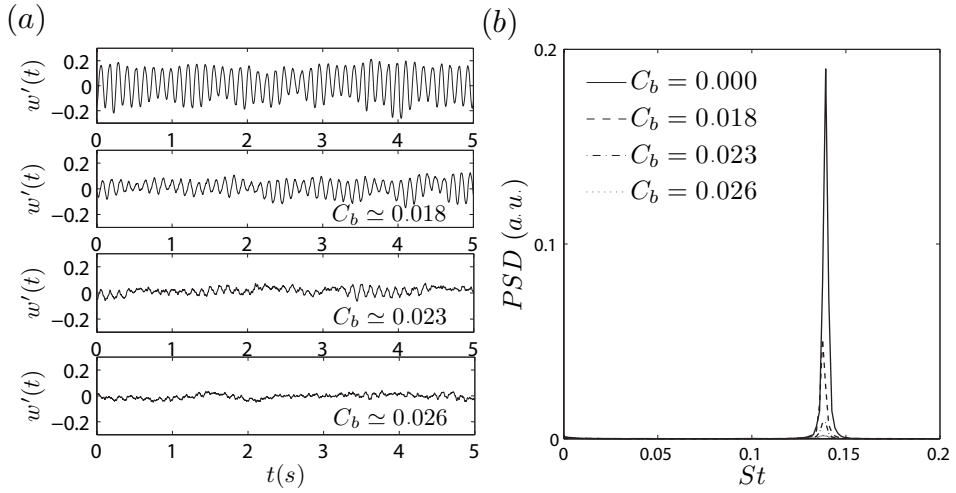

Figure 3.3: (a) Evolution of streamwise velocity fluctuations, $w'(t)$, with homogeneous base bleed, for $C_b = 0, 0.018, 0.023$ and 0.026, at $z = 3$ and $Re = 500$; and (b) corresponding power spectral densities.

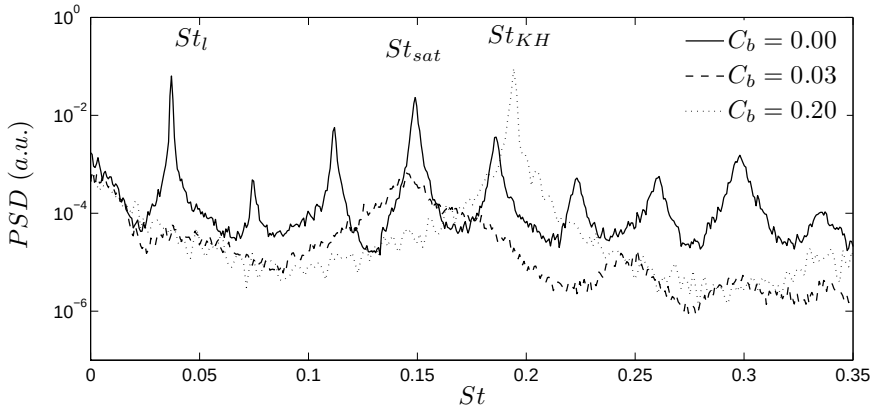

Figure 3.4: Power spectral densities, PSD with homogeneous base bleed, for $C_b = 0, 0.03$ and 0.2, at $z = 7$ and $Re = 590$.

said, a value of $C_b = 0.03$ is at least required to lower the energy of the fundamental peak one order of magnitude, although there is still a clear shedding component at the wake. The existence of a broad peak at St_{sat} with high C_b, can be due to the fact that the instability is no longer absolutely unstable, i.e. the SS mode would be retrieved, but a convective instability is present [132, 14], and that incoming perturbations from the wind tunnel are amplified within this range of frequencies close to St_{sat}. Nevertheless, further work would be needed to evaluate such a frequency response to external perturbations. Additionally, Fig.3.4 illustrates also that there is a limit in the stabilization provided by base bleed, since for a large bleed coefficients C_b, there is a second type of peak at St_{KH} that could be associated to a base jet instability (e.g. Kelvin-Helmholtz).

To quantify the stabilization process associated to increasing C_b at a fixed value of Re, as well as to obtain the corresponding critical values of $C^*_{b2}(Re)$, we decided to follow a procedure similar to that used by Schumm *et al.* [133]. Thus, the saturated oscillation amplitude, normalized with the value without base bleed, $|A|^2_{sat}/|A|^2_{sat}(C_b = 0)$, is plotted in Fig.3.5 as a function of C_b

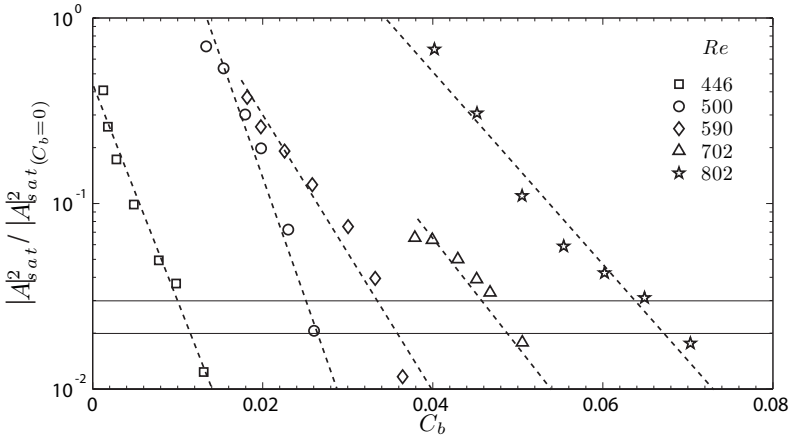

Figure 3.5: Experimental squared normalized saturation amplitude versus bleed coefficient for several Re. Note that solid horizontal lines represents values of marginal amplitude $\epsilon = 0.03$ (3%) and 0.02 (2%) respectively. Included in [15].

for several values of Re. The results of Fig.3.5, which are qualitatively similar to those shown in Fig.18(a) of Schumm *et al.* [133] for the wake of a two-dimensional blunt-based body, demonstrate the stabilizing effect of base bleed in a wide range of Re. Moreover, as already commented, it can be observed in Fig.3.5 that the values of C_b needed to achieve a given value of the normalized oscillation energy increase with Re. Unfortunately, the function $|A|^2_{sat}/|A|^2_{sat\ (C_b=0)}(C_b)$ obtained from these experiments was not linear near criticality, as expected in the case of a Hopf bifurcation in terms of C_b, but showed exponential-like behaviour. Therefore, it seems that the result by Hannemann & Oertel [49] does not apply at all Re (see below). This fact, which can also be inferred from the results shown in Fig. 18(a) of Schumm *et al.* [133], precluded us from performing a linear regression in the neighborhood of the bifurcation point to determine the function $C^*_{b2}(Re)$. Instead, the critical values C^*_{b2} plotted in Fig.3.5 were obtained by applying an exponential fit to the tail of the $|A|^2_{sat}/|A|^2_{sat\ (C_b=0)}(C_b)$ experimental curve, as shown as dashed lines in Fig.3.5. The value of C^*_{b2} was then obtained by the condition $|A|^2_{sat}/|A|^2_{sat,(C_b=0)}(C^*_{b2}) = \epsilon \ll 1$. Although the value of the marginal amplitude $\epsilon = 0.03$ (3 %) was chosen arbitrarily, it can be seen in Fig.3.5 that the value of C^*_{b2} is not very sensitive to its specific value, as illustrated by the solid horizontal lines plotted in the same figure for the particular cases $\epsilon = 0.02$ (2 %) and $\epsilon = 0.03$ (3 %).

A second procedure was also followed in order to obtain C^*_{b2} and to analyze the wake dynamics with base bleed. This second set of experiments consisted in keeping fixed the bleed coefficient, $C_b \geq C^*_{b2}$, and searching for the Reynolds number at which the flow becomes unstable. Thus, once C_b was established, streamwise velocity fluctuations were recorded for increasing Re. Obviously, the energy of the amplitude of the shedding oscillations grows with Re, in the same manner as for $C_b = 0$ (see Chapter 2). Figure 3.6 shows the evolution of the squared saturation amplitude, $|A|^2_{sat}$, versus Re for a constant $C_b = 0.014$. When such a level of base bleed is applied, the wake is stable in a range of Re higher than $Re^{exp}_{co} = 412.4$, and more precisely, no oscillations were observed until $Re \simeq 467.7$. This critical value was obtained after applying a linear extrapolation of the data to zero amplitude, following the Landau model (see Eq.1.18). In the same way as for wakes without base bleed, the linear growth of $|A|^2_{sat}$ with Re extends over a wide range of Re, for which the

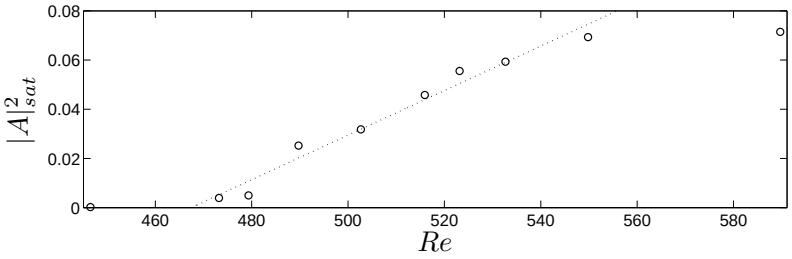

Figure 3.6: Evolution of the streamwise velocity saturation amplitude, $|A|^2_{sat}$, versus Reynolds numbers for $C_b = 0.014$.

complex weakly non-linear model of Stuart-Landau (see Eq.1.13) is expected to be valid. Besides, these experiments were done for several C_b, obtaining several new values of $C^*_{b2}(Re)$, that, along with the values extracted from the first type of experiments, are presented in Fig.3.8.

Considering the BiGlobal stability results, the effect of base bleed on the eigenvalue spectra of linear global modes has been discussed in detail in Sanmiguel *et al.* [127]. Following the same procedure, we present in Fig.3.7 the corresponding results obtained here for the particular case of a body with $\ell = 2$, where the eigenvalues (σ_r, σ_i) are plotted for $Re = 500$, $|m| = 1$, and four different values of $C_b = (0, 0.04, 0.06, 0.08)$. Note from Fig. 3.7 that, as C_b increases, the leading eigenvalues σ_1 and σ_2, corresponding respectively to the steady and oscillatory modes, move towards the stable $\sigma_r < 0$ half-plane. Specifically, Fig.3.7(a) shows that for $C_b = 0$ the oscillatory mode is slightly damped, in agreement with the fact that $Re^{GLS}_{co} = 518$ in this case (see Fig.2.13), and has an associated frequency $\sigma_{i1} \simeq 0.65$. However, it is also observed in Fig.3.7(a) that, since $Re^{GLS}_{cs} = 327$ (see Fig.2.20), the steady state mode is unstable, $\sigma_{r1} > 0$ without base bleed. Figs.3.7(b)-3.7(d) reveal that both growth rates σ_{r1} and σ_{r2} decrease as C_b increases and, in particular, Figs.3.7(c) and 3.7(d) show that $0.06 < C^*_{b1} < 0.08$. More generally, for given values of ℓ, Re and C_b, the conditions $\sigma_{r1} = 0$, $\sigma_{r2} = 0$ were used to determine the critical bleed coefficients C^*_{b1} and C^*_{b2}, respectively.

Fig. 3.8 summarizes the values of the critical base-bleed coefficients obtained using BiGlobal stability analysis (solid and dashed lines) and HWA experiments (asterisks). The GLS results presented correspond to the most unstable azimuthal mode, $|m| = 1$. Moreover, results from numerical simulations performed by Bohorquez *et al.* [15] have been also plotted for comparison and validation, along with the local linear stability analysis included in the same paper. Similar to the case of Re_{cs} discussed in Chapter 2, a perfect agreement is obtained between the direct numerical simulations [15] and BiGlobal stability predictions for the curve $C^*_{b1}(Re)$ (circles and solid line, respectively), demonstrating the capability and accuracy of the BiGlobal stability approach in this case. The accurate determination of $C^*_{b1}(Re)$ by the BiGlobal stability analysis is of practical interest because it allows us to quantify the upper bound for the bleed coefficient required to inhibit not only the steady mode but also the periodic state, at least for the parameter settings investigated here. Note that the condition $C_b > C^*_{b1}(Re)$ defines a region of the (Re, C_b) parameter plane, referred to as *region I* in Fig. 3.8, within which the wake subjected to base bleed is steady and axisymmetric. Figure 3.8 shows also that the trend of the curve $C^*_{b1}(Re)$ is consistent with the existence of an asymptote at large Reynolds numbers, such that $C^*_{b1} \to 0.125$ for $Re \to \infty$.

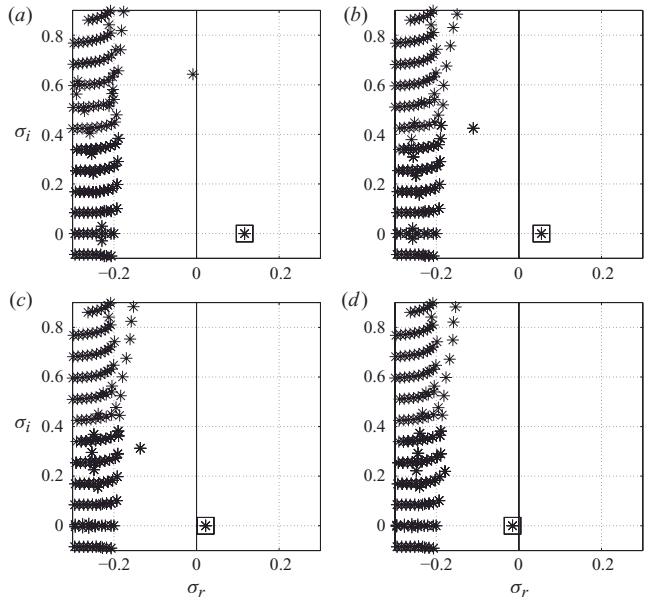

Figure 3.7: Eigenvalue spectra for a body with aspect ratio $\ell = 2$, $Re = 500$, $|m| = 1$ and base bleed coefficients (a) $C_b = 0$, (b) $C_b = 0.040$, (c) $C_b = 0.060$ and (d) $C_b = 0.080$, respectively. The unstable eigenvalue corresponding to the steady bifurcation has been marked with a square. Included in [15].

However, this result must be interpreted with care, since the instability of the shear layer separating from the body base may induce the transition to turbulence in the wake for large enough values of the Reynolds number [117].

For values of C_b such that $C^*_{b2}(Re) < C_b < C^*_{b1}(Re)$, defined as *region II* in Fig. 3.8, the wake is steady and exhibits planar symmetry, as shown by Bohorquez *et al.* [15]. However, when the bleed coefficient is decreased below the critical value C^*_{b2}, i.e. for $C_b < C^*_{b2}(Re)$, the oscillatory mode is destabilized, corresponding to *region III* in Fig. 3.8. In this case, periodic vortex shedding of vortex structures takes place, resembling the cases displayed in Fig. 2.10 for the case without base bleed.

Furthermore, as revealed by Fig. 3.8, the critical values $C^*_{b2}(Re)$ computed with the BiGlobal stability analysis and the local linear analysis [15], respectively shown as crossed and dashed lines, are in good agreement for large enough values of the Reynolds number, $Re \gtrsim 1200$. This result can be explained by noting that the slenderness of the basic flow at criticality increases with C_b, as already pointed out in Sevilla & Martínez-Bazán [135], thereby justifying the use of the quasi-parallel approximation. However for Reynolds number $Re \lesssim 800$ the BiGlobal stability analysis predicts values of C^*_{b2} considerably smaller than those obtained through experiments (that show very good agreement with numerical results from Bohorquez *et al.* [15]), which clearly cannot be used to obtain the critical bleed coefficient in that region. As the Reynolds number decreases, the value of C^*_{b2} given by the BiGlobal analysis decreases for $Re \lesssim 800$, until it becomes zero at $Re = Re^{GLS}_{co} \simeq 518$. The quantitative disagreement between Re_{co} and Re^{GLS}_{co} , respectively obtained through experiments and BiGlobal linear stability analysis, corresponds in Fig. 3.8 to the different intersections points observed in both cases at $C_b = 0$. Accordingly, in the case with base bleed both techniques lead to different values of $C^*_{b2}(Re)$, such that the critical bleed coefficient

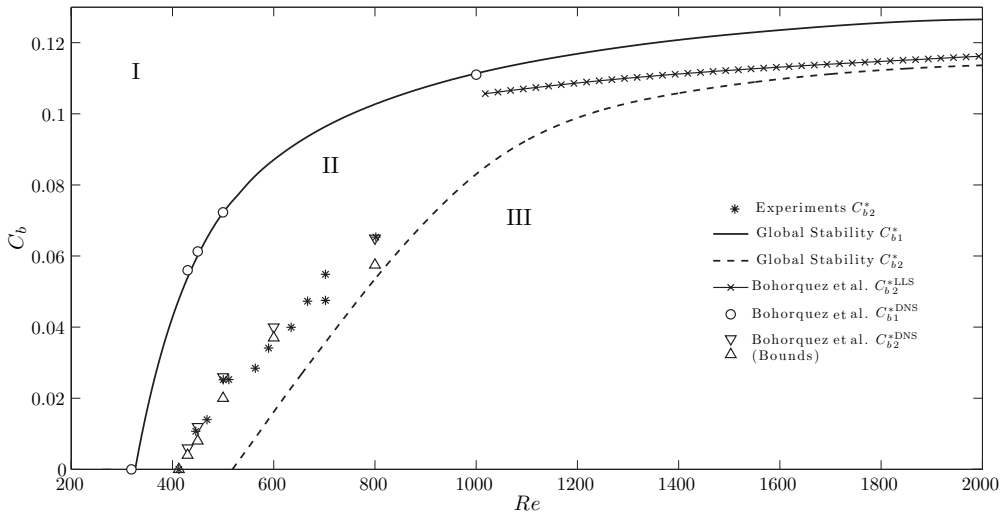

Figure 3.8: Evolution of the critical base bleed coefficients with the Reynolds number for an ellipsoidal rounded nose body of aspect ratio $\ell = 2$, obtained with the GLS analysis and HWA experiments. Results from numerical simulations (DNS) and local linear stability analysis (LLS) by Bohorquez *et al.* [15] are included for comparison and validation. Taken and modified from [15].

predicted by BiGlobal stability analysis (dashed line) for values of the Reynolds number $Re \lesssim 800$ is lower than those obtained with the HWA measurements, indicating that, at these Reynolds numbers, the planar-symmetric wake is more unstable than the axisymmetric wake used as base flow in the linear stability analysis. Nevertheless, notice that the difference between the values of $C^*_{b2}(Re)$ given by the experiments and the linear analysis decreases as Re increases, with a fairly good agreement at $Re = 800$. Figure 3.8 also indicates that, similarly to the case of the critical bleed coefficient C^*_{b1}, the values of C^*_{b2} obtained from the BiGlobal analysis tend to a common asymptotic value such that $C^*_{b2} \to 0.115$, approximately, for $Re \to \infty$ and in the particular case of a body with $\ell = 2$, mimicking the behavior of local linear stability results [15].

Finally, it is noteworthy that the marginal curve $C^*_{b2}(Re)$ has a structure similar to that found by Schumm *et al.* [133] in the case of a two-dimensional blunt-based geometry (see their Figure 18b), which allows us to question the assumption of a dual Hopf bifurcation in terms of both C_b (with Re = constant) and Re (with C_b = constant). In this sense, it has been shown experimentally (see Fig.3.6) that when C_b is kept constant, the energy of the fundamental mode oscillations grows linearly with Re in the vicinity of $Re_{co}(C_b)$; however, no linear behavior exists when C_b increases for a constant Re (see Fig.3.5). In other words, if, at constant Re, there was a Hopf bifurcation in terms of C_b, one could state that $|A|^2_{sat} \propto (C^*_{b2}(Re) - C_b)$. Thus, it should be observed a linear dependence of $|A|^2_{sat}$ with Re only in a region where the neutral curve behaved as $C^*_{b2}(Re) \propto Re$. However, Fig. 3.8 illustrates that $C^*_{b2}(Re)$ is not necessarily a linear function of Re, indicating that the second, oscillatory bifurcation might not correspond to a supercritical Hopf bifurcation in terms of C_b when the Reynolds number is kept constant.

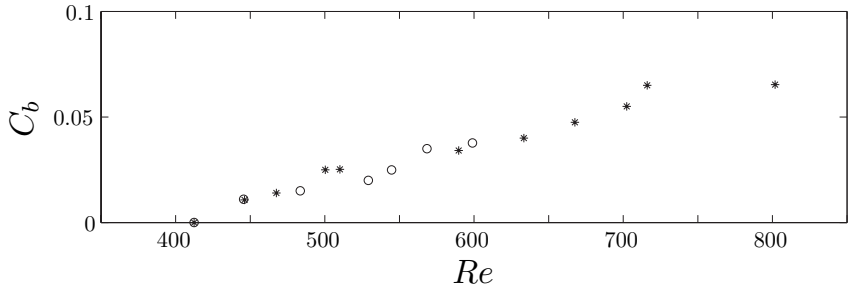

Figure 3.9: Evolution of the experimental critical base bleed coefficients with the Reynolds number for a $\ell = 2$ body, obtained by light base bleed (circles) and homogeneous base bleed (asterisks).

3.3.2 A note on the stabilizing effect of light base bleed (S=0.14)

As already mentioned above, in an extension of a previous work [135], Sevilla & Martínez-Bazán [136] investigated the effect of low-density base-bleed on the stabilization of the wake behind an axisymmetric bluff body [136], finding that the critical base bleed for which the wake becomes absolutely unstable, computed by means of local linear stability analysis, decreased almost linearly as $S = \rho_b/\rho_\infty$ decreased, for $Re = 1200$. This stabilizing effect of low density was attributed to a reduced momentum transport upstream as a consequence of a lower density of the recirculation bubble with respect to the free-stream, due to mass-diffusion through the shear-layer, and was in line with former arguments [161]. In this sense, in order to get insight of this, a priori, efficient stabilizing effect of light base bleed, we tackled this problem by means of HWA measurements at the wake of a $\ell = 2$ body using Helium as bleed fluid at different Re and $C_b = w_b/w_\infty$.

The measurements of streamwise velocity fluctuations downstream of the body base, $w'(t)$, for several Re and C_b, demonstrated a stabilizing effect similar to that encountered using homogeneous base-bleed. In fact, as Fig. 3.9 displays, the critical bleed coefficient that inhibits vortex shedding, C^*_{b2} (obtained in the same manner as for the air base bleed), does not seem to change when the density of the bleed fluid, ρ_b, is different from the free-stream density, ρ_∞. Thus, conversely to what the local linear stability analysis sheds [161, 136], density apparently does not play a major role in the stabilization of the wake. In this sense, although it has been shown that at $Re = 1200$, for the case of homogeneous base bleed, the local analysis fails to predict quantitatively the critical coefficient C^*_{b2} (see Fig. 3.8), when the experimental trend of $C^*_{b2}(Re)$ is considered; it would be logical to expect a similar qualitative behavior in the results obtained by means of both techniques, local linear stability analysis and experiments. Therefore, in order to understand the apparent contradiction in both groups of results with light base bleed, we have planned to perform three-dimensional numerical simulations and BiGlobal stability analysis in the short term, along with additional experiments with heavy base bleed (e.g. by injecting sulfur hexafluoride), to broaden the range of S investigated.

3.4 Rear cavities

In this section we examine the effect of a base cavity on the stability properties of the flow past a slender blunt-based axisymmetric body. BiGlobal linear stability analysis, unsteady three-

dimensional numerical simulations, and wind tunnel experiments were performed, in this Thesis for a body of length-to-diameter ratio $\ell = 2$, to determine the critical Reynolds numbers for the first-steady and the second-oscillatory bifurcations and their dependence with the cavity dimensions.

3.4.1 Cavity effects on the first-stationary bifurcation

Following the BiGlobal linear stability analysis performed with finite differences of sixth order, as described above, for a solid base body of length $\ell = 2$ and Reynolds numbers higher than $Re_{cs} \simeq 326.2$, the flow experiences a first transition to a steady, non-axisymmetric regime, although it exhibits planar symmetry. This first bifurcation corresponds to a three-dimensional, $|m| = 1$, and steady, $\sigma_i = 0$, perturbation. This result is in excellent agreement with that obtained for the same body using spectral methods and described in Chapter 2 [127], $Re_{cs} \simeq 327$.

To show the effect of the cavity length, h/D, on the critical Reynolds number, we performed BiGlobal linear stability analyses varying h/D from 0 to 1. Figure 3.10(a) displays the effect of the cavity length, h/D, on the critical Reynolds number corresponding to the first bifurcation, Re_{cs}, for a cavity with diameter $D_c/D = 29/30$. Note that Re_{cs} increases with h/D, showing the stabilizing effect of the cavity, until it reaches an asymptotic value for $h/D > 0.7$. Thus, the value $h/D \simeq 0.7$ can be considered as a critical cavity length, beyond which no further improvement in Re_{cs} is observed. The addition of a cavity of $h/D > 0.7$ results in an increase in the critical Reynolds number from $Re_{cs} = 326.2$ for a body without cavity to $Re_{cs} = 512$, representing a considerable stability increase of about 57%. In Fig. 3.10(a) we have also plotted (squares) critical Reynolds numbers determined from the three-dimensional numerical simulations for $h/D = 0$, 0.2 and 0.7, with the aim of validating the results provided by the BiGlobal linear stability analyses (the procedure followed to determine Re_{cs} from the numerical simulations can be found in Chapter 2). Note that the relative errors between the global stability and the numerical simulations are lower than 2.5% in the worst case.

Likewise, using BiGlobal linear stability analysis, we studied the effect of the diameter of the cavity D_c/D on the critical Reynolds number, Re_{cs}. Figure 3.10(b) displays the evolution of Re_{cs} with D_c/D for two different cavity lengths, namely $h/D = 0.2$ and 0.7. It can be observed that, for both cavity lengths, the critical Reynolds number exhibits a similar behavior with varying diameter. In fact, the critical Reynolds number, Re_{cs}, does not change for cavity diameters $D_c/D \lesssim 0.6$, independent of the cavity length, however, it increases monotonically for $0.6 \lesssim D_c/D < 1$. Figure 3.10(b) shows that the maximum critical Reynolds number is achieved for $D_c/D \to 1$, a limit impossible to reach in practical applications since it corresponds to a zero-wall cavity thickness. For the three-dimensional model, mathematical singularities developed at the edge-corner of the wall cavity with a thin thickness, which lead to numerical instabilities. Therefore, the maximum cavity diameter studied numerically in the present work was limited to $D_c/D = 0.99$.

In addition to examining the effect of the cavity length on the critical Reynolds number of the first, steady bifurcation, Re_{cs}, we also performed numerical simulations to evaluate the effect, if any, of the cavity dimensions on the drag coefficient, defined here as indicated by Eq.(2.5). Thus, we were able to observe that the effect of the cavity on pressure and viscous components of the drag force is very different. Figure 3.11 shows the effect of the cavity length on the drag coefficients, C_d, C_d^p and C_d^v, relative to those obtained for the solid base body, C_{d0}, C_{d0}^p, C_{d0}^v respectively (see Table 3.3). Furthermore, Fig. 3.11(a) indicates that the pressure drag coefficient can be reduced by

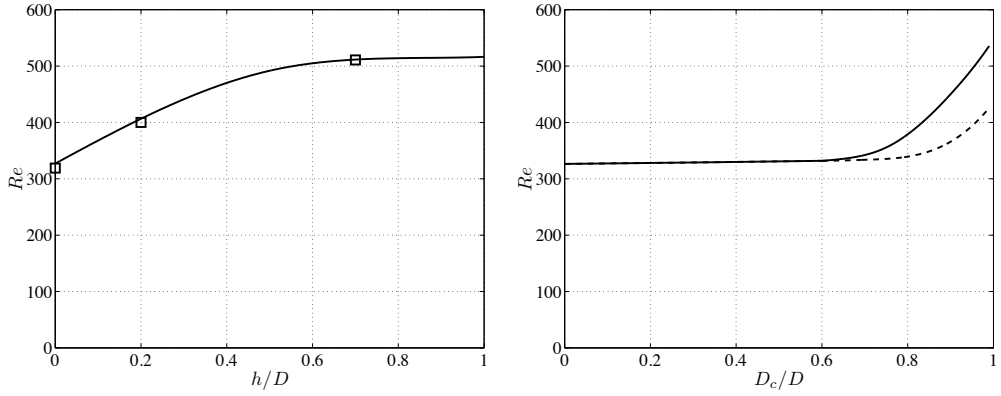

Figure 3.10: (a) Dependence of the critical Reynolds numbers corresponding to the first, stationary bifurcation, Re_{cs}, with the cavity length, h/D, for a cavity diameter of $D_c/D = 29/30$. Comparison between the results given by global linear stability analyses (solid line) and the three-dimensional numerical simulations (squares), for the stationary bifurcation. (b) Effect of the cavity diameter, D_c/D, on the critical Reynolds numbers for the stationary bifurcation. Cavity lengths $h/D = 0.2$ (dashed line) and $h/D = 0.7$ (solid line). Included in [126].

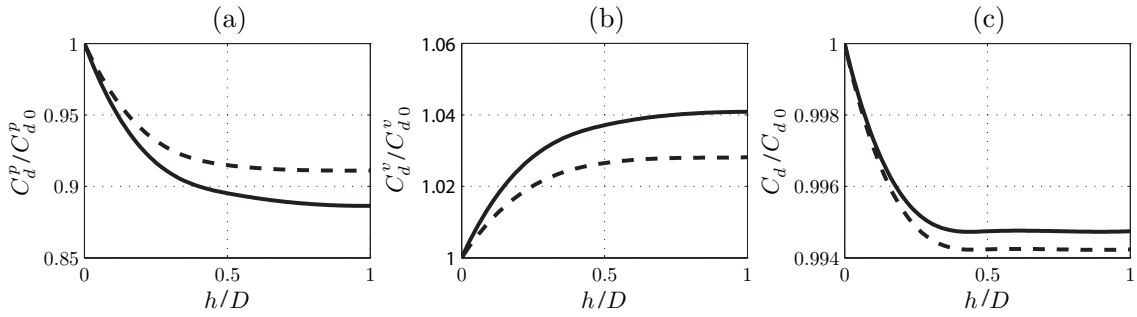

Figure 3.11: Effect of the cavity length on the (a) pressure drag coefficient C_d^p, (b) viscous drag coefficient C_d^v and (c) drag coefficient C_d, for a body of cavity diameter $D_c/D = 29/30$ and Reynolds numbers $Re = 300$ (dashed line) and $Re = 400$ (solid line). The drag coefficients C_{d0}^p, C_{d0}^v and C_{d0} correspond to a body without base cavity, i.e. $D_c/D = 0$. Included in [126].

approximately 10% by varying h/D, with the effect more pronounced for higher Reynolds numbers. However, Fig. 3.11(b) indicates that, in the range of Reynolds number reported here, the viscous drag coefficient increases up to 4% increasing h/D due to the effect of the viscous stresses acting on the inner wall of the cavity. Finally, for these Reynolds numbers, the combined pressure and viscous effects result in a slight reduction of the drag coefficient with increasing cavity depth, until no further improvement is observed for $h/D \gtrsim 0.5$, as shown in Fig. 3.12(c). Nevertheless, more substantial decreases in C_d can be anticipated for higher Reynolds number, for which $C_{d0}^v \ll C_{d0}^p$.

A similar numerical study was carried out to determine the effect of the cavity diameter on the drag coefficient (Fig. 3.12). As in the case of varying cavity length, discussed above, a decrease in the pressure drag coefficient of up to 10% with varying D_c/D was observed (Fig. 3.12a), while C_d^v increased by approximately 4%, as displayed in Fig. 3.12(b). The behaviors of C_d^p and C_d^v with

Re	C_{d0}	C^p_{d0}	C^v_{d0}
300	0.718	0.208	0.510
400	0.609	0.182	0.427

Table 3.3: Drag coefficients of a solid base body, C_{d0}, C^p_{d0} and C^v_{d0}, at Reynolds numbers $Re = 300$ and $Re = 400$.

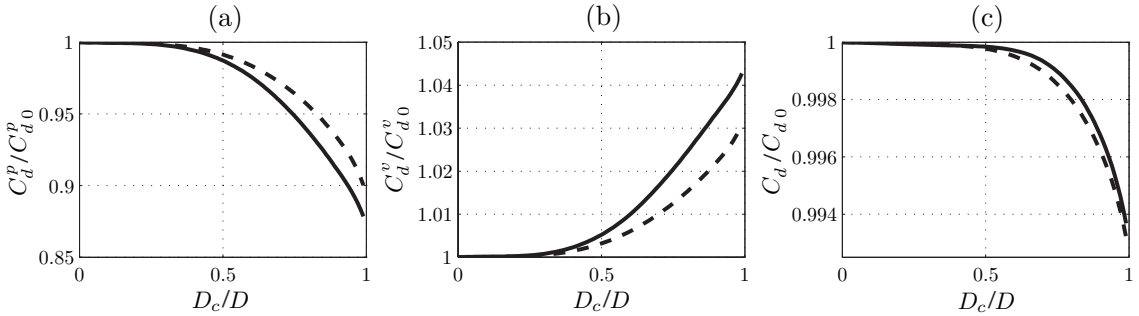

Figure 3.12: Effect of the cavity diameter on the (a) pressure drag coefficient C^p_d, (b) viscous drag coefficient C^v_d and (c) drag coefficient C_d, for a body with a cavity length of $h/D = 0.7$ at Reynolds numbers $Re = 300$ (dashed line) and $Re = 400$ (solid line) respectively.

D_c/D translate into a small decrease of C_d with D_c/D for $D_c/D > 0.5$, reaching a minimum value of about $C_d = 0.993\, C_{d0}$ (0.7% decrease) in the limit $D_c/D \to 1$ as observed in Fig. 3.12(c).

Since the drag coefficient is an integral value of the base flow pressure over the surface of the body, to better understand the asymptotic behavior observed with the cavity length, it is useful to examine the base flow in more detail. Thus, we have plotted in Fig. 3.13 the pressure contours obtained from the steady axisymmetric numerical simulations for four bodies with a cavity of diameter $D_c/D = 29/30$ and lengths $h/D = 0$, 0.2, 0.7 and 1 at $Re = 400$. As shown in Fig. 3.13(a), in the case of a body without a base cavity, a local minimum is located at center of the base, i.e. near $r = 0, z = 0$. However, as the cavity length is increased, this pressure minimum begins to attenuate, consistent with the decrease of the pressure drag coefficient with h/D reported in Fig. 3.11(a). The asymptotic behavior of C^p_d for $h/D > 0.7$ described above can be more clearly understood from Figs. 3.13(c) and 3.13(d), which show that the pressure distribution at the end of the cavity is nearly the same for a body with a cavity of $h/D = 0.7$ as that obtained for a body with a cavity of $h/D = 1$. Moreover, the pressure field outside of the cavity remains unchanged for $h/D > 0.7$. These observations illustrate the asymptotic value achieved by the pressure drag coefficient for $h/D \gtrsim 0.7$, as reported in Fig. 3.11(a).

Finally, let us now briefly describe the effect of the cavity diameter, D_c/D, on the axisymmetric mean base flow, with the aim of understanding the stability behavior shown in Fig. 3.10(b). To that end, we performed axisymmetric, steady numerical simulations for different cavities of length $h/D = 0.7$ and diameters $D_c/D = 0$, 0.6, 0.8 and 0.9 at $Re = 400$. Radial velocity profiles starting at the trailing edge, $U(r = 0.5, z)$, have been plotted in Fig. 3.14(a). Notice that, as D_c/D increases, the local maximum of the radial velocity, located approximately at $z = 0.16$, decreases while moving slightly closer to the body base. However, Fig. 3.14(a) also shows that the local maxima corresponding to bodies with cavity diameters of $D_c/D = 0$ and $D_c/D = 0.6$ have

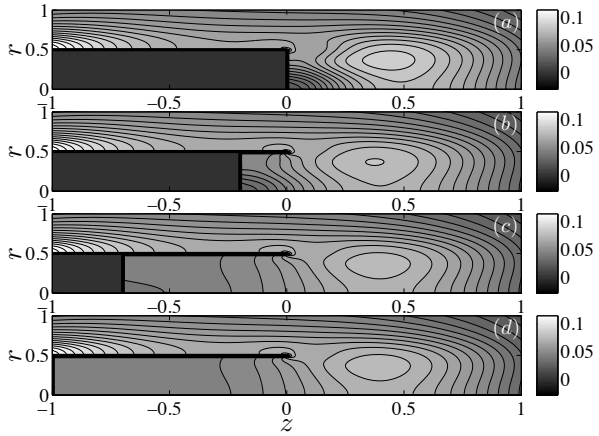

Figure 3.13: Pressure contours of the steady axisymmetric field obtained for four bodies with a cavity of diameter $D_c/D = 29/30$ and lengths (a) $h/D = 0$, (b) $h/D = 0.2$, (c) $h/D = 0.7$ and (d) $h/D = 1$ at $Re = 400$. Included in [126].

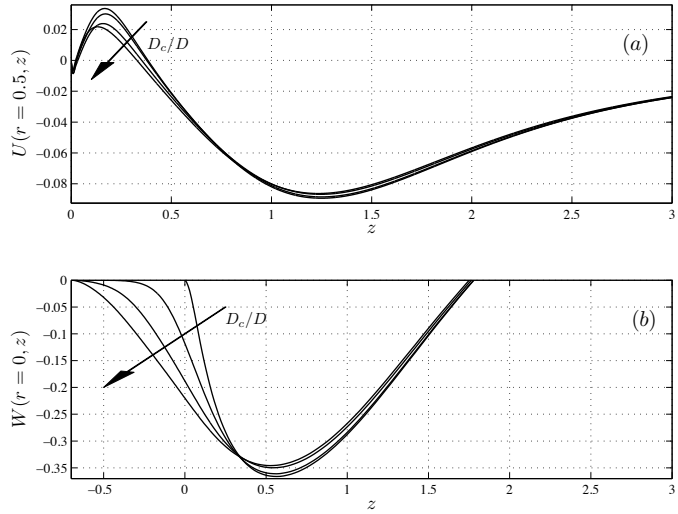

Figure 3.14: Effect of the cavity diameter, D_c/D, on downstream evolution of the axisymmetric (a) radial velocity at $r = 0.5$, $U(r = 0.5, z)$, and (b) axial velocity at $r = 0$, $W(r = 0, z)$, at $Re = 400$. The different curves correspond to cavities of length $h/D = 0.7$ and diameters $D_c/D = 0$, 0.6, 0.8 and 0.9. Included in [126].

similar amplitudes, which might explain the weaker stabilizing effect of the cavity on the flow for $D_c/D < 0.6$. The downstream evolution of the axial mean velocity along the axis, $W(r = 0, z)$, has been shown in Fig. 3.14(b). The figure shows that the minimum axial velocity at the axis increases slightly as D_c/D increases, decreasing the magnitude of the recirculating velocity. Thus, it seems that for smaller cavity diameters the recirculating velocities are larger, producing larger radial velocities close to the rear corner, which perturb the free stream at $r > 0.5$ and destabilize the flow.

Having described the stability effects of adding a cavity of a given length, h, and diameter, D_c, at the base of the body (up to 40% increase of Re_{cs} and drag reduction of nearly 1%), we would

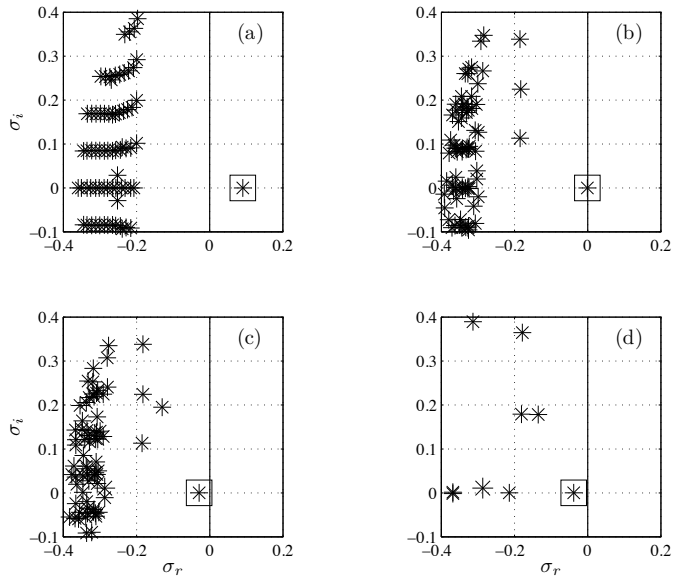

Figure 3.15: Eigenvalue spectra for $|m| = 1$, for four bodies with a cavity of diameter $D_c/D = 29/30$ and lengths (a) $h/D = 0$, (b) $h/D = 0.2$, (c) $h/D = 0.7$ and (d) $h/D = 1$, respectively, at $Re = 400$. Squares indicate the eigenvalues corresponding to the first-stationary bifurcation ($\sigma_i = 0$).

like to analyze the stability characteristics of the flow in greater detail, as given by the global linear stability analysis. The eigenvalue spectra obtained for the azimuthal mode, $|m| = 1$, for four bodies of lengths $h/D = 0$, 0.2, 0.7 and 1, respectively, and a cavity diameter $D_c/D = 29/30$ (close to the optimum $D_c/D \to 1$) at Reynolds number $Re = 400$, have been plotted in Fig. 3.15. It can be observed in Fig. 3.15(a) that, as detailed in Chapter 2, at this Reynolds number, the flow around a body without base cavity, $h/D = 0$, exhibits an unstable ($\sigma_r > 0$) but steady ($\sigma_i = 0$) regime (eigenvalue marked with a square), characterized by the loss of axial symmetry. However, as the cavity length is increased, the growth rate of the unstable mode, σ_{r1}, decreases, and the eigenvalue moves towards the stable half-plane defined by $\sigma_r < 0$. This trend continues for increasing values of h/D until $h/D \approx 0.2$, for which the unstable value is neutralized, as shown in Fig. 3.15(b). Increasing the cavity length from $h/D = 0.2$ to $h/D = 0.7$ produces a decrease of σ_{r1} towards more negative values (Fig. 3.15c) until no further changes are observed in σ_{r1} for bodies of cavity length larger than $h/D = 0.7$ as depicted in Fig. 3.15(d). This result is in agreement with the asymptotic behavior found in both the critical Reynolds number, represented in Fig. 3.10(a), and the drag coefficient, displayed in Fig. 3.11(c), for $h/D > 0.7$. Furthermore, the spatial structure of the global mode is also significantly affected by the increase of the cavity length, as revealed by an examination of the normalized eigenfunctions shown in Fig. 3.16, corresponding to the eigenvalues marked with a square in Fig. 3.15. One of the important effects of the cavity is that the near-field structure is confined within the recess, concurrent with a decrease in eigenfunction amplitudes. In fact, the most intensive part (negative values) of both radial $\hat{u}$ and azimuthal $\hat{v}$ eigenfunctions, decrease in magnitude and move inside the cavity as h/D increases. It is worth mentioning that the eigenfunction with the largest amplitude, for all the cavity lengths, is that corresponding to the axial velocity component $\hat{w}$. Concerning the pressure eigenfuntion, Fig. 3.16(a) shows that, for body without cavity, the minimum occurs at the base of the body, near the axis. However, as the

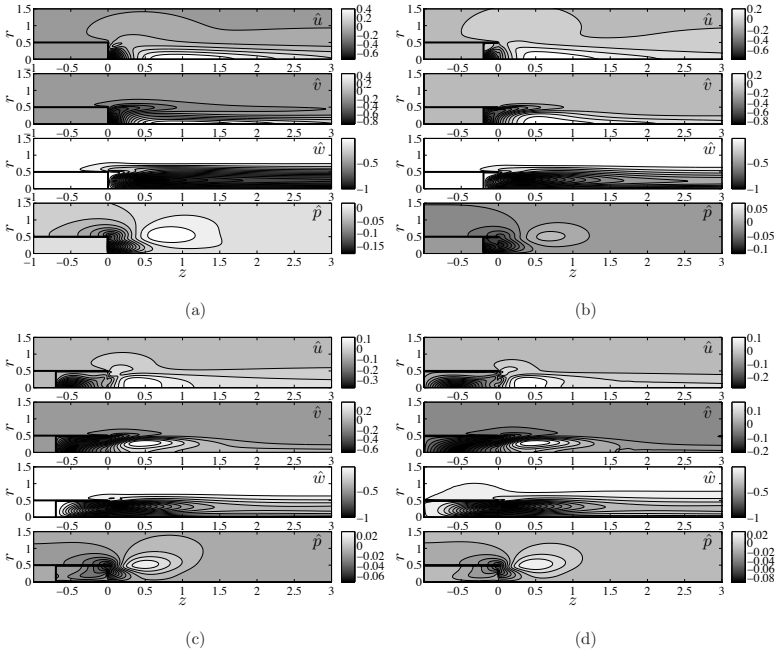

Figure 3.16: Isolines of the real part of the normalized eigenfunctions $\widehat{u}$, $\widehat{v}$, $\widehat{w}$ and $\widehat{p}$ of the eigenvalues marked with the squares in Fig. 3.15, for cavity lengths (a) $h/D = 0$, (b) $h/D = 0.2$, (c) $h/D = 0.7$ and (d) $h/D = 1$. Here, the eigenfunctions are normalized with $\|\hat{\mathbf{q}}\|_\infty$.

cavity length increases, the minimum in the pressure eigenfuntion moves radially and concentrates near the corner of the cavity, see Figs. 3.16(c) and (d). Note that the minimum value of $\widehat{p}$ reduces in magnitude from $\widehat{p}_{min} \approx -0.15$ for a solid body to $\widehat{p}_{min} < -0.06$ for a body with a cavity of length $h/D > 0.7$. Finally, it is apparent in Fig. 3.16 that the shape and the values of all the eigenfunctions are nearly identical for the bodies of length $h/D = 0.7$ and 1.0, which corroborates the asymptotic behavior of the flow stability with varying cavity length, discussed earlier.

3.4.2 Cavity effects on the second-oscillatory bifurcation

Oscillations of the wake downstream of the solid-base body are clearly observed at moderate Reynolds numbers, e.g. $Re = 500$, with three-dimensional unsteady numerical simulations, as displayed in the vorticity contours plotted in Fig. 3.17(a). However, the introduction of a cavity of length $h/D = 0.7$ and diameter $D_c/D = 0.86$, completely suppresses the oscillatory mode, as shown in Fig. 3.17(b). In place of the oscillatory mode, we can observe in Fig. 3.17(b) that the flow has become stationary and, although it is not axisymmetric, exhibits planar symmetry. Notice from Fig. 3.10(b) that for a Reynolds number $Re = 500$ and a cavity length $h/D = 0.7$, the cavity diameter D_c/D should be larger than 0.96 to completely stabilize the flow, and to recover the axisymmetric solution. Figure 3.17(c) also includes a detail of the vorticity contours inside the cavity, showing that the vortical flow extends into the cavity. Thus, it can be observed that the recirculating region forming behind the body penetrates inside the cavity modifying the dynamic of the wake and, consequently, changing the nature of the instability.

With the aim of validating the three-dimensional numerical simulations, we also experimentally

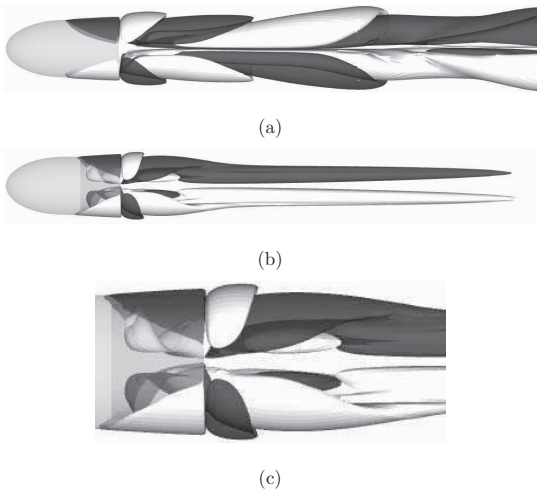

Figure 3.17: Contours of constant streamwise vorticity, $\omega_z = \pm 0.05$, for $Re = 500$. (a) Solid base body and (b) a body with a cavity of length $h/D = 0.7$ and diameter $D_c/D = 0.86$. (c) Detail of the vorticity contours inside the cavity. Included in [126].

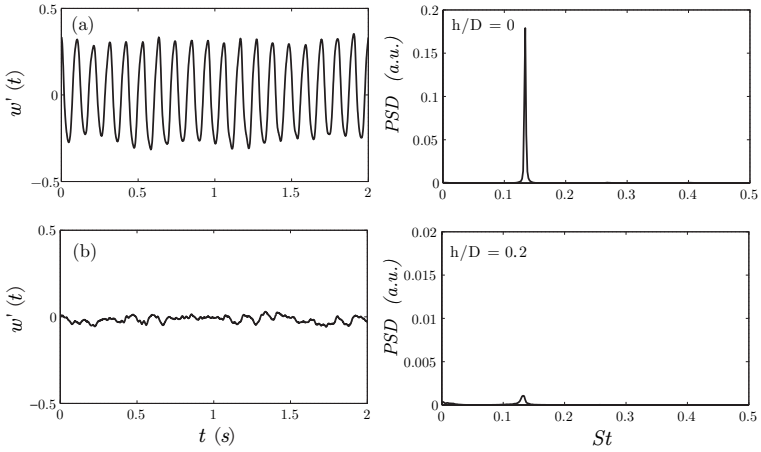

Figure 3.18: Hot-wire measurements of the fluctuations of the streamwise component of the velocity, $w'(t)$, and the corresponding power spectral density at $r = 0$, $z = 3$ for $Re = 465$ and two cavities of diameter $D_c/D = 0.86$ and lengths (a) $h/D = 0$ and (b) $h/D = 0.2$. Included in [126].

measured the critical Reynolds number for the second, oscillatory bifurcation, Re_{co}, for a bullet-like body of length-to-diameter ratio equal to 2, with cavities of diameter $D_c/D = 0.86$ and lengths varying from h/D= 0 to 1.0. The fluctuations of the streamwise component of the velocity, $w'(t)$, were measured at $r = 0$ and $z = 3$ with a hot-wire anemometer. Figure 3.18 shows two examples of the hot-wire measurements of $w'(t)$, along with their corresponding power spectral density, obtained at $r = 0$, $z = 3$ for two bodies with cavity lengths of $h/D = 0$ and 0.2 and $L/D = 2$ with $Re = 465$. It can be clearly observed that the amplitude of the energy spectrum decreases with the addition of a base cavity, illustrating its stabilizing effect. Notice that the scale in the energy spectrum displayed in Fig. 3.18(b) is ten times smaller than that shown in Fig. 3.18(a). It is also notable that the Strouhal number associated to vortex shedding, St_{sat}, does not change

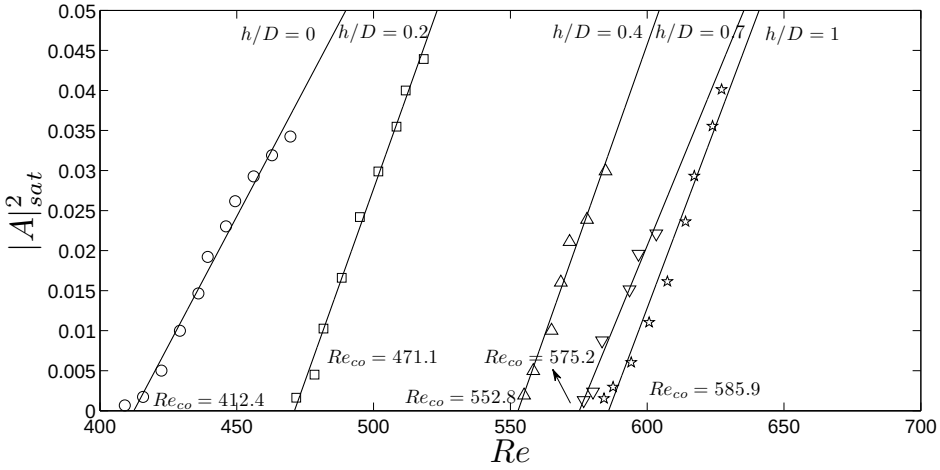

Figure 3.19: Energy of the streamwise velocity fluctuations, w'^2_{fc}, versus the Reynolds number, obtained experimentally, at (r = 0, z = 3) for cavities of diameter $D_c/D = 0.86$ and different lengths, $h/D = 0$, 0.2, 0.4, 0.7 and 1.0. Included in [126].

with variations in cavity length.

To determine the critical value of the Reynolds number, Re_{co}, we examined the evolution of the squared amplitude of the streamwise velocity fluctuations as a function of the Reynolds number, $|A|^2_{sat}(Re)$, obtaining the squared amplitude by integrating the dominant peak at the spectra (see Eq.2.6). The linear increase of $|A|^2_{sat}$ with the Reynolds number near the critical value indicates that the transition to the oscillatory regime corresponds to a Hopf bifurcation [133]. The critical value of the Reynolds number was determined from a linear regression of the experimental measurements of $|A|^2_{sat}$ near criticality, following Eq.(1.18). Figure 3.19 displays the dependence of the energy of the velocity fluctuations, $|A|^2_{sat}$, at $(r = 0, z = 3)$ on the Reynolds number near the critical point, for cavities of different lengths, $h/D = 0$, 0.2, 0.4, 0.7 and 1.0. The figure shows that critical Reynolds number, Re_{co}, increases with the cavity length, h/D, corroborating the earlier observations on the stabilizing effects of the cavity.

Figure 3.20 summarizes the effect of the cavity length on the values of the critical Reynolds numbers corresponding to the oscillatory mode obtained experimentally (solid circles) and from three-dimensional simulations (solid triangles). Because of the considerable computational expense, a smaller number of Reynolds number cases was examined at only four cavity lengths ($h/D = 0$, 0.2, 0.7, 1.0) for the three-dimensional simulations. As a result, the oscillatory bifurcation is not determined as accurately as for the experiments. In Fig. 3.20, we show an upper limit at which the flow is always unstable (oscillating) and a lower limit where the flow is always stable (steady), obtained from the numerical simulations, so that the critical Reynolds number corresponding to the oscillatory bifurcation, Re_{co}, is bounded by these limits. As for the steady mode case, Re_{co} exhibits an asymptotic behavior for $h/D \gtrsim 0.7$. The critical Reynolds number, Re_{co}, in the numerical case (solid triangles), is increased from 413 to an asymptotic value inside the range $650 < Re < 680$, which represents an important stability increase of greater than 60%. In the experimental case (solid circles), this asymptotic value is about $Re \approx 580$. The small differences between the experimental and the numerical results are most likely associated with small misalignments between

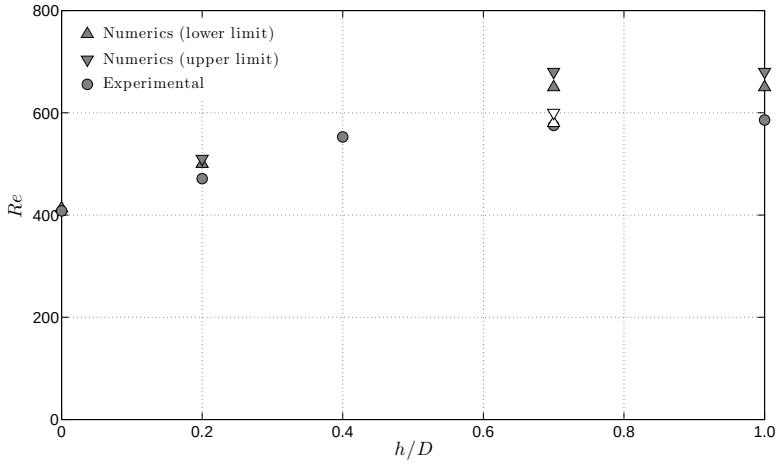

Figure 3.20: Effect of the length of a cavity with $D_c/D = 0.86$ on the critical Reynolds number corresponding to the oscillatory bifurcation, Re_{co}, obtained experimentally and from three-dimensional numerical simulations. Here $\triangledown$ and $\triangle$ correspond to the upper and lower limits obtained numerically for a cavity of $h/D = 0.7$ considering a body misaligned 1° with the free-stream. Included in [126].

the body and the free-stream in the experimental measurements. To show this, we performed a three-dimensional simulation for a cavity of $h/D = 0.7$ considering a body misaligned 1° with respect to the free-stream. The results obtained are shown by the open symbols in Fig. 3.20, again including the upper and lower limits. Notice that the numerical range has changed from, $650 < Re < 680$, to, $580 < Re < 600$, decreasing the differences between the experimental and the numerical results from about 14% to only 2.5%.

3.5 Conclusion

Throughout the present chapter, we have analyzed the influence on the stability properties of the wake behind the $\ell = 2$ body of two different passive control methods, i.e. base bleed (homogeneous and light) and rear cavities, by using different techniques (BiGlobal stability analysis, HWA experiments and three-dimensional numerical simulations). Both control methods have been proven as efficient wake control strategies.

Specifically, base bleed has been found to stabilize the wake in the range of Reynolds numbers considered in this work. More specifically, the parameter plane (Re, C_b), spanned by the Reynolds number and the bleed coefficient, defined here as the bleed to ambient velocity ratio, can be divided into three different regions, as shown in Fig. 3.8 for the particular case of a body with $\ell = 2$. In region I, where $C_b > C^*_{b1}(Re)$, the wake is steady and axisymmetric, and thus completely restabilized due to the effect of base bleed. In region II, defined by $C^*_{b2}(Re) < C_b < C^*_{b1}(Re)$, the wake is steady and planar-symmetric, with a structure similar to that found for $Re_{cs} < Re < Re_{co}$ in the case without base bleed, $C_b = 0$. Finally, in region III, in which $C_b < C^*_{b2}(Re)$, periodic shedding of vortices takes place due to the excitation of the oscillatory mode. The BiGlobal stability analysis predicts that the critical bleed coefficients tend to asymptotic values $C^*_{b1} \to 0.125$ and $C^*_{b2} \to 0.115$ for $Re \gtrsim 2000$. The experiments performed in the case with base bleed show good

agreement with numerical simulations results reported in Bohorquez *et al.* [15], giving similar values of $C^*_{b2}(Re)$ in the range of Reynolds numbers considered, $Re \lesssim 800$. It should be noted that the critical curve $C^*_{b1}(Re)$, which can be precisely predicted by means of a BiGlobal stability analysis with an axisymmetric base flow, is enough to ensure a completely destabilized wake for $C_b > C^*_{b1}(Re)$ in the range of Reynolds numbers reported here. Moreover, its computational cost is much smaller than the fully three-dimensional numerical simulations that would be alternatively needed. Let us finally emphasize that the shear layer separating from the body will induce the transition to turbulence in the wake for sufficiently large values of the Reynolds number, a regime which should be addressed in detail in a future work. To end with the base bleed, initial experimental measurements of light base bleed, by using Helium as an injected gas, have shown qualitative discrepancies with respect to previous works [136], since varying the base density apparently does not change the value of the critical coefficient C^*_{b2}. Further numerical simulations and BiGlobal stability analysis will be carried out in order to shed a bit of light on the encountered differences.

On the other hand, as far as the rear cavities are concerned, we have shown that the addition of a cavity at the base of the $\ell = 2$ body, of length h and inner diameter D_c, improves the stability of the wake and decreases the drag coefficient. In particular, we have reported results obtained from linear stability theory, three-dimensional simulations and experiments. In this sense, we have first analyzed the influence of the cavity dimensions on the critical Reynolds number, Re_{cs}, corresponding to the first, steady bifurcation. To show the effect of the cavity length h/D on the critical Reynolds number reported above, we have performed BiGlobal linear stability analyses with a new version of a finite differences code described in Appendix A, varying h/D from 0 to 1.0, and have shown that Re_{cs} exhibits an asymptotic behavior for $h/D \gtrsim 0.7$. The cavity length, $h/D \approx 0.7$, can thus be considered as a critical cavity length, beyond which no significant change in Re_{cs} is observed. The critical Reynolds number increases from Re_{cs}= 326.2 for a solid body to Re_{cs}= 512 for a body with a cavity of length h/D= 0.7, which represents an important stability increase of about 57%. In addition, we have also performed three-dimensional numerical simulations with the aim of validating the global linear stability analyses. The relative errors between the global stability and the numerical results are lower than 2.5% in the worst case. Similarly, we have studied the effect of the cavity diameter D_c/D on the critical Reynolds number, Re_{cs}. Basically, no effect on Re_{cs} has been observed for the range $0 \leqslant D_c/D \lesssim 0.6$, however, a monotonic increase in Re_{cs} has been found in the range $0.6 \lesssim D_c/D \leqslant 0.99$. In addition to describing the effect of the base cavity on Re_{cs}, we performed steady numerical simulations at $Re \leqslant 400$ to determine the effect of the cavity dimensions on the drag coefficient, C_d. Our simulations indicated that, although an improvement of 10% to 15% can be achieved in the pressure drag coefficient, C_d^p, for bodies with a base cavity, the total drag reduction is, at best, approximately 1%. The low value is due to the fact that the improvement in the pressure drag coefficient, C_d^P, achieved by addition of the cavity, is balanced by an increase in the viscous drag coefficient, C_d^v, associated with increased viscous forces acting on the the inner wall of the cavity. Nevertheless, the relative importance of the viscous contribution is expected to decrease at higher Reynolds numbers and, thus, substantial drag reductions should be achieved.

Concerning the second-oscillatory bifurcation, three-dimensional numerical simulations have been performed to determine the effect of the cavity length on the critical oscillatory Reynolds number, Re_{co}, with comparison to the experimental measurements carried out using hot-wire anemometry in a wind tunnel. As in the case of the steady bifurcation, both experimental and

numerical results exhibit an asymptotic value for $h/D \geqslant 0.7$.

To conclude, we have demonstrated that a cavity placed at the base of an axisymmetric slender body has beneficial effects on both wake stability and drag reduction, showing an asymptotic behavior at cavity lengths $h/D > 0.7$. Our study has been limited to Reynolds numbers below $Re = 700$ due to the high computational cost of the three-dimensional simulations in our facilities. Thus, both a more complete experimental study and three-dimensional direct numerical simulations are needed to examine the behavior of the drag coefficient with varying the cavity dimensions and body lengths and at higher Reynolds numbers.

CHAPTER

FOUR

Wake control through passive methods (II): body rotation

This chapter is intended to analyze the wake of a spinning bullet-shaped body of length-to-diameter ratio $\ell = 2$, by means of three-dimensional numerical simulations and BiGlobal stability analysis. It focuses on the evolution of the forces, flow regimes and modes that appear depending on the values of the two governing parameters, namely the Reynolds number, Re, and the dimensionless angular velocity, $\Omega = \omega D/(2\,w_\infty)$, where ω is the angular velocity of the body, which were varied in the ranges $Re < 450$ and $0 \leq \Omega \leq 1$. It is shown that the (Re, Ω) parameter plane can be divided into five regions, corresponding to the destabilization of several instability modes. In the range $0 \leq \Omega \lesssim 0.2$, three different flow regimes take place as Re increases keeping constant Ω: axisymmetric regime; *frozen* regime, emerging at $Re = Re_{c1}(\Omega)$, where axially-elongated structures co-rotate with the body with a different angular velocity; and *spiral flow* regime, bifurcating at $Re = Re_{c2}(\Omega)$, that leads to a swirling configuration of vortices curling up around the axis, caused by a combination of the frozen mode and the vortex shedding. However, at $\Omega \simeq 0.2$, a new *frozen spiral mode* takes place for large enough values of Re, where two counter-rotating vortices spiral around the axis, as a result of a lock-in process of the vortex shedding associated to the unsteady spiral regime, being this mode the single unstable mode found numerically for $0.225 \leq \Omega \leq 0.4$. These results are in good agreement with those of the GLS, that show how for $\Omega < 0.25$ a linear eigenmode with azimuthal number $m = -1$ becomes unstable at a critical value of $Re = Re_{c1}$ that increases with Ω, leading to the low-frequency *frozen state*. In the range $0.25 \leq \Omega < 0.52$ a different eigenmode with $m = -1$ becomes unstable at $Re = Re_{c3}$, explaining the high-frequency *frozen spiral* wake. However, for $\Omega \geq 0.52$ and low values of Re, the wake is destabilized by a third $m = -1$ oscillatory mode of intermediate frequency, that becomes dominant at higher Ω, and it is characterized again by a *frozen spiral* state according to the three-dimensional simulations.

The text of this chapter, in part, is a reprint of the material as it appears in the papers: (1) "Laminar flow past a spinning bullet-shaped body at moderate angular velocities", by J. I. Jiménez-González, E. Sanmiguel-Rojas, A. Sevilla and C. Martínez-Bazán, accepted for publication in the Journal of Fluids and Structures [58]; and (2) "Global modes of the wake behind a spinning bullet-shaped body", by J. I. Jiménez-González, A. Sevilla, E. Sanmiguel-Rojas and C. Martínez-Bazán, submitted for publication in Physics of Fluids [59].

4.1 Introduction

In Chapter 2 it was discussed how the unstable regimes of the wake behind a bullet-shaped body at low Re, namely, the SS and RSP modes, affect the hydrodynamics forces acting on the body, whose consequences were outlined in Chapter 3. The complex phenomenology occurring justifies the broad work existing in the literature regarding control mechanisms for afterbodies, and, within this frame, two passive methods were presented in Chapter 3, proving their efficiency to stabilize the unstable wake. Following this idea, and due to their potential practical applications, it is interesting to explore new ways of stabilizing the wake by means of alternative forcing mechanisms, aimed at recovering the axisymmetry of the flow under proper conditions. The latter idea is linked to modifications of the stability properties of the flow while leading to different flow patterns, so that investigating the effect of body rotation on the flow transitions can be an appealing approach. In addition, a submerged body in an axial flow with streamwise rotation is a relevant configuration in engineering applications such as projectile flight, where spin acts as a stabilizing mechanism, or in turbomachinery. It must be emphasized that, in these particular applications, the Reynolds number is usually very large and the corresponding flows are thus turbulent, in contrast with the laminar flows studied in the present work. However, in recent years there has been an increasing interest in the development of microscale systems, for which our results could be of direct applicability. In particular, many biologically-inspired microscale robotic systems, with potential applications in diagnostics and therapeutics, use propulsion systems based on rotating slender bodies like helical filaments [111]. Moreover, many promising designs of combustion-based micro-power-generation devices consist of a cylindrical bluff-body spinning inside a coaxial micro-channel, where the flow is in the laminar regime [154]. Clearly, a detailed characterization of the onset of instability in the flow around spinning blunt-based bodies will be helpful in developing efficient designs for such microrobots and micro-combustors.

Despite of the interest of the applications, the works dealing with the regimes of the wake behind spinning bodies are scarce, and they are mostly devoted to high transitional Reynolds numbers. Thus, the transition to turbulence in the high-Reynolds-number boundary layer flow around a sphere rotating in the streamwise direction has been the focus of many experimental and analytical studies over the past century. Luthander & Rydberg [83] determined experimentally that the critical Reynolds number associated to the transition to a turbulent boundary layer depends strongly on the rotation parameter, Ω. In particular, the separation point moves towards the equator due to the adverse pressure gradient induced by the spin [128, 52]. These facts were later confirmed by Kobayashi *et al.* [67], among others. Regarding spinning afterbodies or bullet-shaped bodies, only a few studies can be found in the literature. In particular, using boundary-layer theory, Schlichting [128] studied the laminar flow around an axisymmetric Rankine half-body, finding that spin stabilizes the boundary layer due to the favorable pressure gradient induced by body rotation.

In the laminar regimes, similar studies have been performed in the case of rotating spheres to model the flow of particles or droplets with rotation, that appear in many engineering applications. Thus, several researchers have investigated the effect of transverse rotation of the sphere on its wake stability properties and on the hydrodynamic forces [122, 107, 12, 70]. Moreover, Kim & Choi [64] studied numerically the flow around a spinning sphere for $Re \leq 300$ and $0 \leq \Omega \leq 1$. They observed that, at a fixed value of $Re = 250$ and for small enough values of Ω, the wake structures rotate about the axis at a constant angular velocity different from that of the sphere. Consequently,

they referred to this behavior as a *frozen wake* because the vortical structures maintain their shape and strength while swirling around the axis. Interestingly, a frozen wake implies a constant lift force, since the two components of the lift vector oscillate with constant amplitude, but with a phase shift of one quarter of the total period [116]. For values of Re above the second bifurcation for the stationary sphere ($Re \approx 272$, see for instance [42]), Kim & Choi [64] showed that, for several specific values of Ω, the streamwise rotation may also lead to frozen states. However, prior to reaching this state, the wake undergoes a complex rearrangement process, as described by Pregnalato *et al.* [118]. All these structures were also found by Niazmand & Renksizbulut [104], who showed that streamwise rotation promotes flow separation and transition to unsteady regimes in the wake. Furthermore, they showed that, as Ω increases, the separation point moves upstream, leading to an enlargement of the recirculation region, and an associated increase in the drag force. Lately, Pier [113] has shed light on the issue, describing the different modes appearing at the wake of a spinning sphere in the range of rotation parameters $0 \leq \Omega \leq 1$.

Regarding stability analysis and unstable modes, Pier [113] performed a linear stability analysis showing that the first non-axisymmetric azimuthal Fourier component was responsible for the onset of instability at the wake of a spinning sphere, leading to the co-rotating frozen flow. These results resemble others reported in the literature of swirling flows. For instance, it is well known that vortex breakdown occurs as a consequence of the destabilization of an unstable global mode of azimuthal number $m = 1$ (for ansatzs of perturbations in the form $\exp i[m\theta - \sigma t]$), characterized by a co-rotating wave, see e.g. [41, 105]. Similarly, Khorrami [62] found viscous long-wave $m = 1$ co-rotating instabilities with a temporal stability analysis of the Batchelor's vortex, for moderate Re and swirl parameter values. However, the subject concerning modes at the wake of spinning bodies has to be still thoroughly addressed to understand the underlying nature and its similarities and differences with other swirling flows.

That said, apart from the sphere, very little attention has been paid in the past to the laminar flow around other axisymmetric spinning bodies. Therefore, the main objective of this chapter is to present a detailed numerical study and BiGlobal stability analysis of the effect of streamwise rotation on the flow transitions, hydrodynamic forces acting and unstable modes on a spinning $\ell = 2$ bullet-shaped body, considering moderate Reynolds numbers and rotation parameters, in the ranges $Re \leq 440$, and $0 \leq \Omega \leq 1$, respectively. We describe briefly the problem and techniques in Section 4.2. Next, the different unstable regimes found through the three-dimensional simulations, are described by means of their topology and hydrodynamical forces in Section 4.3. Unstable global linear modes giving rise to the different wake states are presented in Section 4.4. Finally, main conclusions are outlined in Section 4.5.

4.2 Problem definition and techniques

4.2.1 Problem definition

The flow configuration is illustrated in Fig.1.1, and consists of a bullet-like body of length-to-diameter ratio $\ell = 2$, aligned with the free stream, that rotates along the streamwise direction with a constant angular velocity, ω. Two non-dimensional parameters characterize the flow, namely the Reynolds number, $Re = \rho w_\infty D/\mu$, and the rotation parameter, $\Omega = \omega D/2w_\infty$, defined as the ratio between the azimuthal velocity at the surface of the body and the free stream velocity. However, the

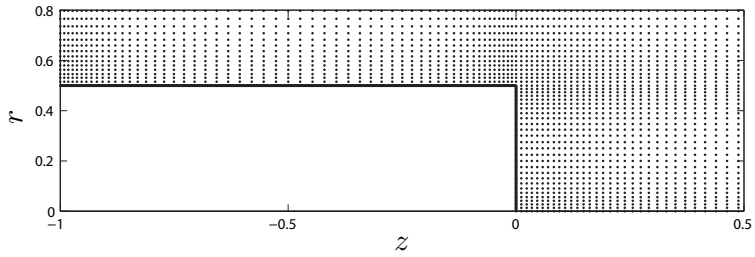

Figure 4.1: Detail of the axisymmetric GLS computational domain, for a spinning $\ell = 2$ body.

investigation presented in this chapter is limited to laminar flows and moderate angular rotation, i.e. $Re < 450$ and $0 < Re \leq 1$.

4.2.2 BiGlobal Linear Stability analysis

The GLS analysis was performed by means of the finite difference code introduced in Chapter 2 for wakes behind bodies with cavities, and that is widely detailed in Appendix A. Thus, the first step was the computation of the base flow (Eqs.1.4 and 1.5) with ANSYS Fluent®, that gives rise to a base flow with swirl velocity component, $\mathbf{U}(\mathbf{x}) = [U(r,z), V(r,z), W(r,z)]$ and $P(r,z)$. Next, the linear operators of the EVP (Eq.1.10) were discretized into a computational grid (see Appendix A for details), whose size was determined by means of the convergence study presented below. Figure 4.1 shows a detail of the grid used to solve the EVP problem, where it is possible to observe how the nodes are clustered around the wall and edge of the body to resolve properly the gradients of flow variables. Once the discretization was done, the discrete generalized EVP (Eq.A.7) was transformed into a standard one, by means of the shift-and-invert strategy, and solved with the Arnoldi algorithm, with 80 iterations.

As said, a convergence study was performed to check the accuracy of results and to select the optimal grid size. Table 4.1 shows the values of the two leading eigenvalues found for $Re = 350$ and $\Omega = 0.5$, using four different grids, together with the associated computational time. The grid resolution was successively increased by a factor of $\sqrt{1.3}$ in each coordinate between consecutive grids, such that the number of nodes increased by a factor of approximately 1.3. The column corresponding to $\epsilon_{j,j+1}(\%)$ shows the relative errors obtained between two consecutive grids for the growth rate of the next-to-leading eigenmode, $\Re[\sigma_2]$, since this magnitude has the largest associated error for all grids, when compared to $\Im[\sigma_{1,2}]$ or $\Re[\sigma_1]$. From the results of Table 4.1 it can be deduced that the relative differences between the results obtained with grids #1 and #2 are very small as far as real and imaginary parts of the eigenvalues are concerned, being the maximum relative error of 0.12%. The latter reason, together with the fact that the computational time associated to grid #1 is almost twice as large as that associated to grid #2, motivated our selection of grid #2 in all the calculations reported hereafter.

The GLS analysis was carried out for $0 < \Omega \leq 1$ and $150 < Re < 430$, in order to characterize the first transitions from the axisymmetric state towards different unstable regimes and to obtain their corresponding critical Reynolds number. The overestimation of Re_{co} for the body without rotation ($\Omega = 0$) with the GLS analysis, precluded us from studying any further transitions once the flow had bifurcated from the axisymmetry, since the assumption of steady axisymmetric base flow would not be realistic. However, this kind of study was performed by means of three-dimensional

Grid	n_g	σ_1	σ_2	$\epsilon_{j,j+1}(\%)$	$t_{\mathrm{EVP}}(s)$
1	83000	$-0.02054 + 0.69332\,i$	$-0.04280 + 0.95797\,i$	0.12	18900
2	63900	$-0.02052 + 0.69251\,i$	$-0.04275 + 0.95836\,i$	7.27	9900
3	49200	$-0.02057 + 0.69553\,i$	$-0.04586 + 0.95955\,i$	4.60	5800
4	38000	$-0.02146 + 0.69713\,i$	$-0.04797 + 0.95949\,i$	-	3600

Table 4.1: Grid convergence study based on the two leading eigenvalues, σ_1 and σ_2 respectively, found for $\Omega = 0.5$ and $Re = 350$, for several meshes of size ratio $n_{g(j+1)} \simeq n_{g(j)} \times 1.3$. Also shown are the maximum relative error, $\epsilon_{j,j+1}(\%) = \{\Re[\sigma_2(j)] - \Re[\sigma_2(j+1)]\}/\Re[\sigma_2(j)] \times 100$, and the computational time needed to solve the EVP, $t_{\mathrm{EVP}}(s)$.

	Mesh #1	Mesh #2	Mesh #3	n	$\mathrm{GCI}_{3,2}(\%)$	$\mathrm{GCI}_{2,1}(\%)$
$v(r = 0.5, \theta, z = 1)$	0.18251	0.18213	0.18156	1.755	1.877	1.503
$w(r = 0.5, \theta, z = 5)$	0.79453	0.79642	0.79927	1.777	2.113	1.404

Table 4.2: Order of the method, n, and grid convergence index, $\mathrm{GCI}_{j+1,j}$, defined in Eq.(3.3), obtained using the azimuthal velocity, v, and the axial velocity, w, at two different points. The simulations were performed at $Re = 350$ and $\Omega = 0.5$.

numerical simulations.

4.2.3 Numerical techniques

Three-dimensional numerical simulations were performed with OpenFOAM®, aiming at describing the flow topology and regimes at the wake of the same spinning $\ell = 2$ body, for $0 < \Omega \leq 0.6$ and $Re < 440$. The computational domain and numerical schemes used were detailed in Chapter 2, and the size of the mesh was selected based on the convergence index study described in Section 3.2.4. The meshes showed in Table 3.2, without rear cavity in this case, were tested also when rotation was applied, and, specifically, at $Re = 350$ and $\Omega = 0.5$, which corresponds to an axisymmetric steady flow as it will be shown later. Thus, Table 4.2 displays the values of $v(r = 0.5, \theta, z = 1)$ and $w(r = 0.5, \theta, z = 5)$ obtained for the three meshes, that provided with an estimation of the discretization order, defined in Eq.(3.2), of $n \simeq 1.755$ and $n \simeq 1.777$, respectively. Note that these values of n are very close to those obtained without rotation in Table 3.2, so that swirl does not affect the performance of the tested meshes. Furthermore, the grid convergence indexes (see Eq.3.3) $GCI_{2,1}$ and $GCI_{3,2}$ were again small (close to a grid independent solution), and similar, so that, using the same argument of compromise between accuracy and time consumption, commented in Section 3.2.4, we performed all the simulations for a spinning body with the medium size mesh.

On the other hand, to provide further validation of the size of the computational domain and the numerical schemes implemented when spin is applied to the body, a comparison with reference data was done. To that end, several simulations of the flow around a sphere spinning in the streamwise direction were carried out, at $\Omega = 0.1$ and different values of Re. In particular, the outcome of our simulations at $Re = 250$ corresponded to the *frozen state* reported by Kim & Choi [64], among others. Indeed, as shown in Fig. 4.2, the values of the drag and lift coefficients, represented with dash-dotted and solid lines, respectively, remain constant, while the lift vector

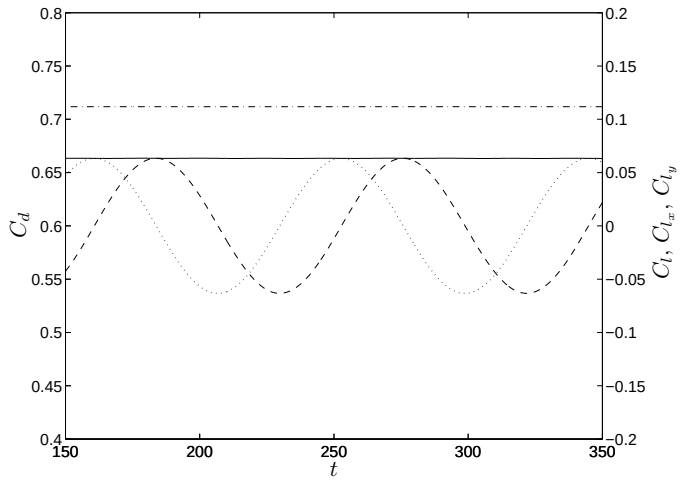

Figure 4.2: Temporal evolution of the drag and lift coefficients for a sphere at $Re = 250$ and $\Omega = 0.1$. Included in [58].

rotates with a constant angular velocity, as revealed by the fact that the C_{l_y} and C_{l_x} coefficients are $\pi/2$ out of phase. Table 4.3 shows a comparison among the values of the drag coefficient obtained from our computations and those reported by Kim & Choi [64] and Poon *et al.* [116]. Furthermore, in order to investigate the possible numerical diffusion introduced by the total variation diminishing scheme [78], we performed simulations using a linear interpolation scheme (CD) of second-order accuracy for the convective term. Note that, at $Re = 250$, the solution did not show spurious numerical oscillations with the CD scheme. Table 4.3 shows that the relative error introduced by a Van Leer limiter (VL) is almost negligible when compared with a CD scheme, and is also very small with respect to the spectral method results of Poon *et al.* [116]. Therefore, it is clear that the second-order-accurate total variation diminishing scheme used in the remainder of this work is appropriate to study the physics of the wake behind a spinning body.

4.3 Flow regimes and dynamics of the wake behind a spinning $\ell = 2$ body.

This section is devoted to present the numerical results obtained, focusing on the effect of moderate rotation on the dynamics of the wake behind the body. In particular, we will discuss the different nonlinear regimes established depending on the values of Re and Ω, for a body with a length-to-diameter ratio $\ell = 2$. An analysis of the dependence of the force coefficients on Re and Ω will also be addressed.

To this end, we performed numerical simulations in the ranges $320 \leq Re \leq 440$ and $0 < \Omega \leq 0.4$, increasing the Reynolds number in steps of $\Delta Re = 10$ for each value of Ω, thus allowing us to characterize the (Ω, Re) parameter plane in detail, including the bifurcations taking place therein, which are studied in terms of the Stuart-Landau model, what required the study of the transition boundaries with smaller increments of Re.

	C_d	ϵ_{C_d} (%)
Kim & Choi [64]	0.7030	-
Poon *et al.* [116]	0.7047	-
Present (VL)	0.7103	0.7946
Present (CD)	0.7064	0.2412

Table 4.3: Drag coefficient, C_d, of a sphere rotating in the streamwise direction at $Re = 250$ and $\Omega = 0.1$, obtained by other authors and in this Thesis, by using a Van Leer limiter (VL), as well as a linear interpolation scheme (CD) for the convective term. The error, $\epsilon_{C_{d_i}} = |C_{d_i} - C_{d_{ref}}|/C_{d_{ref}} \times 100$, was calculated using the results reported by Poon *et al.* [116] as reference.

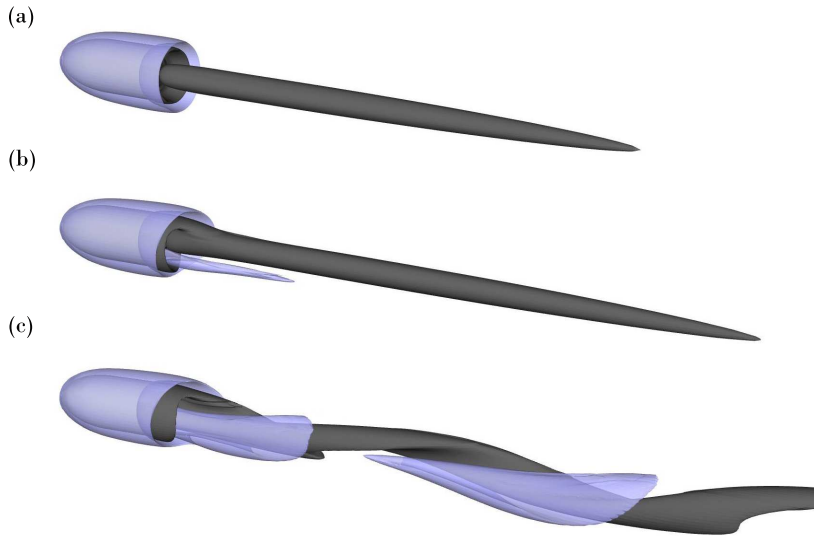

Figure 4.3: Wake structures visualized by contours of constant streamwise vorticity, $\varpi_z = 0.2$ (dark-coloured contour) and $\varpi_z = -0.2$ (light-coloured contour), for a spinning body of aspect ratio $\ell = 2$ and $\Omega = 0.1$ at (a) $Re = 330$, (b) $Re = 370$ and (c) $Re = 430$. Included in [58].

4.3.1 Flow characteristics at $\Omega = 0.1$ and increasing values of *Re*

The numerical simulations for the spinning body revealed that rotation affects the dynamics of the wake, and modifies the transitions described in Chapter 2 for $\Omega = 0$. As depicted in Fig. 4.3(a), for a relatively low value of $\Omega = 0.1$, the wake is steady and axisymmetric at $Re = 330$, a Reynolds number for which the flow is no longer axisymmetric in the case without rotation. However, at $Re \simeq 340$, a new flow regime, similar to the SS mode occurring in the non-rotating body, takes place. As revealed by Fig. 4.3(b), the two counter rotating axial vortices have different shapes and intensities, so that the planar symmetry is no longer preserved. This mode resembles the *frozen state* found by Kim & Choi [64] in the wake of a sphere rotating in the streamwise direction. Indeed, the wake structures co-rotate around the axis along with the spinning body, but with a different angular velocity, $\Omega_{sl} \neq \Omega$, and without change in shape or intensity, as illustrated in Fig. 4.4. Thus, the wake flow is steady when analyzed from a relative reference frame that rotates

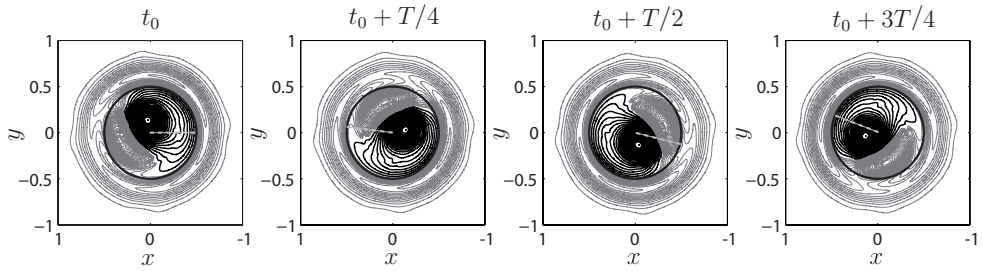

Figure 4.4: Temporal evolution of streamwise vorticity contours at $z = 1$ during a period of revolution $T = 2\pi/\Omega_{sl}$ (dark contours are positive values while light contours represent negative values). Notice that, as the solid body, the fluid structures rotate in the positive z direction, although with a rotation velocity, Ω_{sl}, different from that of the body, Ω. In this figure the base of the body is shown with a thick line, and a dashed line has been included to identify the body rotation. Included in [58].

with the angular velocity of the vortical structures, Ω_{sl}.

As can be seen in Fig. 4.3(b) for $Re = 370$, the solid-body rotation of the body base feeds the thread of positive streamwise vorticity, $\varpi_z = 0.2$ (dark contour), whereas the streamwise thread with negative axial vorticity, $\varpi_z = -0.2$ (light contour), is much weaker, and localized near the body. The resulting wake structures are then a combination of the production of streamwise vorticity in the natural wake, due to the tilting of azimuthal vorticity at the edge of the body (see [148] for a detailed discussion in the case of the sphere wake), and the injection of vorticity by means of rotation. As will be seen below, the competition of both mechanisms determines the different wake states found for increasing values of Ω. An interesting feature of the flow around the spinning body, that is absent in the non-rotating case, is the existence of negative streamwise vorticity associated to the swirling boundary layer, as revealed by the light contour surrounding the body in Fig. 4.3. By comparing the flow at $Re = 330$ (Fig. 4.3a), and that at $Re = 370$ (Fig. 4.3b), it is clear that, close to the first bifurcation, the effect of rotation is to inhibit the thread of negative axial vorticity, thus stabilizing the axisymmetric state. Therefore, body rotation stabilizes the first unstable mode, and increases the critical Reynolds number associated to the first bifurcation, denoted here Re_{c1}, so that $Re_{c1}(\Omega)$ is an increasing function of Ω (see also Fig. 4.19). Notice that Re_{c1} at $\Omega = 0$ corresponds with Re_{cs} in Chapter 2.

For a constant value of $\Omega = 0.1$, the frozen mode prevails for values of the Reynolds number up to approximately $Re = 410$. However, as shown in Fig. 4.3(c), at $Re \simeq 420$ a second bifurcation takes place, the frozen wake being substituted by an *unsteady spiral wake*, similar to that described by Pier [113] in the case of a sphere. This new mode is characterized by the axial rotation of the dominant thread with positive ϖ_z, while vortices with negative ϖ_z are shed from the base of the body. Note that this new regime is analogous to the Reflectional Symmetry Preserving (RSP) mode for the static body, but without the corresponding planar symmetry, as demonstrated below by analyzing the modal frequencies.

To properly characterize the instability modes, it proves convenient to examine the temporal evolution of the hydrodynamic forces, evaluating the effect of body rotation on the lift and drag coefficients, C_l and C_d respectively, defined in Eqs. (2.4) and (2.5).

As mentioned above, after the first bifurcation leading to a non-axisymmetric frozen state,

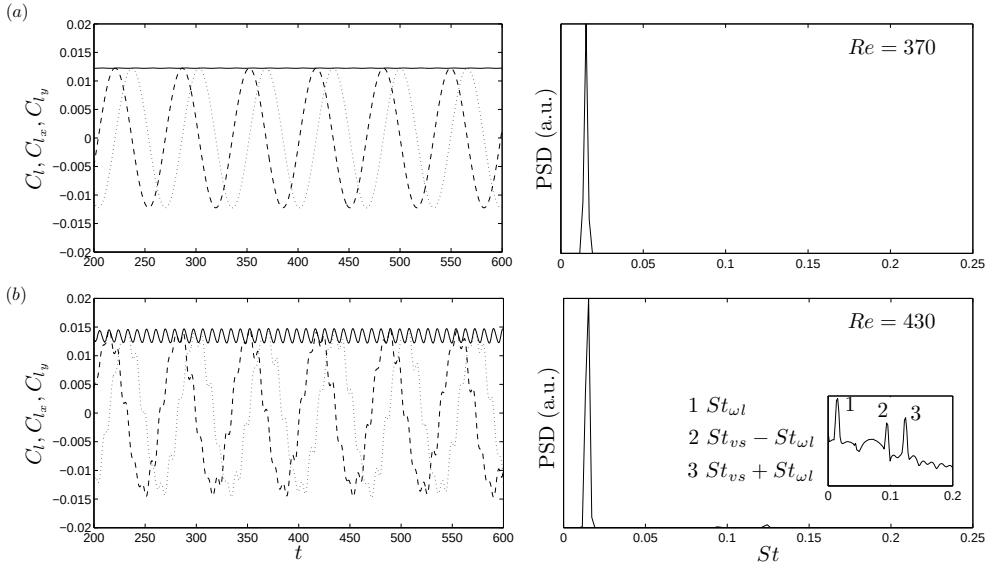

Figure 4.5: Left column: Time series of C_l (solid line), C_{l_x} (dashed line) and C_{l_y} (dotted line), for a rotating body of aspect ratio $\ell = 2$ and $\Omega = 0.1$ at (a) $Re = 370$ and (b) $Re = 430$. Right column: Power Spectral Density associated to C_{l_x}. The inset displays a zoom of the spectrum at $Re = 430$, in semi-logarithm scale, showing the presence of three characteristic frequencies, namely $St_{\omega l}$ and $St_{\rm vs} \pm St_{\omega l}$. Included in [58].

at $Re > Re_{c1}$, the wake performs a rigid-body rotation around the symmetry axis, resulting in constant values of C_d and C_l. This feature of the frozen state is illustrated in Fig. 4.5(a), where it can observed that the two components of the lift coefficient in the x and y coordinates, C_{l_x} and C_{l_y} respectively, oscillate with the same frequency, but with a phase shift equal to $T/4$, where $T = 2\pi/\Omega_{sl}$ is the period of revolution of the vortical structures, since they are purely monochromatic sine and cosine shapes. Consequently, the magnitude of the lift, $C_l = \sqrt{C_{l_x}^2(t) + C_{l_y}^2(t)}$, remains constant in this regime. When viewed from the inertial frame, depicted in Fig. 1.1, each quarter of period the lift vector is subsequently aligned either with the x-axis or with the y-axis, giving rise to oscillating signals for both lift components with zero mean, $\overline{C}_{l_y} = \overline{C}_{l_x} = 0$, and period equal to T, so that the angular velocity of the frozen structures is $\Omega_{sl} = 2\pi\, St_{\omega l}$. Here, the Strouhal number associated to the rigid-body rotation of the wake as a whole, $St_{\omega l}$, is easily obtained from a spectral analysis of either of the lift components, C_{l_x} or C_{l_y}. Indeed, as shown in Fig. 4.5(a), the wake at $Re = 370$ is characterized by a spectrum with a single peak given by the spin of the wake. The subscript l associated to $St_{\omega l}$ stands for *low frequency*, and has been introduced at this point for convenience, since it will be shown below that a different *high frequency* frozen regime exists for higher values of Ω.

It will prove useful to consider a relative reference frame S', rotating with an angular velocity Ω_{sl} with respect to the inertial frame. The components of the lift coefficient in the rotating frame,

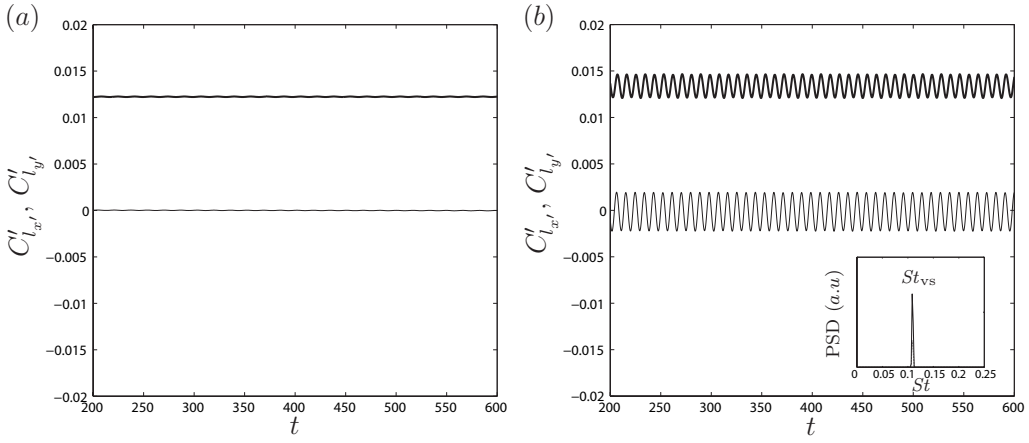

Figure 4.6: Time series of the lift components $C'_{l_{x'}}$ (solid line) and $C'_{l_{y'}}$ (dotted line) in the frame of reference S', that rotates with an angular velocity Ω_{sl}, for (a) $Re = 370$ and (b) $Re = 430$. The inset in Fig. 4.6(b) displays the Power Spectral Density of $C'_{l_{x'}}$ and $C'_{l_{y'}}$, showing the characteristic vortex shedding frequency, $St_{\rm vs}$. Included in [58].

	$Re = 340$	$Re = 370$	$Re = 410$	$Re = 420$	$Re = 430$	$Re = 440$
$St_{\omega l}$	0.0153	0.0153	0.0154	0.0154	0.0155	0.0155
$St_{\rm vs}$	-	-	-	0.1081	0.1085	0.1109
$St_0^{\rm DNS}$	-	-	-	0.1247	0.1268	0.1284
$St_0^{\rm EXP}$	-	-	-	0.1231	0.1232	0.1260

Table 4.4: Values of characteristic Strouhal numbers for $\Omega = 0.1$ at different Re, for the frequency associated to the wake rotation, $St_{\omega l}$, and the spiral vortex shedding frequency, $St_{\rm vs}$. Also included are the values of the vortex shedding Strouhal numbers obtained numerically, $St_0^{\rm DNS}$, and experimentally, $St_0^{\rm EXP}$, reported in Chapter 2 for a non-rotating body.

$C'_{l_{x'}}$ and $C'_{l_{y'}}$, can be obtained through the transformations,

$$C'_{l_{x'}} = C_{l_x}\cos(\Omega_{sl}t + \phi) + C_{l_y}\sin(\Omega_{sl}t + \phi), \tag{4.1}$$

$$C'_{l_{y'}} = -C_{l_x}\sin(\Omega_{sl}t + \phi) + C_{l_y}\cos(\Omega_{sl}t + \phi), \tag{4.2}$$

where ϕ is an arbitrary initial phase. The time evolutions of $C'_{l_{x'}}$ and $C'_{l_{y'}}$ are plotted in Figs. 4.6(a)-(b) for $Re = 370$ and 430 respectively, showing that, since the frozen mode is steady in the reference system S', both components are constant at $Re = 370$. Thus, this mode is equivalent to the SS mode for the non-rotating body, inducing a lift force whose direction and magnitude remain constant in the rotating frame S'.

On the other hand, in the unsteady spiral mode, shown in Fig. 4.3(c) for the particular case of $Re = 430$, and occurring when the Reynolds number is larger than a second critical value, $Re > Re_{c2}$, the flow is characterized by oscillating values of $C_l(t)$ and $C_d(t)$ at the same frequency, $St_{\rm vs}$, due to the vortex shedding phenomenon illustrated in Fig. 4.5(b). Consequently, at this Reynolds number, the power spectral densities associated to $C_{l_x}(t)$ and $C_{l_y}(t)$, exhibit

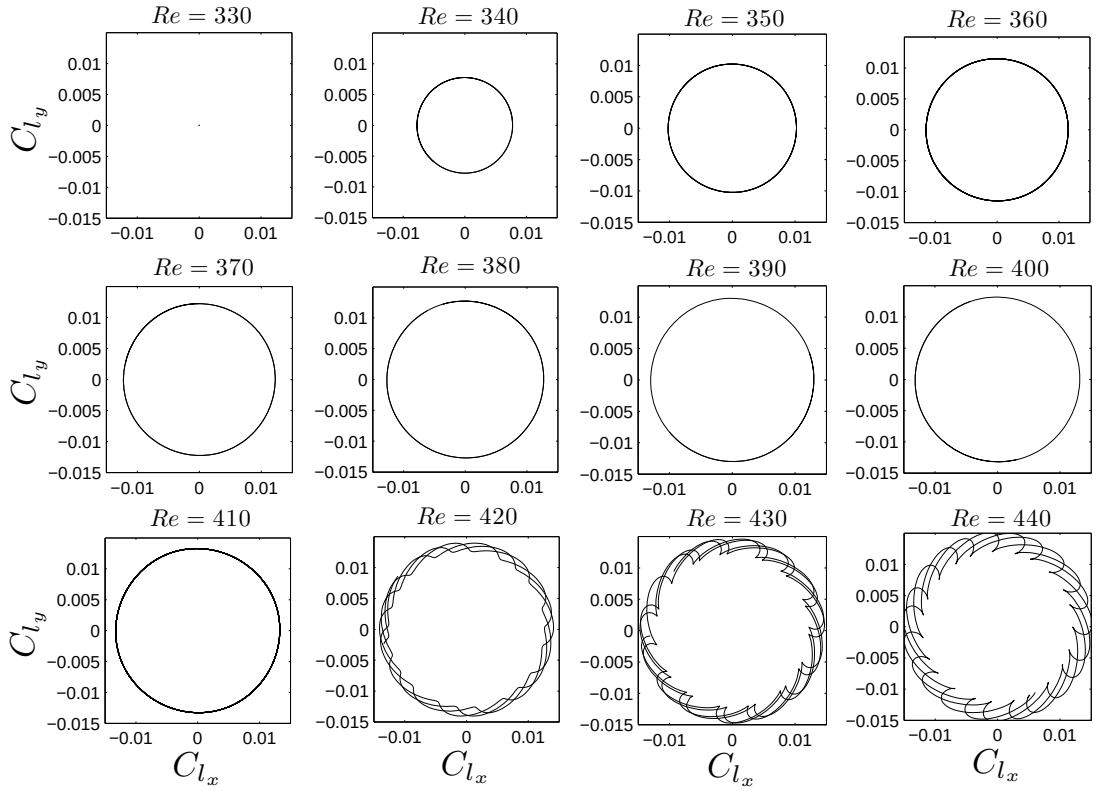

Figure 4.7: Phase diagrams of the lift components for different Reynolds numbers at $\Omega = 0.1$. Included in [58].

three different characteristic frequencies in the inertial frame of reference. Indeed, the spectrum shown in Fig. 4.5(b) reveals that the C_{l_x} signal has an energetic low frequency at $St_{\omega l}$, due to the rotation of the fluid structures, and two other higher characteristic frequencies, given by $St_{\rm vs} + St_{\omega l}$ and $St_{\rm vs} - St_{\omega l}$ respectively. Here $St_{\rm vs}$ represents the vortex shedding frequency, and the two higher frequencies appear as a consequence of the fact that, in the unsteady spiral mode, near the criticality, the lift coefficient can be approximated by the weakly non-linear expansion, $C_l(t) = \overline{C}_l + \Delta C_l \cos(2\pi\, t\, St_{\rm vs} + \phi_{\rm vs})$, taking advantage of the weak amplitude of the shedding and of the fact that harmonics are still feeble in the vicinity of the onset (see Chapter 2), so that the signal is dominated by the characteristic shedding frequency. Thus, since its projection on the x-axis is $C_{l_x}(t) = C_l(t)\cos(2\pi\, t\, St_{\omega l} + \phi_{\omega l})$, one has

$$\begin{aligned} C_{l_x}(t) &= \overline{C}_l \cos(2\pi t\, St_{\omega l} + \phi_{\omega l}) + \\ &+ \frac{\Delta C_l}{2}\cos[2\pi t\ (St_{\rm vs} + St_{\omega l}) + \phi_{\rm vs} + \phi_{\omega l}] + \\ &+ \frac{\Delta C_l}{2}\cos[2\pi t\ (St_{\rm vs} - St_{\omega l}) + \phi_{\rm vs} - \phi_{\omega l}], \end{aligned} \tag{4.3}$$

where $\overline{C}_l$ and ΔC_l are, respectively, the mean and oscillation amplitude of the lift coefficient and $\phi_{\rm vs}$ and $\phi_{\omega l}$ are arbitrary initial phases. However, when the lift components are analyzed in the rotating frame S', they oscillate with a single frequency $St_{\rm vs}$, as shown in Fig.4.6(b), related to

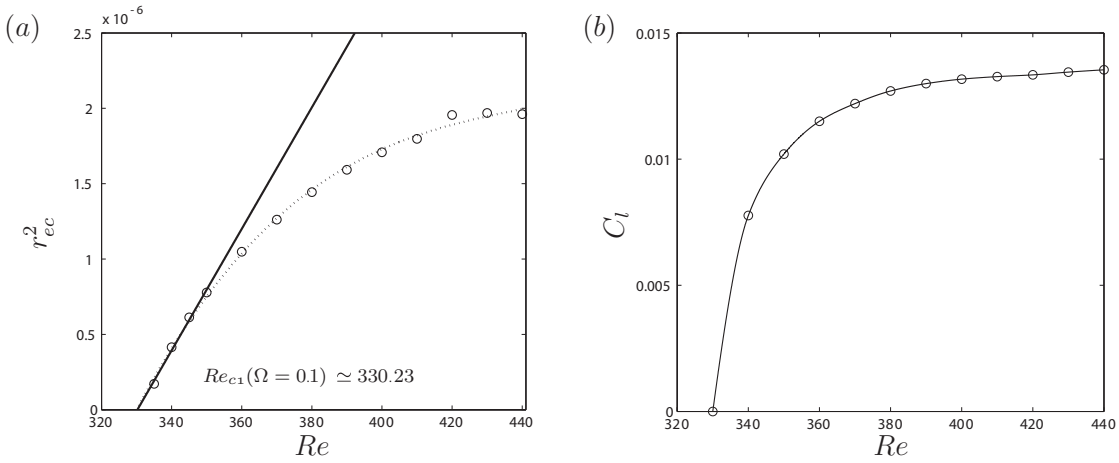

Figure 4.8: (a) Squared centroid eccentricity of the contours of velocity magnitude at $z = 1$ versus the Reynolds number, together with a linear fit (solid line), and a cubic polynomial fit (dotted line); and (b) lift coefficient C_l as a function of Re (time averaged values for $Re = 420, 430$ and 440), for $\Omega = 0.1$. Included in [58].

the vortex shedding frequency described in Chapter 2 in the case of $\Omega = 0$. Indeed, Table 4.4 shows the values of $St_{\omega l}$ and $St_{\rm vs}$ for different Reynolds numbers, together with the corresponding values obtained both numerically, $St_0^{\rm DNS}$, and experimentally, $St_0^{\rm EXP}$, in the case of a non-rotating body (see Chapter 2). Note that $St_{\omega l}$ barely changes with Re, while $St_{\rm vs}$ is a slightly increasing function of Re. In fact, $St_{\rm vs}$ is close to the values reported in Chapter 2 for $Re \geq Re_{co}$ at $\Omega = 0$, being $St_{\omega l}$+$St_{\rm vs}$ nearly equal to the corresponding vortex shedding frequency obtained at $\Omega = 0$. This result indicates that the unsteady spiral mode has the same physical origin as the oscillatory RSP mode in bodies without rotation. Further evidence for the latter equivalence can be obtained by analyzing the limiting behavior of $St_{\rm vs}$ as $\Omega \to 0$. For example, Table 4.5 shows the values of $St_{\rm vs}$ at $Re = 430$ and $0 \leq \Omega \leq 0.15$. It is seen that the frequency at which vortex shedding takes place in the RSP mode for the non-rotating body, $\Omega = 0$, is similar to that shown by the rotating structure at $\Omega = 0.05$, however, the value of $St_{\rm vs}$ decreases with the rotation parameter.

	$\Omega = 0$	$\Omega = 0.05$	$\Omega = 0.1$	$\Omega = 0.15$
$St_{\rm vs}$	0.1235	0.1206	0.1085	0.1030
$St_{\omega l}$	0	0.0078	0.0155	0.0193

Table 4.5: Values of $St_{\rm vs}$ and $St_{\omega l}$ for low Ω at $Re = 430$.

In view of the results presented in the previous paragraph, it is clear that $St_{\omega l}$ is a *rotation* or *spin* Strouhal number, characterizing the rigid-body co-rotation of the wake induced by the spinning motion of the body, while $St_{\rm vs}$ is a *vortex-shedding* Strouhal number.

Since the temporal evolution of the lateral forces directly resemble the instability modes that are active in the spinning wake at given values of Re and Ω, a very useful tool to describe the transitions occurring at increasing Re are the phase diagrams of the two lift components, $C_{l_x}(t) - C_{l_y}(t)$ [113]. In particular, Fig. 4.7 shows a few periods of evolution of the lift vector in the

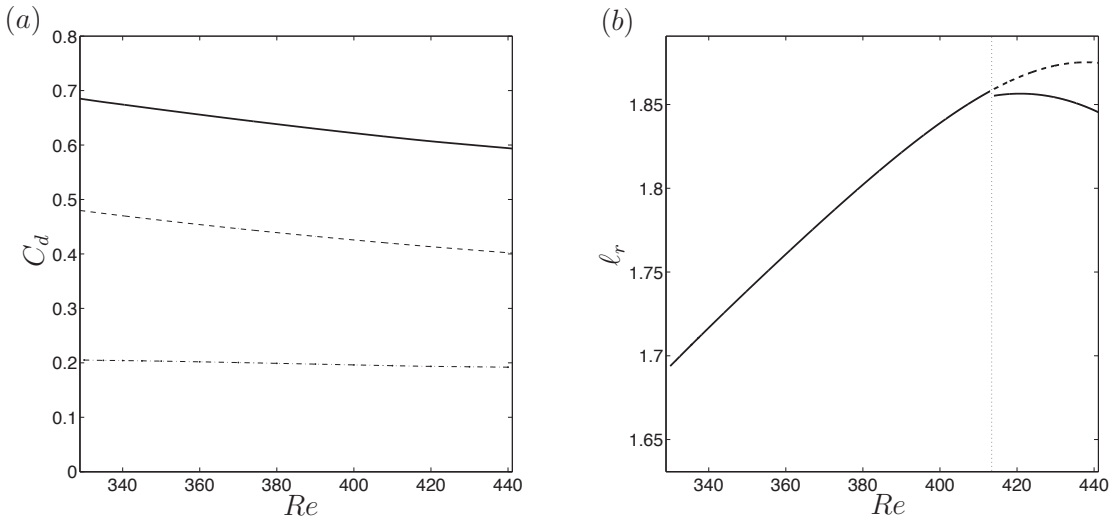

Figure 4.9: (a) Total drag coefficient C_d (solid line), viscous drag C_d^v (dashed line) and pressure drag C_d^p (dash-dotted line), and (b) dimensionless recirculation length ℓ_r as a function of Re (time averaged value for $Re = 420, 430$ and 440), for $\Omega = 0.1$. The dashed line in Fig. 4.9(b) represents the extrapolation of ℓ_r considering a non-bifurcated flow. Included in [58].

(x, y)-plane, illustrating the behavior of the three modes described above for $\Omega = 0.1$, i.e. the axisymmetric mode ($Re < Re_{c1} \approx 340$), where the lift force is zero, the frozen mode ($Re_{c1} \approx 340 \leq Re < Re_{c2} \approx 420$), for which the lift magnitude remains constant, and the unsteady spiral mode ($Re \geq Re_{c2} \approx 420$), characterized by a fluctuating lift magnitude caused by the spiral vortex shedding phenomenon described above. From the results of Fig. 4.7 it can be deduced that the mean value of C_l increases with Re (see Fig.4.8b), as a result of the increase of the eccentricity of the structures downstream of the base. The latter fact is illustrated in Fig. 4.8(a), which depicts the Re-dependence of the squared centroid eccentricity, r_{ec}^2, based on the contours of velocity magnitude in the (x, y)-plane, obtained at $z = 1$.

Another interesting feature is the decrease of the drag coefficient with Re. Indeed, as shown in Fig. 4.9(a), the viscous contribution to the drag force decreases substantially with Re, whereas the pressure drag barely changes within the range of Reynolds numbers explored in the present work. The slight dependence of the pressure drag coefficient with Re can also be inferred by studying the evolution of the pressure coefficient, $C_p = 2\,(p - p_\infty)$, shown in Fig. 4.10. In fact, this figure displays the instantaneous C_p distribution in the (y_m, z)-plane, where the y_m-axis is oriented along the direction of maximum lift, together with the instantaneous streamlines projected onto the same plane. The contours represented in Fig. 4.10 show that the overall values of C_p remain almost constant for increasing Re, but are shifted at the base, defining the direction of the lift vector and its growing magnitude with Re. Furthermore, the streamlines shown in Fig. 4.10 reveal that the axisymmetric toroidal recirculation region, observed at $Re = 330$, evolves towards a tilted structure as Re increases, with two azimuthally projected spirals, namely an upper spiral close to the base, formed by the fluid particles entrained from the outer flow, as well as a lower one, through which the particles are ejected into the wake. The length of the recirculation region defined by

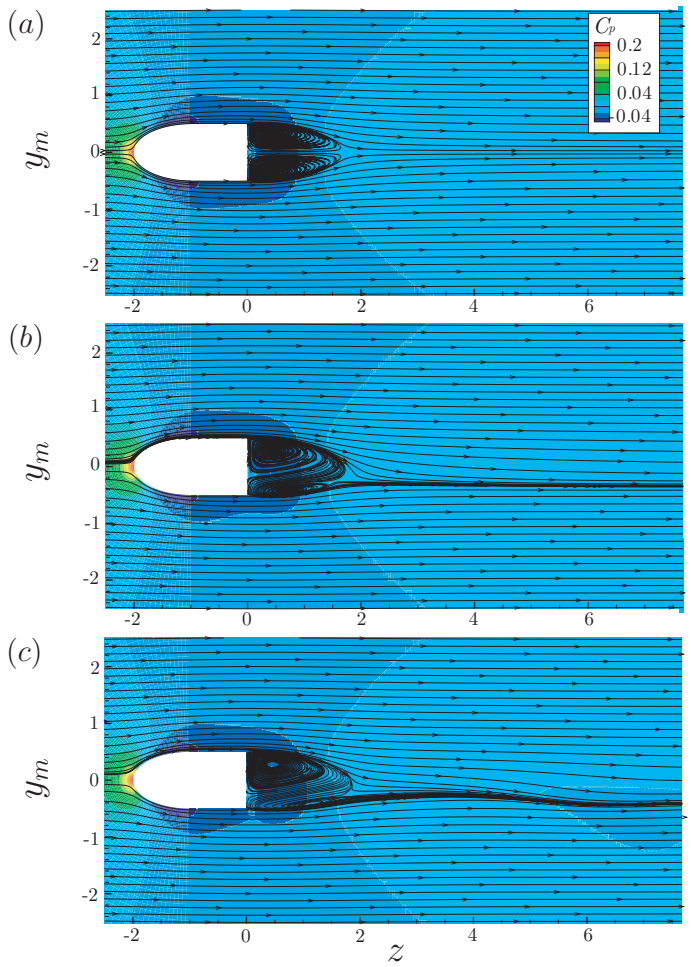

Figure 4.10: Instantaneous projected streamlines and contours of the pressure coefficient, C_p, in the (y_m, z)-plane, where y_m is aligned with the direction of maximum lift, for $\Omega = 0.1$ and (a) $Re = 330$, (b) $Re = 370$ and (c) $Re = 430$. Included in [58].

these structures, ℓ_r, increases with the Reynolds numbers, as shown in Fig. 4.9(b), which exhibits the signature of the transition that takes place in the wake between $Re = 410$ and 420, since the behavior of ℓ_r changes qualitatively in this range of Re. In addition, an extrapolation of ℓ_r for $Re > 410$, considering a non-bifurcated flow, has been also represented with dashed line in this figure.

4.3.2 Analysis of the bifurcations for $\Omega = 0.1$

In Section 4.3.1 two unstable regimes have been reported as Re increases for $\Omega = 0.1$, namely, the *frozen* and the *unsteady spiral* states. Both regimes emerge as a consequence of deformation through rotation of the SS and RSP states described in Chapter 2 for $\Omega = 0$, and present particularities regarding their characteristic frequencies and forces. In principle, although no quantitative determination have been done so far, critical Reynolds numbers seem to be also modified by rotation, and the nature of the bifurcations giving rise to the regimes detailed could have been likewise

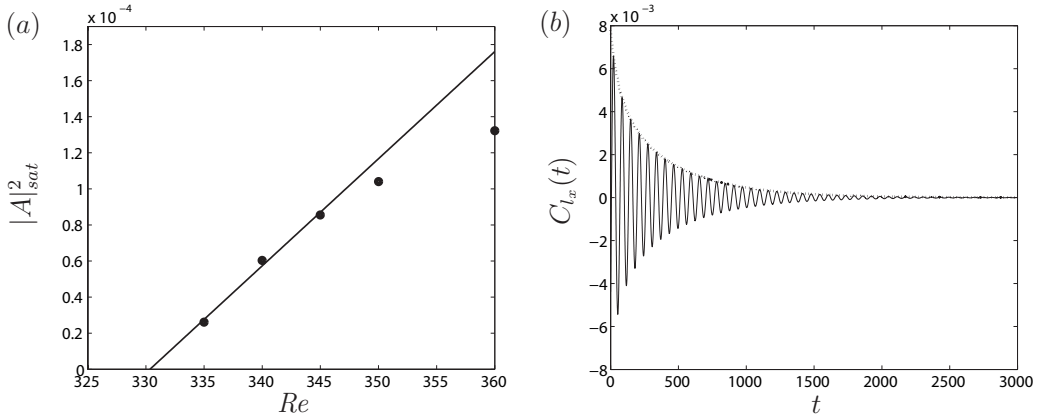

Figure 4.11: (a) Determination of $Re_{c1}(\Omega = 0.1)$ by linear fit of the energy of the saturated amplitude of C_{l_x}, $|A|^2_{sat}$, versus Re. (b) Determination of the temporal decay rate of lift component $C_{l_x}(t)$ at $Re = 330$, beginning the simulation from the saturated solution at $Re = 340$. Included in [58].

affected. Hence, this section is devoted to characterize these transitions and to study their nature by means of the Stuart-Landau model, introduced in Section 1.2.2.

As Eq. (1.18) indicates, close to Re_c, the energy of the temporal oscillations, $|A|^2_{sat}$, of any signal that is zero prior to the bifurcation should vary linearly with $Re - Re_c$. In addition, even though the value of $|A|_{sat}$ depends on position, Re_c is uniquely defined, so that the value of any global variable, such as C_{l_x}, could be used as a measure to obtain the value of $Re_{c1}(\Omega)$. Furthermore, due to the fact that the saturated amplitude of C_{l_x} corresponds to that of C_l for frozen states, the value of Re_{c1} can be easily obtained by a linear regression of C_l^2 as a function of Re, represented in Fig. 4.11(a) for $\Omega = 0.1$. In particular, the linear fit applied to the data series shown in Fig. 4.11(a) yields a value of $Re_{c1} = 330.41$.

On the other hand, two other methods, already introduced in Chapter 2, were used to characterize the transition. First, by using the fact that the squared centroid eccentricity, r^2_{ec}, of a field variable at a fixed position in the wake, grows linearly with $Re - Re_{c1}$ close to the transition (see Fig.2.8). In this case, using the velocity distribution magnitude contours at $z = 1$, we obtained by linear extrapolation $Re_{cs} \simeq 330.2$ for $\Omega = 0.1$ (see Fig. 4.8a), which is in fact very close to the value given by the aforementioned fit of lift components. Moreover, we analyzed the dependence of the temporal growth or decay rate of the mode with Re close to the transition, like it was done in Chapter 2 to determine Re^{DNS}_{co}, and, again, the amplification or decay rates were obtained by monitoring the evolutions of the forces acting on the body. As mentioned, at $Re = 330$ the wake is steady and axisymmetric, so that an initially perturbed signal (e.g. beginning the simulation from the saturated solution at $Re = 340$) will be damped eventually, as can be observed in Fig. 4.11(b). The decay rate can be then computed through an exponential fit, giving $\sigma_{Re=330} \simeq -0.0022$. We proceeded likewise for $Re = 340$, using the axisymmetric steady saturated signal at $Re = 330$ as initial condition, and fitted the exponential amplification of the oscillation, obtaining $\sigma_{Re=340} \simeq 0.0074$. Therefore, by linear regression between both values of σ, $Re_{c1} \simeq 332.3$ was obtained, in good agreement with the values given above.

Furthermore, as indicated in Section 2.4, the supercritical nature of the bifurcations can be

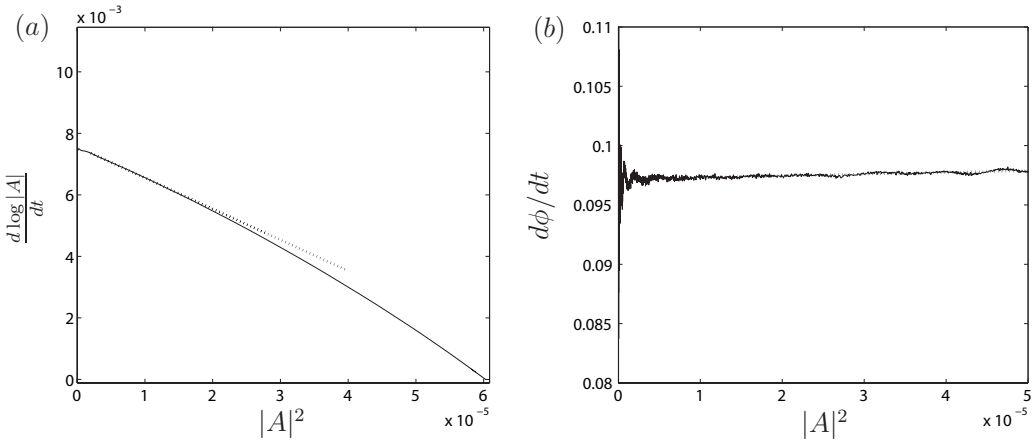

Figure 4.12: Stuart-Landau model for the first bifurcation: (a) Instantaneous growth rate $d\log|A|/dt$ and (b) instantaneous frequency $d\phi/dt$, versus $|A|^2$, at $Re = 340$ and $\Omega = 0.1$. Included in [58].

quantified by determining the coefficients of the Landau equation (see Eq.1.13). Thus, since both the lift coefficient and the velocity signals downstream the body give identical values of global parameters, like σ_r, σ_i and c [147], either the lift components or the lift magnitude were chosen here, depending on the transition, as the real part of the complex amplitude $A(t)$. The first bifurcation can be considered as a regular bifurcation in the reference frame S', which rotates with the frozen wake at an angular velocity Ω_{sl}. However, viewed from the inertial reference frame, the outcome of the first bifurcation is an unsteady wake, and, therefore, it can also be seen as a Hopf bifurcation. Thus, by using one of the lift components, e.g. C_{l_x}, both the amplitude and phase equations of the Stuart-Landau model can be applied, as depicted in Fig. 4.12. Moreover, for the bifurcation to be supercritical, the amplitude of the oscillating signal, $\Re[A(t)] = C_{l_x}(t)$, must saturate after a linear growth, showing that l_r in Eq. (1.14) is positive. The latter fact translates into a negative slope in Fig. 4.12(a), allowing us to determine the coefficients, namely $\sigma_r = d\log A/dt[|A|^2 = 0] \simeq 0.0075$, and $l_r = d(d\log A/dt)/d(|A|^2) \simeq 100.7$, obtained through the slope of the linear fit close to the y-axis (dotted line). On the other hand, the phase Eq.(1.15) can be analyzed by processing the transient oscillatory signal by means of a Hilbert transform (see Section 2.4). In particular, Fig. 4.12(b) shows Eq. (1.15), where $\sigma_i = d\phi/dt[|A|^2 = 0] \simeq 0.097$ is the linear growth rate, and $li \simeq -14.4$ is obtained from a linear fit (dotted line). Thus, at $Re = 340$, the Landau constant $c = l_i/l_r \simeq 0.14$.

As explained in Section 4.3.1, the second transition gives rise to an asymmetric vortex-shedding regime, where the axial vorticity threads twist around the axis (see Fig. 4.3). These facts translate in non-monochromatic spectra of velocity and forces with respect to the inertial reference frame. However, viewed from the relative reference frame S', that rotates with angular velocity Ω_{sl}, the spectra of both $C'_{l_{x'}}$ and $C'_{l_{y'}}$ are practically monochromatic (harmonics display still weak amplitudes), with a peak at $St_{\rm vs}$ (see Fig. 4.13a). Therefore, we can conclude that a Hopf bifurcation occurs in the frame S', and the oscillations of $C_l(t)$, reflecting the vortex shedding phenomenon, properly describe the dynamics of this new mode, allowing us to study the corresponding bifurcation with the Stuart-Landau model. Specifically, the value of Re_{c2} can be obtained by means of applying Eq. (1.18), which describes the dependence of the energy on Re, to the oscillations of

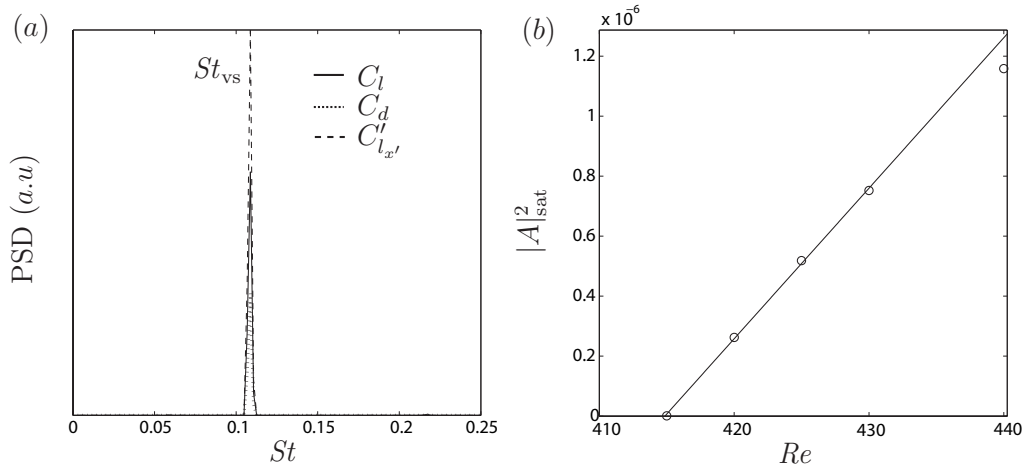

Figure 4.13: (a) Power Spectral Density (in arbitrary units) of $C_l(t)$ (solid line), $C_d(t)$ (dotted line) and $C'_{l_{x'}}(t)$ (dashed line) for an arbitrary initial phase, at $Re = 425$ for $\Omega = 0.1$, and (b) squared saturation amplitude of the lift magnitude, $|A|^2_{sat}$, as a function of Re. Included in [58].

the lift magnitude, $C_l(t)$. The squared saturation amplitude, $|A|^2_{sat}$, was computed, according to Eq.(2.6), by integrating the dominant peak of the Power Spectral Density at $St_{\rm vs}$, obtained from the temporal evolution of $C_l(t) - \overline{C}_l(t)$. Figure 4.13(b) shows the evolution of $|A|^2_{sat}$ with Re, from which the critical Reynolds number Re_{c2} is determined by a linear regression close to the threshold, providing $Re_{c2} \simeq 414.8$, slightly larger than the value $Re_{co} \simeq 413$ obtained for the body without rotation (see Section 2.3). Note that, as happened for the first transition, the saturation of the amplitude away from the bifurcation point indicates that l_r in Eq. (1.14) is positive, and thus that the present transition is also supercritical.

To precisely analyze the transient and determine the nature of the second bifurcation, we also used the amplitude and phase equations, as shown in Fig. 4.14 for $Re = 420$, at a distance $Re - Re_{c2} \simeq 5$ ($[Re - Re_{c2}]/Re_{c2} \simeq 1.24\%$) from the bifurcation point. As can be seen in Fig. 4.14, although the processed data exhibit some noise, it is evident that the transient behavior can be captured satisfactorily by means of the Stuart-Landau model (1.13), providing, for $Re = 420$, $\sigma_r \simeq 0.0035$, $\sigma_i \simeq 0.675$, $c = l_i/l_r = 1025/(-2033) \simeq -0.50$ (see Fig. 4.14). The value of $c(\Omega = 0.1)$ is close to $c(\Omega = 0) \simeq -0.542$, reported in Section 2.4, obtained numerically for a $Re - Re_{c2} \simeq 2$. The small difference between them could be due, either to the different value of Ω, or to the fact that c is known to increase as the distance to the bifurcation, $(Re - Re_c)$, decreases (see for instance [147]).

4.3.3 Flow characteristics for $\Omega \leq 0.4$

To explore a larger region of the $Re - \Omega$ plane, a parametric study similar to that described in the previous section was performed for several values of Ω, and increasing values of Re. Again, the Stuart-Landau model, described above, was applied to study the nature of the bifurcations found at increasing values of Ω, also allowing us to find the corresponding critical Reynolds numbers.

For $\Omega < 0.2$, we observed the same sequence of bifurcations for increasing Re, as those described in Section 4.3.1 for $\Omega = 0.1$, namely axisymmetric, frozen and unsteady spiral regimes.

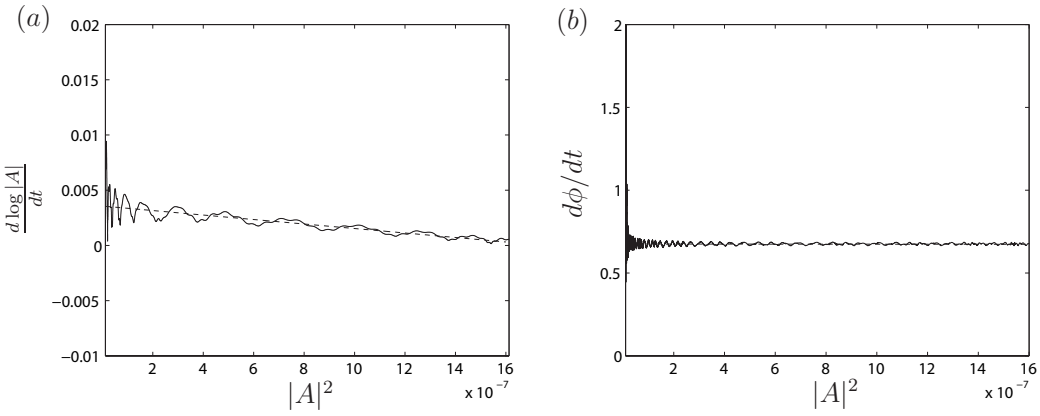

Figure 4.14: Stuart-Landau model for the second bifurcation: (a) Instantaneous growth rate $d\log|A|/dt$ and (b) instantaneous frequency $d\phi/dt$, versus $|A|^2$, at $Re = 420$ and $\Omega = 0.1$. Included in [58].

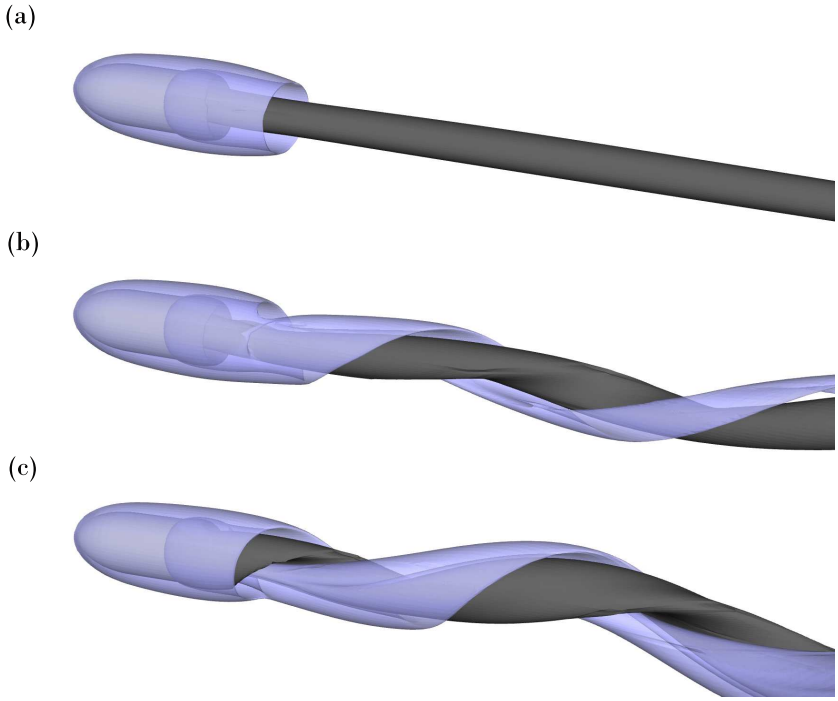

Figure 4.15: Vortical structures visualized by streamwise vorticity contours, $\varpi_z = \pm 0.2$, for $\Omega = 0.2$ at (a) $Re = 380$, (b) $Re = 390$ and (c) $Re = 430$. Included in [58].

However, the numerical simulations revealed that the transition from the axisymmetric flow to a non-axisymmetric frozen regime takes place at increasing values of Re_{c1} as Ω increases, indicating the stabilizing effect of rotation on the first bifurcation. For example, $Re_{c1}(\Omega = 0.05) \simeq 323.5$, whereas $Re_{c1}(\Omega = 0.15) \simeq 347.5$ and $Re_{c1}(\Omega = 0.2) \simeq 375.4$. Furthermore, body rotation also

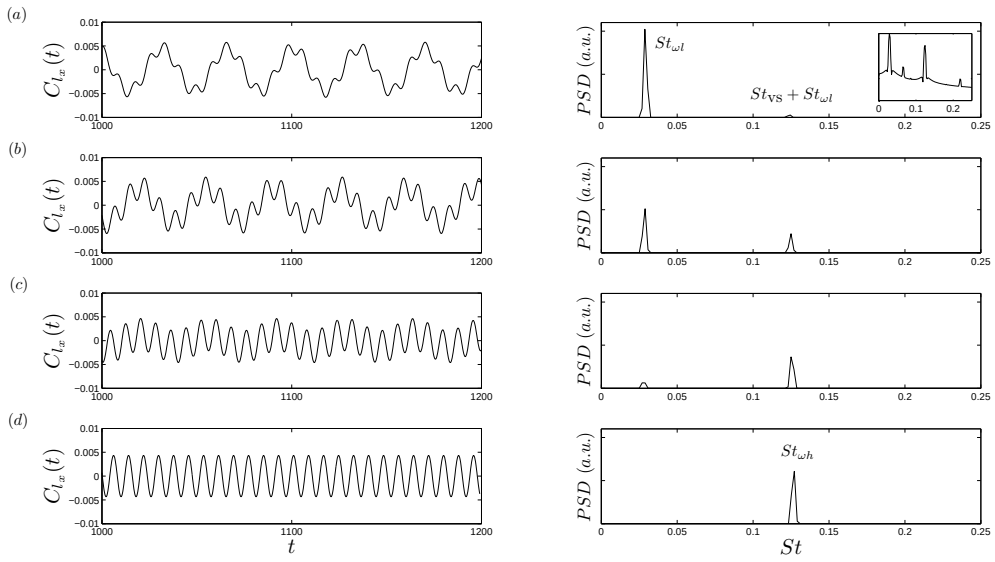

Figure 4.16: Time series of the lift component $C_{l_x}(t)$ (left side) and Power Spectral Density (right side) for $\Omega = 0.2$ and: (a) $Re = 390$, (b) $Re = 400$, (c) $Re = 410$ and (d) $Re = 420$. Included in [58].

stabilizes the second bifurcation for small enough values of Ω, since $Re_{c2}(\Omega = 0) = 413$[1] while $Re_{c2}(\Omega = 0.05) \simeq 424$. However, for $\Omega > 0.05$, Re_{c2} starts to decrease with the rotation parameter, being, for instance $Re_{c2}(\Omega = 0.15) \simeq 390$.

Let us now briefly discuss the vortical structures observed in the wake at $\Omega = 0.2$. As can be seen in Fig. 4.15(a) for $Re = 380 > Re_{c1}(\Omega = 0.2)$, in the frozen regime, the thread with negative streamwise vorticity is much weaker than in the case $\Omega = 0.1$, shown in Fig. 4.3(b), due to the release of positive vorticity from the base of the body. Thus, for $\Omega = 0.2$, the frozen state is characterized by a thread of positive axial vorticity that is much stronger than its negative counterpart, having a very small eccentricity prior to the second bifurcation at Re_{c2}. In the latter unsteady spiral regime, shown in Fig. 4.15(b), the shedding of vortices is barely noticeable at the level of $\varpi_z = \pm 0.2$ considered, since the angular momentum overcomes the axial inertia of the flow. In fact, the structures are arranged in a way that resembles a corkscrew, and are shed downstream with a frequency $St_{\rm vs}$, as shown in the spectra displayed in Fig. 4.16(a). The value of $St_{\rm vs}$ is close to that found for $\Omega = 0.1$ and $Re \geq 420$ (see Fig. 4.5).

Furthermore, at $Re_{c3} < 420$ a transition to a new *high-frequency frozen regime* was identified, having monochromatic signals of $C_{l_x}(t)$ and $C_{l_y}(t)$, and constant values of C_l and C_d, as can be inferred from Fig. 4.17. A spectral analysis revealed that the spiral vortex structures shown in Fig. 4.15(c) rotate with a frequency $St_{\omega h}$, almost identical to $St_{\rm vs} + St_{\omega l}$, appearing in the analysis of the lift components in the spiral vortex shedding regime, as Fig. 4.16 demonstrates. In fact, it can be observed that the energy of the peak at $St_{\rm vs} + St_{\omega l}$, associated to vortex shedding, grows with Re for $Re > Re_{c2}$, while that associated to $St_{\omega l}$ becomes less energetic as Re increases, being the former peak the leading one at $Re = 410$. Therefore, the frequency related to the new frozen

[1]Notice that Re_{c2} at $\Omega = 0$ corresponds with Re_{co} in Chapter 2.

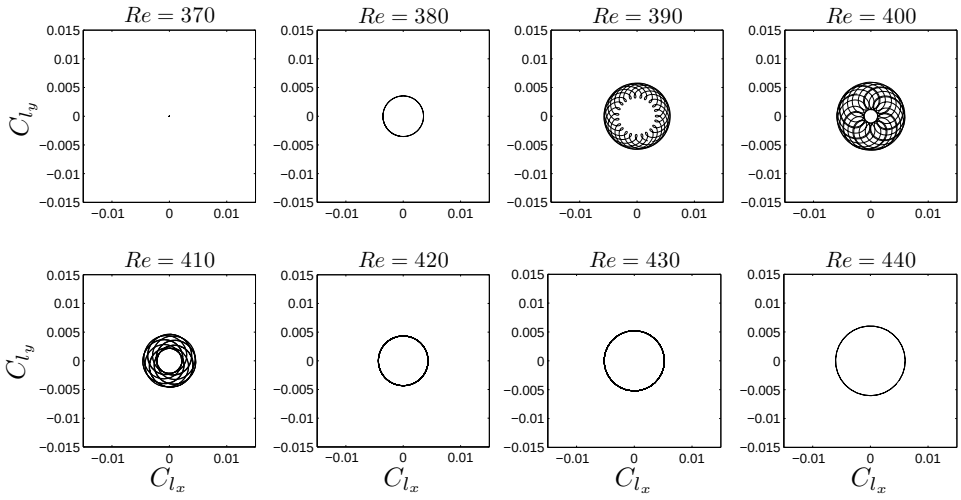

Figure 4.17: Phase diagrams, C_{l_x} vs C_{l_y}, for $\Omega = 0.2$ and different values of Re indicated in the plots. Included in [58].

regime results from a lock-in phenomenon at the frequency $St_{\text{vs}} + St_{\omega l}$.

To precisely determine the nature of the new bifurcation, that takes place between $410 < Re_{c3} < 420$ at $\Omega = 0.2$, we followed the procedure described in Section 4.3.2 to analyze the temporal growth or decay rate of the fluctuating lift and drag signals, at Reynolds numbers close to the critical one. The study revealed that the wake undergoes a Hopf bifurcation when analyzed in the rotating reference system, S', changing from a steady flow to an oscillatory one at $Re_{c3} \simeq 411$ and decreasing Re. In addition, by applying the Stuart-Landau model to the transient behavior of the wake at $Re = 410$, it was observed that the new bifurcation found at Re_{c3} corresponds to a supercritical one.

If Ω is increased up to $\Omega = 0.25$, the pattern of transition changes, observing just a single transition towards the high-frequency frozen state. Indeed, at $\Omega = 0.25$, the axisymmetry-breaking bifurcation leads directly to the spiral frozen wake at a certain critical value of the Reynolds number, in the range $380 < Re < 390$, this mode prevailing up to the highest value of Re investigated in the present work, as can be deduced from Fig. 4.18. The same scenario described for $\Omega = 0.25$ was also observed for $\Omega = 0.3$ and 0.4. Furthermore, after comparing the values of the main and secondary frequencies of the lift components for different Ω and Re, listed in Table 4.6, it seems evident that the frequency associated to the new frozen regime, $St_{\omega h}$, arises from the aforementioned lock-in phenomenon at $St_{\text{vs}} + St_{\omega l}$, observed for $\Omega = 0.2$. Thus, the wake rotates with an angular velocity $\Omega_{sh} = 2\pi\, St_{\omega h}$, higher than in the first frozen regime observed at $\Omega \leq 0.2$. Consequently, by analogy with the fourth mode reported at $\Omega = 0.2$, the critical Reynolds number at which this transition occurs for $\Omega \geq 0.25$ will be also denoted Re_{c3}. Finally, it can also be inferred from Table 4.6 that, for the low-frequency frozen mode, Ω_{sl} increases linearly with Ω for a fixed value of Re.

The different flow regimes reported in this section can be conveniently mapped in the (Ω, Re) parameter plane, shown in Fig. 4.19, where the axisymmetry-breaking bifurcation at $\Omega = 0.225$ is included in order to increase the resolution around the junction between all regimes. In fact, this

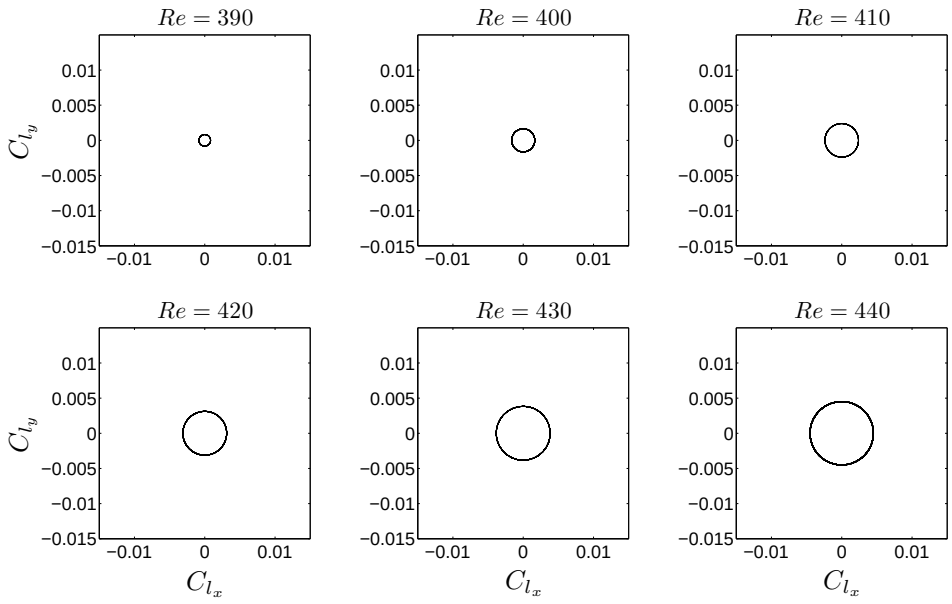

Figure 4.18: Phase diagrams, C_{l_x} vs C_{l_y}, for $\Omega = 0.25$ and different values of Re indicated in the plots. Included in [58].

	$Re = 380$	$Re = 390$	$Re = 400$	$Re = 410$	$Re = 420$
$\Omega = 0.1$	0.0153	0.0153	0.0153	0.0154	0.0154
					(0.1215)
$\Omega = 0.2$	0.0287	0.0287	0.0288	0.125	0.1271
		(0.1245)	(0.125)	(0.0278)	
$\Omega = 0.25$	-	0.1288	0.1290	0.1302	0.1317
$\Omega = 0.3$	-	0.1320	0.1312	0.1348	0.1348
$\Omega = 0.4$	-	0.1398	0.1417	0.1436	0.1441

Table 4.6: Frequencies associated to main and secondary (in brackets, when exists) peaks of lift components spectra, obtained for $\Omega = 0.1$, 0.2, 0.25, 0.3 and 0.4 at several values of Re close to Re_{c2} and Re_{c3}. For monochromatic spectra, values correspond to $St_{\omega l}$ ($\Omega \leq 0.2$ and $Re \leq 410$) and $St_{\omega h}$ ($\Omega \geq 0.2$ and $Re \geq 390$).

plane can be divided into four regions: the wake is axisymmetric in Region I, whose size grows with Ω. The transition at Re_{c1} leads to a frozen state inside Region II, up to a value of $\Omega \simeq 0.225$. In region II, the angular velocity of the wake is given by Ω_{sl}. When Re is increased past Re_{c2}, an unsteady spiral wake takes place, inside Region IIIa, whose main feature is the presence of vortex shedding. This mode is equivalent to the RSP mode occurring in bodies without rotation. Provided $\Omega \geq 0.2$, the spiral frozen regime, Region IIIb, is reached at Re_{c3}, for which the wake rotates as a solid body with an angular frequency Ω_{sh}, and whose origin is linked to the vortex-shedding mode present in Region IIIa. Moreover, Region IIIb is the only unstable region found for $0.225 \lesssim \Omega \leq 0.4$, at least within the range of Re studied in this Thesis.

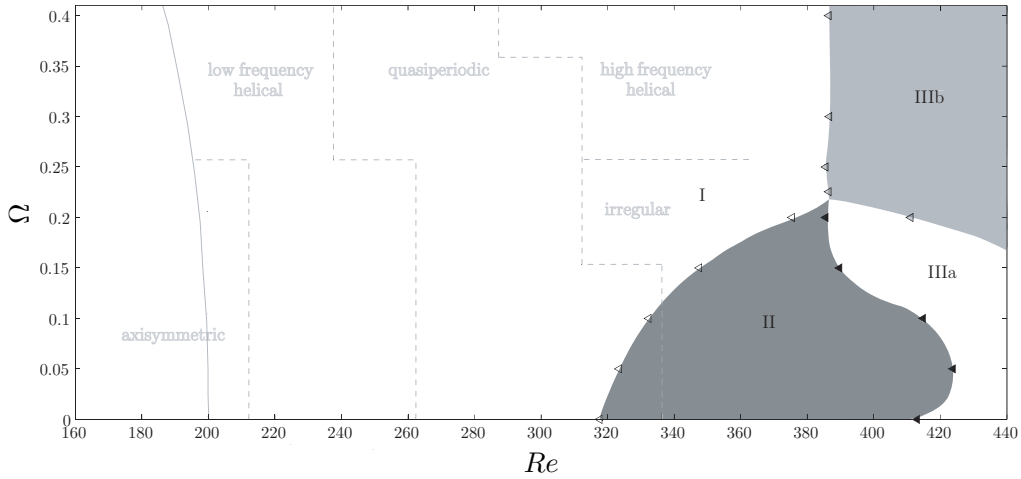

Figure 4.19: Bifurcation diagram for the spinning bullet-shaped body in the (Ω, Re) parameter plane, where the transitions are identified by means of different symbols: ◁ - Re_{c1}, ◀ - Re_{c2} and ◀ -Re_{c3}. The different wake states correspond to the following Regions: I-axisymmetric, II-frozen, IIIa-spiral unsteady and IIIb-spiral frozen. Additionally, the regimes found by Pier [113] for the sphere have been included for comparison (see grey dashed lines and grey tags), together with the transition $Re_{c1}(\Omega)$ (grey continuous line). Included in [58].

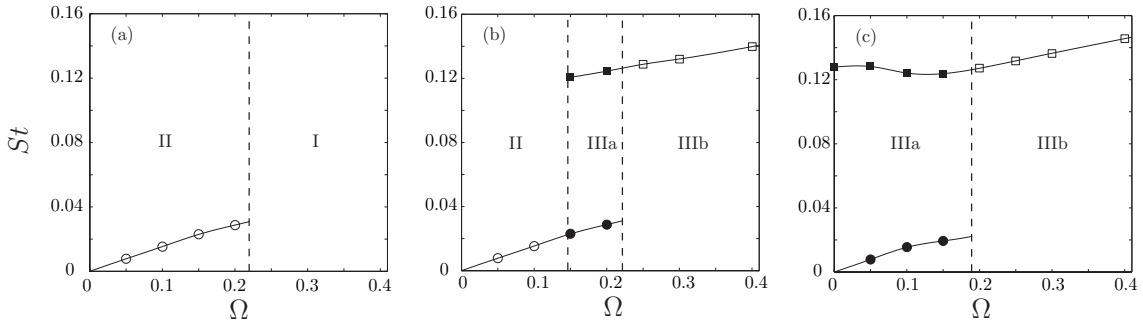

Figure 4.20: Evolution with Ω of the Strouhal numbers $St_{\omega l}$ (○-frozen, ●-spiral unsteady), $St_{\rm vs} + St_{\omega l}$ (■-spiral unsteady) and $St_{\omega h}$ (□-spiral frozen) at: (a) $Re = 380$, (b) $Re = 390$ and (c) $Re = 430$. Vertical dashed lines stand for the different transitions found for increasing Ω. Included in [58].

Let us now discuss the characteristic frequencies, angular velocities and force coefficients associated to the different flow regimes identified in Fig 4.19. Figure 4.20 depicts the Ω-dependence of the characteristic wake frequencies, namely $St_{\omega l}$ (hollow circles for the frozen Region II, and solid circles for Region IIIa), $St_{\rm vs} + St_{\omega l}$ (solid squares, defined in Region IIIa), and $St_{\omega h}$ (hollow squares, corresponding to Region IIIb), for Re = 380 (a), 390 (b) and 430 (c). The transitions between the different regimes are represented with vertical dashed lines in Fig. 4.20. For Region II, it can be observed in Figs. 4.20(a)-(b) that $St_{\omega l}$ always increases with Ω, independently of Re, but with a slope that decreases near the transitions to Regions I or IIIb, depending on the value of Re. In addition, Fig. 4.20(b) also shows that, at $Re = 390$, the value of $St_{\rm vs} + St_{\omega l}$ increases linearly with Ω, and matches the spin Strouhal number $St_{\omega h}$ associated to Region IIIb, where the

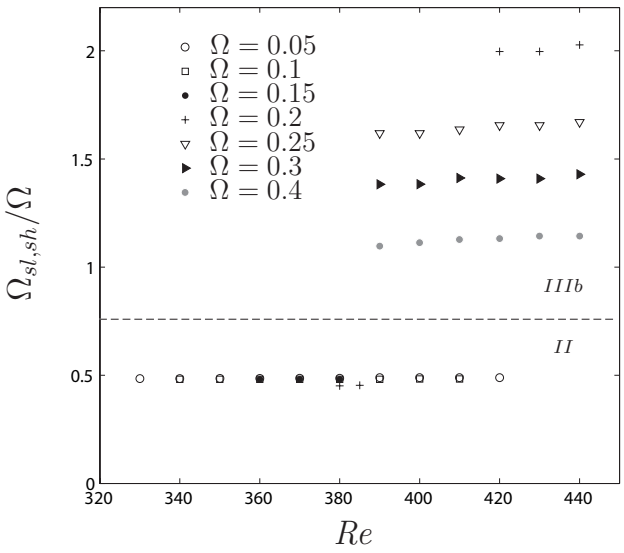

Figure 4.21: Evolution of the ratios Ω_{sl}/Ω and Ω_{sh}/Ω with Re for different values of Ω, corresponding respectively to the frozen Regions II and IIIb shown in Fig. 4.19. Included in [58].

flow has already bifurcated to the frozen spiral mode. However, at $Re = 430$, $St_{\rm vs} + St_{\omega l}$ decreases initially in the range $0 \leq \Omega \leq 0.15$, but shows the same behavior as in the case $Re = 390$ for $\Omega \geq 0.15$, even before the structures lock-in takes place.

Regarding the frozen regimes, associated to Regions II and IIIb of Fig. 4.19, the most important parameter is the angular velocity of the wake structures. As already mentioned, Regions II and IIIb are characterized by the solid-body rotation of the wake, with an angular velocity different from that of the body. Figure 4.21 shows the evolution of the ratio Ω_{sl}/Ω and Ω_{sh}/Ω with Re for both frozen flow regimes, where it can be clearly seen that Ω_{sl}/Ω has a nearly constant value around 0.48 inside Region II. However, in the spiral frozen mode (Region IIIb), the wake rotates faster than the body, with a value of Ω_{sh}, that decreases as Ω increases. In particular, note that Ω_{sh}/Ω increases slightly with Re, since, as shown in Table 4.6, $St_{\omega h}$ increases with the Reynolds number.

For the values of $Re = 380, 390, 430$, we also analyzed the dependence of C_d and C_l on Ω. Thus, Fig. 4.22(a) shows the evolution of the time-averaged drag coefficient, $\overline{C}_d$, showing that it increases quadratically with Ω, in agreement with the prediction of Schlichting [128]. Note also that the behavior of $\overline{C}_d$ is similar for the three Reynolds numbers studied, showing a smooth dependence irrespective of the transitions between regimes. A different behavior is observed for $\overline{C}_l$ in Fig. 4.22(b). For $Re = 380$, an increase in Ω translates into a slight reduction of $\overline{C}_l$ within the first frozen mode, due to a reduction of the eccentricity of the wake structures, until a critical value of Ω is reached at which $\overline{C}_l = 0$, since the axisymmetry is recovered. At $Re = 390$ and $Re = 430$, $\overline{C}_l$ follows the same trend in the range $0 \leq \Omega \leq 0.2$, since at low Ω the contribution of $St_{\omega l}$ to the wake in Region IIIa is dominant over that of $St_{\rm vs} + St_{\omega l}$ (see Fig. 4.16). However, for larger values of Ω, $\overline{C}_l$ tends to a constant value, but different from zero, achieved at higher values of Ω for increasing values of Re. Furthermore, as already indicated for $\Omega = 0.1$, the value of $\overline{C}_l$ increases with Re.

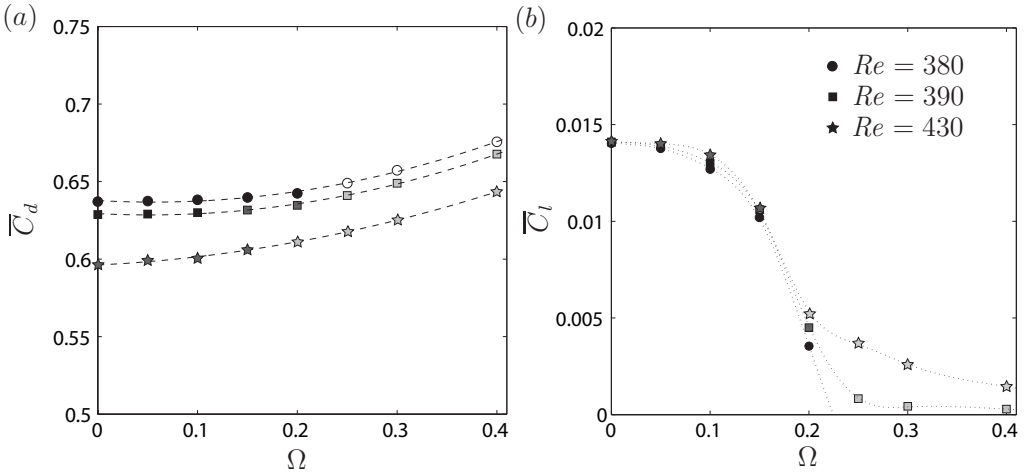

Figure 4.22: (a) Mean drag coefficient $\overline{C}_d$ and (b) mean lift coefficient $\overline{C}_l$ as functions of Ω, for $Re = 380$, $Re = 390$ and $Re = 430$, and different modes (I-empty symbols, II-black filling symbols, IIIa-dark grey filling symbols and IIIb-light grey filling symbols). Dashed lines in (a) represent quadratic fits. Included in [58].

4.3.4 Flow characteristics for $0.4 < \Omega \leq 0.6$

The numerical simulations presented so far were very time-consuming, especially for Re close to bifurcations, at any Ω. Consequently, the thorough parametric study in Re, with increments of $\Delta Re = (5, 10)$, and the determination of critical Reynolds turned out to be a tough task, and therefore, was restricted to $\Omega \leq 0.4$, since the purpose of the work was mainly to study the deformation through rotation of the unstable modes found for $\Omega = 0$ (see Chapter 2). However, a qualitative, less resolved, parametric study was performed for $0.4 < \Omega \leq 0.6$, in order to figure out whether new unstable regimes were encountered at higher rotation parameters, or conversely, those included in the diagram depicted in Fig.4.19, were the only existing ones in the range $Re \leq 440$, in line with what occurs for the case of the sphere (see Pier [113] for $\Omega \leq 1$).

Thus, it was observed that, increasing Ω up to 0.5, in the range $320 \leq Re \leq 440$ investigated, did not affect the flow regimes significantly, since just the *high frequency spiral frozen* mode at large Re was found. Figure 4.23(a) shows the phase diagrams $(C_{l_y} - C_{l_x})$ for several Reynolds numbers, where it can be observed how at low Re the flow is axisymmetric, and the transition towards the spiral frozen regime takes place between $Re = 380$ and 400, what would indicate that $Re_{c3}(\Omega = 0.5)$ does not differ much from the values reported for $0.225 \lesssim \Omega \leq 0.4$. However, when $\Omega = 0.55$, a new frozen mode takes place at $Re = 340$, as illustrated in Fig.4.23(b). The topology of this new regime resembles that of the frozen state present at large Re, as the streamwise vorticity iso-surfaces displayed in Fig.4.24 demonstrates. Nevertheless, this new co-rotating *spiral frozen* state seems to have a different nature since the Strouhal number associated with the rotation of the vortical structures is clearly lower than the one related to the *high-frequency frozen* regime, $St_{\omega h}$, as Table 4.7 lists, and considerably higher than the $St_{\omega l}$ of the *low-frequency frozen* regime at low Ω. Hence, we denote this new regime as *medium frequency frozen* regime, and identify the corresponding Strouhal as $St_{\omega m}$. If Ω is further increased up to 0.6, the new medium-frequency frozen state is present at $Re = 340$ and 380 (see Fig.4.23c and Table 4.7), and more precisely, it is shown that the

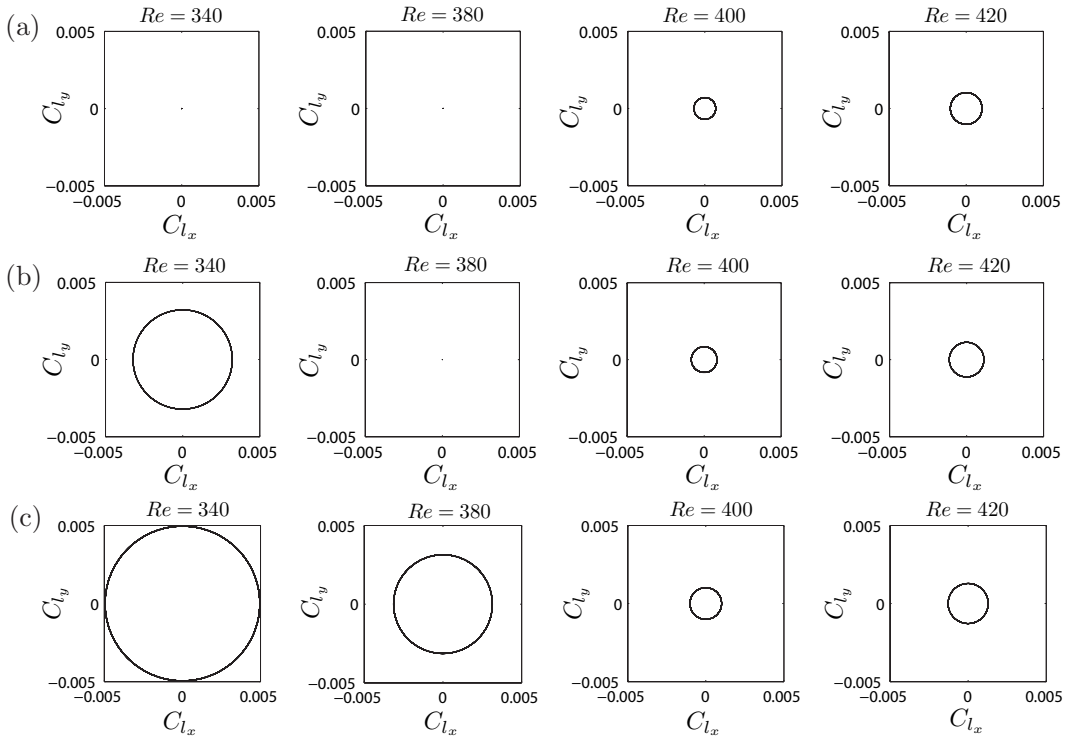

Figure 4.23: Phase diagrams, C_{l_x} vs C_{l_y}, for (a) $\Omega = 0.5$, (b) $\Omega = 0.55$ and (c) $\Omega = 0.6$, and different values of Re indicated in the plots.

transition towards this new state must lie between $Re = 380$ and 400. In fact, at $Re = 400$ the wake features a high-frequency frozen mode, so that within the interval $380 < Re < 400$ there might be two transitions as Re increases, that could give rise to two distinct patterns of regimes at the wake, depending whether the medium-frequency frozen bifurcates from an axisymmetric state or not. The first option would lead the flow from the medium-frequency frozen state towards an axisymmetric flow at $Re = Re_{c4}$, and, subsequently, at $Re = Re_{c3}$ towards the high-frequency frozen regime. On the other hand, the second option would consist in a first bifurcation from the medium-frequency state towards a non-linear combination of the latter state with the high-frequency mode, and later, at higher Re, a new bifurcation towards the high-frequency frozen state. This issue will be thoroughly addressed in Section 4.4, with the help of the BiGlobal stability analysis.

	$Re = 340$		$Re = 380$		$Re = 400$		$Re = 420$	
Ω	$St_{\omega m}$	C_l	$St_{\omega m}$	C_l	$St_{\omega h}$	C_l	$St_{\omega h}$	C_l
0.5	-	0	-	0	0.1519	0.0007	0.1538	0.0010
0.55	0.1106	0.0032	-	0	0.1583	0.0008	0.1589	0.0011
0.6	0.1134	0.0050	0.1134	0.0031	0.1621	0.0010	0.1656	0.0013

Table 4.7: Strouhal numbers associated to the lift components spectra, and lift coefficient, C_l, for $\Omega = 0.5, 0.55$ and 0.6, at $Re = 340, 380, 400$ and 420.

Finally, as it can be deduced from Fig.4.23, the new frozen mode has a higher lift coefficient than the high-frequency frozen state (see Table 4.7), what could be related to a higher eccentricity of the vortical structures and a larger growth of the amplitude of the unstable global mode with the distance to criticality, $|Re - Re_c|$.

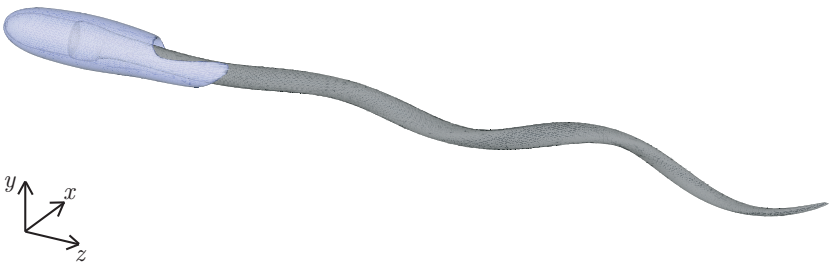

Figure 4.24: Isosurfaces of streamwise vorticity, $\varpi_z = 0.2$ (dark-coloured contour), and $\varpi_z = -0.2$ (light-coloured contour) for a spinning bullet-shaped body with $\Omega = 0.55$ and $Re = 340$.

4.4 Unstable global modes at the wake of a spinning $\ell = 2$ body

From a practical point of view, the region of axisymmetric flow is of great interest, since its border in the (Ω, Re)-plane provide with boundaries of complete stabilization for a spinning body with motion at moderate values of Ω and Re. On the other hand, as mentioned, three-dimensional numerical simulations are extremely time-consuming at marginally stable cases, rendering it expensive to characterize the transients and to determine the critical values of Re. Therefore, it was considered interesting to use the BiGlobal linear stability analysis as a tool to extend the previous work towards larger ranges of Ω and Re, and to explore its capability to predict stability properties of the axisymmetric flow and transitions arising from it. Furthermore, the BiGlobal linear stability analysis could provide valuable information about the physics at a considerably smaller cost.

In this sense, the stability results obtained for a range of rotation parameters $0 \leq \Omega \leq 1$ are presented, which are varied in increments of $\Delta\Omega = 0.05$ (or 0.01 within some distinguished regions). To properly capture the transitions from the axisymmetric wake towards other unstable states, different ranges of Reynolds numbers were covered for each value of Ω, with small increments of $\Delta Re = 10$ to accurately track the bifurcations that take place for increasing values of the rotation parameter, and to compare them with those reported in the precedent section. Finally, a discussion about the structure of the eigenfunctions and the nature of the unstable modes is also included.

4.4.1 Stability characteristics for $\Omega \leq 0.4$

According to the results reported in Chapters 2 and 3, the BiGlobal eigenvalue problem for the non-rotating bullet-shaped body revealed a picture consistent with the numerical findings described

therein. Indeed, it was found that, as the Reynolds number increases, the axisymmetric flow is subsequently destabilized by a non-oscillatory mode and an oscillatory one, both with azimuthal number $|m| = 1$. Likewise, in the case of a rotating body studied in the present chapter, the only unstable global modes that were found, at least within the ranges of Re and Ω investigated, have $m = \pm 1$, while those with $m = 0$ and $m = \pm 2$ are always stable. It is important to point out that in all the calculations reported hereafter, we set $m = -1$ without loss of generality, since the eigenvalue problem stated in Eq.(1.10) is invariant under the transformation $(m, \sigma, \hat{\mathbf{q}}) \rightarrow (-m, \sigma^*, \hat{\mathbf{q}}^*)$, where the asterisk denotes the complex conjugate.

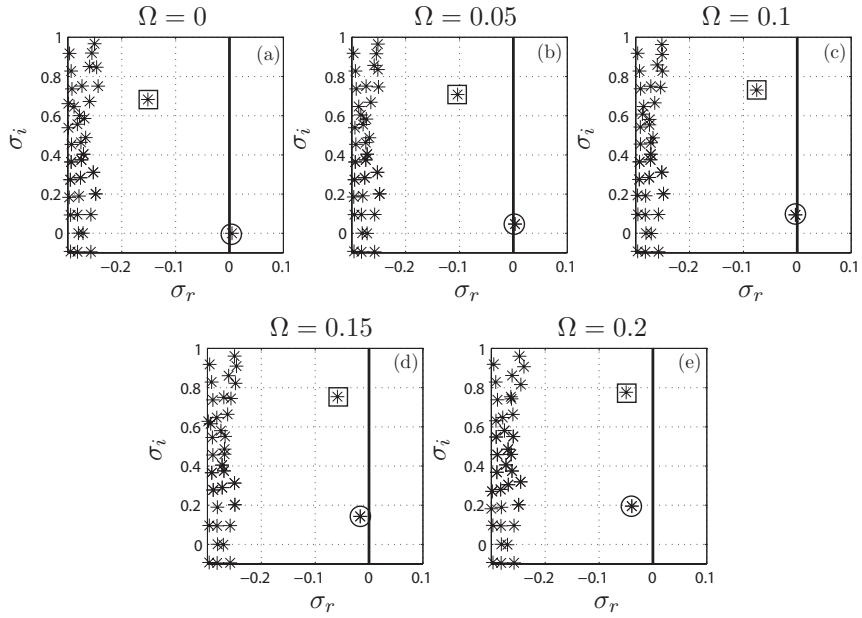

Figure 4.25: Eigenvalue spectra for $Re = 330$, $m = -1$ and: (a) $\Omega = 0$, (b) $\Omega = 0.05$, (c) $\Omega = 0.1$, (d) $\Omega = 0.15$ and (e) $\Omega = 0.2$. The circled mode stands for the LF mode (SS mode at $\Omega = 0$), while the squared one represents the HF mode.

The results of the BiGlobal stability analysis reported herein are in good agreement with the direct numerical simulations of the rotating body. As an example, the effect of rotation on the stability of the axisymmetric state for $Re = 330$ and $m = -1$ is illustrated in Fig. 4.25, where the global eigenvalue spectrum is plotted for several values of Ω in the range $0 \leq \Omega \leq 0.2$. In the case without rotation, shown in Fig. 4.25(a), there is only one unstable eigenvalue (circled), whose imaginary part is zero and is responsible for the SS mode (see Chapter 2). The second least stable eigenmode appearing in Fig. 4.25(a) (squared) is stable and oscillatory, being related with the RSP mode that appears at higher values of the Reynolds number (see Chapter 2). In the presence of body rotation, Figs. 4.25(b)-(e) reveal that the leading eigenmode is no longer steady, as in the case without rotation, being substituted by an eigenmode with a non-zero imaginary part that will hereafter be referred to as *low frequency mode* or LF mode. The instability of the LF mode is responsible for the bifurcation towards the *frozen state* described above (see Fig. 4.3b). Moreover, as expected from the characteristics of the frozen state revealed by previous direct numerical simulations, the angular frequency of the LF mode, σ_i, increases with Ω, and it is

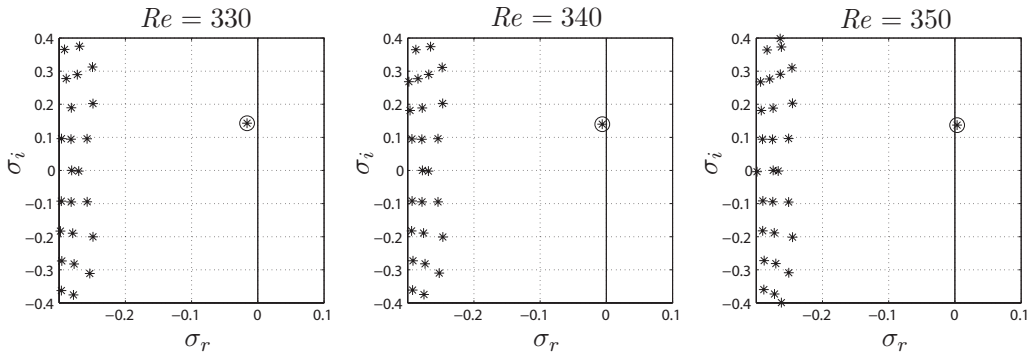

Figure 4.26: Eigenvalue spectra for $\Omega = 0.15$, $m = -1$ and: (a) $Re = 330$, (b) $Re = 340$ and (c) $Re = 350$.

stabilized by rotation, since increasing Ω decreases the real part of the corresponding eigenvalue, σ_r. For the particular value of $Re = 330$, the LF mode becomes neutrally stable at a critical value of $\Omega \simeq 0.1$ (Fig. 4.25c). Thus, the linear stability analysis predicts that the axisymmetric state is stable for $Re = 330$ and $\Omega \gtrsim 0.1$, in agreement with previous numerical simulations (see Section 4.3.1). On the other hand, the oscillatory mode related with the RSP state in the case without rotation (squared eigenvalue in Fig. 4.25) is destabilized by the spin together with an increase in its frequency, since the corresponding values of σ_r and σ_i increase with Ω. Considering that reflectional symmetry is not preserved when the body spins, it seems reasonable to denote this eigenmode as the *high frequency mode* or HF mode.

Figure 4.26 reveals that, for a constant value of $\Omega = 0.15$, the flow is destabilized as Re increases, since the real part of the leading eigenmode (LF mode) becomes larger and eventually crosses the imaginary axis at a critical value of the Reynolds number Re_{c1}. To compute the value of Re_{c1} we take advantage of the fact that, close to the transition, the growth rate σ_r of the leading eigenvalue increases linearly with Re, as pointed out in[17] (see also Fig. 4.27a). Thus, we obtain Re_{c1} by linearly interpolating the values of σ_r obtained for two different values of Re close to the marginal conditions. In the particular case with $\Omega = 0.15$ (Fig. 4.26), the critical Reynolds number is $Re_{c1}(\Omega = 0.15) \simeq 346.5 > Re_{c1}(\Omega = 0) \simeq 325.2$, so that rotation stabilizes the first bifurcation. From the stability results it is also deduced that the frequency of the LF mode, σ_i, barely depends on Re for a fixed value of Ω. Note that both findings are in agreement with the numerical simulations reported in Section 4.3.1. Moreover, for $Re > Re_{c1}$, the values of the Strouhal number predicted by the stability analysis, namely $St = \sigma_i/2\pi$, are in good quantitative agreement with those extracted from the numerical simulations close to criticality, corresponding to $St_{\omega l}$. Consequently, our linear stability analysis is able to properly capture the main features of the first bifurcation from the axisymmetric flow to the frozen state. Indeed, Table 4.8 shows the values of Re_{c1} obtained from the numerical simulations, Re_{c1}^{DNS} and from the stability analysis, Re_{c1}^{GLS}, for different values of the rotation parameter Ω. Also shown in Table 4.8 are the values of St under slightly supercritical values of the Reynolds number corresponding to each value of Ω, as well as the relative errors in both predictions.

The picture described above applies to a range of values of the rotation parameter $0 < \Omega \lesssim 0.2$, for which the LF mode is the only relevant one to understand the bifurcation scenario at increasing

Ω	Re_{c1}^{GLS}	St^{GLS}	Re_{c1}^{DNS}	St^{DNS}	$\epsilon_{Re_{c1}}(\%)$	$\epsilon_{St}(\%)$
0	325.21	0	319	0	1.9467	0
0.05	326.99	0.00743	323.5	0.00772	1.0788	3.7565
0.1	333.56	0.01466	332.3	0.01532	0.3792	4.3081
0.15	346.49	0.02182	347.5	0.02298	0.2906	5.0479
0.2	370.2	0.02802	375.4	0.02872	1.3852	2.4373

Table 4.8: The values of Re_{c1} and St predicted by the global stability analysis (GLS) for different values of Ω (St obtained at $Re = 330, 340, 350$ and 380 for $\Omega = 0.05, 0.1, 0.15$ and 0.2, respectively), compared with those obtained from the numerical simulations (DNS). The relative errors, $\epsilon_f(\%) = |f_{GLS} - f_{DNS}|/f_{DNS} \times 100$, being f either Re_{c1} or St, are also shown.

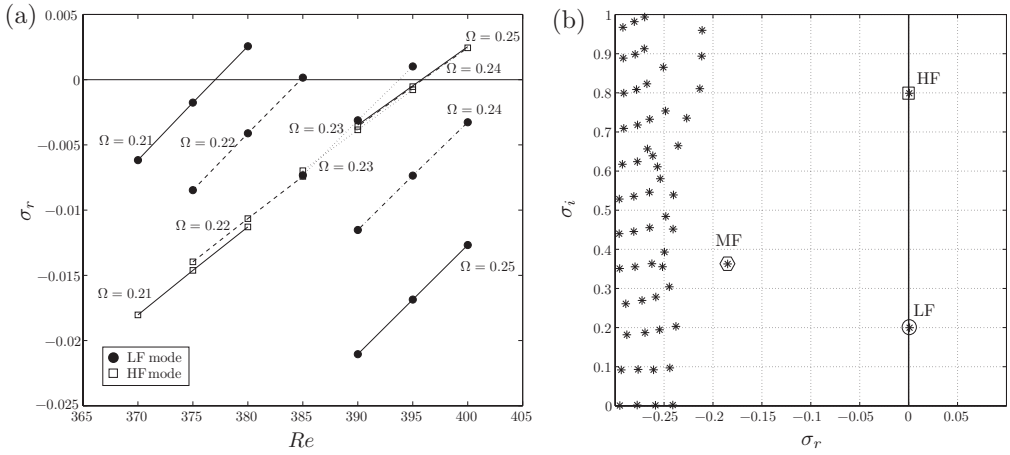

Figure 4.27: (a) Growth rate, σ_r, as a function of Re for the two leading eigenvalues, namely the LF mode (•) and the HF mode (□), for $0.21 \leq \Omega \leq 0.25$ and $m = -1$ (binding lines represent linear fits); and (b) eigenvalue spectrum for $\Omega = 0.232$, $Re = 395$ and $m = -1$.

Re. However, as pointed out before (see Fig. 4.25), at $\Omega = 0.2$ the growth rates of the LF and HF modes are similar for a slightly subcritical Reynolds number $Re = 330 < Re_{c1}$. Thus, it is expected that the HF mode plays a role at higher values of Ω. In fact, the numerical simulations (see Section 4.3.3) revealed that, for $\Omega = 0.25$ and increasing Re, the flow undergoes a bifurcation at $Re = Re_{c3}$ towards a different *frozen spiral regime*, similar to that depicted in Fig.4.15(c), and characterized by the rotation of the flow structures in the wake without change in shape or intensity, but with an angular frequency much larger than that associated with the frozen state emerging from the LF mode. Hence, a natural explanation for the onset of the spiral frozen regime is that the HF mode becomes destabilized at a smaller value of Re than the LF mode for sufficiently large values of Ω and, in particular, for $\Omega = 0.25$. Indeed, Fig. 4.27(a) shows the dependence of σ_r with Re for both the LF and HF modes, calculated for several values of the rotation parameter in the range $0.2 \leq \Omega \leq 0.25$. The results of Fig. 4.27(a) reveal that, for a certain value of the rotation parameter Ω_{c1} within the range $0.23 < \Omega_{c1} < 0.24$, the LF and HF modes become unstable at the *same* critical value of the Reynolds number, i.e. $Re_{c1}(\Omega_{c1}) = Re_{c3}(\Omega_{c1})$, where we have denoted Re_{c3} as the

Ω	Re_{c3}^{GLS}	St^{GLS}	Re_{c3}^{DNS}	St^{DNS}	$\epsilon_{Re_{c3}}(\%)$	$\epsilon_{St}(\%)$
0.25	395.78	0.1290	388.09	0.1288	1.9815	0.1553
0.3	397.10	0.1334	388.87	0.1321	2.1164	0.9841
0.4	395.34	0.1414	388.20	0.1417	1.8393	0.2117

Table 4.9: Critical Reynolds numbers for the destabilization of the HF mode, Re_{c3}, and Strouhal numbers obtained at $Re = 400$, for several values of Ω. Also shown are the values obtained in Section 4.3.3 with direct numerical simulations (DNS). The relative errors, $\epsilon_f(\%) = |f_{GLS} - f_{DNS}|/f_{DNS} \times 100$, being f either Re_{c3} or St, are also listed.

critical Reynolds number at which the HF mode is destabilized, according to the corresponding definition in Section 4.3.3. Moreover, it is also deduced from Fig. 4.27(a) that $Re_{c1} < Re_{c3}$ (resp. $Re_{c3} > Re_{c1}$) for $\Omega < \Omega_{c1}$ (resp. $\Omega > \Omega_{c1}$). Therefore, the first bifurcation taking place in the flow at increasing Reynolds numbers crucially depends on the value of Ω, such that the LF and HF modes are first destabilized for $\Omega < \Omega_{c1}$ and $\Omega > \Omega_{c1}$, respectively. The analysis of the eigenvalues provides the values $\Omega_{c1} \simeq 0.232$ and $Re_{c1,3} \simeq 395$, as Fig. 4.27(b) depicts. Another noteworthy feature of the spectrum displayed in Fig. 4.27(b) is the existence of a third distinguished eigenvalue in the stable half-plane ($\sigma_r < 0$), whose frequency is intermediate between those of the LF and HF modes. This new mode will be denoted as *medium frequency mode* or MF mode, and will be shown below to become dominant at large enough values of Ω.

According to the numerical simulations (Section 4.3.3), the nonlinear spiral frozen state (see Fig.4.15c) prevails for $\Omega > \Omega_{c1} \simeq 0.232$, up to at least $\Omega = 0.4$. In addition the simulations revealed that Re_{c3} barely changes with Ω. Both results are in agreement with the behavior of the HF mode, as can be deduced from Fig. 4.28, which shows the spectra for $\Omega = 0.25, 0.3$ and 0.4 in the vicinity of the transition, and also from Table 4.9. Figure 4.28 and Table 4.9 indicate that, for $0.25 \leq \Omega \leq 0.4$, the HF mode is destabilized within a range of Reynolds numbers $390 \leq Re \leq 400$, in fair agreement with the values obtained in Section 4.3.3. Table 4.9 shows that, although the relative errors between GLS and DNS results are slightly larger than those obtained for Re_{c1} (see Table 4.8), they are nevertheless below 2.12%. Concerning the characteristic frequencies, Table 4.9 displays the values of St obtained at a slightly supercritical Reynolds number $Re = 400$, where it can be seen that the relative differences between the GLS and DNS results are below 1%. Moreover, Fig. 4.28 shows that the LF mode is stabilized as Ω increases at constant Re. At the same time, the MF mode becomes destabilized, although it is still stable at $\Omega = 0.4$ (see Figs. 4.28c-d).

Figure 4.29 shows the real part of the axial velocity eigenfunction, $\Re(\hat{w})$, normalized with $\|\hat{q}\|_\infty$, associated to the leading eigenvalue obtained at three different slightly supercritical conditions, namely $(\Omega, Re) = (0, 330)$, $(0.15, 350)$ and $(0.25, 400)$ in Figs. 4.29(a)-(c), respectively. In the case without rotation, $\Omega = 0$, Fig. 4.29(a) shows the steady elongated structures obtained in Chapter 2, that lead to the SS state in the nonlinear regime (see Chapter 2). However, when rotation is applied, the spatial structure of the wake changes qualitatively depending on the value of Ω compared with the critical value Ω_{c1}. Indeed, for a value of the rotation parameter $\Omega = 0.15 < \Omega_{c1}$, Fig. 4.29(b) reveals a pattern with a large but finite axial wavelength, corresponding to the LF eigenmode, that is responsible for the low-frequency frozen state found in the direct numerical simulations (see Section 4.3.3). Let us point out that the frozen structures found in the DNS have a wavelenth $\lambda_{DNS} \sim 39$ in the near wake, while the LF eigenmode provides $\lambda_{LF} \sim 43$, in fair agreement with

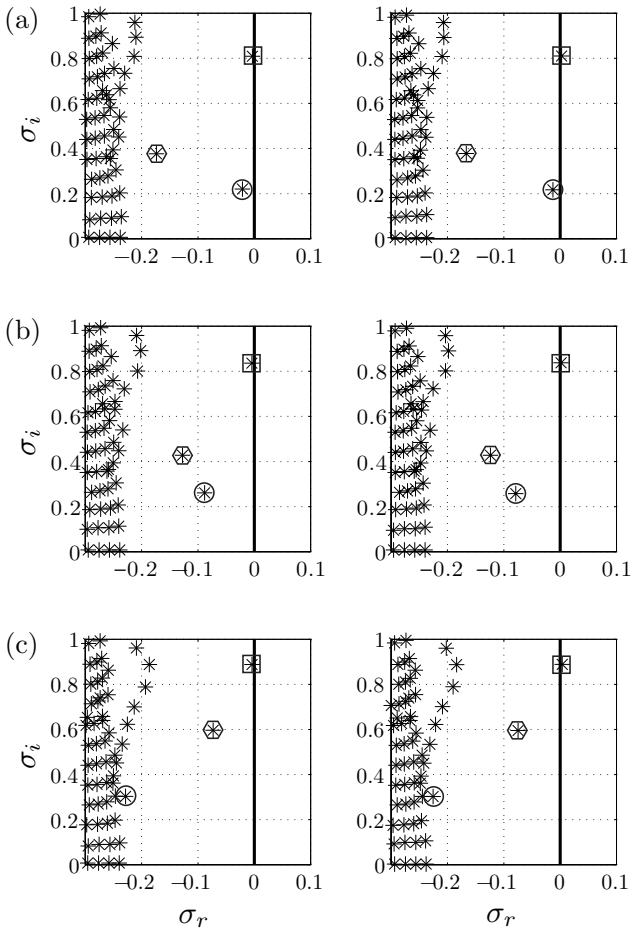

Figure 4.28: Eigenvalue spectra for $Re = 390$ (left column), $Re = 400$ (right column) and $m = -1$ when (a) $\Omega = 0.25$, (b) $\Omega = 0.3$ and (c) $\Omega = 0.4$.

the DNS results (the viscous dissipation that weakens the vortices far downstream and hinders their identification accounts for the small discrepancies). On the other hand, Fig. 4.29(c) shows that, when $\Omega = 0.25 > \Omega_{c1}$, the HF eigenmode leads to a wake pattern with a much smaller characteristic axial wavelength, being $\lambda_{HF} \sim 6.4$, while the DNS provides a similar value of $\lambda_{DNS} \sim 6.6$ for the corresponding frozen spiral state (Section 4.3.3).

A fundamental feature of the flow in the supercritical regime is the co-rotating or counter-rotating nature of the bifurcated structures. The numerical simulations performed in Section 4.3.3 indicated that the wake structures are co-rotating in both, the low-frequency frozen regime, as well as in the high-frequency spiral frozen state, in agreement with the global stability analysis performed herein. Indeed, Fig. 4.30 depicts one period of the temporal evolution of the normalized axial velocity disturbance,

$$\Re(w') = \frac{|\hat{w}|}{\|\hat{q}\|_\infty} e^{\sigma_r t} \cos\left[\sigma_i t + m\theta + \arctan\left(\frac{\Im(\hat{w})}{\Re(\hat{w})}\right)\right], \tag{4.4}$$

for two different cases dominated either by the LF mode (Fig. 4.30a, where $\Omega = 0.15$ and $Re = 350$) or the HF mode (Fig. 4.30b, with $\Omega = 0.25$ and $Re = 400$). It is deduced from Fig. 4.30 that,

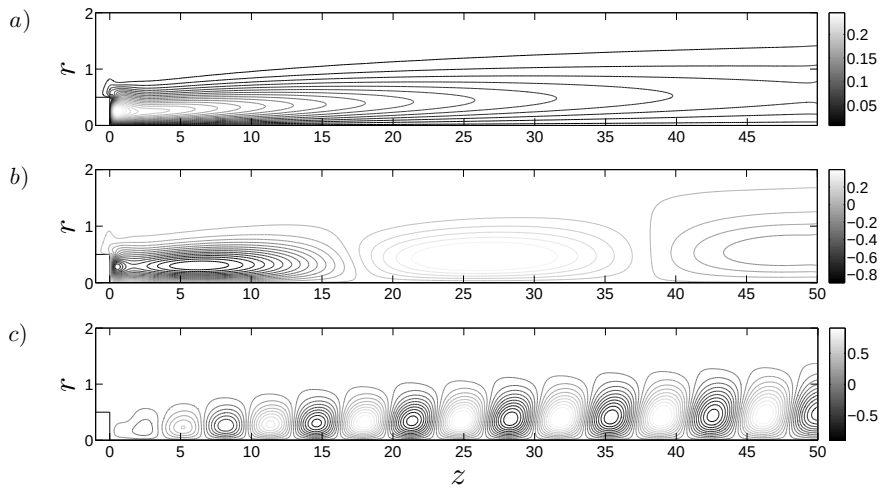

Figure 4.29: Isocontours of the real part of the normalized axial velocity eigenfunction, $\Re(\hat{w})/\|\hat{q}\|_\infty$, associated to the leading eigenvalue at (a) $\Omega = 0$ and $Re = 330$, (b) $\Omega = 0.15$ and $Re = 350$, and (c) $\Omega = 0.25$ and $Re = 400$.

in both cases, the disturbances rotate in the positive azimuthal direction, i.e. with the angular velocity vector oriented in the positive z-direction, in agreement with the co-rotation found in the numerical simulations. It is worth pointing out that the same conclusion can be inferred directly from the following argument: the infinitesimal time increment of the disturbance phase, $\sigma_i dt + m d\theta$, is zero in a reference frame that rotates with the angular velocity of the structures, namely $\mathrm{d}\theta/\mathrm{d}t = -\sigma_i/m$. Therefore, a given global eigenmode corresponds to a counter-rotating structure if σ_i and m have the same sign, while it is co-rotating if σ_i and m have opposite signs, as in the case of the LF, MF and HF modes found in the present work.

4.4.2 Stability characteristics for $0.4 < \Omega \leq 1$

Once the stability analysis has been successfully applied to understand the transitions found in the numerical simulations (see Section 4.3.3), in the range of rotation parameters $\Omega \leq 0.4$, the present section is devoted to report the results of an extended investigation, where the rotation parameter is increased up to a value $\Omega = 1$.

Figure 4.31 shows that, as Ω increases, the axisymmetric state may be destabilized by either the MF or the HF eigenmodes, depending on the value of Re. In particular, although at $Re = 400$ the HF mode is still responsible for the transition found by increasing Ω, the MF eigenvalue is first destabilized at $\Omega \simeq 0.55$ at a smaller value of $Re = 340$. The latter result is representative of the transition scenario at high enough values of Ω and low enough values of Re. However, the behavior of the MF mode at constant Ω and varying Re is more complicated than those found for the LF and HF modes. Indeed, from Fig. 4.32 it is deduced that, for $\Omega = 0.55$, the MF mode is unstable within a range of Reynolds numbers $Re^l_{c4} \approx 220 \leq Re \leq Re^h_{c4} \approx 340$. The real part of the normalized axial velocity associated to the MF eigenmode, $\Re(\hat{w})/\|\hat{\mathbf{q}}\|_\infty$, obtained for a rotation velocity $\Omega = 0.55$ at $Re = 340$ is displayed in Fig. 4.31(a) (bottom plot), where it can be seen that

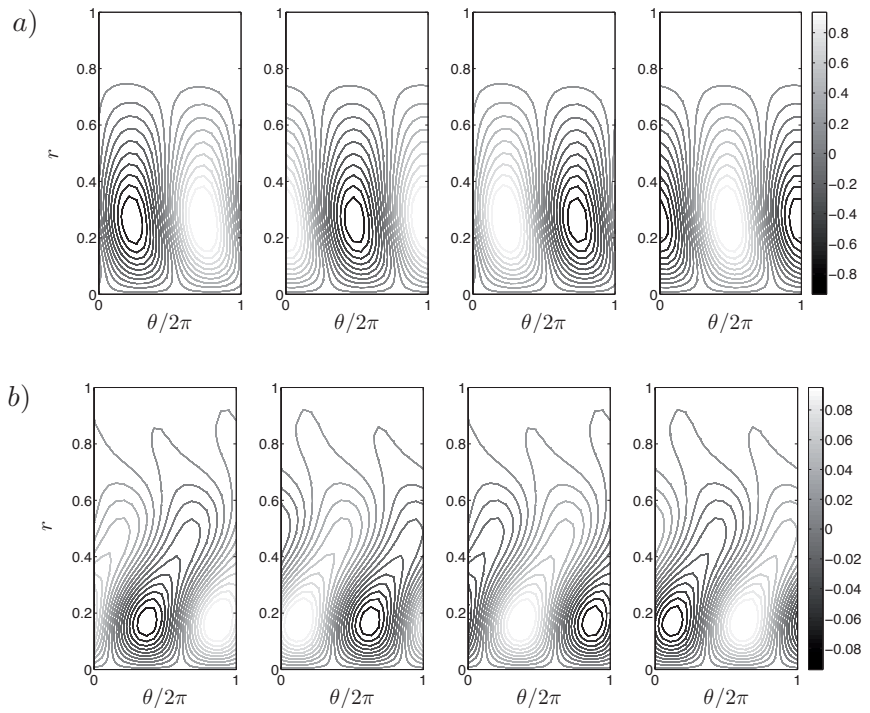

Figure 4.30: Snapshots of the temporal evolution of the contours of normalized axial velocity disturbance, $\Re(w')$, defined in Eq.(4.4), associated to the leading eigenmode, evaluated at $z = 1$, for (a) $\Omega = 0.15$ and $Re = 350$, (b) $\Omega = 0.25$ and $Re = 400$. The time interval between snapshots is $T/4$, being $T = 2\pi/\sigma_i$.

the spatial structure is similar to that of the HF mode, shown in Fig. 4.31(b).

According to the numerical simulations (see Section 4.3.4), the destabilization of the MF mode leads the flow towards the co-rotating *medium-frequency spiral frozen* regime. In this sense, Table 4.10 shows the values of the frequencies predicted by the numerical simulations and the global stability analysis. Note the good quantitative agreement found between them, with relative errors $\epsilon_{St} < 4\%$. Concerning the periodicity of the axial structures, the results from Direct Numerical Simulations and Global Linear Stability analyses, respectively, provide local wavelengths $\lambda_{DNS} \sim 8$ and $\lambda_{GLS} \sim 7.6$ in the near wake, for $\Omega = 0.55$ and $Re = 340$.

	$Re = 340$			$Re = 400$		
Ω	St_{DNS}	St_{GLS}	$\epsilon_{St}(\%)$	St_{DNS}	St_{GLS}	$\epsilon_{St}(\%)$
0.55	0.1106	0.1138	2.768	0.1583	0.1567	0.960
0.6	0.1134	0.1175	3.527	0.1621	0.1626	0.297

Table 4.10: Strouhal numbers obtained through global stability analysis, St_{GLS}, and three-dimensional numerical simulations, St_{DNS}, determined numerically, for $\Omega = 0.55$ and $\Omega = 0.6$, at $Re = 340$ and 400. The relative error, $\epsilon_{St}(\%) = |St_{GLS} - St_{DNS}|/St_{DNS} \times 100$, is also shown.

The neutral curve associated to the MF mode was tracked within the ranges of Reynolds

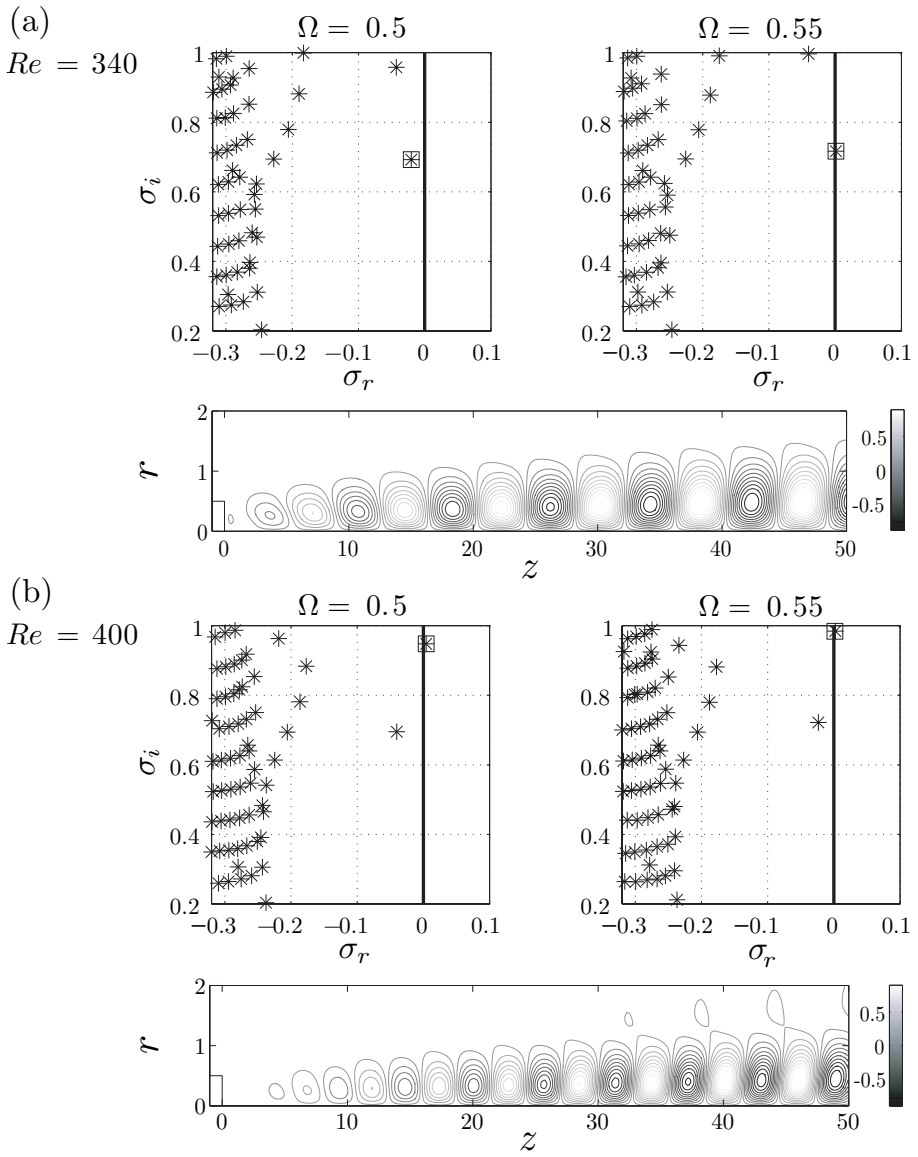

Figure 4.31: Eigenvalue spectra and contours of the real part of the normalized axial velocity leading eigenfunction, $\Re(\hat{w})/\|\hat{\mathbf{q}}\|_\infty$, for (a) $Re = 340$ and (b) $Re = 400$. Each subfigure, (a) and (b), displays spectra for $\Omega = 0.5$ (left top) and $\Omega = 0.55$ (right top), and contours of $\Re(\hat{w})/\|\hat{\mathbf{q}}\|_\infty$ for $\Omega = 0.55$ (bottom).

number and rotation parameter $170 \leq Re \leq 400$ and $0.5 \leq \Omega \leq 1$, respectively. The outcome of this procedure is shown in Fig. 4.33, where the critical conditions obtained from the direct numerical simulations are also displayed. The corresponding unstable region, denoted as IV in Fig. 4.33, exists only for $\Omega \geq \Omega_{min} \simeq 0.509$ approximately, for which the critical Reynolds number is $Re_{c4}(\Omega_{min}) \simeq 274$. Note from Fig. 4.33 that Re_{c4} increases with Ω for $Re > Re_{c4}(\Omega_{min})$, while the value of Re_{c3} remains almost constant, both marginal curves intersecting at $\Omega_{c2} \simeq 0.625$ and $Re_{c4}(\Omega_{c2}) \simeq 396$. On the other hand, Re_{c4} decreases as Ω increases for $Re < Re_{c4}(\Omega_{min})$, inferring

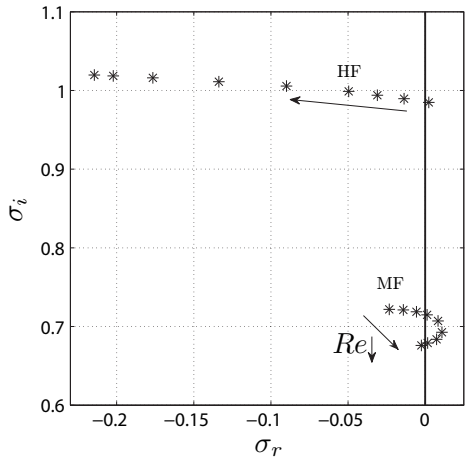

Figure 4.32: Eigenvalue spectra obtained for a body rotating with a velocity $\Omega = 0.55$ at $Re = 400, 380, 360, 340, 300, 270, 240, 220$ and 210. Arrows indicate the direction of decreasing Re.

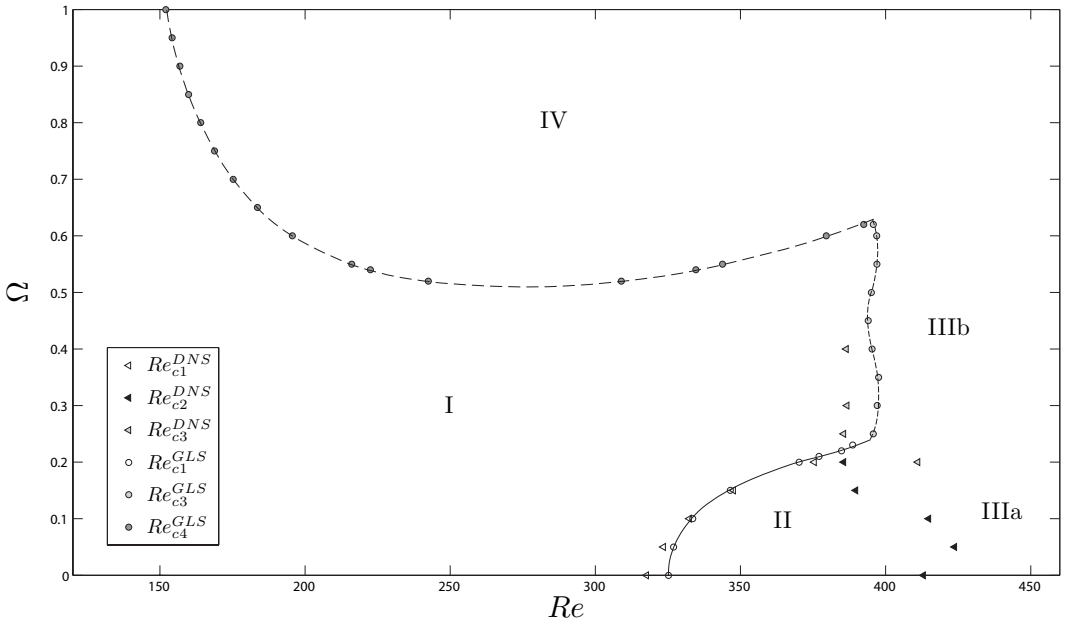

Figure 4.33: Bifurcation diagram in the (Ω,Re) parameter plane, according to the results of numerical simulations (DNS) and global stability analysis (GLS). The different wake states correspond to the following regions: I axisymmetric, II frozen, IIIa spiral unsteady, IIIb high-frequency spiral frozen and IV medium-frequency spiral frozen.

the possible existence of an asymptote for $\Omega > 1$, so that region IV could be bounded by a region of axisymmetric flow (regime I) at low enough values of Re independently of the value of Ω. Finally, in the region where both the HF and MF modes coexist, we expect the existence of a new unsteady regime due to the nonlinear interaction between both global modes, although further numerical

simulations will be required to clarify this issue.

4.4.3 Physical interpretation of results

The unstable modes described so far are the outcome of the deformation through centrifugal force and azimuthal shear of the axial shear modes associated with the wake of non-rotating bodies, and their behavior and onset could be explained through the competition among these effects. According to Johnson & Patel [60], the axisymmetry breaking bifurcation that takes place in the wake of a sphere is the consequence of an azimuthal instability, whereby an azimuthal pressure gradient promotes the flow between upper and lower vortices core in the near wake (see Fig.2.6b for clarification) and opens the recirculation bubble releasing fluid from it, giving rise to axial vorticity tails at the wake. Due to the planar symmetry of the SS mode, the flow between cores occurs in both positive and negative azimuthal directions. When rotation is applied, at the base, an axisymmetric linear distribution of azimuthal velocity is imposed. Then, the above referred flow induced between the two vortex cores is reduced in the azimuthal direction opposite to the spin, diminishing the intensity of the axial vorticity thread in this direction, and promoting the one rotating with the base (as can be observed in Fig.4.3b, it results into an injection of positive vorticity from the base). This effect becomes stronger as the angular velocity of the body increases, until eventually the axisymmetry is retrieved at a critical value of Ω, what is indeed observed for $Re < 400$.

To shed some light on the physical mechanisms governing the stability of the axisymmetric state, Fig. 4.34 shows the evolution with z of axial velocity and static pressure at the axis, $W(r = 0, z)$ and $P(r = 0, z)$ respectively, as well as the downstream evolution of the radial velocity at $r = 0.5$, $U(r = 0.5, z)$, for several values of Ω and $Re = 400$, close to the marginal conditions for a wide range of Ω. From the results of Fig. 4.34(a) it is deduced that, as Ω increases, the recirculation region enlarges and the maximum backflow velocity decreases, leading to a decrease in the radial gradient of axial velocity, similar to the effect of base bleed [135]. The resulting reduction of axial shear stabilizes the wake, since reverse flow is known to promote local absolute instabilities [98]. In addition, Fig. 4.34(b) reveals a decrease in the radial velocity close to the trailing edge, $(r = 0.5, z = 0)$, thereby reducing the outwards radial displacement of the incident boundary layer. Clearly, these effects contribute to the stabilization of the wake observed for low values of Ω, leading to the recovery of the axisymmetric steady state for $Re < 400$. However, it is also deduced from Fig. 4.34(b) that, when Ω becomes large enough, this stabilizing effect is hindered by the centrifugal mechanism, that induces the increase of the radial velocity near the trailing edge. At the same time, Fig. 4.34(a) shows the appearance of an inflection point in the centerline axial velocity near the body (at $z = 0.3$ approximately), that at higher angular velocities could form a second core of recirculation and constitute a phenomenon that may resemble a *vortex breakdown*, although this hypothesis should be explore in the future. This is a consequence of the existence of a weak adverse axial pressure gradient near the body base (Fig. 4.34c), that might contribute to the destabilization of the axisymmetric flow at large values of Ω. The results depicted in Figure 4.34(c) also show that the base pressure decreases as Ω increases, leading to an increase in the drag force (as the numerical simulations already pointed out), while the axial location of the minimum pressure displaces downstream, reflecting the enlargement of the recirculation region.

Let us finally discuss our results in the light of related studies that deal with the stability of rotating flows, as well as with the theory of equivariant bifurcations. The introduction of

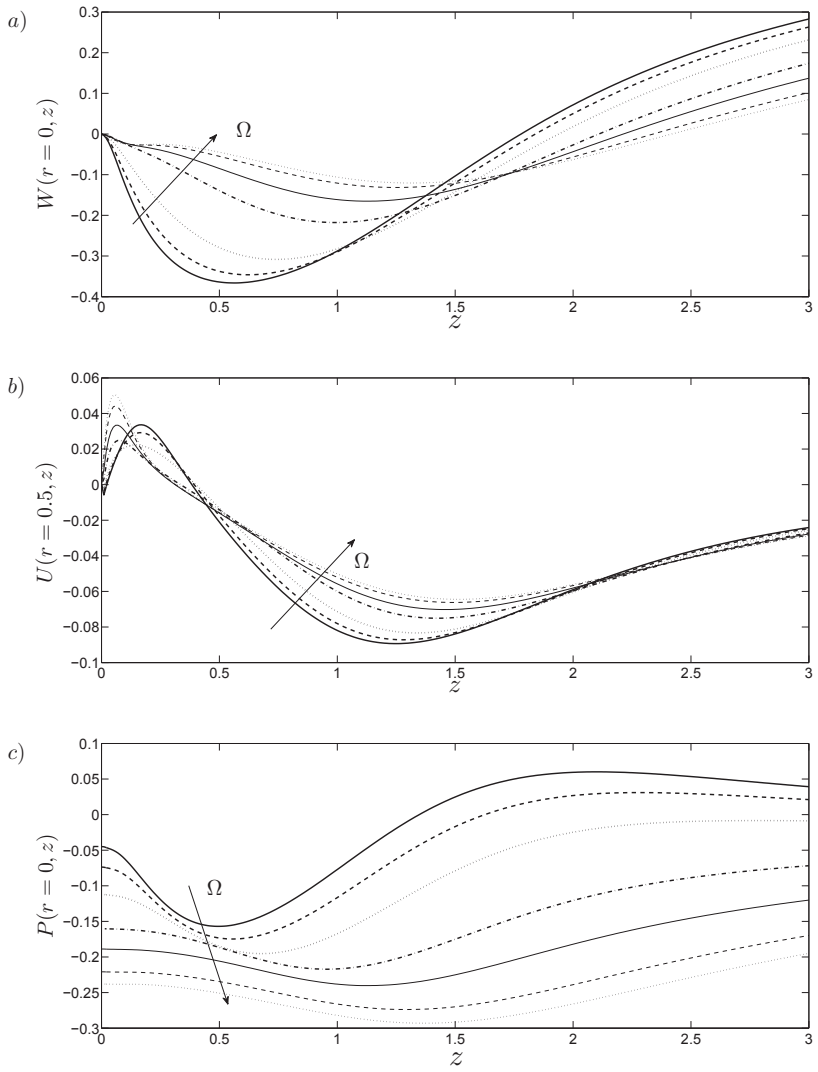

Figure 4.34: Effect of the rotation parameter Ω on the base flow (a) axial velocity and (c) pressure at the axis $r = 0$, $W(r = 0, z)$ and $P(r = 0, z)$ respectively, and (c) radial velocity U at $r = 0.5$, $U(r = 0.5, z)$, for $\Omega = 0, 0.15, 0.25, 0.4, 0.5, 0.6$ and 0.65, when $Re = 400$.

body rotation results in axisymmetry breaking through supercritical Hopf bifurcations (see Section 4.3.2), associated to the LF, MF and HF eigenmodes found in the stability analysis. Note that this bifurcation behavior has been previously reported in other configurations like enclosed rotating flows [81], or a counterrotating Taylor-Couette flow [75, 29]. This fact is a consequence of the invariance of the base flow under arbitrary rotations around the symmetry axis, constituting a $SO(2)$-symmetric configuration which, as revealed by the theory of equivariant bifurcations, leads to *rotating waves*, i.e. solutions that are steady in a reference frame that rotates with an appropriate angular velocity [123]. The numerical simulations performed clearly demonstrate that the low-frequency, medium-frequency and high-frequency frozen wakes, that appear as a consequence of the destabilization of the LF, MF and HF eigenmodes respectively, indeed match the characteristics

of *rotating wave* states On the other hand, once the next-to-leading eigenmode becomes unstable the wake adopts a quasiperiodic motion with two characteristic frequencies through another Hopf bifurcation (see Section 4.3.2), featuring an intrinsic unsteadiness that leads to vortex shedding in the wake, similar to the *modulated wave* states that appear in Taylor-Couette Flow [44] and other enclosed swirling flows [13].

4.5 Conclusion

Numerical simulations and global linear stability analysis were performed to study the laminar flow past a spinning bullet-shaped body of length-to-diameter ratio $\ell = 2$, with moderate dimensionless rotation velocity, $0 \leq \Omega \leq 1$ for $Re < 450$. They revealed that the sequence of bifurcations that take place at increasing values of Re, change considerably with Ω. In particular, a small amount of rotation was shown to modify the unstable modes observed at $\Omega = 0$, namely the steady-state (SS) and the reflectional symmetry-preserving (RSP) modes. More importantly, it was found that spin acts as a stabilizing mechanism, since axisymmetry can be retrieved for $Re > Re_{cs}$ and moderate values of Ω, being linked this recovery of axisymmetry with the injection of even axial vorticity in the wake through the base.

Thus, according to numerical simulations, for $\Omega < 0.225$, the axisymmetry prevailing in the flow field at low values of Re is broken through a supercritical Hopf bifurcation at $Re_{c1}(\Omega)$, leading to a flow that is unsteady when observed from an inertial frame, denoted *low-frequency frozen state* (Region II in Fig. 4.19). The most prominent feature of the frozen regime is the fact that the wake performs a solid-body rotation with an angular velocity $\Omega_{sl} = 2\pi St_{\omega l}$, inducing constant values of lift and drag. Within this region, the angular velocity of the wake increases linearly with Ω, such that $\Omega_{sl}/\Omega \simeq 0.48$ in the range of Reynolds numbers studied here. This mode resembles the SS mode in non-rotating bodies since, in a reference system S' rotating with an angular velocity Ω_{sl}, the wake is steady. Although the frozen mode observed in the bullet-like body is similar to that reported in the case of a sphere [64, 104, 116, 113], some differences exist. Thus, unlike in the case of the sphere, where Re_{c1} decreases with Ω [113], rotation has a stabilizing effect on the bullet-shaped body, with Re_{c1} increasing with Ω. Consequently, a more detailed study would be needed to properly compare both geometries, and understand the differences observed.

If the Reynolds number is increased, a new transition takes place at Re_{c2}, characterized by a flow that is unsteady when analyzed from any reference system. The resulting *unsteady spiral wake* (Region IIIa of Fig. 4.19) is a combination of vortex shedding, similar to the RSP mode occurring at $\Omega = 0$, and the rotation of the wake caused by the spinning body. In this new regime, the lift and drag coefficients are no longer constant but oscillate with a characteristic shedding frequency, St_{vs}. However, the projection of $C_l(t)$ on any direction contained in the plane perpendicular to the axis, shows two characteristic frequencies at $St_{\omega l}$ and $St_{\mathrm{vs}} + St_{\omega l}$, the latter becoming dominant as Ω increases. Furthermore, this second transition is a supercritical Hopf bifurcation in the rotating frame S', and is strongly affected by the rotation rate. Indeed, the associated critical Reynolds number, Re_{c2}, initially increases with Ω for $0 < \Omega \lesssim 0.05$, but decreases for $\Omega \gtrsim 0.05$ until it coincides with Re_{c1} around $\Omega \simeq 0.225$.

At $\Omega \simeq 0.2$, a third transition takes place at $Re_{c3} > Re_{c2}$, giving rise to a new *spiral frozen regime* (Region IIIb of Fig. 4.19), where the structures are arranged in a frozen spiral whose angular velocity is given by $\Omega_{sh} = 2\pi St_{\omega h}$. The spectra of the lift components in Region IIIa

revealed that the angular velocity of the wake in Region IIIb derives from a lock-in phenomenon produced when Ω is increased within Region IIIa, since the structures progressively arrange and rotate at a pace that is initially defined by $St_{\omega l}$, but become locked to $St_{\omega l} + St_{\mathrm{vs}}$ in the vicinity of the bifurcation, where the spiral frozen mode emerges with $St_{\omega h} = St_{\omega l} + St_{\mathrm{vs}}$. However, unlike in the low-frequency frozen mode, the wake-to-body angular velocity ratio, Ω_{sh}/Ω, decreases as Ω increases. Moreover, this new frozen mode represents the only unstable mode found for $\Omega \geq 0.225$, so that the wake undergoes just one bifurcation, directly from the axisymmetric state to the frozen spiral regime, at Re_{c3}, whose value is nearly independent of Ω. Again, an equivalence can be found with the *high-frequency helical* mode found by Pier [113] for the sphere. Besides, the simulations performed in the range $0.4 < \Omega \leq 0.6$ showed the existence of a new frozen spiral regime at low values of Re, where the vortical structures co-rotate with an angular velocity, $\Omega_{sh} = 2\pi St_{\omega m}$, being $St_{\omega m} < St_{\omega h}$. Therefore, this new regime was denoted *medium-frequency spiral frozen* mode.

Concerning the effect of body rotation on the force coefficients, we found that the mean drag coefficient, $\overline{C}_d$, grows quadratically with Ω, independently of Re [128], whereas an abrupt reduction of the mean lift force, $\overline{C}_l$, is achieved for sufficiently large values of Ω. Indeed, our simulations revealed that $\overline{C}_l$ decreases slowly with rotation up to $\Omega \simeq 0.15$, while it plummets for $\Omega \gtrsim 0.15$, tending to a small constant value that decreases as Re decreases. Additionally, although no parametric characterization was done, it was shown that the medium-frequency frozen spiral state features a much higher lift force than in the high-frequency spiral frozen state for the same Ω.

On the other hand, a detailed characterization of the bifurcations and unstable modes, giving rise to the nonlinear regimes, found by means of the numerical simulations, was provided by the stability analysis, that showed a good agreement with the numerical simulations, completing the picture for wider ranges of Ω and Re. Thus, three different co-rotating linear global modes with azimuthal symmetry $m = -1$ were identified, each of them dominating the instability of the axisymmetric state in different regions of the (Re, Ω) parameter plane. The first mode was a *low-frequency mode*, destabilized for $\Omega \leq 0.232$ and $Re > Re_{c1}(\Omega)$, whose associated eigenfunction features structures with large axial wavelength, and is responsible for the nonlinear *frozen state* observed in the simulations. In the range of rotation parameters $0.232 < \Omega < 0.62$, a different *high-frequency mode* becomes destabilized for $Re > Re_{c3}(\Omega)$, with a much smaller axial wavelength, that gives rise, in the nonlinear regime, to the *high-frequency frozen spiral* state. Finally, a new *medium-frequency mode* was found, that is destabilized for $\Omega > 0.51$ within a range of Reynolds numbers that widens with increasing Ω, and whose nonlinear counterpart was identified with the *medium-frequency spiral frozen* state. Finally, the frozen nature of the nonlinear regimes arising through Hopf bifurcations from the axisymmetry, was explained in terms of *rotating waves* occurrence when the base flow presents a $SO(2)$ symmetry, as happens in the case of steady swirling flows.

CHAPTER
FIVE

Conclusions and future work

5.1 General conclusions

The work presented in this Thesis focuses on the characterization of laminar wakes behind axisymmetric blunt-based bodies with rounded ellipsoidal nose (bullet-shaped bodies) at low Reynolds numbers, which are of high interest in numerous engineering applications. Stability properties and flow regimes have been investigated with the help of hot-wire experiments, three-dimensional numerical simulations and BiGlobal stability analysis, allowing us to describe the unstable global modes and bifurcations taking place at the flow, providing with valuable information for possible control strategies in wakes behind slender bluff bodies. Besides, several passive control methods have been applied satisfactorily to stabilize the wake behind bullet-shaped bodies, namely, base bleed, rear cavities and spin, which in general allow to retrieve the axisymmetry under certain conditions. In the following, we collect the main conclusions and ideas that were developed and exposed in Chapters 2, 3 and 4.

Chapter 2 has been devoted to analyze the natural laminar wake behind a bullet-shaped body, focusing on the instabilities taking place for increasing Re up to $Re = 2000$, and evaluating the the effect of the body length-to-diameter ratio in the range $1 \leq \ell \leq 10$ on the instability properties. Thus, it has been shown that a first steady bifurcation takes place at a critical value of the Reynolds number, $Re_{cs}(\ell)$. A steady bifid wake develops from the bifurcation, consisting of a pair of symmetric elongated counter-rotating streamwise vortices (SS mode). A second oscillatory bifurcation has been shown to exist at a higher value of the Reynolds number, $Re_{co}(\ell)$. As in the case of the sphere, the vortex shedding emerging from this transition preserves the symmetry, constituting a *reflectional symmetry preserving mode* (RSP mode) [34]. Both bifurcations are shown to occur due to the destabilization of two subsequent $|m| = 1$ global linear modes, and their onset values increase with ℓ. Besides, when compared to experiments and numerical simulations, the BiGlobal linear stability analysis overestimates the value Re_{co}, as a consequence of the use of an axisymmetric basic flow for $Re > Re_{cs}$, being this error considerably higher than in the case of the sphere [102, 112] and disk [102, 34], and growing the difference $(Re_{co}^{GLS} - Re_{co}^{exp})$ with ℓ. These differences have been discussed in terms of the relative gap $\Delta = (Re_{co} - Re_{cs})/Re_{cs}$ for the disk [34] ($\Delta \ll 1$), but neither the value of Δ nor the saturated amplitude of the the steady state mode evaluated at Re close to Re_{co}, larger in the case of the sphere than in the bullet-shaped $\ell = 2$ body, can explain alone the discrepancies encountered regarding the sphere. Moreover, a new Hopf bifurcation at $Re_{co2} \simeq 493.2$ has been reported, leading towards a regime with vortex shedding modulation of low frequency and locking process at higher Re. Finally, the supercritical nature of the bifurcations and the transients have been determined with the Stuart-Landau model,

which describes properly the non-linear behavior of the wake for a range of $Re > Re_{co}$ with $(Re - Re_{co}) \sim 0.1 Re_{co}$.

In Chapter 3 we have analyzed the influence on the stability properties of the wake behind the $\ell = 2$ body of base bleed and rear cavities. The stabilizing effect of homogeneous base bleed have been discussed in the parameter plane (Re, C_b), that outlines how the bifurcations towards SS and RSP modes are modified by base bleed. Two critical bleed coefficients were determined experimentally and with stability analysis, namely, $C^*_{b1}(Re)$ and $C^*_{b2}(Re)$, referring to bleed values inhibiting the SS and RSP modes, respectively. It has been demonstrated that these values grow with Re, and according to the BiGlobal stability analysis, tend to asymptotic values $C^*_{b1} \to 0.125$ and $C^*_{b2} \to 0.115$ for $Re \gtrsim 2000$. In this sense, the use of an axisymmetric base flow at $C_b < C^*_{b2}$ for the GLS analysis underestimates the value of C^*_{b2} for $Re \lesssim 800$. However, since at large Re high values of C_b are required to inhibit vortex shedding, the flow is more slender and the axisymmetric base flow assumption is somewhat more realistic close to the transition at C^*_{b2}, what translates into more acceptable GLS predictions, that seem to follow the experimental results trend at lower Re. On the other hand, unlike the type of bifurcations taking place in terms of Re_{co}, we have evidenced that the destabilization of the RSP mode with decreasing C_b and constant Re, at C^*_{b2}, is not a Hopf bifurcation. Finally, experimental measurements of light base bleed, have shown that C^*_{b2} does not depend on the base density, conversely to what is reported in the literature [136]. A more comprehensive study is needed to shed light on this issue. On the other hand, it has been shown that the addition of a cavity at the base of the $\ell = 2$ body, of length ratio $0 < h/D \leq 1$ and inner diameter ratio $0 < D_c/D \leq 0.99$, improves the stability of the wake and decreases the drag coefficient. GLS analyses and numerical simulations have shown that increasing cavity aspect ratios, h/D, provide with larger Re_{cs}, which exhibits an asymptotic behavior for $h/D \gtrsim 0.7$, i.e. a critical value, beyond which no change is observed. A similar study on the effect of D_c/D, indicated that, practically, there is no effect on Re_{cs} for the range $0 \leqslant D_c/D \lesssim 0.6$, although, a monotonic increase in Re_{cs} has been found in the range $0.6 \lesssim D_c/D \leqslant 0.99$. Besides, steady simulations proved that improvements of 10% to 15% can be achieved in the pressure drag coefficient, C^p_d, a results that is, nevertheless, hindered by an increment in the viscous drag C^v_d coefficient accounting for the viscous forces in the inner walls. This negative effect is expected to decrease with Re, and hence, an important drag reduction should be achieved at higher Reynolds number. Concerning the second-oscillatory bifurcation, the same stabilizing asymptotic effect described earlier was found for Re_{co} using experiments and numerical simulations, reaching a limit on the stabilization for $h/D \geqslant 0.7$.

Chapter 4 has been devoted to the study of the laminar flow past a rotating $\ell = 2$ body, with moderate dimensionless rotation velocity, in the ranges $\Omega \leq 1$ and $Re < 450$, using numerical simulations and GLS analysis. It has been demonstrated that a small amount of rotation modifies the unstable modes observed at $\Omega = 0$ and the pattern of bifurcations, and such modifications have been reflected in a parametric $(\Omega - Re)$ map. More importantly, it has been found that spin acts as a stabilizing mechanism, since axisymmetry can be retrieved for $Re > Re_{cs}$ and moderate values of Ω, being linked this reestablishment of axisymmetry with the injection of even axial vorticity in the wake through the base. In this sense, numerical simulations showed that, for $\Omega < 0.225$, the axisymmetry-breaking at $Re_{c1}(\Omega)$ (whose value increases with Ω) leads the flow towards a deformed version of the SS mode through rotation, i.e. a *low-frequency frozen state*, for which the wake performs a solid-body rotation with an angular velocity Ω_{sl}, featuring constant values

of lift and drag. Consequently, it is steady when viewed from a reference system S' rotating with Ω_{sl}. On the other hand, at $Re_{c2}(\Omega) > Re_{c1}(\Omega)$, the flow evolves towards a deformed RSP mode, denoted as *unsteady spiral wake*, that is a combination of vortex shedding and the rotation of the wake caused by the rotating body. Re_{c2} initially increases with Ω, but decreases for $\Omega \gtrsim 0.05$ until it coincides with Re_{c1} around $\Omega \simeq 0.225$. In this new regime, the lift and drag coefficients oscillate with a characteristic shedding frequency. At $\Omega \simeq 0.2$, a third transition takes place at $Re_{c3} > Re_{c2}$, giving rise to a new co-rotating *high-frequency frozen spiral state*, where the structures are arranged in a frozen spiral whose angular velocity is given by Ω_{sh}, that has been proven to derive from a locking process of the aforementioned shedding frequency. This new frozen mode represents the only unstable mode found for $0.225 \lesssim \Omega \leq 0.5$, so that the wake undergoes just one bifurcation, directly from the axisymmetric state to the frozen spiral regime, at Re_{c3}, whose value is nearly independent of Ω. However, at low Re and $\Omega \geq 0.55$, a new co-rotating *medium-frequency frozen spiral state* takes place (with angular velocity $\Omega_{\omega h}$). The described regimes feature quite distinct characteristic hydrodynamics forces and frequencies, whose evaluation allowed us to identify properly the different states of the wake.

On the other hand, the GLS analysis results were in good agreement with the numerical simulations, showing that all the unstable regimes arising at different bifurcations reported from the axisymmetry region were due to respective destabilizations of co-rotating $m = -1$ global linear modes, namely: a *low-frequency* mode giving rise to the low-frequency frozen state; a *high-frequency* mode associated to the high-frequency frozen spiral state; and a *medium-frequency* mode related to the medium-frequency frozen spiral state. The latter mode is present at the wake for $\Omega > 0.52$ and $Re > Re^{l}_{c4}(\Omega)$, whose value decays with Ω. Finally, a discussion on the *frozen* modes nature has been also held in terms of analogies with other swirling flows, concluding that they are rotating waves arising as a consequence of the base flow SO(2) symmetry degree.

5.2 Future work

Along this Thesis some issues have been left open, with the aim at tackling them in the future, and they can be considered priorities, since they are necessary to complete the picture describe throughout this dissertation. In this sense, the first topic to address should be the understanding of differences on the BiGlobal stability analysis predictions between the sphere and the bullet-shaped body. A discussion about the possible influence of the parameter $\Delta = (Re_{co} - Re_{cs})/Re_{cs}$ was held for a disk, but this argument is not applicable for the sphere and $\ell = 2$ body, since their Δ are similar. Moreover, it was shown that the saturated amplitude just below Re_{co} was larger in the case of the sphere than the $\ell = 2$ body. Hence, a deeper characterization of the stability properties might be carried out (for instance by means of weakly non-linear expansions approaches), in order to look for a possible explanation of such differences, and to explore if it might be even the magnitude of the single value of Re_{co} what affects the results. As far as base bleed is concerned, it was proven experimentally by means of light bleed, that density does not affect apparently the stabilization levels of the wake at different Re, since C^{*}_{b2} are similar for air and Helium, conversely to what has been published in the literature. Therefore, additional numerical simulations dealing with light and heavy base bleed are planned to try to shed some light on the influence of density on the stability of the wake, and work out this discrepancies. Regarding body rotation, it was shown that spin acts as a stabilizing mechanism for low values of Ω, conversely to

what occurs in the case of the sphere. Evaluation of the iso-surfaces of axial vorticity suggested that the key for such differences could be the sign of the vorticity injected through the base. However, a profound understanding of the mechanism is missing, so that a deeper study is proposed also to try to provide with an answer about the influence of geometry.

Besides, a natural extension of the work is a detailed global stability analysis of the turbulent wake behind bullet shaped bodies, that represents a more realistic flow among many industrial applications, i.e. aerospace industry, turbomachinery, among others. To that end, it would be necessary to modify the BiGlobal stability code described in Appendix A, in order to include the terms corresponding turbulent fluctuations and turbulent viscosity to the linear operator $\mathcal{A}$. The base flow, consisting now in a mean flow and turbulent fluctuations, could be solved, for instance, by means of OpenFOAM® or ANSYS Fluent®, using *Large Eddy Simulation* model, that represents with better fidelity small scale structures than RANS models.

On the other hand, the stability analysis of the direct problem performed during this Thesis was linear asymptotic (modal) analysis that provides with the small perturbations behavior prediction for long temporal frames. However, it fails to predict the short term dynamics and evolution of the perturbations, which can be related to important transient growth of energy that triggers non-linearities and modifies the behavior of the flow for the long-time frame. Transient growth is associated to nonorthogonality of eigenfunctions and, therefore, the spectrum cannot capture this short-term dynamics [150, 130]. It is well known, that transient growth is associated to non-normality of the global evolution operator from a global point of view [130, 24]. The non-normality of the operator $\mathcal{A}$ [1], is related to the advection of perturbations, $\mathbf{U}(\mathbf{x})\nabla\mathbf{u}$ (the advection term in the adjoint operator $\mathcal{A}^+$ transports upstream the adjoint perturbations), and the non-parallelism of the flow. In this sense, a proof of the convective non-normality of the flow is given usually by the different spatial structures of direct and adjoint global modes. On the non-normality of $\mathcal{A}$, depends the intensity on the response to harmonic forcing (open loop control), the transient growth of initial perturbations, and the sensitivity of the global spectrum. On one hand, the receptivity of a stable flow to a local forcing (that triggers the amplifier behavior and consequent transient growth) is given by the magnitude of the dominant global adjoint mode, being its intensity associated to the non-normality degree ($<\mathbf{a},\mathbf{d}>$); and on the other hand, the sensitivity or receptivity to basic flow modifications is related to the magnitude of the local scalar product $|\mathbf{a}^*,\mathbf{d}|$. The sensitivity of the spectrum and, therefore, the determination of global mode frequency (*wave maker*), is set by the region where adjoint and direct modes overlap, that in the case of wakes is located in the near region, at the end of the separation bubble for cylinders [43], or inside the recirculation region for axisymmetric bodies [88], rendering them more suited for passive control methods [90]. The non-normality of wakes behind bluff bodies is moderate (the validity of Landau model close to the threshold bifurcations is an indication in this sense [24]), due to the strong non-parallelism existing at the recirculation, but, anyway, important transient growth can occurs at the wake, as it has been shown, for instance, for cylinders [1, 162]. Therefore, it would be of great interest to extend our present study to a more complete analysis on the stability properties of the wake behind bullet-shaped bodies, focusing on the receptivity to forcing and sensitivity of the spectrum (in line with other words existing in the literature [89, 143]), and optimal perturbations, i.e. initial

[1] An operator $\mathcal{A}$ is non-normal if it does not commute with its adjoint, $\mathcal{A}^+\mathcal{A} \neq \mathcal{A}\mathcal{A}^+$. A natural measurement of the non-normality of $\mathcal{A}$ is brought by the inner product between adjoint, $\mathbf{a}$, and direct, $\mathbf{d}$, eigenmodes of $\mathcal{A}$: $<\mathbf{a},\mathbf{d}> = \int \mathbf{a}^*\mathbf{d}\ d\mathbf{x}$; denoting * complex conjugate.

perturbations maximizing the energy gain at given times.

In this sense, a first approach to these topics is presented in Appendix B, which shows a study on the local stability properties of a parallel round jet, describing asymptotic (temporal modal analysis) and short-time (adjoint modal analysis and optimal perturbation) dynamics of perturbations. This Appendix is the outcome of the work performed during two research stays at the *Institute de Mécanique des Fluides de Toulouse* (France), under the supervision of Dr. Pierre Brancher and Dr. Christophe Airiau, to whom the author of the present Thesis is indebted, for their inestimable help during these research training periods, teaching him about different modal and non-modal stability techniques.

APPENDIX

A

Description of the BiGlobal Linear Stability code

The purpose of the present Appendix is to describe in detail the code developed at the Fluid Mechanics Research Group of the University of Jaén, to perform BiGlobal linear stability analyses for wakes behind bullet-shaped bodies using MATLAB®. As mentioned in Chapter 3, there are two versions of the code that differ basically on the way the discretization of linear operators $\mathcal{A}$ and $\mathcal{B}$ (see Eqs.1.11 and 1.12) is done. In the first version of the code, described in [127], the discretization of the spatial operators and variables is performed using Chebyshev-Gauss-Lobatto points and Lagrangian interpolating polynomials, with the help of the MATLAB® DMSuite Package [156]. As detailed in Chapter 2, the computational domain consists of multiple subdomains, where the field variables are discretized using Gaus-Lobatto points, and differentiation is achieved by means of piecewise Lagrangian polynomials (setting continuity for derivatives at boxes boundary points). The code initially developed (suitable for base flows without flow swirl) has some geometrical limitations and the memory requirements become very large when the azimuthal velocity component needs to be considered, since the global interpolation of spectral methods provides with dense matrices (this issue will be addressed again below). Hence, a new version, which was used for the study of wakes behind bodies with rear cavities (see Chapter 3) and spinning bodies (see Chapter 4), was developed in order to obtain sparser matrices and more geometric flexibility. This second version implements finite differences of $\mathcal{O}(6)$ to compute the spatial derivatives in $\mathcal{A}$ and $\mathcal{B}$, and maps the variables into a grid made up by large domains, instead of the multiple spectral boxes or subdomains used with the first version of the code. Nevertheless, the structure of both versions is similar, and the different steps of the general code, detailed in Fig.A.1, are followed in both cases.

As seen in the diagram shown in Fig.A.1, the process consist basically of five steps, namely: base flow computation, base flow solution interpolation into final computational domain, EVP assembly, EVP solver and postprocessing. The only differences existing between both versions are related to the construction of the grid (step 2a) and the differentiation matrices (step 3a). Both the generation of the new grid and the differentiation through finite differences will be explained in detail below.

A.1 Base flow computation and grid interpolation

As described in Chapter 2, Eqs.(1.4) and (1.5) are solved, within the domain displays in Fig.1.1, by means of the finite volume code ANSYS Fluent®, that provides with the steady axisymmetric base flow, $\mathbf{U}^0(\mathbf{x}) = [U^0(r,z), V^0(r,z), W^0(r,z)]$ and $P^0(r,z)$, where the superscript 0 denotes original base flow. Appropriate boundary conditions are set for the boundaries defined in Fig.1.1, thus

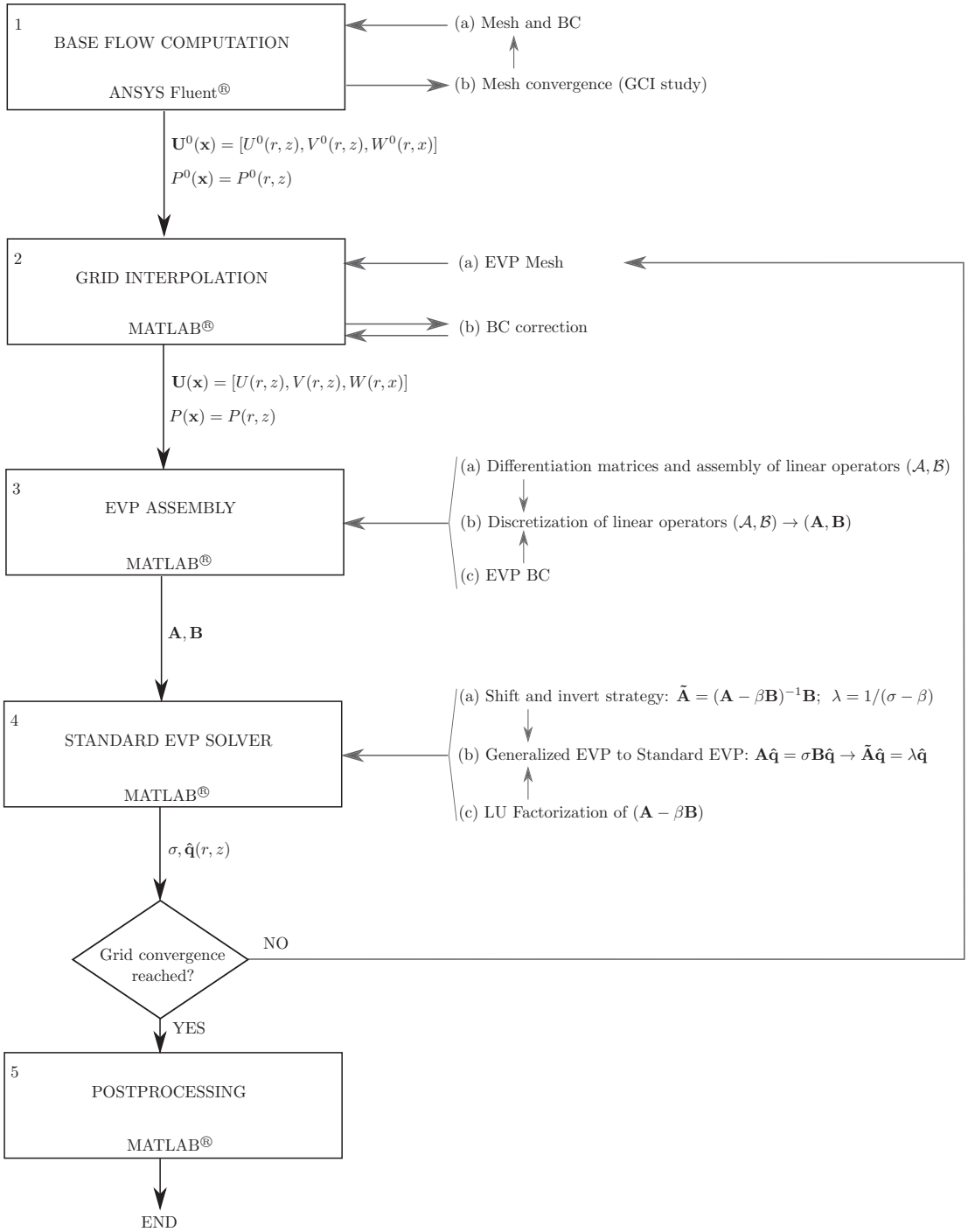

Figure A.1: Diagram of the BiGlobal linear stability code and different steps followed.

generally,

$$\mathbf{U}^0(\mathbf{x}) = (0, 0, w_\infty), \quad \mathbf{x} \in \Sigma_i, \tag{A.1}$$

$$\mathbf{U}^0(\mathbf{x}) = (0, \omega r, 0), \quad \mathbf{x} \in \Sigma_w, \tag{A.2}$$

$$\mathbf{U}^0(\mathbf{x}) = (0, \omega r, w_b), \quad \mathbf{x} \in \Sigma_b, \tag{A.3}$$

$$\mathbf{n} \cdot \mathbf{U}^0(\mathbf{x}) = 0, \quad \mathbf{x} \in \Sigma_f, \tag{A.4}$$

$$P^0(\mathbf{x}) = \mathbf{n} \cdot \nabla \mathbf{U}^0(\mathbf{x}) = 0, \quad \mathbf{x} \in \Sigma_o, \tag{A.5}$$

together with the axis condition into Σ_a. Note that, in Eqs.(A.2) and (A.3), $\omega = 0$ for problems of natural wakes, base bleed and bodies with cavities, whilst in Eq.(A.3), $w_b \neq 0$ only when base bleed is applied. Equations (1.4) and (1.5) are discretized with second order accuracy, by using the midpoint rule for surface integrals in combination with linear interpolation schemes, and computing pressure values on a staggered control volume, since large pressure gradients might appear when swirling exists. The steady state problem is solved implementing a SIMPLE algorithm with under-relaxation.

The estimation of the discretization error in each particular case was done through a *Grid Convergende Index* study on three consecutively refined grids, introduced by Roache [121] and based on the Richardson extrapolation [120], that assumes a monotone convergence when grids are sufficiently fine. The convergence index is defined as $GCI_{j+1,j}(\%) = 3|(f_{j+1} - f_j)/[f_j(\alpha^n - 1)]| \times 100$, where f refers to any integral quantity or field value on the coarse, $j+1$, or the fine, j, grids, $n = log[(f_{j+2} - f_{j+1})/(f_{j+1} - f_j)]/log(\alpha)$ is the calculated convergence order, and $\alpha = (N_j/N_{j+1})^{1/2}$ the grid refinement ratio in each coordinate. Among the different studies performed along the Thesis, as example it is shown here the computation of wakes with swirl, that represents a more computational demanding problem than those of natural wakes or base bleed. Thus, $GCI_{j+1,j}$ is computed for two field values at the near wake of a spinning body, namely, the value of azimuthal velocity, V^0, at the location ($r = 0.5,\ z = 1$), and axial velocity, W^0, at ($r = 0.5,\ z = 5$), being the grid refinement ratio $\alpha \simeq \sqrt{2}$. Table A.1 shows the values obtained, where it is seen how the grid convergence index is reduced as the number of nodes is increased, i.e., $GCI_{2,1} < GCI_{3,2}$, what proves that the solution is converging towards the grid-independent one, and that further increments in N will not improve much the accuracy of the solution but will increase the computational time. Thus, grid #1 will be used to calculate the velocity and pressure fields for the base flow. On the other hand, as mentioned by Ferziger & Peric [39], the estimated convergence order depends on the grid resolution at the zone where the magnitude used for the GCI study is monitored, and since we are interested on the near wake, the grids have been refined thoroughly in this region, providing with values of convergence index almost identical for both $V^0(r = 0.5, z = 1)$ and $W^0(r = 0.5, z = 5)$, $n_V \simeq 2.067$ and $n_W \simeq 2.000$ respectively, what agrees with the theoretical second order discretization schemes set in the finite volume code. Therefore, a grid with approximately 52.000 cells has been adopted to solve with ANSYS Fluent®, the different base flows of the problems described throughout this dissertation.

Once the first step in diagram of Fig.A.1 is completed, the solution is interpolated into a new structured computational grid that is used to solve the EVP problem (see Eq.1.10), where the linear operators, $\mathcal{A}$ and $\mathcal{B}$ (Eqs.1.11 and 1.12), are discretized and mapped. Unlike the grid used for the spectral collocation code version (see Fig.2.4), the grids required by finite-differences differentiation matrices are simpler, as Fig.A.2 displays. The grid of n_g nodes consists of three

$Mesh$	N	$V^0(=0.5,\ z=1)$	$GCI_{j+1,j}(\%)$	$W^0(r=0.5,\ z=5)$	$GCI_{j+1,j}(\%)$
#1	103700	0.03774	0.23467	0.80607	0.03908
#2	52000	0.03771	0.48076	0.80618	0.07668
#3	26200	0.03764	–	0.80640	–
n	–	2.067	–	2.000	–

Table A.1: Grid convergence index for the basic flow, $GCI_{j+1,j}$, applied to the particular case of $\Omega = 0.1$ and $Re = 330$, obtained for the azimuthal, V^0, and the axial, W^0, components of the velocity, at two different downstream locations near the body base, being $\alpha = 2^{1/2}$, $n_V \simeq 2.07$ and $n_W \simeq 2.00$.

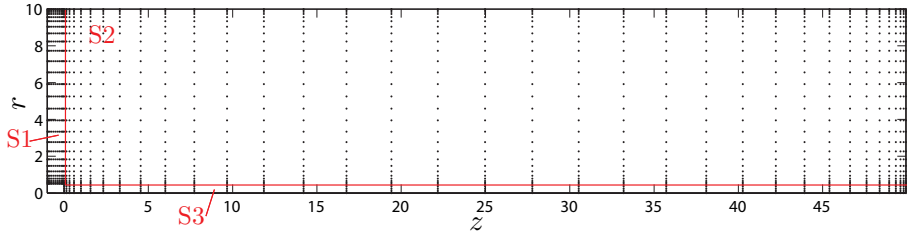

Figure A.2: Low resolution example of a grid used to interpolate the basic flow (U^0, V^0, W^0), calculated by ANSYS Fluent®, and to obtain the EVP basic flow, (U, W, W), for the BiGLS code of finite differences of $\mathcal{O}(6)$, where $S1, S2, S3$ denote the subdomains into which the grid is divided.

subdomains (five when there is a cavity) where points are distributed non-uniformly, increasing the resolution near the subdomain boundaries. This allows to increase the resolution at the near wake, where larger gradients of the physical magnitudes exist. The distribution of points is done, in each subdomain, according to the function,

$$x_i = y_i - \xi \sin(2\pi y_i), \qquad i = (0, 1, \ldots, n), \tag{A.6}$$

where y_i is the uniform initial distribution and x_i is the final distribution of points in any coordinate, either r or z, normalized by its length (L_{x_i}), n is the number of points, and $\xi \leq 1/(2\pi)$ is a stretching factor, whose values vary with coordinate and subdomain, and is chosen to obtain similar spacing between nodes at the subdomains junctions. To interpolate the basic flow, $[U^0(r,z), V^0(r,z), W^0(r,z)]$ and $P^0(r,z)$, calculated by ANSYS Fluent®, into the EVP mesh, obtaining the final basic flow to be used in the EVP problem, $[U(r,z), V(r,z), W(r,z)]$ and $P(r,z)$, a cubic interpolation scheme was used. After the interpolation process, boundary conditions (see Eqs.A.1-A.5) ought to be again imposed in the new grid. The interpolation provides finally with the base flow used as input of our EVP problem, i.e. $\mathbf{U}(\mathbf{x}) = [U(r,z), V(r,z), W(r,z)]$ and $P(r,z)$. The computational grids adapted for the EVP problem contain approximately $n_g \sim 10^4 - 10^5$ nodes, as it is seen in Table 3.1.

A.2 EVP assembly

Step 3 in the BiGLS code (Fig.A.1) consists in assembling the EVP problem, what starts building the differentiation matrices and the assembly of the linear operators $(\mathcal{A}, \mathcal{B})$ (Eqs.1.11 and 1.12). The differentiation matrices provide with the first and second derivatives included in $\mathcal{A}$ (Eq.1.11).

Such matrices are constructed in such a way that their products with a vector gives a vector of derivatives: $f' = Df$, $f'' = D2f$, being D and $D2$ matrices and f the vector form of any base flow or perturbed field variables components, (U, V, W, P) and $(\hat{u}, \hat{v}, \hat{w}, \hat{p})$, respectively; while f' and f'' are their derivatives. The derivation of f' and f'' is done through finite differences of $\mathcal{O}(6)$ for the second version of the code, used in Chapters 3 and 4, whose process is detailed in Section A.2.1. The use of $f' = Df$ and $f'' = D2f$ implies that $(\mathcal{A}, \mathcal{B})$ must be discretized, giving rise to $(\mathbf{A}, \mathbf{B})$, that alongside the setting of convenient boundaries conditions, define the discrete form of the original EVP (Eq.1.10),

$$\mathbf{A}\hat{\mathbf{q}} = \sigma\mathbf{B}\hat{\mathbf{q}}, \tag{A.7}$$

where $\mathbf{A}$ and $\mathbf{B}$ are $4n_g \times 4n_g$ matrices, and $\hat{\mathbf{q}} = [\hat{u}, \hat{v}, \hat{w}, \hat{p}]$ is now the eigenfunctions column vector of size $4n_g$, being n_g the total grid points. Both $\mathbf{A}$ and $\mathbf{B}$ are sparse matrices with diagonal structure of the submatrices A_{ij}, B_{ii} $(i, j = 1, 2, 3, 4)$, due to the vector arrangement of $\hat{\mathbf{q}}$. In fact, regarding $\mathbf{B}$, as Eq.(1.12) shows, B_{22}, B_{33} and B_{44} are identity matrices, whose role is mapping the eigenfunctions onto the computational grid. On the other hand, the structure of $\mathbf{A}$ and its sparsity are displayed in Fig.A.3, being the submatrices A_{ij} $(i, j = 1, 2, 3, 4)$ the discrete form of the operator components in Eq.(1.11). The color code in Fig.A.3 illustrates the sparsity degree of the submatrices. Thus, operators (A_{21}, A_{32}, A_{43}) have higher density since they involve, among other terms, the Laplacian (second spatial derivatives) of the perturbation components, $[\hat{u}, \hat{v}, \hat{w}, \hat{p}]$. Then, according to the differentiation schemes of $\mathcal{O}(6)$ implemented (see Section A.2.1), it implies the use of field variables in 15 points (8 in each direction, see Fig.A.4c), and therefore (A_{21}, A_{32}, A_{43}) have 15 diagonals with no null coefficients. Besides, submatrices $(A_{11}, A_{13}, A_{24}, A_{44})$ are the discretization of terms including first partial derivatives $(\partial/\partial r, \partial/\partial z)$ of any $[\hat{u}, \hat{v}, \hat{w}, \hat{p}]$, so that they have 7-diagonals arrangement (see Fig.A.4a and b) and, therefore, are slightly sparser than the first group analyzed. The remaining of the submatrices of $\mathbf{A}$ are 1-diagonal or empty. Thus, terms including both radial and axial derivation of base flow components (A_{23}, A_{41}), or either first or second derivatives with respect to the azimuthal coordinate (A_{12}, A_{22}, A_{31}), are single diagonal matrices. Finally, (A_{14}, A_{42}) are formally null matrices, although after implementing the boundary conditions, A_{14} will contain some no-null coefficients (light grey colored matrix in Fig.A.3).

In this sense, as step 3(c) in Fig.A.1 illustrates, once $\mathbf{A}$ and $\mathbf{B}$ are assembled, convenient boundary conditions must be set. Standard boundary conditions for global instability problem are chosen [146], namely,

$$\hat{\mathbf{u}} = (0, 0, 0), \quad \mathbf{x} \in \Sigma_i' \cup \Sigma_w \cup \Sigma_f, \tag{A.8}$$

$$\hat{u} = \hat{v} = \partial\hat{w}/\partial z = \hat{p}\,\mathbf{n} - Re^{-1}\mathbf{n} \cdot \nabla\hat{\mathbf{u}} = 0, \quad \mathbf{x} \in \Sigma_o, \tag{A.9}$$

treating the pressure implicitly by means of the incompressibility condition (Eq.1.6) at each boundary (this treatment accounts for the fact that submatrix A_{14} is not completely null). At the symmetry axis, Σ_a, the same regularity conditions used in Khorrami *et al.* [63], are imposed,

$$\mathbf{x} \in \Sigma_a : \quad \begin{cases} |m| = 0, & \hat{u}, \hat{v}, \partial\hat{w}/\partial r = 0, \\ |m| = 1, & \hat{u} \pm i\hat{v} = 2\partial\hat{u}/\partial r \pm i\partial\hat{v}/\partial r = \hat{w} = 0, \\ |m| > 1, & \hat{\mathbf{u}} = (0, 0, 0). \end{cases} \tag{A.10}$$

Obviously, homogeneous boundary conditions related to $\hat{\mathbf{q}}$ are imposed by setting to one diagonal entries in $\mathbf{A}$ and zero in $\mathbf{B}$, for the index corresponding the boundary at hand. Likewise, conditions

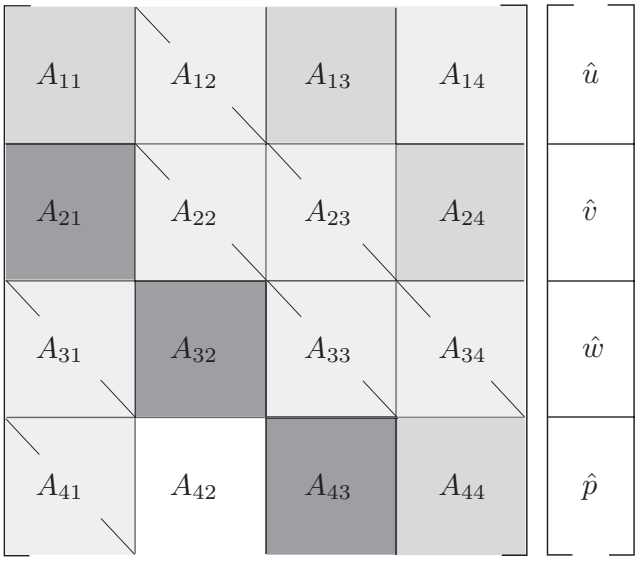

Figure A.3: Structure of the discrete linear operator **A** and sparsity degree, from dark grey (dense matrix) to not-colored (empty matrix).

involving derivatives add 7 non-null entries to submatrices of **A** (see Fig.A.4). At this point, the discrete generalized EVP of Eq.(A.7) is assembled and complete. However it still remains unexplained the procedure followed to build the differentiation matrices, D and $D2$, and their differences with respect to spectral matrices.

A.2.1 Differentiation matrices

As mentioned at the Introduction of the present Appendix, in order to achieve a more flexible geometry representation, the first and second spatial derivatives appearing at the linear operator $\mathcal{A}$ (Eq.1.11) are obtained by using explicit central finite differences of $\mathcal{O}(6)$, whose truncation order is maintained at the one-sided differentiation formulae used to treat the boundary or near-boundary points.

The explicit finite difference formulae have been obtained following the general technique of Taylor series linear combination (see e.g. Moin [96]). In the case at hand, central schemes of $\mathcal{O}(6)$ on a non-uniform grid are sought, what implies a 7 point stencil, i.e., $f_{i-3}, f_{i-2}, f_{i-1}, f_i, f_{i+1}, f_{i+2}, f_{i+3}$, for the first derivative (8 points for the second, see below); as it can be easily seen, being i the index related to the spatial location x_i where the derivative is computed. Due to the grid non-uniformity, six characteristic spatial increments must be defined, namely,

$$h_{i+k} = x_{i+k} - x_i; \quad k \in \mathbb{Z} \ / \ k = [-3, 3]. \tag{A.11}$$

Thus, in order to obtain the scheme for the first derivative, the linear combination of Taylor series can be formulated in the following way,

$$f_i' + \sum_{k=-3}^{3} a_k f_{i+k} = \mathcal{O}(h^6), \tag{A.12}$$

	f_i	f_i'	f_i''	f_i'''	$f_i^{(iv)}$	$f_i^{(v)}$	$f_i^{(vi)}$
f_i'	0	1	0	0	0	0	0
$a_{-3}f_{i-3}$	a_{-3}	$a_{-3}h_{i-3}$	$a_{-3}\frac{h_{i-3}^2}{2!}$	$a_{-3}\frac{h_{i-3}^3}{3!}$	$a_{-3}\frac{h_{i-3}^4}{4!}$	$a_{-3}\frac{h_{i-3}^5}{5!}$	$a_{-3}\frac{h_{i-3}^6}{6!}$
$a_{-2}f_{i-2}$	a_{-2}	$a_{-2}h_{i-2}$	$a_{-2}\frac{h_{i-2}^2}{2!}$	$a_{-2}\frac{h_{i-2}^3}{3!}$	$a_{-2}\frac{h_{i-2}^4}{4!}$	$a_{-2}\frac{h_{i-2}^5}{5!}$	$a_{-2}\frac{h_{i-2}^6}{6!}$
$a_{-1}f_{i-1}$	a_{-1}	$a_{-1}h_{i-1}$	$a_{-1}\frac{h_{i-1}^2}{2!}$	$a_{-1}\frac{h_{i-1}^3}{3!}$	$a_{-1}\frac{h_{i-1}^4}{4!}$	$a_{-1}\frac{h_{i-1}^5}{5!}$	$a_{-1}\frac{h_{i-1}^6}{6!}$
a_0f_i	a_0	0	0	0	0	0	0
a_1f_{i+1}	a_1	a_1h_{i+1}	$a_1\frac{h_{i+1}^2}{2!}$	$a_1\frac{h_{i+1}^3}{3!}$	$a_1\frac{h_{i+1}^4}{4!}$	$a_1\frac{h_{i+1}^5}{5!}$	$a_1\frac{h_{i+1}^6}{6!}$
a_2f_{i+2}	a_2	a_2h_{i+2}	$a_2\frac{h_{i+2}^2}{2!}$	$a_2\frac{h_{i+2}^3}{3!}$	$a_2\frac{h_{i+2}^4}{4!}$	$a_2\frac{h_{i+2}^5}{5!}$	$a_2\frac{h_{i+2}^6}{6!}$
a_3f_{i+3}	a_3	a_3h_{i+3}	$a_3\frac{h_{i+3}^2}{2!}$	$a_3\frac{h_{i+3}^3}{3!}$	$a_3\frac{h_{i+3}^4}{4!}$	$a_3\frac{h_{i+3}^5}{5!}$	$a_3\frac{h_{i+3}^6}{6!}$

Table A.2: Coefficients matrix for the Taylor expansions linear combination.

where f_i' is the approximated value of first derivative at x_i, a_k are the coefficients of the linear combination, f_{i+k} the function value at x_{i+k}, and h the biggest of the spatial increments defined in Eq.(A.11). The functional values at x_{i+k} are expressed as Taylor expansions,

$$f_{i+k} = f_i + h_{i+k}f_i' + \frac{h_{i+k}^2}{2!}f_i'' + \frac{h_{i+k}^3}{3!}f_i''' + \frac{h_{i+k}^4}{4!}f_i^{(iv)} + ...\frac{h_{i+k}^5}{5!}f_i^{(v)} + \frac{h_{i+k}^6}{6!}f_i^{(vi)} + \frac{h_{i+k}^7}{7!}f_i^{(vii)} + h.o.t. \tag{A.13}$$

The linear combination of the expansions for all f_{i+k}, can be arranged in a table (see Table A.2), that will help canceling out coefficients related to low-order terms. Thus, its first column is the left-hand side of Eq.(A.12), and the first seven terms of its right-side can be obtained as the sum of the addition of rows times the column first element, for all the remaining columns, namely,

$$\begin{aligned} f_i' + \sum_{k=-3}^{3} a_k f_{i+k} = {} & (a_{-3} + a_{-2} + a_{-1} + a_0 + a_1 + a_2 + a_3)f_i + \\ & (1 + a_{-3}h_{i-3} + a_{-2}h_{i-2} + a_{-1}h_{i-1} + a_1h_{i+1} + a_2h_{i+2} + a_3h_{i+3})f_i' + \\ & (a_{-3}\frac{h_{i-3}^2}{2!} + a_{-2}\frac{h_{i-2}^2}{2!} + a_{-1}\frac{h_{i-1}^2}{2!} + a_1\frac{h_{i+1}^2}{2!} + a_2\frac{h_{i+2}^2}{2!} + a_3\frac{h_{i+3}^2}{2!})f_i'' + \cdots . \end{aligned} \tag{A.14}$$

Now the procedure consists in setting to zero the coefficients of the right-hand side of Eq.(A.14) whose order is the desired truncation order or lower, so that given by the first unmatched coefficient, i.e. the sixth order is achieved by matching all term below $\sum_{k=-3}^{3} a_k(h_{i+k}^7/7!)f^{(vii)}$. Hence, the following linear system must be solved for $a_{-3}, a_{-2}, a_{-1}, a_0, a_1, a_2, a_3$, in order to obtain the sixth-

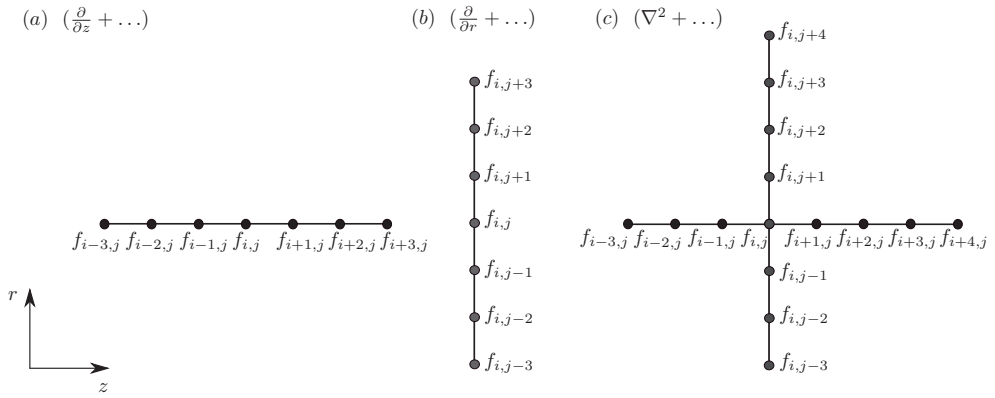

Figure A.4: Schemes of computational points involved in the $\mathcal{O}(6)$ differentiation and discretization of some components of linear operator $\mathcal{A}$ (Eq.1.11), affecting the field variable f. Coefficients of differentiation matrices and other terms in Figs.A.4(a),(b) and (c) are omitted.

order central scheme for the first derivative f_i',

$$\begin{cases} a_{-3}+a_{-2}+a_{-1}+a_0+a_1+a_2+a_3=0, \\ a_{-3}h_{i-3}+a_{-2}h_{i-2}+a_{-1}h_{i-1}+a_1h_{i+1}+a_2h_{i+2}+a_3h_{i+3}=-1, \\ a_{-3}\frac{h_{i-3}^2}{2!}+a_{-2}\frac{h_{i-2}^2}{2!}+a_{-1}\frac{h_{i-1}^2}{2!}+a_1\frac{h_{i+1}^2}{2!}+a_2\frac{h_{i+2}^2}{2!}+a_3\frac{h_{i+3}^2}{2!}=0, \\ a_{-3}\frac{h_{i-3}^3}{3!}+a_{-2}\frac{h_{i-2}^3}{3!}+a_{-1}\frac{h_{i-1}^3}{3!}+a_1\frac{h_{i+1}^3}{3!}+a_2\frac{h_{i+2}^3}{3!}+a_3\frac{h_{i+3}^3}{3!}=0, \\ a_{-3}\frac{h_{i-3}^4}{4!}+a_{-2}\frac{h_{i-2}^4}{4!}+a_{-1}\frac{h_{i-1}^4}{4!}+a_1\frac{h_{i+1}^4}{4!}+a_2\frac{h_{i+2}^4}{4!}+a_3\frac{h_{i+3}^4}{4!}=0, \\ a_{-3}\frac{h_{i-3}^5}{5!}+a_{-2}\frac{h_{i-2}^5}{5!}+a_{-1}\frac{h_{i-1}^5}{5!}+a_1\frac{h_{i+1}^5}{5!}+a_2\frac{h_{i+2}^5}{5!}+a_3\frac{h_{i+3}^5}{5!}=0, \\ a_{-3}\frac{h_{i-3}^6}{6!}+a_{-2}\frac{h_{i-2}^6}{6!}+a_{-1}\frac{h_{i-1}^6}{6!}+a_1\frac{h_{i+1}^6}{6!}+a_2\frac{h_{i+2}^6}{6!}+a_3\frac{h_{i+3}^6}{6!}=0. \end{cases}$$

The system was solved by means of the MATLAB® symbolic calculus library, although for the sake of conciseness and clarity, the solution for the different coefficients is omitted here.

For the second derivative, the same procedure was followed, in order to obtain a sixth order central finite difference scheme. Unlike the first derivative, the second derivative involves values of the computed variable at 8 points, so that,

$$f_i''=b_{-3}f_{i-3}+b_{-2}f_{i-2}+b_{-1}f_{i-1}+b_0f_i+b_1f_{i+1}+b_2f_{i+2}+b_3f_{i+3}+b_4f_{i+4}, \tag{A.15}$$

where $(b_{-3},b_{-2},b_{-1},b_0,b_1,b_2,b_3,b_4)$ are constants. Additionally, one-sided first and second derivative formulas have been calculated likewise for points located at the computational boundaries (e.g. $k=[0,6]$ in Eq.A.11 for first derivative) or the two following near-boundary points close to it.

The formulae derived for f_i' and f_i'' can be easily arranged as products of row vectors, containing the coefficients a_k and b_k of Eqs.(A.14) and (A.15) respectively, and column vectors with the values of the variable at the points involved, f_{i+k}, where $k=[-3,3]$ and $k=[-3,4]$ for inner points with first and second derivative centered expressions respectively. To compute the derivatives in all the points of a given coordinate as vectors f' and f'', the coefficients row vectors (corresponding both boundaries or near-boundaries point and inner points) for both the first and second derivatives, are arranged to form the matrices D and $D2$, so that $f'=Df$ and $f''=D2f$.

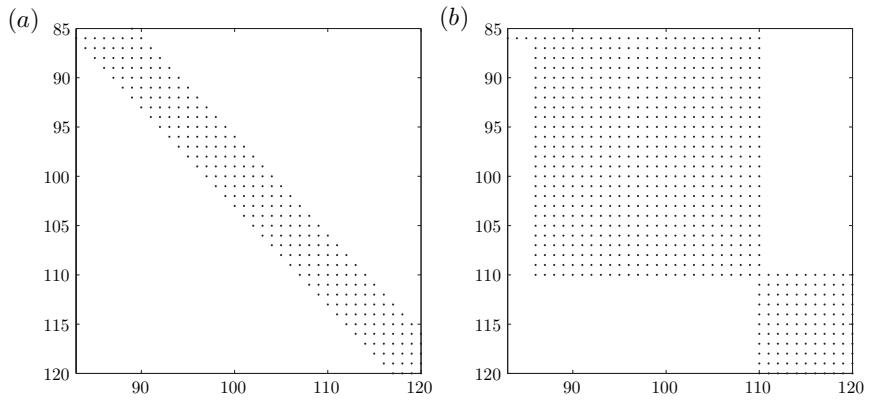

Figure A.5: Detail of the differentiation matrix D2 structure, obtained by means of (a) finite differences of $\mathcal{O}(6)$ and (b) spectral methods using Langrangian polynomials interpolation of $n = 10$. Discontinuity of pattern in (b) is due to the change of spectral box.

Regarding the linear operator $\mathcal{A}$ (Eq.1.11), the formulae derived above imply that the terms of $\mathcal{A}$ containing the first spatial derivative in a single coordinate need values of the variable computed at 7 points (see Fig.A.4a and b), while second derivatives imply the use of 15 points, since they appear in $\mathcal{A}$ as a Laplatian and two coordinates must be evaluated (Fig.A.4c).

To end with this section, it must be emphasized that the structure of matrix $\mathbf{A}$ arising when the discretization is done by means of finite differences is sparser than that emerging when the differentiation is accomplished with spectral methods using Lagrangian polynomials interpolation, since the latter method involves all the points belonging to the subdomain considered. A proof of such a dense pattern can be observed in Fig.A.5, where an amplified detail of matrices D2 computed by both methods is shown. The sparsity of finite differences matrices translates into faster computations, although higher grid resolution is needed to match the properties offered by spectral methods. However, the global nature of spectral methods and their higher accuracy, that could be an advantage against the lower order of finite differences, are hindered by the second order used to obtain the base flow, so, considering such limitation, finite differences arises as a more competitive method, since shorter computational times and less RAM memory are required with an acceptable degree of accuracy. For the case of spinning bodies, the matrix $\mathbf{A}$ is denser per se, due to the terms associated to the azimuthal velocity component of the base flow, V, and that is the reason why finite differences were used to carry out the stability analysis of Chapter 4.

A.3 Standard EVP solver

The discrete generalized EVP, Eq.(A.7), in the case at hand, represents a large problem to be solved by means of a QZ algorithm (it must be considered that the size of the grid used are of $\mathcal{O}(10^5)$ nodes), that would recover the full spectrum, since it requires the storage of two arrays for the discretized matrices $\mathbf{A}$ and $\mathbf{B}$, and two for the results obtained [145]. Hence, an iterative Arnoldi algorithm [7] was used to compute a few leading eigenvalues, since just a few discrete eigenvalues are of interest for this problem [102]. The algorithm was applied after transforming

β	σ_1
$0.2 + 0.2\,i$	$-0.03909734831 + 0.19475625648\,i$
$0.2 + 0.6\,i$	$-0.03909734838 + 0.19475625872\,i$

Table A.3: Effect of β on the leading eigenvalue σ_1 obtained with the Arnoldi method ($m_A = 100$) for the EVP of a spinning $\ell = 2$ body at $Re = 330$ and $\Omega = 0.2$.

the generalized EVP (Eq.A.7) to a standard EVP, with the help of a *shift and invert* strategy,

$$\tilde{\mathbf{A}}\hat{\mathbf{q}} = \lambda\hat{\mathbf{q}}, \quad \text{with} \begin{cases} \tilde{\mathbf{A}} = (\mathbf{A} - \beta\mathbf{B})^{-1}\mathbf{B} \\ \lambda = \frac{1}{\sigma - \beta} \end{cases}, \tag{A.16}$$

being β the shift parameter. The requirement of the $(\mathbf{A} - \beta\mathbf{B})$ matrix inverse computation, that the shift-and-invert transformation poses, was tackled through a previous LU decomposition of $(\mathbf{A}-\beta\mathbf{B})$, what made the inversion process much more efficient. In order to perform the calculations for the eigenvalues recovery around β, we used the routine `eigs` implemented in MATLAB®, and based on the ARPACK library [76]. An extensive description of the algorithm can be found in the literature (see e.g. [50, 84]), but the basic idea is to build a Krylov subspace of size $m_A \ll 4n_g$, whose set of vectors are obtained after application of the Jacobian matrix $\tilde{\mathbf{A}}$ to an initial vector $\mathbf{v_1}$ of unit norm, so that $\mathcal{K}_{m_A}(\tilde{\mathbf{A}}, \mathbf{v_1}) = \mathbf{v_1}, \tilde{\mathbf{A}}\mathbf{v_1}, \ldots, \tilde{\mathbf{A}}^{m_A-1}\mathbf{v_1}$. This orthonormal basis, $\mathbf{V}_{m_A}$, is used to create a Hessenberg matrix reduction of $\tilde{\mathbf{A}}$, $\mathbf{H}_{m_A}$, whose eigenvalues (Ritz-values) approximate the eigenvalues of $\tilde{\mathbf{A}}$, and the projection of its eigenfunctions, $\hat{\mathbf{y}}$, onto the physical space are the eigenfunctions of $\tilde{\mathbf{A}}$, $\hat{\mathbf{q}} = \mathbf{V}_{m_A}\hat{\mathbf{y}}$.

In this sense, as pointed out by Theofilis [145], the convergence provided by the Arnoldi method for the least stable eigenmodes is a function of the proximity of the sought eigenvalue, σ, and the shift parameter, i.e. $|\beta - \sigma|$; but it mostly depends on the number of Arnoldi method iterations m_A, i.e. the size of the Hessenberg matrix constructed from Krylov basis. Thus, when m_A is large enough, the influence of $|\beta - \sigma|$ vanishes. To select m_A, some tests were performed for different shift parameters, and the variations found for the leading spectrum eigenvalue when $m_A \geq 75$ were of $\mathcal{O}(10^{-10})$. Consequently, all the eigenvalue calculations reported in this Thesis were based on a conservative value of $m_A = 100$, to obtain better convergence for the stable part of the spectrum. A proof of the eigenvalue convergence and near independency of β, when m_A is large ($m_A = 100$), is given by Table A.3, where the leading eigenvalue σ_1 of two spectra corresponding two different values of β, for the wake behind a spinning body of $\ell = 2$ is shown ($Re = 330, \Omega = 0.2$) . It is seen that the frequency, σ_i, is more sensitive to β than the growth rate, σ_r, but for both cases, the variations are close to round-off error order.

On the other hand, the sensitivity of the EVP eigenvalues regarding the grid size, n_g, must be studied in order to obtain finally a converged solution. This convergence analysis was performed for each problem individually and their results can be found in the corresponding chapters (i.e. 3 and 4). The size of grids that provide with converged solutions varies from one application to another, but lies generally between 45.000 and 65.000 approximately (as long as finite differences are used).

A.4 Postprocessing

The variables involved in the EVP (Eq.A.7) were mapped on a collocated grid and, therefore, spurious oscillations might emerge with short length scales determined by the grid cells size, so that appropriate filtering was applied after the calculation of the eigenfunctions, $\hat{\mathbf{q}}$, to get rid of this undesirable large wavenumber noise. To perform this task, compact finite difference schemes [77] were used. The filter applied derives from a compact finite difference scheme of fourth order, and has the three-diagonal form,

$$\alpha\hat{f}_{i+1} + \hat{f}_i + \alpha\hat{f}_{i-1} = af_i + \frac{b}{2}(f_{i+1} + f_{i-1}) + \frac{c}{2}(f_{i+2} + f_{i-2}), \tag{A.17}$$

where $\hat{f}_{i-1}, \hat{f}_i$ and $\hat{f}_{i+1}$ represent the filtered value at i, $i-1$ and $i+1$, respectively. Expanding in Taylor series, and matching coefficients, the following values of a, b and c are obtained,

$$a = \frac{1}{8}(6\alpha + 5), \quad b = \frac{1}{2}(1 + 2\alpha), \quad c = -\frac{1}{8}(1 - 2\alpha). \tag{A.18}$$

A value of $\alpha = 0.45$ was set, since it provided with an efficient low pass filter and allowed us to smooth the solution of $\hat{\mathbf{q}}$, discarding short wavelength oscillations (see Lele [77] for more details). The eigenfunctions plotted throughout this document are the outcome of the filtering process described here.

APPENDIX
B

Long-time and short-time evolution of perturbations for parallel round jets

This appendix presents the work performed during two research stays at the *Institute de Mécanique des Fluides de Toulouse* (France), under the supervision of Dr. Pierre Brancher, who guided the author of this Thesis throughout these research training periods, and to whom the author is highly indebted, due to the great help and attention received. The work focuses on the local stability properties of a round parallel jet of parametric base flow, for varying aspect ratios $1/\theta$, where θ stands for the ratio between the shear layer momentum thickness and the jet radius, and covering the range $10 \leq Re \leq 10000$. Three different approaches were used to tackle the problem, namely, an asymptotic study with help of a modal temporal stability analysis to study the long-time frame; a non-modal optimal perturbation analysis to study the short-time transient dynamics and to evaluate the possibility of a strong transient growth; and finally a modal temporal stability analysis of the adjoint problem, to describe the finite-time transient dynamics. A discussion about the differences encountered in the predictions and the nature of transient mechanism is also included. It must be emphasized that the final goal of this study was to evaluate the capability of the aforementioned techniques, employed in a canonical problem, as is the case of jets with parametric velocity profiles, in order to apply them eventually to wake control problems.

Finally, the text included in this Appendix corresponds to a reprint of the material as it appears in the manuscript: *"Long-time and short-time evolution of perturbations for parallel round jets", by J. I. Jiménez-González, P. Brancher and C. Martínez-Bazán*; to be submitted for publication to Physics of Fluids.

B.1 Introduction

The study of round jets as a basic configuration for stability problems has been carried out by many authors in the past [9, 91, 30, 100, 94, 93, 2]. Depending on the kind of base profile, the unstable azimuthal modes number varies. In inviscid flows, it has been analytically shown [9] that the fully developed profile jets (referred to as FDP the following), like the Gaussian function or the profile derived by Landau & Lifschitz [74], are only unstable to helicoidal perturbations (azimuthal wavenumber $m = 1$) with axial wavenumber, k, smaller than some critical value related to the jet radius. On the other hand, when the base flow has a steep velocity gradient (like the hyperbolic-tangent [91] or "top-hat" profile; TH from now on) the range of unstable azimuthal wavenumber is large [115], including also axisymmetric perturbations ($m = 0$). In fact, Abid *et al.* [2] proved, using asymptotic expansion and Squire's theorem, that when the shear layer thickness is vanishing the axisymmetric disturbances are the most unstable, since helical modes are equivalent to three

dimensional perturbations. Between these two extreme cases, the stability behavior of round jets is characterized by a transition for the most unstable azimuthal mode when the velocity profile changes. As later spatial instability analysis [26] indicated, when the shear layer thickness increases for TH jets along the axis, the number of unstable azimuthal modes becomes smaller. In the limit, a FDP jet is reached and only $m = 1$ would lead to amplified oscillations and would control the jet evolution. It was demonstrated that for high aspect ratios $1/\theta$, where θ stands for the shear layer momentum thickness made dimensionless with the jet radius, R, the growth rates for $m = 0$ and $m = 1$ are comparable (as it had been already pointed [139]), decreasing their values when this aspect ratio diminishes. Indeed, for profiles that support several unstable azimuthal modes, $m = 0$ and $m = 1$ are always those with larger growth rate and if $1/\theta$ is lowered, eventually only them remain unstable, being $m = 1$ the most amplified. In the temporal frame, some initial stability comparison [18] between the helical and axysimmetrical mode growth rates were made for several $1/\theta$, and the transition from one mode to another as the most unstable perturbation can be inferred by examining the results, though no quantification of this transition has been made. Furthermore, a thorough spatiotemporal inviscid analysis has been done by Coenen *et al.* [25] for light jets, showing important differences on the properties of dominant azimuthal modes of instability, both $m = 0$ and $m = 1$, when the length of the nozzle from where the jets emerge (parameter that characterizes the jet profile) and jet-to-ambient density ratio are modified. Thus, following this idea for jets of density ratio equals 1, a parametric study on the temporal behaviour of azimuthal perturbations could help to complete the picture of round jets instability when profiles vary.

On the other hand, viscous analyses have shown similar behaviours to those found in inviscid cases for axisymmetric and helical modes when the basic profiles correspond to FDP and TH jets [100]. Furthermore, for given disturbances, the oscillation growth rates seem to be greater as the Reynolds number increases [79], since the viscosity plays a stabilizing role in axisymmetric primary flows [9]. A thourough analysis on the viscosity influence will be carried out to understand how it affects the stability properties of the different jet configurations.

The classical approach used to deal with the hydrodynamic stability of round jets has been the modal stability analysis, which considers the basic flow perturbed by disturbances expressed as superposition of complex Fourier modes, and leads to temporal asymptotic results. Hence, this classical analysis fails to predict short-time evolution of the perturbations, which can be related to important transient growth of energy that triggers non-linearities and modifies the behavior of the flow for the long-time frame. The outcome could be quite different from that foreseen by the modal analysis. Then, a comparison between long-time and short-time results is necessary to describe consistently the stability properties of the flow.

Transient growth existence is related to nonorthogonality of the modes [130], and then, even stable flows to normal modes can suffer increase of energy at short time. The mechanisms involved in the short term growth in parallel shear flows are usually the two-dimensional Orr mechanism [109] and the lift-up effect [33, 72]. The former consists on the tilting of initial perturbations in the direction of the shear, and even though it was first described by Orr [109] for inviscid Couette flow, it has been also found in viscous flows [37, 38]. On the other hand, when the disturbance has a three-dimensional nature, its evolution generates the development of streaks in the the streamwise direction, due to the lifting up of fluids elements when shear is present. Thus, for the problem at hand of round jets involving perturbations of low azimuthal numbers, i.e. $m = 0$ and $m = 1$, only Orr mechanism is expected to occur.

The general problem of finding the initial condition that reaches the maximum of energy gain at a given time (optimal perturbations problem), was treated, among others, by Butler & Farrel [20] through a variational method. This approach has the inconvenience of needing a vector base involving the continuous part of the spectrum, which is composed by oscillating modes that are difficult to resolve through a discrete aproximation. To overcome this difficulty, several new approaches have been implemented. Thus, Corbet and Bottaro [27] used an optimal control approach for swept boundary layers, developing a direct-adjoint technique, that we will adapt for the present work.

Moreover, there is an underlying idea regarding the excitation of the most unstable (or less stable) mode for long time analysis, and it is the optimal excitation of this mode, i.e. the initial condition that creates the maximum transient growth in such a way that the unstable mode emerges faster. The optimal excitation of a given eigenmode corresponds to the eigenmode itself for self-adjoint eigenvalue problems. However, Farrel [37] proved that for a non-normal problem, like Poiseuille's flow, the optimal excitation is quite different from the target eigenmode. Thus, using the property of biorthogonality of eigenmodes and its adjoints [28], it can be asserted that for a general case, the optimal initial condition is the adjoint of the eigenmode chosen. The latter means that if we want to see emerging the most unstable mode of a system, for an initial fixed energy, in a long time frame, then the initial condition must be the adjoint of the most unstable direct mode. Hence, through the stability analysis of the adjoint system, we can obtain the maximum growth rate for the perturbation when time tends to infinity. A second parametric asymptotic study, corresponding to the adjoint system, is performed to predict possible discrepancies derived from transient growth, and a new comparison between axisymmetrical and helical azimuthal numbers is set.

The goal of this work is then, to analyze the critical aspect ratio for parametric *tanh* profiles jets for which the most unstable azimuthal mode changes from $m = 1$ to $m = 0$ for the long-time evolution. To complete the picture, results obtained through an adjoint system stability analysis are presented, and compared to the predictions of the direct system. Finally, an optimal perturbation analysis for short times is done to check the structure of the initial condition.

B.2 Problem formulation and numerical method

The following numerical approaches were first introduced by Antkowiak and Brancher [5] to study the stability properties of a Lamb-Oseen vortex. Further details about these methods can be found in Antkowiak [4].

B.2.1 Steady flow

The basic flow is an axisymmetric parallel jet with only axial velocity, hence, we use cylindrical coordinates (r, θ, z) to define velocity components and pressure as follows,

$$\begin{pmatrix} \mathbf{U} \\ P \end{pmatrix} = \begin{pmatrix} U_r \\ U_\theta \\ U_z \\ P \end{pmatrix} = \begin{pmatrix} 0 \\ 0 \\ U(r) \\ P(r) \end{pmatrix}. \tag{B.1}$$

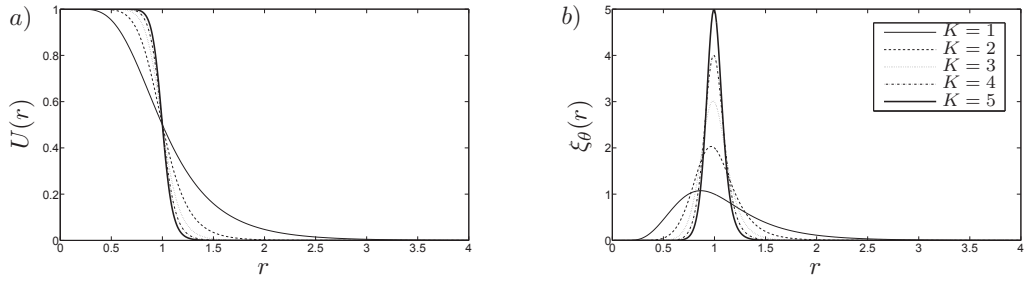

Figure B.1: (a) Base flow velocity profiles and (b) vorticity of profiles for different $K = 1/4\theta$.

The base velocity profile is characterized by a dimensionless parameter, here denoted as aspect ratio (or momentum thickness parameter [30]), defined by the ratio between the shear layer momentum thickness, and the jet radius as,

$$\theta = \int_0^\infty U(r)\,[1 - U(r)]\,dr. \tag{B.2}$$

The velocity profile chosen is

$$U(r) = \frac{1}{2}\left\{1 + \tanh\left[K\left(\frac{1}{r} - r\right)\right]\right\}, \tag{B.3}$$

where $K = 1/4\theta$. Note that in Eqs.(B.2) and (B.3), $U(r)$ and θ are dimensionless variables using the jet velocity at $r = 0$, U_j, and the jet radius, R, respectively. This dimensionless base flow is the one studied by Michalke [92] and Crighton & Gaster [30], among others. As can be expected (Fig.B.1), the shear layer gradient becomes steeper as the aspect ratio increases, leading to higher peaks of azimuthal vorticity (the vorticity vector has only azimuthal component, $\xi_\theta = -dU(r)/dz$, as shown in Fig.B.1b). These velocity profiles will be considered as frozen, so that we perform a classical local stability analysis under the assumption of frozen parallel flow (some comments about the limits of this assumption can be found in section B.3.1).

B.2.2 Modal stability analysis

The stability analysis considers the base flow perturbed by small amplitude disturbances. The equations that define the evolution of these perturbations are obtained after injecting them in the base flow, to give $(\mathbf{U} + \mathbf{u}', P + p')^T$ as the study flow, and linearizing Navier-Stokes equations around the base flow. The perturbed flow Navier-Stokes equations are in the form,

$$\nabla \cdot (\mathbf{U} + \mathbf{u}') = 0, \tag{B.4}$$

$$\frac{\partial(\mathbf{U} + \mathbf{u}')}{\partial t} + \nabla \cdot [(\mathbf{U} + \mathbf{u}') \cdot (\mathbf{U} + \mathbf{u}')] = -\nabla P + p' + \frac{1}{Re}\nabla^2(\mathbf{U} + \mathbf{u}'), \tag{B.5}$$

where Re is the *Reynolds number* based on the jet radius, R, and defined as $Re = U_j R/\nu$; being ν the kinematic viscosity of the fluid. Providing that the perturbation amplitude is asymptotically small, the terms concerning self-interaction of the perturbation can be neglected. Thus, after using mass conservation equation, and doing some manipulation, we can define a system that expresses the problem in a compact way,

$$\mathbf{F}(\mathbf{u}') = \mathbf{L}\frac{\partial \mathbf{u}'}{\partial t} + \mathbf{C}\mathbf{u}' - \frac{1}{Re}\mathbf{D}\mathbf{u}' = 0, \tag{B.6}$$

where

$$\mathbf{L} = \begin{pmatrix} 1 & 0 & 0 & 0 \\ 0 & 1 & 0 & 0 \\ 0 & 0 & 1 & 0 \\ 0 & 0 & 0 & 0 \end{pmatrix}, \tag{B.7}$$

$$\mathbf{C} = \begin{pmatrix} \gamma & -2\Omega(r) & 0 & \dfrac{\partial}{\partial r} \\ \frac{\kappa^2}{2\Omega(r)} & \gamma & 0 & \frac{1}{r}\dfrac{\partial}{\partial \theta} \\ \dfrac{\partial U(r)}{\partial r} & 0 & \gamma & \dfrac{\partial}{\partial z} \\ \dfrac{\partial}{\partial r} + \frac{1}{r} & \frac{1}{r}\dfrac{\partial}{\partial \theta} & \dfrac{\partial}{\partial z} & 0 \end{pmatrix}, \tag{B.8}$$

$$\mathbf{D} = \begin{pmatrix} \nabla^2 - \frac{1}{r^2} & \frac{-2}{r^2}\dfrac{\partial}{\partial \theta} & 0 & 0 \\ \frac{2}{r^2}\dfrac{\partial}{\partial \theta} & \nabla^2 & 0 & 0 \\ 0 & 0 & \nabla^2 & 0 \\ 0 & 0 & 0 & 0 \end{pmatrix}, \tag{B.9}$$

with $\Omega(r)$ representing the angular velocity (null in the problem at hand) and κ the epicyclic frequency [4], and

$$\nabla^2 = \frac{1}{2}\frac{\partial}{\partial r}\left(r\frac{\partial}{\partial r}\right) + \frac{1}{r^2}\frac{\partial^2}{\partial \theta^2} + \frac{\partial^2}{\partial z^2}, \tag{B.10}$$

$$\gamma = \Omega(r)\frac{\partial}{\partial \theta} + U(r)\frac{\partial}{\partial z}. \tag{B.11}$$

The system coefficient independence regarding the azimuthal and axial coordinates is a consequence of the basic flow spatial homogeneity on θ and z, and temporal on t. Then, an eigenmodes problem is formed, where solutions on the following exponential form are to be sought:

$$\mathbf{u}'(r, \theta, z, t) = \hat{\mathbf{u}}(r) e^{i(m\theta + kz - \sigma t)}. \tag{B.12}$$

Here $\hat{\mathbf{u}}$ are the eigenfunctions, m is the azimuthal wavenumber ($\in \mathbb{N}$), and k is the axial wavenumber ($\in \mathbb{R}^+$). The term σ can be decomposed into $\sigma_r + i\sigma_i$, where σ_r is the global mode angular frequency and σ_i is the growth rate of the perturbation. This exponential dependence allows us to substitute the partial derivative operators $\partial/\partial t$, $\partial/\partial \theta$ and $\partial/\partial z$, for $-i\sigma$, im and ik respectively. Thus, the system (B.6) leads to a classical eigenvalue problem that can be solved to obtain the spectrum. Finally we have,

$$(\mathbf{C_{m,k}} - \frac{1}{Re}\mathbf{D_{m,k}})\hat{\mathbf{u}} = -i\sigma \mathbf{L_{m,k}}\hat{\mathbf{u}}, \tag{B.13}$$

being $-i\sigma$ the eigenvalues and $\mathbf{C_{m,k}}$,$\mathbf{D_{m,k}}$ and $\mathbf{L_{m,k}}$ the operators of (B.6) after the substitution of derivatives.

Moreover, some simplifications can be achieved. Let us introduce the compact variable $\mathbf{v} = (\hat{u}_r, \hat{u}_\theta)^T$ and express the axial velocity and pressure in terms of $\mathbf{v}$ as,

$$\hat{u}_z = -\frac{1}{ik}\left(\frac{1}{r}\frac{\partial r\hat{u}_r}{\partial r} + \frac{im}{r}\hat{u}_\theta\right), \tag{B.14}$$

$$\hat{p} = -\frac{1}{k^2}\left\{\left(\frac{\partial}{\partial t} + \gamma - \frac{1}{Re}\nabla^2_{m,k}\right)\left(\frac{1}{r}\frac{\partial r\hat{u}_r}{\partial r} + \frac{im}{r}\hat{u}_\theta\right)\right\}, \tag{B.15}$$

thus, we can define a new compact system,

$$F(\mathbf{v}) = L\frac{\partial \mathbf{v}}{\partial t} + C\mathbf{v} - \frac{1}{Re}D\mathbf{v}, \tag{B.16}$$

where the operator matrices have changed, and are now,

$$L = \begin{pmatrix} 1 & 0 \\ 0 & 1 \end{pmatrix} + b_1 b_2^T, \tag{B.17}$$

$$C = \begin{pmatrix} \gamma_{m,k} & -2\Omega \\ \frac{\kappa^2}{2\Omega} & \gamma_{m,k} \end{pmatrix} + b_1\gamma_{m,k}b_2^T - b_1\left(\frac{\partial U(r)}{\partial r}, 0\right), \tag{B.18}$$

$$D = \begin{pmatrix} \nabla^2_{m,k} - \frac{1}{r^2} & -2\frac{im}{r^2} \\ 2\frac{im}{r^2} & \nabla^2_{m,k} - \frac{1}{r^2} \end{pmatrix} + b_1\nabla^2_{m,k}b_2^T. \tag{B.19}$$

The operators are composed of the aforementioned **L**, **C** and **D**, and a contribution associated to some intermediate operators,

$$b_1^T = \frac{1}{ik}\left(\frac{\partial}{\partial r}, \frac{im}{r}\right) \qquad b_2^T = \frac{1}{ik}\left(\frac{\partial}{\partial r} + \frac{1}{r}, \frac{im}{r}\right), \tag{B.20}$$

$$\nabla^2_{m,k} = \frac{1}{r}\frac{\partial}{\partial r}\left(r\frac{\partial}{\partial r}\right) - \frac{m^2}{r^2} - k^2 \qquad \gamma_{m,k} = im\Omega(r) + ikU(r), \tag{B.21}$$

imposing as boundary conditions: regularity at the origin and decay at infinity.

B.2.3 Transient Growth analysis

As was detailed before, optimal perturbations are initial conditions that maximize the gain of energy at a given time, $t = \tau$, being the energy gain a quantification of the perturbation transient growth. A natural measure of the perturbation intensity is its kinetic energy; hence, we define the gain as the ratio between the kinetic energy at the target time and the energy at the beginning,

$$G(\tau) = \frac{E(\tau)}{E(0)}, \tag{B.22}$$

being

$$E(\tau) = \frac{1}{2}\int_0^\infty (\hat{u}_r^{*T}\cdot\hat{u}_r + \hat{u}_\theta^{*T}\cdot\hat{u}_\theta + \hat{u}_z^{*T}\cdot\hat{u}_z)rdr, \tag{B.23}$$

with $\hat{u}^{*T}_{r,\theta,z}$ denoting transpose conjugate velocity components.

Large time transient: Adjoint problem

At large time ($\tau \to \infty$) the optimal initial condition is the adjoint mode of the most unstable (or less stable) direct mode. The unstable direct mode emerges then faster, with an extra gain that can been quantified through the gain ratio,

$$\eta = \frac{G_{max}(t)}{G_1(t)} = \frac{G^+(t)}{e^{2\omega_i t}}, \tag{B.24}$$

being $G^+(t)$ the energy gain given by the excitation through the adjoint mode, and $G_1(t)$ the energy gain when the initial condition is the direct mode, with ω_i as the growth rate of the most unstable mode.

The Lagrange identity [51] is used to derive the adjoint system in the compact way,

$$F^+(\mathbf{a}) = -L\frac{\partial \mathbf{a}}{\partial t} + C^+\mathbf{a} - \frac{1}{Re}D\mathbf{a} = 0 \quad + b.c., \tag{B.25}$$

where $\mathbf{a}$ are the adjoint perturbations and C^+ represents the adjoint operator of C. Moreover, L and D are the same as for the direct system, i.e. they are self-adjoint operators. To solve this adjoint problem, we apply the same pseudospectral approach as for the direct problem, looking for solutions in the form of normal modes,

$$\mathbf{a}(r,\theta,z,t) = \hat{\mathbf{a}}(r)e^{i(m\theta+kz-\sigma^+ t)}. \tag{B.26}$$

The axial and azimuthal wavenumbers are real for a temporal study, hence, they coincides for both adjoint and direct systems. On the other hand, the relation between the adjoint and direct modes and its growth rates, can be found by using the biorthogonality condition [51]. Then, assuming a given disturbance (k and m) there are two sets of discrete modes, direct ($\hat{\mathbf{v}}_{\mathbf{d,f}}$) and adjoint ($\hat{\mathbf{a}}_{\mathbf{d,g}}$), with respective complex frequencies, $\sigma_{d,f}$ and $\sigma^+_{d,g}$, being f and g the corresponding direct and adjoint indexes, respectively. From the following relation,

$$(\sigma_{d,f} - \sigma^{+*}_{d,g})(\hat{\mathbf{a}}_{\mathbf{d,g}}, \hat{\mathbf{v}}_{\mathbf{d,f}}) = 0, \tag{B.27}$$

where * denotes complex conjugate, it can be obtained the biorthogonal condition,

$$\begin{cases} if \quad f \neq g \quad (\hat{\mathbf{a}}_{\mathbf{d,g}}, \hat{\mathbf{v}}_{\mathbf{d,f}}) = 0, \\ if \quad f = g \quad \sigma_{d,f} = \sigma^{+*}_{d,g}. \end{cases} \tag{B.28}$$

Condition (B.28) anticipates the transient growth existence, since it remarks the non-orthogonality of a direct mode and its counterpart adjoint.

Once arranged the adjoint problem in the form of a classical eigenvalue problem, we are interested on the solution concerning the most unstable direct mode, $\hat{\mathbf{v}}_{\mathbf{d,max}}$, and its adjoint counterpart, $\hat{\mathbf{a}}_{\mathbf{d,max}}$. From here, the energy gain provided by the adjoint system can be easily computed by using the general expression derived by Ortiz & Chomaz [110] for large time,

$$\ln G^+(t) = \ln\left(\frac{1}{(\hat{\mathbf{v}}_\mathbf{1}, \hat{\mathbf{a}}_\mathbf{1})^2}\right) + 2\omega_i t, \tag{B.29}$$

where $(\hat{\mathbf{v}}_\mathbf{1}, \hat{\mathbf{a}}_\mathbf{1})$ is the inner product of the normalized modes, $\hat{\mathbf{v}}_\mathbf{1} = \hat{\mathbf{v}}_{\mathbf{d,max}}/\|\hat{\mathbf{v}}_{\mathbf{d,max}}\|$ and $\hat{\mathbf{a}}_\mathbf{1} = \hat{\mathbf{a}}_{\mathbf{d,max}}/\|\hat{\mathbf{a}}_{\mathbf{d,max}}\|$, and $\omega_i = \Im(\sigma_{d,max})$. The inner product appearing is defined as follows,

$$(\mathbf{p}, \mathbf{q}) = \int_0^\infty (\bar{\mathbf{p}} \cdot \mathbf{q}) r dr \quad + c.c. \tag{B.30}$$

Short and Finite-time transient: Optimal Perturbation analysis

Unlike the modal analysis, the short-time transient study is dealt as an initial value problem, what means that it is assumed that disturbances do not present temporal homogeneity as in Eq.(B.12), but only spatial (streamwise and azimuthal coordinates), looking then for perturbation solutions in the following form,

$$\mathbf{v}(r,\theta,z,t) = \hat{\mathbf{v}}(r,t)e^{i(m\theta+kz)}, \tag{B.31}$$

for the compact system. Hence, the problem has to be solved through temporal integration of Navier-Stokes equations (Eq.B.6). The optimal perturbation searching represents an optimization problem, and we will deal with it using the approach described by Corbett and Botaro [27]. The problem involves maximizing the energy gain, defined in Eq.(B.22), as an objective function, constrained by the compact Navier-Stokes equations and their boundary conditions. Furthermore, we add a new variable, $\mathbf{v_0}$, which is the perturbation at the initial time and that will be used as the control. We can introduce the following Lagrangian functional,

$$\mathcal{L}(\mathbf{v},\mathbf{v_0},\mathbf{a},\mathbf{c}) = G(\tau) - <F(\mathbf{v}),\mathbf{a}> - (H(\mathbf{v},\mathbf{v_0})\cdot\mathbf{c}), \tag{B.32}$$

where $\mathbf{a}(r,t)$ and $\mathbf{c}(r)$ are adjoint (or co-state) variables that work as Lagrange multiplier, whereas the last term imposes the obligation for the initial condition, which must match the control, $H(\mathbf{v},\mathbf{v_0}) = \mathbf{v}(0) - \mathbf{v_0}$. The inner products appearing in the equation correspond to Eq.(B.30) and

$$<\mathbf{p},\mathbf{q}> = \int_0^\tau \int_0^\infty (\bar{\mathbf{p}}\cdot\mathbf{q})rdrdt \quad + c.c. \tag{B.33}$$

The problem reduces to find the set $(\mathbf{v},\mathbf{v_0},\mathbf{a},\mathbf{c})$ corresponding to a stationary Lagrangian funtional, $\mathcal{L}$, by setting to zero the directional derivative with respect to an arbitrary variation in the set of variables. In the case of the state variable $\mathbf{v}$,

$$\frac{\partial\mathcal{L}}{\partial\mathbf{v}}\cdot\delta\mathbf{v} = \lim_{\epsilon\to 0}\frac{1}{\epsilon}[\mathcal{L}(\mathbf{v}+\epsilon\delta\mathbf{v},\mathbf{v_0},\mathbf{a},\mathbf{c}) - \mathcal{L}(\mathbf{v},\mathbf{v_0},\mathbf{a},\mathbf{c})], \tag{B.34}$$

what, taking into account Eq.(B.32) and defining the energy scalar product as $[\mathbf{v_1},\mathbf{v_2}] = (\mathbf{v_1}, L\mathbf{v_2})$, so that $[\mathbf{v},\mathbf{v}]/4 = E(t)$, gives

$$\frac{\partial\mathcal{L}}{\partial\mathbf{v}}\cdot\delta\mathbf{v} = \lim_{\epsilon\to 0}\frac{1}{\epsilon}\left[\frac{[\mathbf{v}+\epsilon\delta\mathbf{v},\mathbf{v}+\epsilon\delta\mathbf{v}]}{E_0} - \frac{E_t}{E_0} - <F(\mathbf{v}+\epsilon\delta\mathbf{v}),\mathbf{a}> + <F(\mathbf{v}),\mathbf{a}> \right.$$
$$\left. -(H(\mathbf{v}+\epsilon\delta\mathbf{v}),\mathbf{c}) + (H(\mathbf{v},\mathbf{v_0}),\mathbf{c})\right]. \tag{B.35}$$

From the third term of the evaluated limit, provided that F is a linear operator, the product $<F(\delta\mathbf{v}),\mathbf{a}>$ arises. Moreover, after some integration, the adjoint operator F^+ appears in the other side of the product, allowing us to define the adjoint system showed in Eq.(B.25) for the co-state variable, $\mathbf{a}$, when the variation of the Langrangian is set to zero. Proceeding likewise for the rest of the limit terms, we obtain the transfer condition between direct and adjoint systems at $t=\tau$,

$$\mathbf{a}(\tau) = \frac{2}{E_0}\mathbf{v}(\tau), \tag{B.36}$$

and the compatibility condition,

$$\mathbf{c} = \mathbf{L}\mathbf{a}(0). \tag{B.37}$$

The optimality condition can be derived by combining the result of the derivative $(\partial\mathcal{L}/\partial\mathbf{v_0})\delta\mathbf{v_0} = 0$,

$$\mathbf{c} = 2\frac{E_t}{E_0}\mathbf{v_0}, \tag{B.38}$$

and Eq.(B.37), to give,

$$\mathbf{v_0} = \frac{1}{2}\frac{E_0^2}{E_\tau}\mathbf{a}(0). \tag{B.39}$$

On the other hand, the two remaining variations of $\mathcal{L}$, with respect to $\mathbf{a}$ and $\mathbf{c}$, recover the constraints $F(\mathbf{v}) = 0$ and $H(\mathbf{v}, \mathbf{v_0}) = 0$ respectively.

The strategy followed is an iterative algorithm that, starting from any chosen intimal condition that satisfies the control constraint, integrates direct system first to $t = \tau$, and later the adjoint one backwards in time, after applying the transfer condition Eq.(B.36). Now, the optimal condition Eq.(B.39) provides a new guess to iterate again. This method only assures a local extreme [27], but the formulation used by Luchini [82] guarantees the convergence of the process to a global maximum. In this formulation, the optimal initial condition is the eigenvector of largest eigenvalue of the operator $\mathbf{U}(\tau)^+\mathbf{U}(\tau)$, being $\mathbf{U}(\tau)$ the propagator defined as $\mathbf{v}(\tau) = \mathbf{U}(\tau)\mathbf{v}(0)$. The convergence of the method is always ensured, except for the case of an initial condition that is orthogonal to the optimal perturbation.

B.2.4 Coordinate transform and treatment of singularities

In order to solve numerically the direct and adjoint eigenvalue problems and to ensure accuracy in the approximation, a pseudospectral Chebyshev technique was implemented [40]. The infinite radial coordinate is first mapped onto a Chebyshev space, $s \in [-1, +1]$, using the Gaus-Lobatto grid on the form,

$$s_j = \cos\frac{(j-1)\pi}{2N+1} \quad j = 1, ..., 2N+2. \tag{B.40}$$

This grid and the differentiation matrices were computed with the DMSuite [156] package in MATLAB®. Then, an algebraic mapping function [22] was applied to adjust the grid into a points distribution so that $r \in]-\infty, +\infty[$, taking afterwards only the positive semi-infinite grid ($r > 0$). This function,

$$r(s) = \gamma s/\sqrt{1-s^2}, \tag{B.41}$$

depends upon a stretching factor, γ, that controls the points spreading after imposing the radius of the penultimate point, r_{max}, and that is defined through $\gamma = r_{max}\sqrt{(1-s_{2N+1}^2)}/s_{2N+1}$, being s_{2N+1} the penultimate point of the Gaus-Lobatto grid. With this transformation the radial derivatives are calculated as $d/dr = d/ds\ ds/dr$, where d/ds is computed with the derivation matrix; and the points -1 and $+1$ correspond to $-\infty$ and $+\infty$ respectively. To apply the boundary conditions at $s = \pm 1$ (perturbation velocity and its derivative are null), we simply eliminate the first and last

columns and lines of the general differentiation matrix dealing only with the internal collocation points, $j = 2, ..., 2N + 1$.

A geometric singularity at the axis ($r = 0$) arises from the use of cylindrical coordinates. In order to avoid it and to ensure the regularity in its neighbouring, we will exploit the parity properties [61] of functions with azimuthal dependence like $e^{im\theta}$. The symmetry parity relations are:

$$p(-r, z) = (-1)^m p(r, z), \tag{B.42}$$

$$u_r(-r, z) = -(-1)^m u_r(r, z), \tag{B.43}$$

$$u_\theta(-r, z) = -(-1)^m u_\theta(r, z), \tag{B.44}$$

$$u_z(-r, z) = +(-1)^m u_z(r, z), \tag{B.45}$$

indicating that if m is odd (or even), p and u_z are odd (even respectively) whereas u_r and u_z are even (odd respectively). By using them, the smoothness of the function in the vicinity of the axis is assured and furthermore, the calculation can be restricted to half of the domain ($r > 0$).

To deal with the singularity, the solution is projected on the N first even Chebyshev polynomial (T_{2j}) for even functions, and on the N first odd polynomial (T_{2j+1}) for odd functions. The expansions allow to obtain a problem of order $2N + 2$, an even number of collocation points, that is useful since no point is placed at the axis. Thus, pole conditions can be overlooked and only parity is imposed [160]. On the other hand, the derivation operators D_i (that solve d^i/dr^i) are affected by these parity conditions, so that even and odd functions have different schemes. To obtain them [4], "symetrization" relations can be used, having the advantage to limit the storing requirements. Thus, we divided the collocations matrices MD_i (d/ds) in four submatrices ($MD_i^{11}, MD_i^{12}, MD_i^{21}, MD_i^{22}$) of $N \times N$ elements (after applying boundary conditions at $s = \pm 1$) and define mirror matrices, $ND_i^{kl}(c, d) = MD_i^{kl}(c, N+1-d)$, to form the derivation matrices, D_i, for fields with the same parity than m and fields with a different one,

$$D_{i,odd} = MD_i^{22} - (-1)^m ND_i^{21}, \tag{B.46}$$

$$D_{i,even} = MD_i^{22} + (-1)^m ND_i^{21}. \tag{B.47}$$

As it has been mentioned, the approach used here does not impose the pole conditions, but as was proved by Fabre & Jacquin [35] and Fabre *et al.* [36] for the q-vortex and the Lamb-Oseen vortex respectively, accurate results with spectral accuracy are found when N is large enough.

B.2.5 Numerical convergence and validation

The influence of the number of discretization points in the basic profile shear layer (where the steep gradient is located) on the convergence is significant, but a large number of points will imply a higher computational cost. Therefore a compromise between convergence and time calculation has to be reached. The shear layer points number depends on the number of Chebyshev points and on the maximum radius for the mapping, so that an optimal combination for these two parameters must be sought. To do so, several issues must be taken into account. We know that the larger the aspect ratio $1/\theta$, the steeper the profiles near the shear layer are, requiring a more compact grid in its vicinity to ensure a smooth solution. As can be inferred from Eq.(B.41), a small r_{max} will ensure a highly clustered grid close to the origin and shear layer. Nevertheless, if the axial

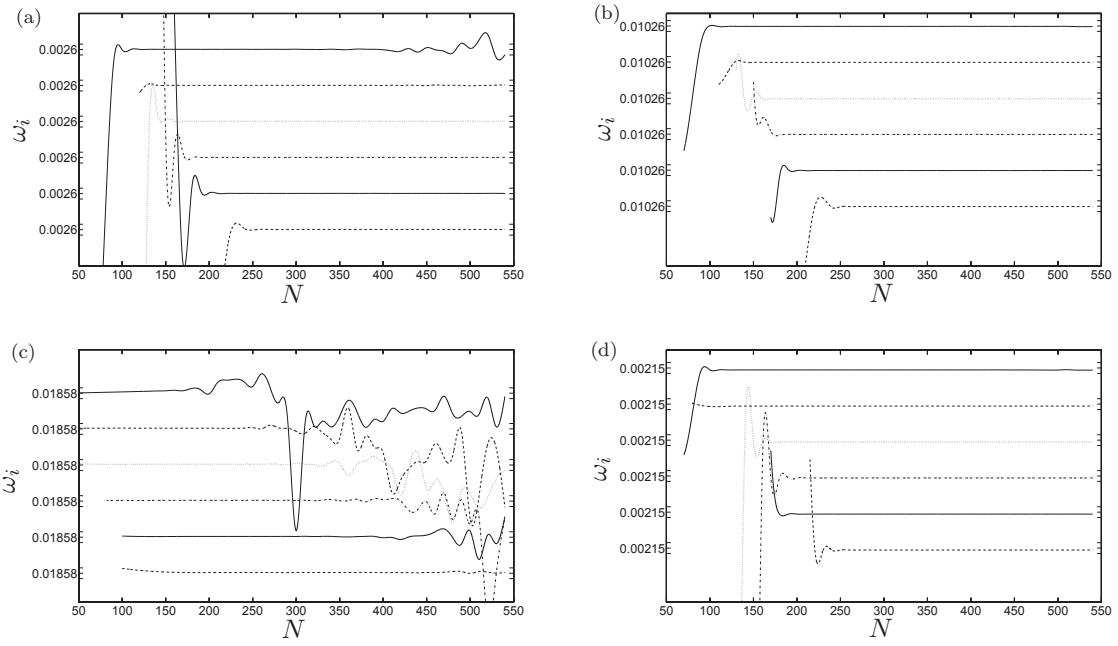

Figure B.2: Effect of mapping parameters N and r_{max} on amplification factors for: $1/\theta = 30$ ($Re = 75$), a) $k = 0.5$ and b) $k = 4.65$; and $1/\theta = 4$ ($Re = 10000$), c) $k = 0.1$ and d) $k = 2$. Each graphic depicts, from top to bottom, tests corresponding: $r_{max} = 100$, 200, 300, 400, 500 and 800. The ticks around centered values of ω_i denote an interval $\Delta\omega_i = \pm 1.5 \cdot 10^{-5}$.

Reference	Re	k	ω_r
Lessen & Singh [79]	37.9	0.3989	0.08
Morris [100]	37.64	0.44	0.1
Kulkarni & Agarwal [69]	37.68	0.4505	0.104
Xie & Lin [160]	37.683	0.459	0.103
Present	37.679	0.4481	0.1031

Table B.1: Comparison of Re_{cr} for fully developed jet.

wavenumber, k, is too small, the value of the penultimate point must be increased to map properly the flow, due to the fact that the approximated function decays exponentially as r tends to infinity. In this sense, in the limit $1/\theta \longrightarrow \infty$ (cylindrical vortex sheet), the velocity potential eigenfunction [9] can be expressed as $\Phi(kr) = DK_n(kr)$, standing K_n for the modified Bessel function of the second kind, wich decays exponentially as $\sim 1/\sqrt{kr}\ e^{-kr}$ when $r \longrightarrow \infty$. Thus, we might need to increase the number of collocation points to ensure a good resolution in the shear layer, but, as was expressed before, this would go against the computational performance.

Another problem arises when the number of collocation points becomes too large. Spectral methods imply the use of full and ill-conditioned matrices [151], creating some instabilities when the number of points overcome some threshold. To work out this contradictory problem of grid parameter choice, we performed some convergence tests for two kind of base flows: a highly 'top-hat' jet ($1/\theta = 30$) and a developed profile ($1/\theta = 4$). These two values represent the two extreme

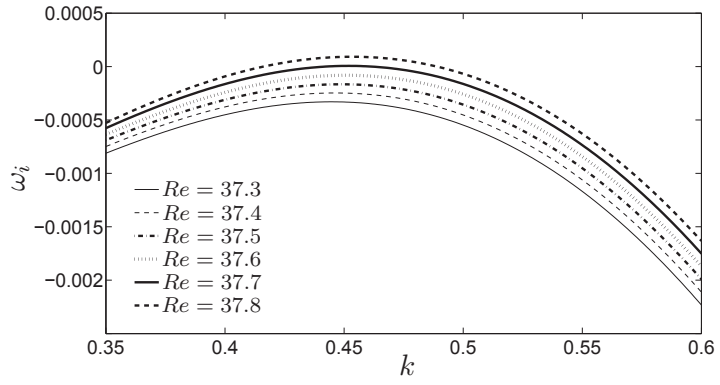

Figure B.3: Perturbation growth rate for a fully developed jet as a function of Re and k.

cases of our parametric study, even though they are far from the critical ratios for which the transitions between most unstable azimuthal modes takes place. Thus, choosing the numerical parameters by looking for the convergence of these cases, will ensure the accuracy of the results obtained for the rest. On the other hand, to asses the influence of Re we will take advantage of the fact that for smaller Re the transition takes place for high aspect ratios whereas for large Re it occurs for lower aspect ratios, so that we perform the convergence tests at $Re = 75$ and $Re = 10000$ for $1/\theta = 30$ and $1/\theta = 4$ respectively.

As a stability problem, we are interested in the growth rate of the perturbation that corresponds to the most unstable mode, ω_i, i.e. the mode with the largest positive or least negative imaginary part. If the growth rate is positive, then the flow will be temporally unstable. Hence, we will focus on the convergence of the most amplified mode for the two kinds of base flow mentioned before. First, a preliminary parametric study on k for $1/\theta = 30$ ($Re = 75$) and $1/\theta = 4$ ($Re = 10000$) are performed to obtain the loci or neutral perturbations for which $\omega_i = 0$, calculating for the most unstable azimuthal number for each case: $m = 0$ for the former and $m = 1$ for the latter. For the first case, the unstable region corresponds approximately to $k \in [0.471, 4.97]$, whereas for the latter it gives $k \in [0, 2]$. Thus, we define finally our convergence tests for $k = 0.5$ and $k = 4.65$ when $1/\theta = 30$, and $k = 0.1$ and $k = 2$ when $1/\theta = 4$, which are axial wavenumbers sufficiently smaller and larger to those of interest in our problem framework, so that the convergence task is representative. We carry out analysis to get the evolution of ω_i as N is increased, for different r_{max}, whose results are shown in Fig.B.2. As can be inferred from it, for all r_{max} a constant value for ω_i is reached after some oscillation when N is small, so that the larger the r_{max}, the larger the number of points needed for the mode to be converged. It is proved that there is always an interval in N for which the r_{max} curves overlap, providing the same results. The upper limit of this interval is imposed by the spectral instability at large N, that gives rise to new oscillations in the value of the amplification rate. This limit appears early for all radius in the case shown in Fig.B.2(c), i.e. for the developed jet and $k = 0.1$, not even converging when $r_{max} = 100$, indicating how critical this parameter is when the perturbation has a small axial wavenumber. For the final calculation to be accurate enough, the choice of numerical parameters must lie on the converged limit for all the extreme cases tested; and on the other hand, a small value of N should be picked to reduce the computation time. Taking into account these considerations, $N = 200$ and $r_{max} = 300$ stand out as an optimal combination to meet the necessities and were chosen as default values for the

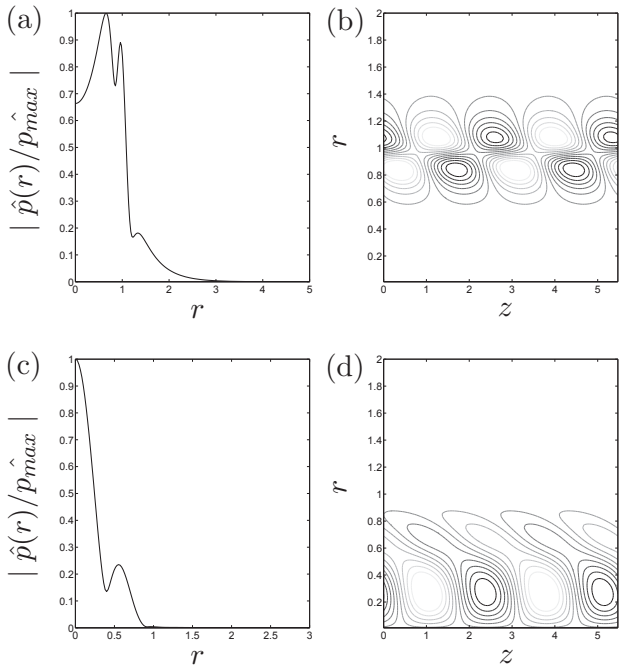

Figure B.4: Pressure eigenfunctions and azimuthal vorticity for: (a,b) SL mode and (c,d) JC mode for an axisymmetric perturbation with $k = 2.297$ and a jet profile of $1/\theta = 10$ when $Re = 1000$.

parametric study.

Finally, to validate the spectral approach used here for the linear stability analysis, we compare the results for the following fully developed jet with algebraic velocity profile,

$$U(r) = \frac{1}{(1+r^2)^2}, \tag{B.48}$$

with those obtained by several authors in the past [79, 100, 69, 160]. We calculated the critical Re number by looking for the growth rate curve, $\omega_i(k)$, that becomes tangent to the line $\omega_i = 0$, when the azimuthal mode is $m = 1$ (most unstable azimuthal mode for this sort of flow). As can be seen in Fig.B.3, as Re is increased, the curve maximum approaches the positive values (unstable region), until eventually for $Re_{cr} = 37.679$ it reaches $\omega_i = 0$. The axial wavenumber and frequency corresponding to the critical perturbation were found to be $k = 0.4481$ and $\omega_r = 0.1031$. A comparison with some other works is presented in Table B.1, that shows a good agreement with our results. On the other hand, the validation of the optimal perturbation code was given by Antkowiak [4], for a Lamb-Oseen vortex.

B.3 Results and discussion

B.3.1 Temporal stability: modal analysis

The temporal modal analysis of a round jet presents only one unstable mode for a given perturbation if the problem is unstable (positive growth rate), and corresponds to a *shear layer mode* (SL), i.e.: a mode that is concentrated within the shear layer region. Then, all the analysis along the

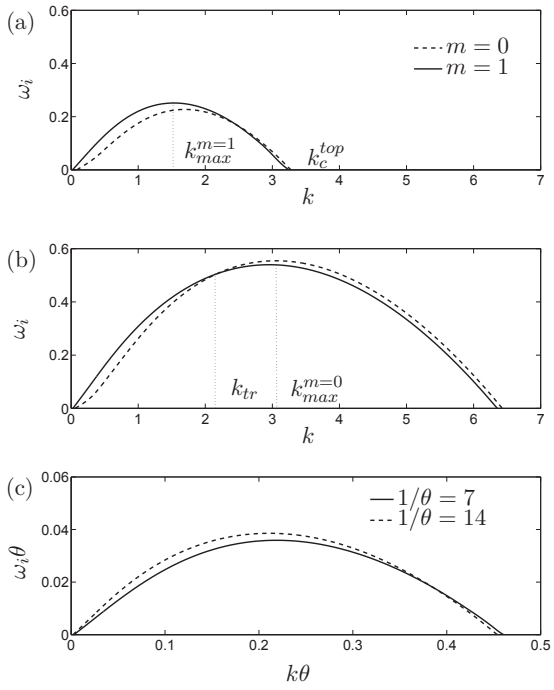

Figure B.5: Growth rate for azimuthal modes $m = 0$ and $m = 1$ when (a) $1/\theta$ =7 and (b) $1/\theta = 14$ and Re =1000. (c) Growth rate for $m = 1$ scaled with the aspect ratio.

work will be devoted to the variation of the stability properties of this unstable mode. Nevertheless, some comment must be done about another kind of modes encountered in stability problems of round jets. By performing a spatial-temporal stability analysis of round jets, a second kind of unstable modes called *jet column modes* appears [56]. They are characterized by a pressure eigenfunction with its maximum at the axis (Fig.B.4) and their importance is due to the fact that they are dominant over SL modes for axisymmetric disturbances for low group velocities [80]. The temporal modal approach picks these modes for axisymmetric perturbations as stable modes, and they are found as part of the less damped modes in the discrete branch of the spectrum. To check their influence on the transient dynamics, several test were performed, confirming that their energy gain is always smaller than those obtained for SL modes. Hence, no further mention will be done throughout this work about jet column modes.

Parametric study

The goal of this section is to evaluate the evolution of the most unstable azimuthal mode, either $m = 0$ or $m = 1$, when Re and $1/\theta$ are varied. The procedure to characterize the trends given by the axysimmetric ($m = 0$) and the helicoidal ($m = 1$) azimuthal modes in this long-time analysis has been the following: once Re and $1/\theta$ are set, we have performed calculation to compare the growth rate ω_i curves versus axial wavenumber, k, for both azimuthal modes. Keeping constant the Re value, we have proceeded for a wide range of $1/\theta$, varying from small values (FDP jets) to larger values (TH jets), and reporting the maximum value of ω_i for each curve.

Let us first take a look at the results when Re is constant. The Figs.B.5(a)-(b) depict the

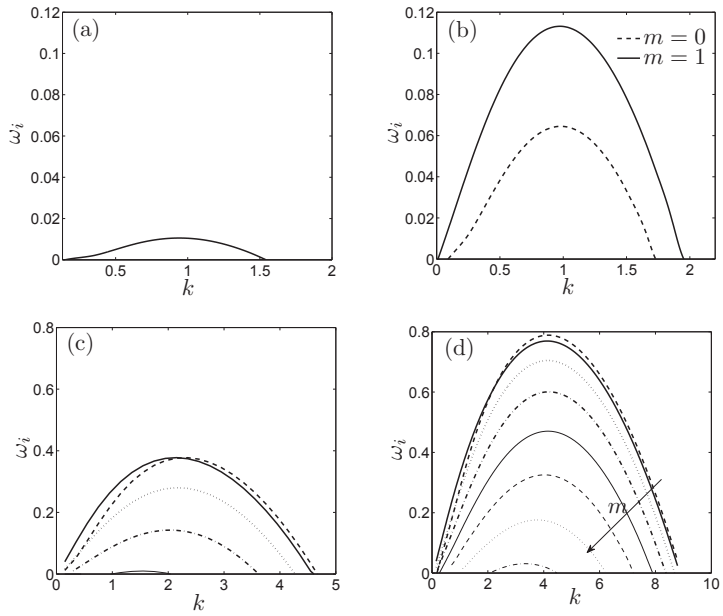

Figure B.6: Unstable azimuthal modes when $Re = 1000$ and: (a) $1/\theta = 2$, (b) $1/\theta = 4$, (c) $1/\theta = 10$ and (d) $1/\theta = 20$. Arrow indicates the sense of growing m.

growth rate of the two most unstable azimuthal modes, $m = 0$ and $m = 1$, depending on the axial wavenumber k, for $Re = 1000$ and two aspect ratios: $1/\theta = 7$ and 14. It is clear for the lower ratio (Fig.B.5a) that the helicoidal mode is more unstable than the axysimmetrical mode, even if there is a range in k which defines a secondary region with $m = 0$ as the most unstable mode, slightly above the helicoidal mode growth rate. On the other hand, if the aspect ratio is increased up to a value of $1/\theta = 14$ (Fig.B.5b), the results show a different form. The axysimmetric mode curve is now above the helicoidal mode one for most of axial wavenumbers, indicating that there must have been a critical aspect ratio, $1/\theta_{cr}$, above which $m = 0$ has become the most unstable mode in general. This critical point appears when the curve growth rate maximum, ω_i^{max}, for $m = 0$ has reached the same value that ω_i^{max} for $m = 1$. On the other hand, two important axial wavenumbers can be defined for a curve $\omega_i(k)$ of a given azimuthal number. Thus, k_{max} corresponds to the value that gives the curve largest growth rate, ω_i^{max}; and a cut-off value that we will denote as k_c^{top} since for some jet profiles there is as well a low cut-off at large wavelengths. As can be seen in Fig.B.5(c), k_c scaled clearly with $1/\theta$ and likewise, $\omega_i(k)$ and k_{max} do so with small discrepancies.

For very small aspect ratios, the only unstable mode existing is the helicoidal mode. When $1/\theta$ grows, eventually, the axysimmetric mode becomes unstable as well, for a value that depends on Re. Actually, the bigger the aspect ratio is, the more azimuthal modes become unstable (Fig.B.6). Thus, for $Re = 1000$, when $1/\theta = 2$ only $m = 1$ is unstable, but when $1/\theta = 20$ the unstable modes range from $m = 0$ as the most amplified, to $m = 7$. This is the consequence of an overall growth for ω_i (larger amplification) as the $1/\theta$ is increased for all azimuthal modes: for very small aspect ratios, the only unstable mode existing is the helicoidal mode (Fig.B.6a), but when the aspect ratio grows, eventually, the axysimmetric mode becomes unstable as well (Fig.B.6b), for a value that depends on Re. This growing trend is accompanied by a displacement of the curve maximum

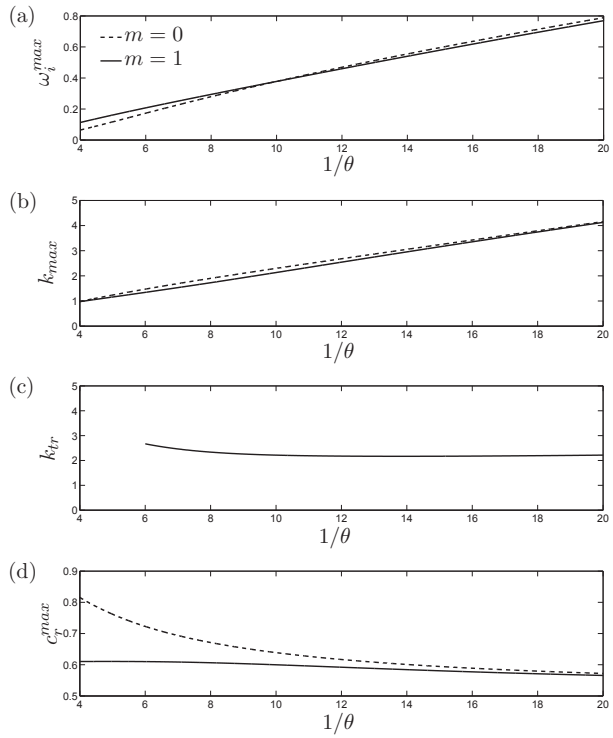

Figure B.7: Evolution of the main stability properties with $1/\theta$ when Re =1000.

to larger values of k, as well as an enlargement of the unstable interval of k. This behavior is not uniform for both azimuthal modes, creating then a crossing between the curves that splits up the unstable axial wavenumber interval into two zones. These region are delimited by a transition axial wavenumber, k_{tr} (see Fig.B.5b), that determines the change in the dominating azimuthal perturbation between high and low axial wavenumbers, dominating $m = 1$ over $m = 0$ to the left of the crossing. The evolution of this transition axial wavenumber with $1/\theta$ will indicate the relative shift grade between modes.

To get a complete idea of the evolution of curves as $1/\theta$ changes for a constant Re, it is necessary to observe the axial wavenumber corresponding to ω_i^{max}, maximum of $\omega_i(k)$, k_{max}, k_{tr} and its phase velocity, defined as $c_r^{max} = \omega_r^{max}/k_{max}$; being ω_r^{max} the angular frequency of the mode corresponding to the maximum of curves $\omega_i(k, m)$. As can be seen in Fig.B.7(d), in general, c_r^{max} decays for $m = 0$ when we increase $1/\theta$, while for $m = 1$ it does so softly after a small growth for really low ratios. When $1/\theta \longrightarrow \infty$, both azimuthal numbers reach the stable value of 0.5 given by the limit of Kelvin-Helmholtz instability for plane shear layers. Moreover, $c_r^{max}(m = 0)$ is always bigger than $c_r^{max}(m = 1)$ for all $1/\theta$ studied. As far as the k_{max} is concerned, the trends are crescent and almost linear with a constant growth, as can be deduced from Fig.B.7(b). Again, k_{max} is always higher for $m = 0$ than $m = 1$. On the other hand, if we pay attention to the intersection axial wavenumber between curves, k_{tr}, we will be able to accurately quantify the relative shift. In Fig.B.7(c) we can see that, starting from $1/\theta = 6$ since below it the curves do not intersect each other, the crossing point moves initially toward smaller values of k as the aspect ratio grows, until a point from where it start to rise slightly. Even if k_{tr} recovers, the interval to the left of

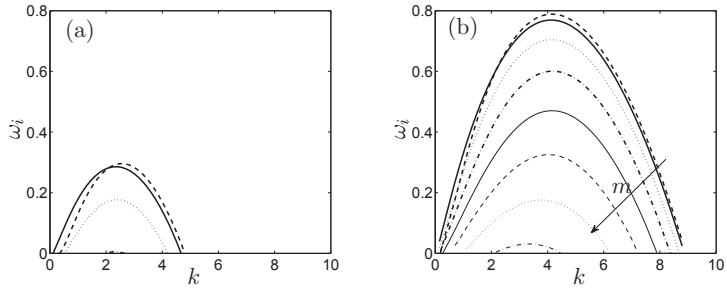

Figure B.8: Unstable azimuthal modes when $1/\theta = 20$ and: (a) $Re = 100$ and (b) $Re = 1000$. Arrow indicates the sense of growing m.

the intersection, where $m = 1$ stands out, represents a smaller range in comparison with the right interval as the aspect ratio grows, indicating that $m = 0$ becomes more and more dominant over a larger number of unstable k. This idea can be deduced from the Figs.B.5(a)-(b) where it can be observed how, when $1/\theta$ is small, the crossing takes place at the right side of both k_{max}, close to k_c^{top}; whereas when $1/\theta$ is large, even though the intersection has barely been shifted, the interval ruled by $m = 1$ confined to the left has become relatively small compared to the right interval. This effect becomes more pronounced for larger aspect ratios due to the fact that k_c^{top} increases (at the same pace than k_{max}), and can be quantified by the computation of the ratios $k_{tr}/k_{max}(m)$, whose values are shown in Table B.2 for some $1/\theta$.

$1/\theta$	6	7	8	9	10	11	14	20
$k_{max}(m=0)$	1.4715	1.692	1.9	2.101	2.297	2.489	2.867	4.157
$k_{max}(m=1)$	1.3422	1.532	1.726	1.927	2.131	2.337	2.749	4.127
k_{tr}	2.6359	2.4626	2.3351	2.2584	2.2146	2.1884	2.1673	2.2149
$k_{tr}/k_{max}(m=0)$	1.7913	1.4554	1.2290	1.0749	0.9641	0.8792	0.7097	0.5328
$k_{tr}/k_{max}(m=1)$	1.9639	1.6074	1.3529	1.1720	1.0392	0.9364	0.7339	0.5367

Table B.2: Summary of k_{max} and k_{tr} values for several $1/\theta$ and $Re = 1000$.

Along with k_{tr}, a good parameter to complete the problem about which azimuthal mode is more unstable at a fixed aspect ratio can be the maximum of the growth rate curve, $\omega_i^{max}(m)$. A comparison between both $\omega_i(m = 0)$ and $\omega_i(m = 0)$ help to infer quickly which mode is prevailing for most of the unstable axial wavenumbers. Thus, as it has been showed, when $1/\theta$ is small the $m = 1$ curve is above $m = 0$, whereas it is the other way around for large $1/\theta$, indicating a change in the behavior at some value of $1/\theta$. Figure B.7(a) depicts the evolution of ω_i for both azimuthal modes with the aspect ratio when $Re = 1000$, showing how there is an intersection (that corresponds to the critical point at where change between overall dominant modes occurs) at $1/\theta_{cr} \simeq 9.9946$.

Once we have qualitative and quantitatively explained the evolution of stability properties when Re is constant, we proceed now to describe what happens when Re is modified. The results showed for $Re = 1000$ can be considered inviscid since almost no differences have been found between these and those derived from $Re = 10000$. Nevertheless, when Re decreases, the stability

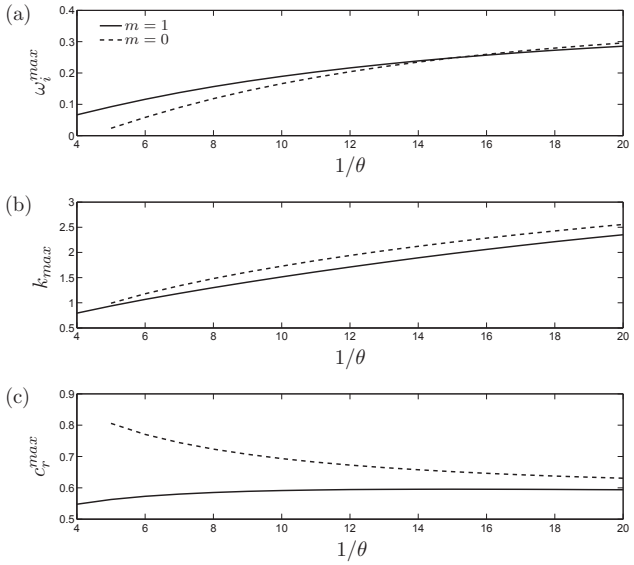

Figure B.9: Evolution of the main stability properties with $1/\theta$ when Re =100.

properties change considerably. Let us take a look at Fig.B.8, where all the unstable azimuthal modes are depicted when $1/\theta = 20$, for $Re = 100$ and $Re = 1000$ (also presented in Fig.B.6d). As can be seen, when the viscosity is dominant, only $m = 0, 1, 2$ and 3 are unstable. Moreover, this stabilizing effect is reinforced by a shortening of the unstable range of axial wavenumbers, and overall smaller growth rates for all the perturbations. In this sense, a deeper look at the results confirms that, as has been pointed out in the past for inviscid cases [9], for a given disturbance in m, and set k for a given aspect ratio, the value of ω_i grows with Re and seems to reach its greatest at infinity. Then, viscosity has a stabilizing influence for azimuthal modes, even though it does not have the same quantitatively impact on both $m = 0$ and 1. Furthermore, it has been found as well a left cut off in k for $m = 0$ (whose value tends to 0 as $1/\theta$ grows) and the crossing between curves (k_{tr}) does not change much.

On the other hand, the dependencies of k_{max} and c_r^{max} with $1/\theta$ seem to be similar when Re decreases, although some minor considerations must be taken. First, as a consequence of the stabilization due to viscosity, $m = 0$ is stable under $1/\theta = 5$ for $Re = 100$. In Fig.B.9, the evolutions of ω_i^{max}, k_{max} and c_r^{max} with $1/\theta$ are gathered. It is shown how $k_{max}(m = 0)$ is bigger than $k_{max}(m = 1)$ always, and how the growth that $k_{max}(m)$ shows is not as linear as the one found for $Re = 1000$. As far as the phase velocity of the maximum is concerned, $c_r^{max}(m = 0)$ decreases continuously with the aspect ratio, whereas $c_r^{max}(m = 1)$, after an initial growth, shows a quite slow decrease, remaining almost constant for the aspect ratios studied. Finally, in Fig.B.9(a) is observed how the critical $1/\theta$, from where the dominant azimuthal mode changes, has been shifted to a larger value, $1/\theta_{cr} \simeq 15.15$. We can conclude then, that there is a strong influence of the viscosity on this parameter.

The evaluation of the influence of Re on $1/\theta_{cr}$ will define, in parametrical terms, a practical border between two regions representing the dominant unstable mode, represented in Fig.B.10. Nevertheless, some comments on the limits of validity of the frozen basic flow assumption must be

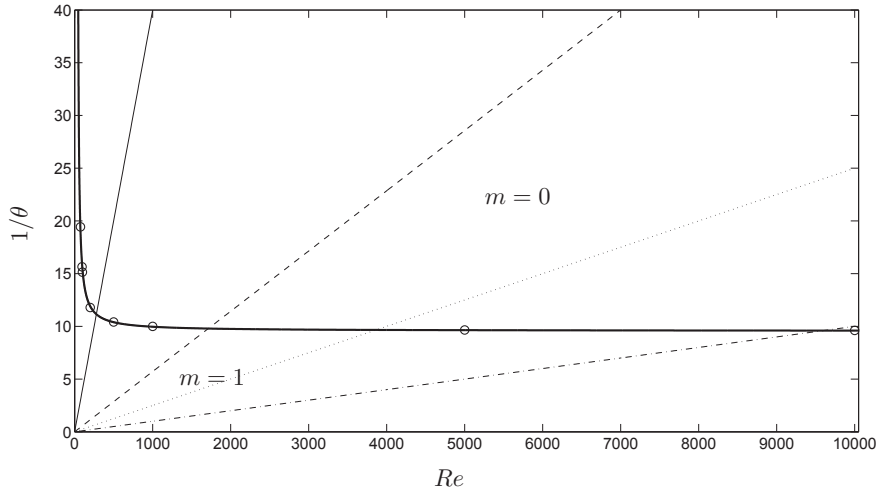

Figure B.10: Dependence of $1/\theta_{cr}$ on Re (and most unstable modes according to regions). Thin lines show constant values of Re_θ: 25 (solid), 175 (dashed), 400 (dotted) and 1000 (dashed-dotted).

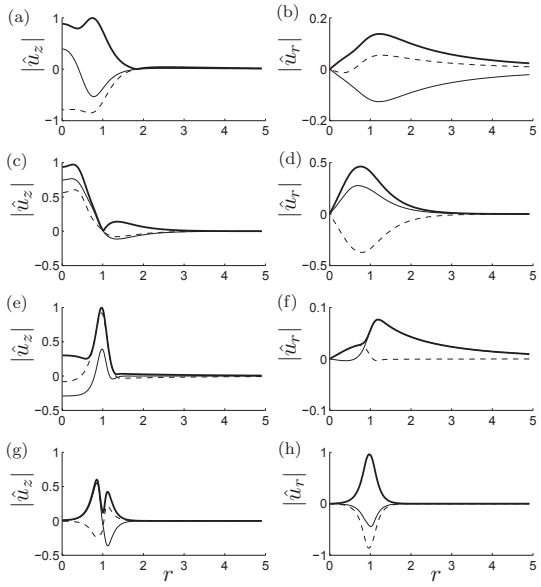

Figure B.11: Eigenfunctions of u_z and u_r for $m = 0$, obtained at $Re = 1000$ and: (a-b) $1/\theta = 4$ and $k = 0.3$, (c-d) $1/\theta = 4$ and $k = 1.7$, (e-f) $1/\theta = 16$ and $k = 0.3$, (g-h) $1/\theta = 16$ and $k = 7.2$. Values are normalized with $\sqrt{E}$. Note that absolute values (thick solid lines), real parts (thin solid lines) and imaginary part (dashed lines) of $\hat{u}_r$ and $\hat{u}_z$ are represented.

made. In this sense, we have to pay attention to the Reynolds number based on the shear layer thickness, Re_θ. The small length scale could be used to define a limit for which the assumption of no diffusion becomes inaccurate. Thus, $Re_\theta \gg 1$ is necessary to obtain relevant results, what means that for large $1/\theta$ and small Re (based on R), we should be careful interpreting the results. Within this frame, we compute parametric studies for several Re to obtain the transition between

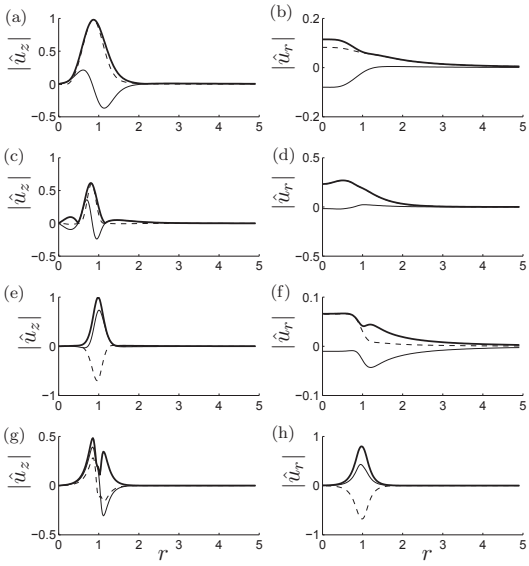

Figure B.12: Eigenfunctions of u_z and u_r for $m = 1$, obtained at $Re = 1000$ and: (a-b) $1/\theta = 4$ and $k = 0.3$, (c-d) $1/\theta = 4$ and $k = 1.7$, (e-f) $1/\theta = 16$ and $k = 0.3$, (g-h) $1/\theta = 16$ and $k = 7.2$. Values are normalized with $\sqrt{E}$. Note that absolute values (thick solid lines), real parts (thin solid lines) and imaginary part (dashed lines) of $\hat{u}_r$ and $\hat{u}_z$ are represented.

dominant azimuthal modes. When presented versus Re, the curve described by $1/\theta_{cr}$ has two limits: $1/\theta_{cr} \longrightarrow 9.56$ as $Re \longrightarrow \infty$, and $1/\theta_{cr} \longrightarrow \infty$ as $Re \longrightarrow 33.8^{-}$. Both are deduced from the equation used to fit the trend, $1/\theta_{cr} = 390/(Re - 33.8) + 9.56$, with a coefficient $C^2_{fit} = 0.9961$. The interpretation of Fig.B.10 is straightforward: when the combination of parameters ($1/\theta$, Re) is within the region $m = 0$, the flow will develop vortex rings for most of the unstable axial wavenumbers, as a consequence of the flow destabilization through the axisymmetric perturbation; and for the region $m = 1$ the flow will develop mostly an helicoidal azimuthal structure.

Eigenfunctions

To finish the section of linear stability analysis, we plot and compare the structures of eigenfunctions and vorticity for both azimuthal numbers studied when $Re = 1000$. To get a representative picture of the stability properties of parametric jets, we compute the modes for a small aspect ratio or FDP jet ($1/\theta = 4$), and a TH jet, with thin shear layer ($1/\theta = 16$). Figures B.11 and B.12 depict the radial profiles of the eigenfunctions of axial velocity, $\hat{u}_z$, and radial velocity, $\hat{u}_r$, of the most unstable mode for each disturbance, for two axial wavenumber. Azimuthal and axial vorticity eigenfunctions are also shown in Figs.B.13 and B.14 respectively. Obviously, only exists axial vorticity when $m = 1$. Finally, in Fig.B.15, a comparison is established for the the two azimuthal numbers for the disturbance defined by the growth rate curves intersection axial wavenumber, k_{tr}, when $1/\theta = 1/\theta_{cr}(Re = 1000)$.

The axisymmetrical azimuthal mode (Fig.B.11) shows always at the z-axis vanishing radial velocity, and high values of axial velocity that decrease as the aspect ratio grows. The similarity with plane shear layers confines the eigenfunctions at $r = 1$. Furthermore, the eigenfunctions of radial velocity for low wavenumbers have slower radial decrease than those corresponding to large

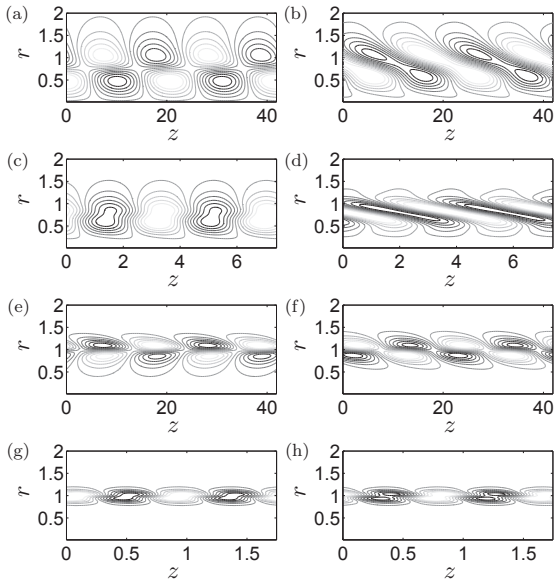

Figure B.13: Isocontours of azimuthal vorticity obtained at $Re = 1000$ and $m = 0$ (left column) and $m = 1$ (right column), for: (a-b) $1/\theta = 4$ and $k = 0.3$, (c-d) $1/\theta = 4$ and $k = 1.7$, (e-f) $1/\theta = 16$ and $k = 0.3$, and (g-h) $1/\theta = 16$ and $k = 7.2$.

values of k, a fact that was already exposed in Section B.2.5. Unlike the axisymmetric mode, the helical eigenmode ($m = 1$), shown in Fig.B.12, is characterized in general by the vanishing of the axial velocity in $r = 0$, due to the boundary condition at the axis, and a concentration around the shear layer location ($r = 1$), while the radial component of velocity, initially concentrated near the z-axis for small k, moves towards outer positions as the axial wavenumber is increased, until it reaches the shear and vanishes at the axis for large k (see Fig.B.12h). In the limit of very thin shear layer and large k, the eigenfunctions of both azimuthal modes resemble each other, due to the fact that the absence of curvature and the concentration of vorticity in $r = 1$ recovers the Kelvin-Helmhotz instability for plane shear layers [130]. Furthermore, for small axial wavenumbers the mode is affected by the curvature and its structure is distorted.

On the other hand, as can be expected, the structures of azimuthal and axial vorticity are confined in a smaller region in the radial direction as the shear layer diminishes. Similarly, an increasing axial wavenumber for a fixed shear layer parameter has a similar effect, shrinking the mode around $r = 1$, and forcing the merging of outer and inner counterrotating vortices.

B.3.2 Transient Growth

Large time analysis

As was mentioned before, the optimal initial condition for large time frame is the adjoint mode. This means that the excitation through the adjoint mode generates a transient growth in such a way that the gain reached is maximum when the time frame is large ($\tau \longrightarrow \infty$). To understand the mechanism that allows to retrieve the exponential growth of the most unstable direct mode with an extra gain, we must study the structure of the adjoint mode first. Figure B.16 depicts azimuthal vorticity contours for the direct and its counterpart adjoint modes of three helical ($m =$

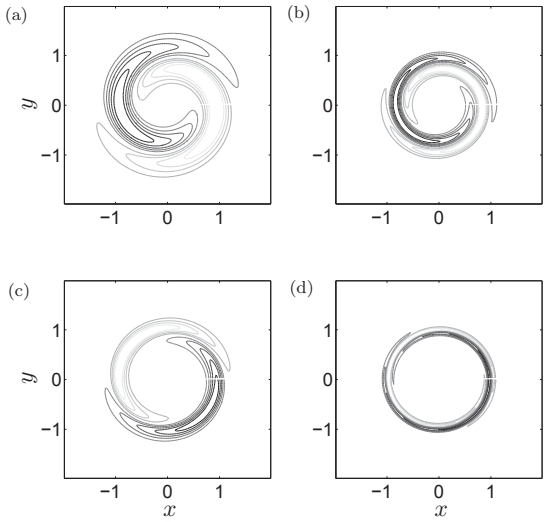

Figure B.14: Isocontours of axial vorticity obtained at $Re = 1000$ and $m = 1$ for: (a) $1/\theta = 4$ and $k = 0.3$, (b) $1/\theta = 4$ and $k = 1.7$, (c) $1/\theta = 16$ and $k = 0.3$, (d) $1/\theta = 16$ and $k = 7.2$.

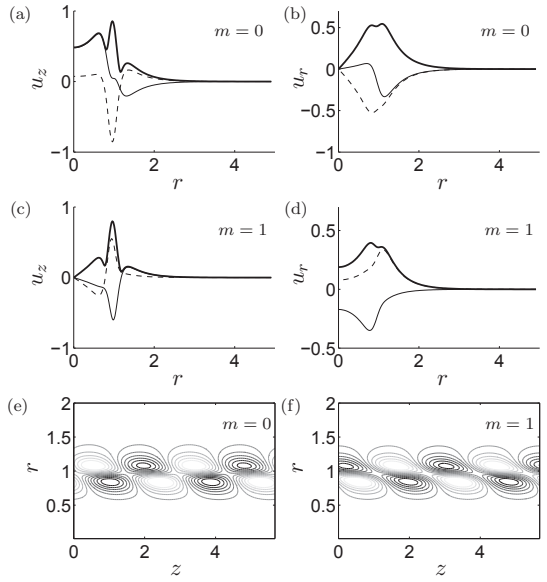

Figure B.15: Structure of eigenfunctions for the dominant mode, obtained at $Re = 1000$, $1/\theta_{cr}$ and $k = k_{tr} = 2.2146$. (a-d) Profiles of modulus of u_z and u_r (thick solid), and its real (thin solid) and imaginary parts (thin dashed). (e-f) Isocontours of azimuthal vorticity, Ω_θ.

1) disturbances of small and large axial wavenumbers and the most unstable axial wavenumber (k_{max}), for a base flow with $1/\theta = 10$ and $Re = 1000$. By analyzing the adjoint modes, we can confirm that the Orr mechanism is the responsible for the growth, even when the axial wavenumber is small (e.g.: $k = 0.3$). In all cases, the adjoint mode consists of azimuthal vortices tilted against the mean shear, located in the place where the value of vorticity for the direct mode is nearly zero. As far as the axisymmetric perturbations ($m = 0$) are concerned (Fig.B.17), the adjoint mode has

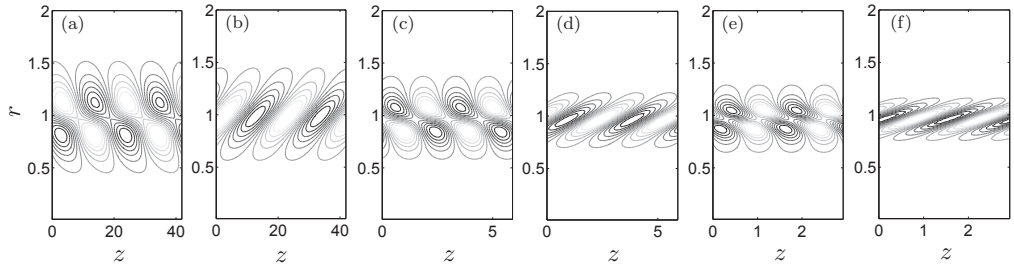

Figure B.16: Isocontours of azimuthal vorticity for the direct (a,c,e) and adjoint (b,d,f) dominant modes, obtained for $1/\theta = 10$, $Re = 1000$ and $m = 1$ when (a,b) $k = 0.3$, (c,d) $k = k_{max} = 2.131$ and (c,d) $k = 4.3$.

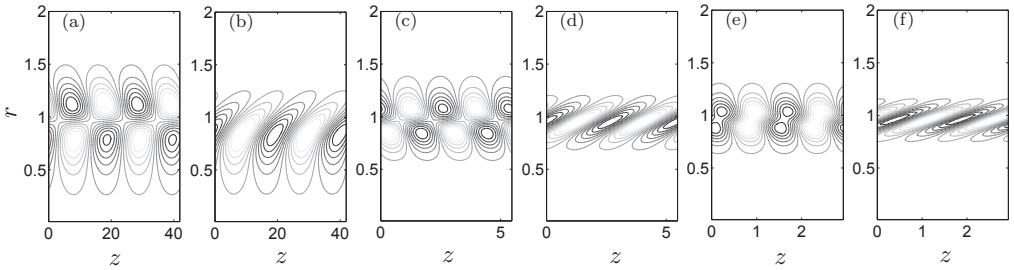

Figure B.17: Isocontours of azimuthal vorticity for the direct (a,c,e) and adjoint (b,d,f) dominant modes, obtained for $1/\theta = 10$, $Re = 1000$ and $m = 0$ when (a,b) $k = 0.3$, (c,d) $k = k_{max} = 2.297$ and (e,f) $k = 4.3$.

also similar structure for sufficiently large k (Figs.B.17d,f), however, for small k, the vortices are not totally oriented against the shear. Even though the outer part of them is tilted, extending along the zero vorticity region, the inner side resembles the inner part of direct mode, overlaping the locations of respective cores, what could indicate that the transient growth mechanism is not so efficient here. Anyway, for most of the axial wavenumbers investigated, the Orr mechanism is clearly identified, something that is somehow logical due to the fact that the disturbances studied are either bidimensional ($m = 0$) or weakly three-dimensional ($m = 1$ and k large enough).

If we focus now on a particular disturbance, we can observe that the excitation by an adjoint mode as initial condition leads to a considerable energy gain for large finite times. In Fig.B.18 we represent the logarithm of the temporal energy gain, obtained for a base flow with $1/\theta = 10$ when $Re = 1000$ and the most unstable disturbances for $m = 0$ and $m = 1$ (the axial wavenumbers correspond to $k = k_{max}(m)$). The modal stability analysis gives an energy growth that is approximated by $G_1(t) \sim e^{2\omega_i t}$, being ω_i the growth rate of the most unstable eigenmode of the given perturbation; but when the initial condition is the adjoint mode, the energy gain given by Eq.(B.29) is asymptotically reached. Thus, the energy gain evolution when the direct mode is optimaly excited (thick solid line, obtained through optimal perturbation analysis) undergoes initially a fast growth, and eventually ($t \simeq 4$ for $m = 0$ and $t \simeq 5$ for $m = 1$ in these cases) reaches an asymptotic growth rate parallel to the direct gain, but with a extra gain that measures the transient, and that can be quantified for both azimuthal modes through η (Eq.B.24). The evolution is characterized by a short time scale, a fact that was already pointed out by Butler & Farrel [20] for Orr mechanism.

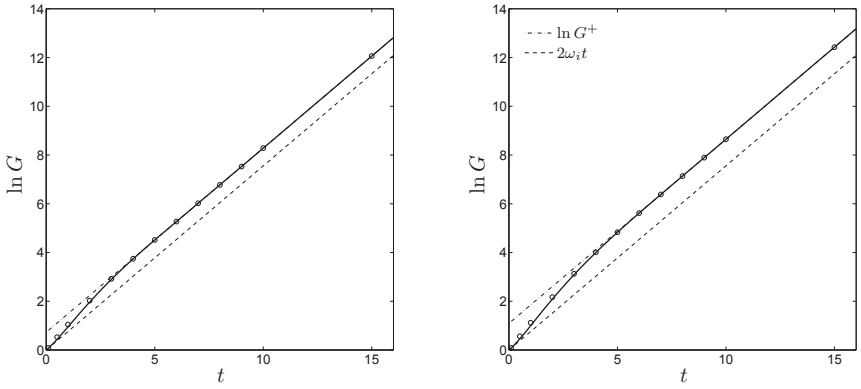

Figure B.18: Energy gain for $1/\theta = 10$ and $Re = 1000$ of the most unstable perturbations for (a) $m = 0$ ($k = k_{max} = 2.297$) and (b) $m = 1$ ($k = k_{max} = 2.131$). The thin dashed-dotted line represents the asymptotic gain predicted by Eq.(B.29) for large time when the direct mode is excited by its counterpart adjoint mode, and the thick solid line is the gain evolution obtained by optimal perturbation analysis when the adjoint mode is the initial condition and τ is large. The dashed line stands for the energy growth given by the direct mode. Circles are the energy gain at each optimal time.

The quantification of η for different axial wavenumbers and Re has been done through a second parametric study, where we compare the gain ratio between azimuthal wavenumbers, with the aim at assessing the validation of the modal stability analysis. We discuss again the influence of viscosity, aspect ratio and axial wavenumbers. Let us start with the anaysis of the influence of Re, when $1/\theta$ is fixed. Figure B.19 depicts the gain ratio, η, for the unstable ranges of k for both azimuthal wavenumbers studied, when $1/\theta = 10$ and $Re = 100$, 1000 and 10000. In general, $m = 1$ experiences always a bigger energy gain than that of $m = 0$ for all values of k and Re, nevertheless, as we will discuss later, it does not mean that the total energy is always higher for all finite time horizons. As can be seen in Fig.B.19(c), in the inviscid limit, the Orr mechanism is more efficient when the axial wavenumbers are large, something that could be expected [20, 46], but for small k, the transient growth leads as well to considerable gain ratios in the case of $m = 1$, when compared to intermediate values of k. When Re decreases, the relative importance of the transient growth at large k diminishes, being too weak related to the gain showed by low k and $m = 1$ when $Re = 100$ (Fig.B.19a). Hence, curvature and viscosity play clearly a stabilizing role. For $m = 0$, we observed how the gain ratio exhibits a feeble behavior when the axial wavenumber tends to zero for all Re investigated, something that could be anticipated by analyzing the adjoint mode structure (Fig.B.17), due to the fact that the overlaping of direct and adjoint structures should lead to large inner products, and consequently to lower η.

We pay attention now to the behavior of η when the aspect ratio is modified for a fixed Re. In Fig.B.20 we show the gain ratio η for $Re = 1000$ and three aspect ratios, $1/\theta = 4$, 10 and 16. As it can be seen, the helicoidal mode is again the one that experiences higher transient energy gain. Furthermore, it is evident that the energy gain is bigger for FDP jets (low aspect ratios) that TH jets. For $1/\theta = 4$ (Fig.B.20a) the difference between the gain growth achieved for $m = 1$ and $m = 0$ is more pronounced, being the mechanism for low k as efficient as for large k for the former azimuthal number (η is minimum for centered axial wavenumber), whereas for $m = 0$, the growth is again weaker at low k. When the aspect ratio increases, the transient growth effect is

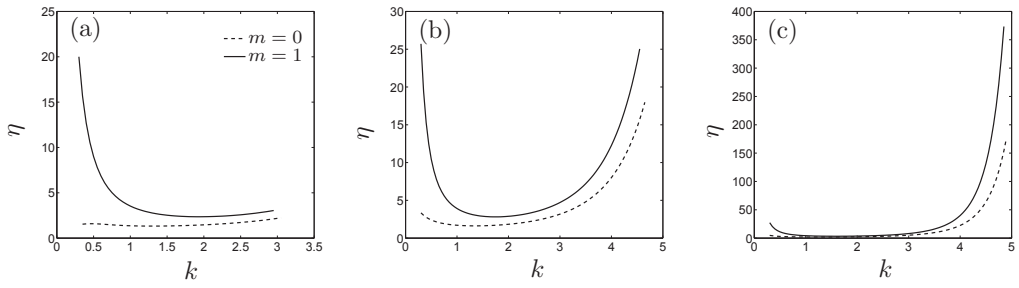

Figure B.19: Gain ratio η for the unstable range of k when $1/\theta = 10$ and: (a) $Re = 100$, (b) $Re = 1000$ and (c) $Re = 10000$.

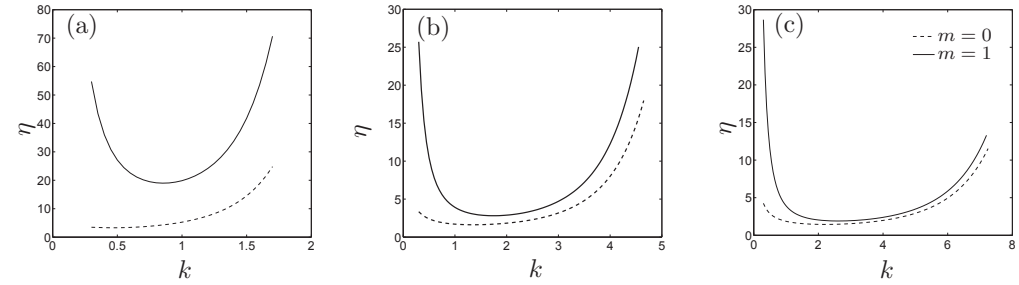

Figure B.20: Gain ratio η for the unstable range of k when $Re = 1000$ and: (a) $1/\theta = 4$, (b) $1/\theta = 10$ and (c) $1/\theta = 16$.

somewhat inhibited at large k.

The fact that the gain ratio is always bigger for disturbances with $m = 1$ (for all values of k, Re and every kind of jet profile studied), does not mean that the total energy is actually bigger for this sort of perturbations when compared to $m = 0$ at all finite-time horizons studied. Indeed, the extra gain implies a larger total gain for $m = 1$ during a short period of time, but if the modal growth rate (ω_i) of $m = 0$ is larger than that of $m = 1$, this mode will eventually emerge as the most unstable, from a critical transition instant that we will denote as τ_{tr}. Let us pay attention to Fig.B.21, where we show the evolution of the gain with respect to the optimal time, for $k = 0.3$ and $k = 4.3$. For the first case (Fig.B.21a), the modal analysis gives a bigger growth rate for $m = 1$ than for $m = 0$. Thus, since the extra gain is bigger as well for the helical mode, there is no doubt about the structures that the flow will develop. However, when k is larger than the transition axial wavenumber, k_{tr}, defined at the asymptotic analysis, $m = 0$ has a larger growth rate, and this mode will emerges after the transient is completed. As can be seen in Fig.B.21(b), during the transient and shortly in the asymptotic regime until τ_{tr}, the mode $m = 1$ is more unstable, but after this point the modal prediction is retrieved; indicating that in general, the short-time dynamics is dominated by the helical mode, what could lead to a different kind of base flow (if the energy gain is big enough to trigger non-linearities) that would render invalid the results of the temporal stability analysis. Then, we should correct the long-time prediction and anticipate the change in the flow between most unstable modes, by computing parametrically the transition time τ_{tr}.

In this sense, Fig.B.21 shows the evolution of τ_{tr} with k for $Re = 1000$ and several aspect ratios.

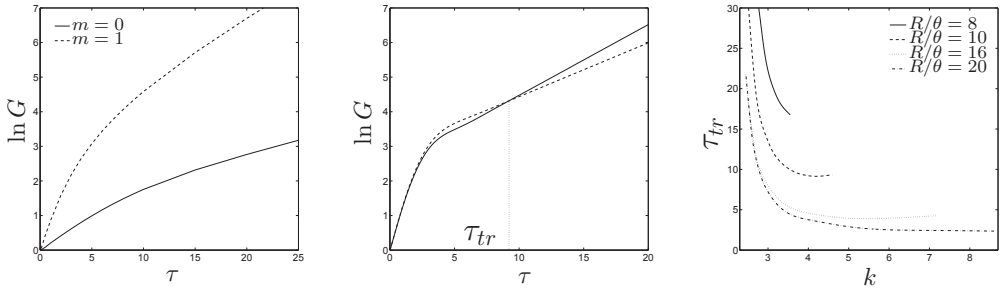

Figure B.21: (a,b) Gain evolution, $G(\tau)$, obtained through optimal perturbation analysis, for $1/\theta = 10$ when $Re = 1000$ and: (a) $k = 0.3$, (b) $k = 4.3$. (c) Evolution of the transition optimal time, τ_{tr}, with k and $1/\theta$ when $Re = 1000$.

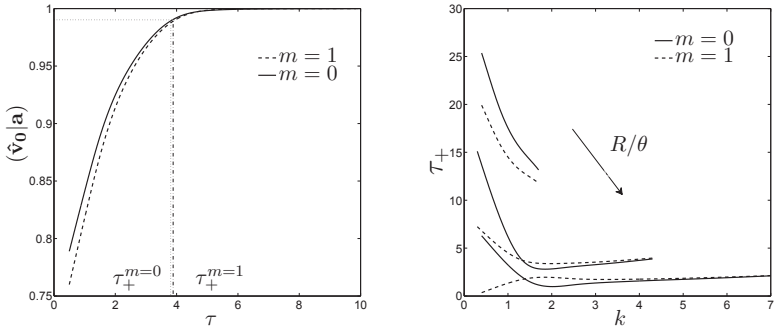

Figure B.22: (a) Evolution with the optimal time of the inner product between the optimal perturbation and the adjoint mode, $(\hat{\mathbf{v}}_\mathbf{0}, \mathbf{a})$, for $1/\theta = 10$ when $Re = 1000$ and $k = 4.3$. (b) Evolution of τ_+ with k for $1/\theta = 4$, 10 and 16, when $Re = 1000$. $1/\theta$ grows in the sense of the arrow.

For a fixed $1/\theta$, below k_{tr} both energy gain temporal evolutions never cross, and the definition of τ_{tr} does not make sense. In the limit, when $k = k_{tr}$ the growth rates are identical and the gain evolutions cross at infinity. For axial wavenumbers above k_{tr}, the difference between growth rates values increases faster than the difference between η, so that the crossing point takes place earlier, and that is why $\tau_{tr}(k)$ decreases as k grows. However, for large k, in the vicinity of the respective cut-off points, $k_c = k(\omega_i = 0)$, the gap $\Delta\eta = \eta(m = 1) - \eta(m = 0)$, increases and τ_{tr} is shifted slightly to higher values. On the other hand, as the aspect ratio grows, the axisymmetric mode becomes more dominant over a larger range of axial wavenumbers (the unstable range of k widens sharply and k_{tr} barely changes), and the difference between growth rates are larger. Thus, the energetic transient growth experienced by the helical mode is reversed soon, at lower τ_{tr} as the jet aspect ratio grows for a fixed k.

Short and finite-time analysis

The optimal perturbation analysis has been carried out following the procedure exposed in Section B.2.3. Some results corresponding the optimal energy gain for different optimal times are included in Fig.B.18 (circles) to compare with the gain evolution for a large optimal time when the adjoint mode is the initial condition (thick solid line), and the asymptotic prediction of the optimal excitation problem (Eq.B.29). As it was exposed, the transient for large optimal time is relatively short,

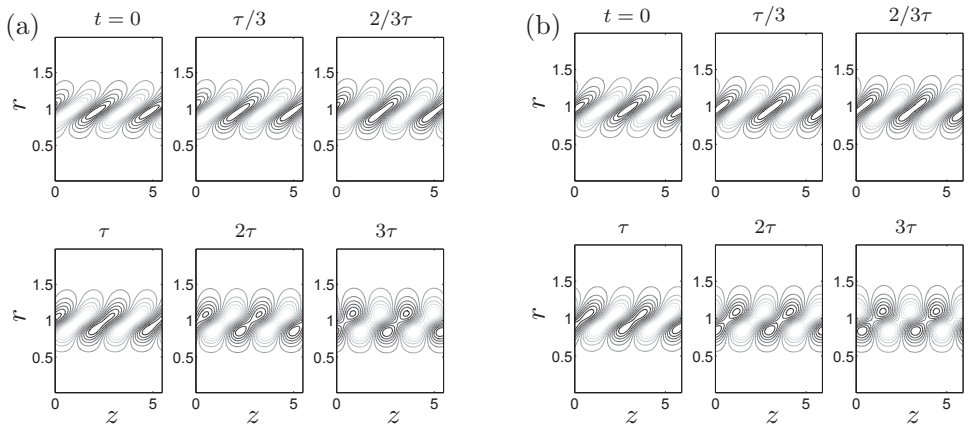

Figure B.23: Isocontours of azimuthal vorticity: Evolution of the optimal initial condition for a time horizon $\tau = 0.5$ and perturbation (a) $m = 0$ and (b) $m = 1$, with $k = k_{max}(m)$ when $1/\theta = 10$ and $Re = 1000$.

especially when k is large (Fig.B.21), since the energy gain reaches soon the asymptote given by the optimal excitation modal study. On the other hand, for the optimal times showed in Fig.B.18, the gain values at each horizon time are quite close to the evolution given by the adjoint mode at large time, what means that the adjoint mode drives the transient growth process for those study cases. A general quantification of this phenomenon and the validity of the long-time optimal perturbation model (Eq.B.29), can be made through the inner product between the optimal perturbation at each optimal time and the adjoint mode. As the horizon time approaches the end of the transient growth, the optimal condition resembles more the adjoint mode, until it becomes the optimal perturbation (initial condition) for a sufficiently large time. At this point, the inner product will grow with τ until eventually achieves the value 1 for large times (Fig.B.22a). To characterize the optimal time from when the adjoint mode leads the transient, we will make use of the parameter τ_+, defined as the time for which the inner product reaches a value of 0.99.

In Fig.B.22(b) we present the evolution of τ_+ with k for three different jet aspect ratios and $Re = 1000$. At first sight, we can say that for a fixed aspect ratio, the adjoint mode drives the process earlier as the axial wavenumber increases; and that increasing $1/\theta$ shorten the transient as well. As far as the difference between azimuthal modes is concerned, only big discrepancies are found when the curvature is big (small k). Thus, we can deduce that for TH jets and not so small axial wavenumbers, the finite-time dynamics could be well described by the modal analysis of the adjoint problem, without necessity of performing optimal perturbation analysis.

The short duration of the transient growth is confirmed by taking a look at the evolution of the structure of the initial condition for different optimal times within the frame of optimal perturbation analysis. We study the time horizons $\tau = 0.5$, 2 and 5, to describe the short-time and finite-time dynamics for perturbations with $k = k_{max}$ for both azimuthal modes. In all cases, the optimal initial conditions for both azimuthal numbers correspond to an array of vortices tilted against the shear, in the way described by the Orr mechanism, and with different slopes depending on the optimal time. For $\tau = 0.5$ (Fig.B.23) we can see how both initial conditions have structures that are less clustered and tilted than the adjoint modes shown in Figs.B.16 and B.17. Thus, they

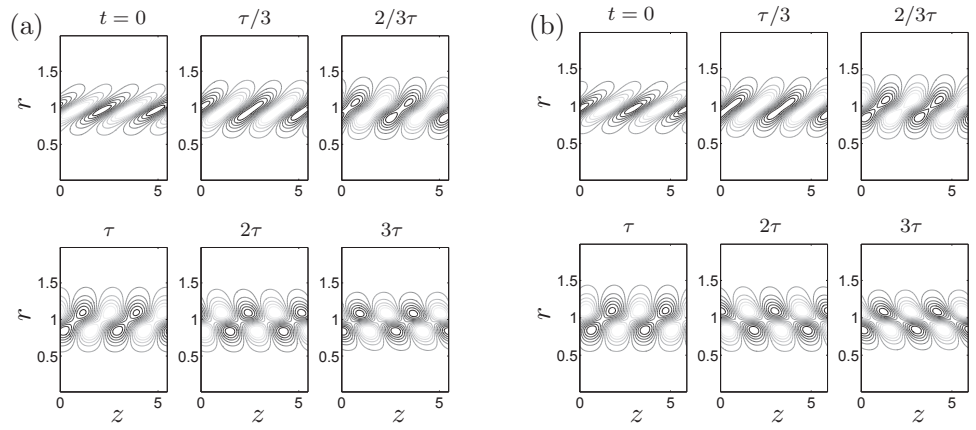

Figure B.24: Isocontours of azimuthal vorticity: Evolution of the optimal initial condition for a time horizon $\tau = 2$ and perturbation (a) $m = 0$ and (b) $m = 1$, with $k = k_{max}(m)$ when $1/\theta = 10$ and $Re = 1000$.

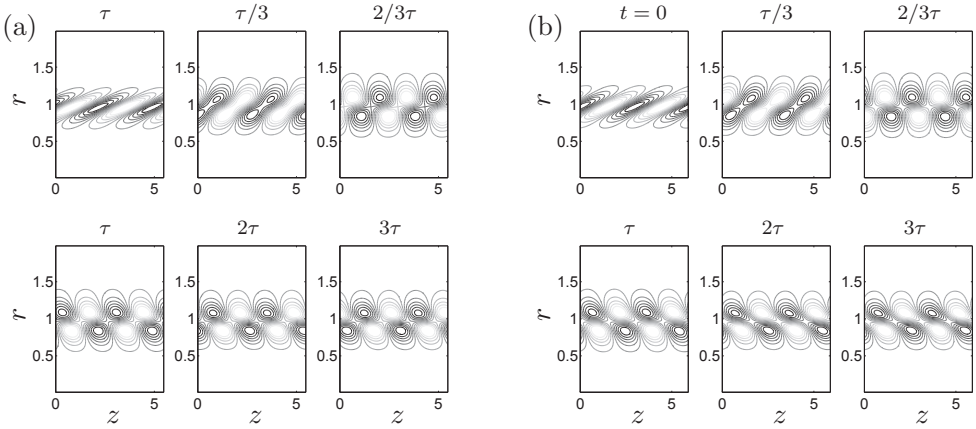

Figure B.25: Isocontours of azimuthal vorticity: Evolution of the optimal initial condition for a time horizon $\tau = 5$ and perturbation (a) $m = 0$ and (b) $m = 1$, with $k = k_{max}(m)$ when $1/\theta = 10$ and $Re = 1000$.

have no time to evolve between $t = 0$ and the optimal time, given optimal responses (at $t = \tau$) that are very similar to the initial conditions, with only some minor modifications in the shape of the cores. Nevertheless the optimal energy gain, obtained at $\tau = 0.5$ ($\ln G(\tau = 0.5)_{m=0} = 0.5235$ and $\ln G(\tau = 0.5)_{m=1} = 0.56066$), is higher than the values obtained through the initialization with the adjoint mode ($\ln G(\tau \longrightarrow \infty)_{m=0} = 0.4396$ and $\ln G(\tau \longrightarrow \infty)_{m=1} = 0.4559$), as can be seen in Fig. B.18. Proceeding likewise, for $\tau = 2$, we find a quicker transient, with initial conditions (more tilted than for $\tau = 0.5$) that develop a second core before the optimal time, and that orientates itself in the direction of the shear when $t = 2\tau$ (at $t = 3\tau$ the direct mode is almost retrieved for both m). The optimal energy gain calculated approaches now the value given by the adjoint mode initialization ($\ln G(\tau = 2)_{m=0} = 2.0246$ and $\ln G(\tau = 2)_{m=1} = 2.1656$ vs $\ln G(\tau \longrightarrow \infty)_{m=0} = 1.9634$ and $\ln G(\tau \longrightarrow \infty)_{m=1} = 2.0856$).

Finally, for a larger horizon time, $\tau = 5$, the initial conditions seem to be already the counterpart adjoint modes of the most unstable direct modes, and the optimal responses are structures that resemble quite the direct modes. At $t = 2\tau$ the evolution ends, since the direct modes are definitely retrieved. The idea that the transient are now led by the adjoint modes can be verified by observing that the energy gain obtained, $\ln G(\tau = 5)_{m=0} = 4.5153$ and $\ln G(\tau = 5)_{m=1} = 4.8311$, and those calculated through adjoint modes initialization, $\ln G(\tau \longrightarrow \infty)_{m=0} = 4.5133$ and $\ln G(\tau \longrightarrow \infty)_{m=1} = 4.8265$, are nearly identical (in Fig.B.18 the points corresponding to $\tau = 5$ overlap the continuous evolutions of the adjoint gain). On the other hand, the model of Eq.(B.29) begins to be valid since the asymptotes defined are almost reached by the optimal response ($\ln G^{+}_{m=0} = 4.505$ and $\ln G^{+}_{m=1} = 4.869$).

As main conclusion, we can say that in general, as was pointed out before, the transient dynamics for all short and finite horizon time studied consist of a fast evolution of the initial condition, which is a characteristic of Orr mechanism that have been already described in the literature.

Bibliography

[1] N. Abdessemed, A. S. Sharma, S. J. Sherwin, and V. Theofilis. Transient growth analysis of the flow past a circular cylinder. *Phys. Fluids*, 21:044103, 2009.

[2] M. Abid, M. Brachet, and P. Huerre. Linear hydrodinamic instability of circular jets with thin shear layers. *Eur. J. Mech. B-Fluid.*, 12(5):683–693, 1993.

[3] E. Achenbach. Vortex shedding from spheres. *J. Fluid Mech.*, 62:209–221, 1974.

[4] A. Antkowiak. *Dynamique aux temps courts d'un tourbillon isolé.* PhD thesis, Université Paul Sabatier de Toulouse, France, 2005.

[5] A. Antkowiak and P. Brancher. Transient energy growth for the lamb-oseen vortex. *Phys. Fluids*, 16(1):L1–L4, 2004.

[6] D. R. Arcas and L. G. Redekopp. Aspects of wake vortex control through base blowing/suction. *Phys. Fluids*, 16 (2):452–456, 2004.

[7] W.E. Arnoldi. The principle of minimized iterations in the solution of the matrix eigenvalue problem. *Q. Appl. Math.*, 9:17–29, 1951.

[8] F. Auguste, D. Fabre, and J. Magnaudet. Bifurcation in the wake of a thick circular disk. *Theor. Comput. Fluid Dyn.*, 24:305–313, 2010.

[9] G.K. Batchelor and E. Gill. Analysis of the stability of axisymmetric jets. *J. Fluid Mech.*, 14:529–551, 1962.

[10] P. W. Bearman. The effect of base bleed on the flow behind a two-dimensional model with a blunt trailing edge. *Aeronaut. Quart.*, 18:207–224, 1967.

[11] E. Berger, D. Scholz, and M. Schumm. Coherent vortex structures in the wake of a sphere and a circular disk at rest and under forced vibrations. *J. Fluids Struct.*, 4:231–257, 1990.

[12] J. L. Best. The influence of particle rotation on wake stability at particle reynolds numbers, Re_p <300-implications for turbulence modulation in two-phase flows. *Int. J. Mult. Flow*, 24:693–720, 1998.

[13] H. M. Blackburn and J. M. Lopez. Modulated rotating waves in a enclosed swirling flow. *J. Fluid Mech.*, 465:33–58, 2002.

[14] P. Bohorquez and L. Parras. Three-dimensional numerical simulation of the wake flow of an afterbody at subsonic speeds. *Theor. Comput. Fluid Dyn.*, 27 (1-2):201–218, 2013.

[15] P. Bohorquez, E. Sanmiguel-Rojas, A. Sevilla, J.I. Jiménez-González, and C. Martínez-Bazán. Stability and dynamics of the laminar wake past a slender blunt-based axisymmetric body. *J. Fluid. Mech.*, 676:110–144, 2011.

[16] V. B. L. Boppana and S. B. Gajjar. Onset of global instability in the flow past a circular cylinder cascade. *J. Fluid Mech.*, 668:304–334, 2011.

[17] G. Bouchet, M. Mebarek, and J. Dušek. Hydrodynamics forces acting on a rigid fixed sphere in early transitional regimes. *Eur. J. Mech. B-Fluid.*, 25:321–336, 2006.

[18] P. Brancher. *Étude numérique des instabilités secondaire de jets.* PhD thesis, Ecole Polytechnique Palaiseau, France, 1996.

[19] C. Brücker. Spatio-temporal reconstruction of vortex dynamics in axisymmetric wakes. *J. Fluids Struct.*, 15:543–554, 2001.

[20] K.M. Butler and B.F. Farrell. Three-dimensional optimal perturbations in viscous shear flow. *Phys. Fluids*, 4(8):1637–1650, 1992.

[21] J. Cai and T. L. Chng. On vortex shedding from bluff bodies with base cavities. *Phys. Fluids*, 21:034109, 2009.

[22] C. Canuto, M. Y. Hussaini, A. Quarteroni, and T. Zhang. *Spectral Methods in Fluid Dynamics.* Springer, 1988.

[23] H. Choi, W.-P. Jeon, and J. Kim. Control of flow over a bluff body. *Annu. Rev. Fluid Mech.*, 40:113–139, 2008.

[24] J.-M. Chomaz. Global instabilities in spatially developing flows: Non-normality and nonlinearity. *Annu. Rev. Fluid Mech.*, 37:357–92, 2005.

[25] W. Coenen, A. Sevilla, and A.L. Sánchez. Absolute instability of light jets emerging from circular injector tubes. *Phys. Fluids*, 20:074104,1–11, 2008.

[26] J. Cohen and I. Wygnanski. The evolution of instabilities in the axisymmetric jet. Part 1. The linear growth of disturbance near the nozzle. *J. Fluid Mech.*, 176:191–219, 1986.

[27] P. Corbett and A. Bottaro. Optimal linear growth in swept boundary layers. *J. Fluid Mech.*, 435:1–23, 2001.

[28] R. Courant and D. Hilbert. Wiley-interscience. *Methods Math. Phys.*, 2:830 pp, 1962.

[29] J. D. Crawford and E. Knobloch. Symmetry and symmetry-breaking bifurcations in fluid dynamics. *Annu. Rev. Fluid Mech.*, 23:341–387, 1991.

[30] D.G. Crighton and M. Gaster. Stability of slowly diverging jet flow. *J. Fluid Mech.*, 77(2):397–413, 1976.

[31] P.G. Drazin. *Introduction to Hydrodynamic Stability.* Cambridge University Press, 2002.

[32] J. Dušek, P. Le Gal, and P. Fraunié. A numerical and theoretical study of the first hopf bifurcation in a cylinder wake. *J. Fluid Mech.*, 264:59–80, 1994.

[33] T. Ellingsen and E. Palm. Stability of linear flow. *Phys. Fluids*, 18(4):487–488, 1975.

[34] D. Fabre, F. Auguste, and J. Magnaudet. Bifurcations and symmetry breaking in the wake of axisymmetric bodies. *Phys. Fluids*, 20:051702, 2008.

[35] D. Fabre and L. Jacquin. Viscous instabilities in trailing vortices at large swirl numbers. *J. Fluid Mech.*, 500:239–262, 2004.

[36] D. Fabre, D. Sipp, and L. Jacquin. Kelvin waves and the singular modes of the Lamb-Oseen vortex. *J. Fluid Mech.*, 551:235–274, 2006.

[37] B. F. Farrell. Optimal excitation of perturbation in viscous shear flow. *Phys. Fluids*, 38(8):2093–2102, 1988.

[38] B. F. Farrell and A. M. Moore. An adjoint method for obtaining the most rapidly growing perturbation to oceanic flows. *J. Phys. Oceanogr.*, 22:338–349, 1992.

[39] J. H. Ferziger and M. Perić. *Computational Methods for Fluid Dynamics*. Springer-Verlag, Berlin, 2002.

[40] B. Fornberg. *A Practical Guide to Pseudospectral Methods*. Cambridge University Press, 1995.

[41] F. Gallaire, M. Ruith, E. Meiburg, J.-M. Chomaz, and P. Huerre. Spiral vortex breakdown as a global mode. *J. Fluid Mech.*, 549:71–80, 2006.

[42] B. Ghidersa and J. Dušek. Breaking of axisymmetry and onset of unsteadiness in the wake of a sphere. *J. Fluid Mech.*, 423:33–69, 2000.

[43] F. Giannetti and P. Luchini. Structural sensitivity of the first instability of the cylinder wake. *J. Fluid Mech.*, 581:167–197, 2007.

[44] M. Golubitsky, V. G. LeBlanc, and I. Melbourne. Hopf birfurcation from rotating waves and patterns in physiscal space. *J. Nonlinear Sci.*, 10:69–101, 2000.

[45] M. Golubitsky, I. Stewart, and D. G. Schaeffer. *Global dynamics of symmetric and asymmetric wakes*. Springer, 1988.

[46] A. Guégan, P. Huerre, and P.J. Schmid. Optimal disturbances in swept hiemenz flow. *J. Fluid Mech.*, 578:223–232, 2007.

[47] K. Gumowski, J. Miedzik, S. Goujon-Durand, P. Jenffer, and J.E. Wesfreid. Transition to a time-dependent state of fluid flow in the wake of a sphere. *Phys. Rev. E*, 77:055308, 2008.

[48] A. Hammond and L. G. Redekopp. Global dynamics of symmetric and asymmetric wakes. *J. Fluid Mech.*, 331:231–260, 1997.

[49] K. Hannemann and H. Oertel Jr. Numerical simulation of the absolutely and convectively unstable wake. *J. Fluid Mech.*, 199:55–88, 1989.

[50] D. S. Henningson and E. Akervik. The use of global modes to understand transition and perform flow control. *Phys. Fluids*, 20:031302, 2008.

[51] D. C. Hill. Adjoint systems ans their role in the receptivity problem for boundary layers. *J. Fluid Mech.*, 292:183–204, 1995.

[52] N. E. Hoskin. The laminar boundary layer on a rotating sphere. *Fifty Years of Boundary Layer Research*, pages 127–131. Braunschweig, 1955.

[53] P. Huerre and P.A. Monkewitz. Local and global instabilities in spatially developing flows. *Annu. Rev. Fluid Mech.*, 22:473–537, 1990.

[54] R. I. Issa. Solution of the implicitly discretized fluid flow equations by operator-splitting. *J. Comput. Phys.*, 62(1):40–65, 1986.

[55] H. Jasak. *Error analysis and estimation in the finite volume method with applications to fluid flows.* PhD thesis, Imperial College, University of Princeton, 1996.

[56] S. Jendoubi and P. J. Strykowski. Absolute and convective instability of axisymmetric jets with external flow. *Phys. Fluids*, 6(9):3000–3009, 1994.

[57] J. Jeong and F. Hussain. On the identification of a vortex. *J. Fluid Mech.*, 285:69–94, 1995.

[58] J. I. Jiménez-González, E. Sanmiguel-Rojas, A. Sevilla, and C. Martínez-Bazán. Laminar flow past a spinning bullet-shaped body at moderate angular velocities. *Under consideration for publication in J. Fluids Struct.*, 2013.

[59] J. I. Jiménez-González, A. Sevilla, E. Sanmiguel-Rojas, and C. Martínez-Bazán. Global modes of the wake behind a spinning bullet-shaped body. *Submitted for publication to Phys. Fluids*, 2013.

[60] T. A. Johnson and V. C. Patel. Flow past a sphere up to reynolds number of 300. *J. Fluid Mech.*, 378:19–70, 1999.

[61] R. R. Kerswell and A. Davey. On the linear instabillity of elliptic pipe flow. *J. Fluid Mech.*, 316:307–324, 1996.

[62] M. R. Khorrami. On the viscous modes of instability of a trailing line vortex. *J. Fluid Mech.*, 225:197–212, 1991.

[63] M. R. Khorrami, M. R. Malik, and R. L. Ash. Application of spectral collocation techniques to the stability of swirling flows. *J. Comput. Phys.*, 81:206–229, 1989.

[64] D. Kim and H. Choi. Laminar flow past a sphere rotating in the streamwise direction. *J. Fluid Mech.*, 461:365–386, 2002.

[65] D. Kim and H. Choi. Laminar flow past a hemisphere. *Phys. Fluids*, 15 (8):2457–2460, 2003.

[66] M. Kiya, H. Ishikawa, and H. Sakamoto. Near-wake instabilities and vortex structures of three-dimensional bluff bodies: a review. *J. Wind Eng. Ind. Aerod.*, 89:1219–1232, 2001.

[67] R. Kobayashi, T. Arai, and M. Nakajima. Boundary layer transition and separation on spheres rotating in axial flow. *Exp. Therm. Fluid Sci..*, 1:99–104, 1988.

[68] R. W. Kruiswyk and J. C. Dutton. Effects of a base cavity on subsonic near-wake flow. *AIAA Journal*, 28:1885–1893, 1990.

[69] T. M. Kulkarni and A. Agarwal. Viscous linear instability of an incompressible round jet. *ISVR Technical Report*, (317), 2007.

[70] R. Kurose and S. Komori. Drag and lift forces on rotating sphere in a linear shear flow. *J. Fluid Mech.*, 384:183–206, 1999.

[71] Y. A. Kuznetsov. *Elements of Applied Bifurcation Theory.* Springer, 1995.

[72] M.T. Landahl. A note on an algebraic instability of inviscid parallel shear flows. *J. Fluid Mech.*, 98(2):243–251, 1980.

[73] L. D. Landau. On the problem of turbulence. *C.R. Acad. Sci. URSS*, 44:311–314, 1944.

[74] L.D. Landau and E.M. Lifshitz. *Fluid Mechanics*. Pergamon Press, 1959.

[75] W. F. Langford, R. Tagg, E. J. Kostelich, H. L. Swinney, and M. Golubitsky. Primary instabilities and bicriticallity in flow between counter-rotating cylinder. *Phys. Fluids*, 31 (4):776–785, 1988.

[76] R.B. Lehoucq, D.C. Sorensen, and C. Yang. *ARPACK Users' Guide. Solution of Large-Scale Eigenvalue Problems with Implicity Restarted Arnoldi Methods*. SIAM, 1998.

[77] S. K. Lele. Compact finite difference schemes with spectral-like resolution. *J. Comput. Phys.*, 103:16–42, 1992.

[78] B. P. Leonard. The ULTIMATE conservative differences cheme applied to unsteady one-dimensional advection. *Comput. Methods Appl. Mech. Eng.*, 88(1):17–74, 1991.

[79] M.P. Lessen and P.J. Singh. The stability of axisymmetric free shear layers. *J. Fluid Mech.*, 60:433–457, 1973.

[80] L. Lesshafft and P. Huerre. Linear impulse response in hot round jets. *Phys. Fluids*, 19:024102–1–024102–11, 2007.

[81] J. M. Lopez, F. Marques, and J. Sanchez. Oscillatory modes in an enclosed swirling flow. *J. Fluid Mech.*, 439:109–129, 2001.

[82] P. Luchini. Reynolds-number-independent instability of the boundary layer over a flat surface: optimal perturbations. *J. Fluid Mech.*, 404:289–309, 2000.

[83] S. Luthander and A. Rydberg. Experimentelle Untersuchungen über den luftwiderstand bei einer um eine mit der Windrichtung parallele Achse rotierende Kugel. *Phys. Z.*, 36:552–558, 1935.

[84] C. Mack. *Global stability of compressible flow about a swept parabolic body*. PhD thesis, Ecole Polytechnique, Laboratoire d'Hydrodynamique (LadHyX), 2009.

[85] J. Magnaudet and G. Mougin. Wake instability of a fixed spheroidal bubble. *J. Fluid Mech.*, 572:311–337, 2007.

[86] L. Mathelin, F. Bataille, and A. Lallemand. Near wake of a circular cylinder submitted to blowing - ii impact on the dynamics. *Int. J. Heat Mass Transfer*, 44:3709–3719, 2001.

[87] P. Meliga, J.-M. Chomaz, and D. Sipp. Global mode interaction and pattern selection in the wake of a disk. *J. Fluid Mech.*, 633:159–189, 2009.

[88] P. Meliga, J.-M. Chomaz, and D. Sipp. Unsteadiness in the wake of disks and spheres: Instability, receptivity and control using direct and adjoint globa lstability analyses. *J. Fluids Struct.*, 25:601–616, 2009.

[89] P. Meliga, D. Sipp, and J.-M. Chomaz. Effect of compressibility on the global stability of axisymmetric wake flows. *J. Fluid Mech.*, 660:499–526, 2010.

[90] P. Meliga, D. Sipp, and J.-M. Chomaz. Open-loop control of compressible afterbody flows using adjoint methods. *Phys. Fluids*, 22:054109, 2010.

[91] A. Michalke. On the inviscid instability of the hyperbolic-tangent velocity profile. *J. Fluid Mech.*, 19(4):543–556, 1964.

[92] A. Michalke. Instabilität eines Kompressiblen Runden Freistrahls unter Berücksichtigung des Einflusses der Strahlgrenzschichtdicke. *Z. Flugwiss.*, 9:319, 1971.

[93] A. Michalke. Survey on jet instability theory. *Prog. Aerosp. Sci.*, 21:159–199, 1984.

[94] A. Michalke and G. Hermann. On the inviscid instability of a circular jet with external flow. *J. Fluid Mech.*, 114:343–359, 1982.

[95] R. Mittal. Planar symmetry in the unsteady wake of a sphere. *AIAA Journal*, 37 (3):388–390, 1999.

[96] Parviz Moin. *Fundamentals of Engineering Numerical Analysis*. Cambridge University Press, 2010.

[97] M. J. Molezzi and J. C. Dutton. Study of subsonic base cavity flowfield structure using particle image velocimetry. *AIAA Journal*, 33:201–209, 1995.

[98] P. A. Monkewitz. A note on vortex shedding from axisymmetric bluff bodies. *J. Fluid Mech.*, 192:561–575, 1988.

[99] T. Morel. Effect of base cavities on the aerodynamic drag of an axisymmetric cylinder. *Aero. Quarterly*, 30:400–412, 1979.

[100] P.J. Morris. The spatial viscous instability of axisymmetric jets. *J. Fluid Mech.*, 77:511–529, 1976.

[101] T Mullin, J. R. T. Seddon, M. D. Mantle, and A. J. Sederman. Bifurcation phenomena in the flow through a sudden expansion in a circular pipe. *Phys. Fluids*, 21:014110, 2009.

[102] R. Natarajan and A. Acrivos. The instability of the steady flow past spheres and disks. *J. Fluid Mech.*, 254:323–344, 1993.

[103] H. Niazmand and M. Renksizbulut. Surface effects on transient three-dimensional flows around rotating spheres at moderate reynolds numbers. *Comp. Fluids*, 32:1405–1433, 2003.

[104] H. Niazmand and M. Renksizbulut. Flow Past a Spinning Sphere With Surface Blowing and Heat Transfer. *J. Fluids Eng.*, 127:163–171, 2005.

[105] K. Oberleithner, M. Sieber, C. N. Nayeri, C. O. Paschereit, C. Petz, H.-C. Hege, B. R. Noak, and I. Wygnanski. Three-dimensional coherent structures in a swirling jet undergoing vortex breakdown: stability analysis and empirical mode construction. *J. Fluid Mech.*, 679:383–414, 2011.

[106] H. Oertel Jr. Wakes behind blunt bodies. *Annu. Rev. Fluid Mech.*, 22:539–564, 1990.

[107] B. Oesterlè and T. Bui Dinh. Experiments on the lift of a spinning sphere in a range of intermediate reynolds numbers. *Exp. Fluids*, 25:16–22, 1998.

[108] D. Ormières and M. Provansal. Transition to turbulence in the wake of a sphere. *Phys. Rev. Lett.*, 83 (1):80–83, 1999.

[109] W.M.F. Orr. The stability or instability of the steady motions of a perfect liquid and of viscous liquid. Part I: A perfect liquid. Part II: A viscous liquid. *P. Roy. Irish Acad. A*, 27(A):9–138, 1907.

[110] S. Ortiz and J. M. Chomaz. Transient growth of secondary instabilities in parallel wakes: anti lift-up mechanism and hyperbolic instability. *Phys. Fluids*, 23:114106, 2011.

[111] K. E. Peyer, A. W. Mahoney, L. Zhang, J. J. Abbott, and B. J. Nelson. *Bacteria-Inspired Microrobots, in Microbiorobotics: Biologically Inspired Microscale Robotic Systems*. Elsevier Inc., Oxford, 2012.

[112] B. Pier. Local and global instabilities in the wake of a sphere. *J. Fluid Mech.*, 603:39–61, 2008.

[113] B. Pier. Periodic and quasiperiodic vortex shedding in the wake of a rotating sphere. *J. Fluids Struct.*, http://dx.doi.org/10.1016/j.jfluidstructs.2012.09.002, 2013.

[114] B. Pier, P. Huerre, and J.-M. Chomaz. Steep nonlinear global modes in spatially developing media. *Phys. Fluids*, 10 (10):2433–2435, 1998.

[115] P. Plaschko. Helical instabilities of slowly divergent jets. *J. Fluid Mech.*, 92(2):209–215, 1979.

[116] K. W. Poon, A. S. H. Ooi, M. Giacobello, and R. C. Z. Cohen. Laminar flow structures from a rotating sphere: Effect of rotating axis angle. *Int. J. Heat Fluid Flow*, 31:961–972, 2010.

[117] A. Prasad and C. Williamson. The instability of the shear layer separating from a bluff body. *J. Fluid Mech.*, 333:375–402, 1997.

[118] C. J. Pregnalato, M. C. Thompson, and K. Hourigan. Flow transitions in the wake of a streawise-rotating sphere. *Conference on Bluff Body Wakes and Vortex-Induced Vibrations (BBVIV3)*, Australia, 2002.

[119] M. Provansal, C. Mathis, and L. Boyer. Bènard-von Kàrman instability: transient and forced regimes. *J. Fluid Mech.*, 182:1–22, 1987.

[120] L. F. Richardson. The approximate arithmetical solution by finite diferences of physical problems involving differential equations with an application to the stresses in a masonry dam. *Trans. R. Soc. London, Ser. A*, 210:307, 1910.

[121] P. J. Roache. Perspective: A method for uniform reporting of grid refinement studies. *J. Fluids Eng.*, 116(3):405–413, 1994.

[122] S. I. Rubinow and J. B. Keller. The transverse force on a spinning sphere moving in a viscous fluid. *J. Fluid Mech.*, 11:447–459, 1961.

[123] D. Ruelle. Bifurcations in the presence of a symmetry group. *Archiv. Ration. Mech. Anal*, 51:136–152, 1973.

[124] J Sahner, T. Weinkauf, and H.-C. Hege. Galilean invariant extraction and iconic representation of vortex core lines. *EUROGRAPHICS - IEEE VGTC Symposium on Visualization (2005). K. W. Brodlie, D. J. Duke, K. I. Joy (Editors)*, 2005.

[125] H. Sakamoto and H. Hanui. A study on vortex shedding from spheres in a uniform flow. *J. Fluids Eng.*, 112:386–392, 1990.

[126] E. Sanmiguel-Rojas, J.I. Jiménez-González, P. Bohórquez, G. Pawlak, and C. Martínez-Bazán. Effect of base cavities on the stability of the wake behind slender blunt-based axisymmetric bodies. *Phys. Fluids*, 23:114103–11, 2011.

[127] E. Sanmiguel-Rojas, A. Sevilla, C. Martínez-Bazán, and J.-M. Chomaz. Global mode analysis of axisymmetric bluff-body wakes: Stabilization by base bleed. *Phys. Fluids*, 21:114102, 2009.

[128] H. Schlichting. Die laminare Strömung um einen axial angeströmten rotierenden Drehkörper. *Ingenieur-Archiv*, 21(4):16–33, 1953.

[129] P. J. Schmid. Dynamic mode decomposotion of numerical and experimental data. *J. Fluid Mech.*, 656:5–28, 2010.

[130] P. J. Schmid and D. S. Henningson. *Stability and Transition in Shear Flows*. Springer-Verlag, 2001.

[131] L Schouveiler and M. Provansal. Periodic wakes of low aspect ratio cylinders with free hemispherical ends. *J. Fluids Struct.*, 15:565–573, 2001.

[132] L Schouveiler and M. Provansal. Self-sustained oscillations in the wake of a sphere. *Phys. Fluids*, 14(11):3846–3854, 2002.

[133] M. Schumm, B. Berger, and P. A. Monkewitz. Self-excited oscillations in the wake of two-dimensional bluff bodies and their control. *J. Fluid Mech.*, 271:17–53, 1994.

[134] V. Schwarz, H. Bestek, and H. Fasel. Numerical simulation of nonlinear waves in the wake of an axisymmetric bluff body. *In 25th AIAA Fluid Dynamics Conference. AIAA Paper*, pages 94–2285, 1994.

[135] A. Sevilla and C. Martínez-Bazán. Vortex shedding in high reynolds number axisymmetric bluff-body wakes: Local linear instability and global bleed control. *Phys. Fluids*, 16:3460–3469, 2004.

[136] A. Sevilla and C. Martínez-Bazán. A note on the stabilization of bluff-body wakes by low density base bleed. *Phys. Fluids*, 18:098102–4, 2006.

[137] G. J. Sheard, M. C. Thompson, and K. Hourigan. Asymmetric structure and non-linear transition behaviour of the wakes of toroidal bodies. *Eur. J. Mech. B-Fluid.*, 23(1):167–179, 2004.

[138] A. R. Shenoy and C. Kleinstreuer. Flow over a thin circular disk at low to moderate reynolds numbers. *J. Fluid Mech.*, 605:253–262, 2008.

[139] P.J.R. Strange and D.G. Crighton. Spinning modes on axisymmetric jets. part 1. *J. Fluid Mech.*, 134:231–245, 1983.

[140] J. T. Stuart. On the non-linear mechanics of hydrodynamic stability. *J. Fluid Mech.*, 4:1–21, 1958.

[141] P. K. Sweby. High resolution schemes using flux limiters for hyperbolic conservation laws. *SIAM J. Numer. Anal.*, 21(5):995–1011, 1984.

[142] S. Taneda. Visual observation of the flow past a sphere at reynolds numbers between 10^4 and 10^6. *J. Fluid Mech.*, 85:187–192, 1978.

[143] J. Tchoufag, J. Magnaudet, and D. Fabre. Linear stability and sensitivity of the flow past a fixed oblate spheroidal bubble. *Phys. Fluids*, 25:054108–24, 2013.

[144] A. Tezuka and K. Suzuki. Three-dimensional global linear stability analysis of flow around a spheroid. *AAIA Journal*, 44(8):1697–1708, 2006.

[145] V. Theofilis. Advances in global linear instability analysis of nonparallel and three-dimensional flows. *Prog. Aerosp. Sci.*, 39:249–315, 2003.

[146] V. Theofilis. Global linear instability. *Annu. Rev. Fluid Mech.*, 43:319–352, 2011.

[147] M. C. Thompson and P. Le Gal. The stuart-landau model applied to wake transition revisited. *Eur. J. Mech. B-Fluid.*, 23:219–228, 2004.

[148] M. C. Thompson, T. Leweke, and M. Provansal. Kinematics and dynamics of a sphere wake transition. *J. Fluids Struct.*, 15:575–585, 2001.

[149] A. Tomboulides and S. Orszag. Numerical investigation of transitional and weak turbulent flow past a sphere. *J. Fluid Mech.*, 416:45–73, 2000.

[150] A .E. Trefethen, L. N. .and Trefethen, S. C. Reddy, and T. A. Driscoll. Hydrodynamic stability without eigenvalues. *Science*, 261:578–584, 1993.

[151] L. N. Trefethen. *Finite Difference and Spectral Methods for Ordinary and Partial Differential Equations*. Unpublished text, 1996.

[152] C. Tropea, A. L. Yarin, and J. F. Foss, editors. *Springer Handbook of Experimental Fluid Mechanics*. Springer-Verlag, Berlin, 2007.

[153] P. R. Viswanath. Flow management techniques for base and afterbody drag reduction. *Prog. Aerosp. Sci.*, 32:79–129, 1996.

[154] J. Wan, A. Fan, K. Maruta, Y. Yao, and W. Liu. Experimental and numerical investigation on combustion characteristics of premixed hydrogen/air flame in a micro-combustor with a bluff body. *Int. J. Hydrogen Energy*, 37:19190–19197, 2012.

[155] A. Weickgenannt and P. A. Monkewitz. Control of vortex shedding in an axisymmetric bluff body wake. *Eur. J. Mech. B-Fluid.*, 19:789–812, 2000.

[156] J. A. C. Weideman and S. C. Reddy. A MATLAB differentiation matrix suite. *ACM Trans. Math. Softw.*, 26(4):465–519, 2000.

[157] C. H. K. Williamson. Vortex dynamics in the wake cylinder wake. *Annu. Rev. Fluid Mech.*, 28:477–539, 1996.

[158] C. J. Wood. The effect of base bleed on a periodic wake. *J. R. Aeronaut. Soc.*, 68:477–482, 1964.

[159] C. J. Wood. Visualization of an incompressible wake with base bleed. *J. Fluid Mech.*, 29:259–272, 1967.

[160] M. L. Xie and J. Z. Lin. An efficient numerical solution for linear stability of circular jet: A combination of Petrov-Galerkin spectral method and exponential coordinate transformation based on Fornberg's treatment. *Int. J. Numer. Meth. Fluids*, 61:780–795, 2009.

[161] M. H. Yu and P. A. Monkewitz. The effect of nonuniform density on the absolute instability of two-dimensional inertial jets and wakes. *Phys. Fluids*, 2:1175–1181, 1990.

[162] L. Zhao, X. Mao, and S. Yang. Transient energy growth in flow past a rotating cylinder. *Europhys. Lett.*, 97:34003, 2012.

Universidad de Jaén / Departamento de Ingeniería Mecánica y Minera / July 2013

PhD Thesis Study of the stability of jets and wakes

Application to the wake past slender bodies with blunt trailing edge

José Ignacio Jiménez González